PERFORMANCE ANALYSIS OF MLGNR AS VLSI INTERCONNECTS

A Thesis Submitted in Fulfillment of the Requirement for the Award of the Degree of

DOCTOR OF PHILOSOPHY

Submitted By

TAJINDER KAUR

Reg. No. 901506024

Under Supervision of

Dr. Mayank Kumar Rai
Associate Professor
ECED

Prof. Rajesh Khanna
Professor
ECED

Department of Electronics and Communication Engineering
THAPAR INSTITUTE OF ENGINEERING AND TECHNOLOGY, PATIALA, PUNJAB

Jan, 2021

DECLARATION

I, Tajinder Kaur hereby declare that the work presented in this thesis entitled "PERFORMANCE ANALYSIS OF MLGNR AS VLSI INTERCONNECTS" in fulfillment of the requirement for the award of degree of Doctor of Philosophy submitted at the Department of Electronics and Communication Engineering, Thapar Institute of Engineering and Technology, Patiala is an authentic record of work carried out under supervision of Dr. Mayank Kumar Rai, Associate Professor, ECED and Prof. Rajesh Khanna, Professor, ECED from January, 2016 to January, 2021. The matter presented in this has not been submitted either in part or full to any other university or institute for the award of any other degree.

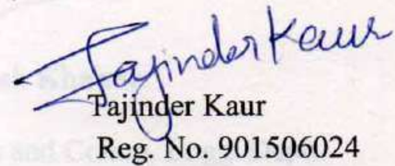

Date: 25/01/2021

Tajinder Kaur
Reg. No. 901506024

CERTIFICATE

It is certified that the work contained in the thesis titled "PERFORMANCE ANALYSIS OF MLGNR AS VLSI INTERCONNECTS" by Tajinder Kaur [Regd. No. 901506024] has been carried out under my/our supervision and that this work has not been submitted elsewhere for any other degree.

Dr. Mayank Kumar Rai
Associate Professor
Electronics and Comm. Engg. Deptt.
TIET, Patiala

Date: 25/01/2021

Prof. Rajesh Khanna
Professor
Electronics and Comm. Engg. Deptt.
TIET, Patiala

Date: 25/01/2021

Dedicated to my Parents and Children

ACKNOWLEDGEMENT

First and foremost, praises and thanks to the God, the Almighty, for His showers of blessings throughout my research work to complete the research successfully.

I would like to express my deep and sincere gratitude to my research supervisors, Dr. Mayank Kumar Rai, Ph.D., Associate Professor and Dr. Rajesh Khanna, Ph.D., Professor, Department of Electronics and Communication, TIET, Patiala for giving me the opportunity to do research and providing invaluable guidance throughout this research. Their dynamism, vision, sincerity and motivation have deeply inspired me. They have taught me the methodology to carry out the research and to present the research works as clearly as possible. It was a great privilege and honor to work and study under their guidance. I am extremely grateful for what they have offered me. I would also like to thank them for their moral support, empathy, and great sense of humor. I am extending my heartfelt thanks to their families for their acceptance and patience during the discussion I had with them on research work and thesis preparation.

Besides my supervisor, I would like to thank the rest of my thesis committee: Dr. Karmjit Singh Sandha, Assistant Professor, ECED, Dr. Rishikesh Pandey, Assistant Professor, ECED and Dr. Seema Bawa, Professor, CSED & Dean of Student Affair (DOSA), TIET for their insightful comments and encouragement, but also for the hard question which incented me to widen my research from various perspectives. I express my sincere gratitude to worthy director Prof. Prakash Gopalan, and Professor & head ECED, Dr. Alpana Agarwal TIET, Patiala for their kind support and co-operation.

I am extremely grateful to my respected parents and siblings for their prayers, care and sacrifices for educating and preparing me for my future. I am very much thankful to my father-in-law, Dr. Mani Singh and husband Jagtar Singh for their unending encouragement, understanding and continuing support to complete this research work. My Special thanks goes to my friend Dinesh Sharma, Assistant Professor (Contractual –III) ECED, TIET, Patiala for the keen interest shown to complete this thesis successfully. I would like to say thanks to my labmates and research colleagues for their constant encouragement. I also thank all the staff of Research section of TIET, Patiala for their genuine support throughout this research work.

Finally, my thanks go to all the people who have supported me to complete the research work directly or indirectly.

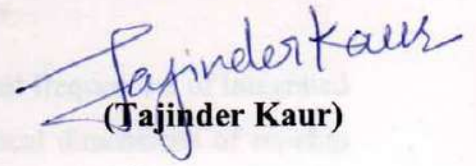

Date: 25/01/2021

(Tajinder Kaur)

Place: Patiala

ABSTRACT

Due to rapid scaling of interconnect dimensions and increased operational frequencies of integrated Circuits (ICs) in the deep submicron (DSM) regime, the lateral and vertical dimensions of on-chip interconnects are reduced and approached the mean-free path of electron, which is about 40 nm for copper (*Cu*) at room temperature. Therefore, the on-chip interconnect delay dominates over the device delay due to its excessive values of equivalent electrical parameters (e.g. *R, L* and *C*) in high-performance very large-scale integrated (VLSI) circuits. The increasing resistivity of *Cu* (due to size effects) together with its low current density (~10^6 A/cm^2) have resulted in its degraded interconnect performance in terms of delay, power dissipation and crosstalk. Hence, the semiconductor industries are looking for an alternative to *Cu* in the DSM regime. Additionally, it has become essential to find a material that is appropriate for potential on-chip interconnect applications to design a high-performance ICs.

Multilayer graphene nanoribbon (MLGNR) viz. a graphene-based carbon nanomaterial has emerged as a potential interconnect material. Graphene that recently drawn considerable attention as a possible alternative for interconnects in the developments of next-generation ICs, which exhibits outstanding physical, mechanical, thermal and electrical properties. Therefore, MLGNR based interconnects have been proposed as the most promising alternative to *Cu* interconnects at DSM technology nodes.

The present work studied the impact of temperature on the performance analysis of capacitively coupled MLGNR interconnects in terms of propagation-delay, power dissipation, power-delay-product (PDP), dynamic crosstalk, functional crosstalk and frequency-spectrum of crosstalk-induced noise at a technology node of 14 *nm*. For this analysis, undoped (neutral) MLGNR (U-MLGNR) as well as intercalation-doped MLGNR (ID-MLGNR) doped with acceptor type intercalate, for instance, stage-II *arsenic pentafluoride* (AsF_5) and *ferrous chloride* ($FeCl_3$), are considered. A driver-interconnect-load (DIL) configuration is employed, in which interconnect is modeled with a temperature-dependent equivalent single conductor (ESC) model. In DIL configuration, for an interconnect line the driver is actuated by a CMOS inverter and load is actuated by a lumped capacitive load (C_L).

A similar studies of aforementioned performance matrices are carried out for capacitively coupled interconnects of mixed carbon-nanotube bundle (MCB) and *Cu*. Based on these performance matrices, the performance of ID-MLGNR interconnects is further compared with their MCBs and *Cu* counterparts at 14 *nm* technology node. Four different structures of MCB viz. MCBs (1-4) with and without tunneling effects are considered. The SPICE simulation results reveal that for about 1*mm* long global interconnect, in single-interconnect configuration, stage-II AsF_5 ID-MLGNR with nearly specular edges have lower delay, power dissipation and PDP (power-delay-product) in comparison to MCBs (1-4) with tunneling effects and conventional *Cu*, over a temperature range from 300 K-500 K. Among the MCBs (1-4) structures, MCB-1 consistently gives better performance in terms of propagation delay within a temperature range from 300 K-500 K. Moreover, for a varied temperature range from 300 K to 500 K,

a significant average relative delay improvement is observed for ID-MLGNR interconnects in comparison to the best delay structure of MCBs i.e. MCB-1 and *Cu* interconnects.

Also, the influence of temperature is examined on the crosstalk performance of the adjacent interconnects of AsF_5 ID-MLGNR. Both functional crosstalk-induced noise and dynamic crosstalk-induced delay in two-coupled interconnects configuration of ID-MLGNR are analyzed. For the specified temperature range of 300 K to 500 K, in case of crosstalk-induced noise, the AsF_5 ID-MLGNR based long interconnects demonstrates superior performance to its MCBs and *Cu* counterparts. Moreover, the temperature-dependent crosstalk-induced delay is observed less with ID-MLGNR in comparison with both MCB and *Cu* interconnects.

Using the temperature-dependent (TD) and temperature-independent (TI) circuit models, the variation of the time duration of crosstalk-induced overshoot at victim's output is also studied at different interconnect lengths (from 200 μm to 1000 μm) of ID-MLGNR. It is noted that the width of the noise pulse obtained using TD circuit models is always less as compared to that obtained using TI circuit models for the entire length of interconnect.

Additionally, the present work investigates the impact of GNR's edge shape in an armchair (AC) and zigzag (ZZ) structures on crosstalk performance of U-MLGNR and ID-MLGNR (both AsF_5 and $FeCl_3$ intercalated) interconnects. A capacitively-coupled DIL configuration is employed to analyse both the functional crosstalk and dynamic crosstalk. It is observed that over a temperature range from 300 K to 500 K, crosstalk-induced low noise peaks in ID-MLGNRs are obtained with ZZ-edges as compared to U-MLGNR. Whereas, the time duration of crosstalk-induced noise is small for ID-MLGNRs with AC-edges. The smaller values of propagation delay and crosstalk-induced delay are obtained with ID-MLGNR (in particular with AC-edges) as compared to U-MLGNR and MCB. It is also observed that AsF_5-intercalated ID-MLGNR outperforms $FeCl_3$-intercalated ID-MLGNR in terms of crosstalk-induced noise and delay.

Furthermore, an analytical frequency-domain model for the capacitively coupled interconnects of MLGNR and MCB is developed. The proposed model provides physical insight into the transient behaviour of coupled interconnects i.e., the input-output transfer function (derived using the fourth-order pade's approximations) of coupled interconnects under dynamic switching conditions is used to analyze its 3-dB bandwidth (BW), delay and stability performance. From the obtained results, it is noted that among the U-MLGNR, ID-MLGNR (viz. AsF_5-intercalated and $FeCl_3$- intercalated), MCB and *Cu* interconnects, AsF_5- intercalated ID-MLGNR exhibits best 3-dB BW performance. Based on the Nyquist stability criterion for relative stability, interconnects of ID-MLGNR are found to be more stable than their U-MLGNR and MCB counterparts, but less stable than *Cu*. Also, a frequency-domain model for complementary metal oxide semiconductor (CMOS) gate driven single MLGNR interconnect is derived. It is noted that using the proposed CMOS-gate based model, a 3-dB BW improvement of 12.25× is obtained with global length (≈1000 μm) AsF_5-doped-MLGNR with respect to linear resistive model. Further, the investigations on temperature-dependent frequency-domain behavior of the capacitively-coupled interconnects under functional switching conditions reveal that the coupled

interconnects of AsF_5-intercalated ID-MLGNR with armchair edges are highly capable of filtering out the noise frequency components with rise in temperature.

The prime objective of this study is to explore the potential of ID-MLGNR as an eminent interconnect material for the technology node defined in the DSM regime (e.g. 14 *nm*). Under the ITRS projection, the performance of the single and coupled ID-MLGNR interconnects is predicted and the results are compared with its *Cu* and MCB counterparts. The results offer valuable insights into the advantages of ID-MLGNR interconnects in the DSM regime.

TABLE OF CONTENTS

Sr. No	Name of the Chapters	Page No
	Declaration………………………………………………………………………………	ii
	Certificate……………………………………………………………………………….....	iii
	Acknowledgement………………………………………………………………………….....	v
	Abstract………………………………………………………………………………………	vi-vii
CHAPTER 1	Introduction and Problem Statements	1-5
1.1	Introduction	1-3
1.2	Problem Statements	3
1.3	Organization of the Thesis	3-5
CHAPTER 2	Prospects of MLGNR as Next Generation On-Chip Interconnects: A Review	6-31
2.1	Introduction	6
2.2	Copper (Cu) as On-Chip Interconnects	6-8
2.3	MLGNR as On-Chip Interconnects	8-12
2.3.1	Fabrication Challenges and Key Issues in GNR Interconnect	9-11
2.3.2	Intercalation Doping in GNR	11-12
2.4	Performance of MLGNR Interconnect	12-28
2.4.1	Single Line Interconnect Performance	12-20
2.4.1.1	Doped and Undoped MLGNR	12-16
2.4.1.2	Temperature-dependent Performance	16-17
2.4.1.3	Frequency-dependent Analysis	17-20
2.4.2	Crosstalk in Adjacent Interconnect Lines	20-28
2.4.2.1	Key Parameters Affecting Crosstalk	20-21
2.4.2.2	Crosstalk in Doped and Undoped MLGNR	21-26
2.4.2.3	Temperature-dependent Crosstalk	26-28
2.5	Interconnect Performance of Other Graphene-based Materials	28-30
2.6	Conclusion	30-31
CHAPTER 3	Temperature Dependent Performance of Single-Line Multilayer Graphene Nanoribbon Interconnect	32-51
3.1	Introduction	32-33
3.2	Temperature Dependent ESC Models of MLGNR Interconnects	33-43
3.2.1	Equivalent RLC Models of MLGNR Interconnects	33-39
3.2.2	ESC Modeling of MCB with Spatial Arrangement	39-43

3.3	Temperature Dependent Impedance Analysis for Nearly Specular ID-MLGNR, four Different Structures of MCB, and *Cu* Interconnects	43-46
3.4	Temperature-Dependent Performance Analyses	46-50
3.4.1	Effect of Tunneling Conductance on MCB Performance	46-48
3.4.2	Temperature-dependent Delay, Power Dissipation, and PDP Analysis of ID-MLGNR, MCB and *Cu* Based Interconnects	48-50
3.5	Conclusion	51
CHAPTER 4	Temperature-Dependent Crosstalk Analysis in Coupled Interconnects of Intercalation Doped Multilayer Graphene Nanoribbon	52-67
4.1	Introduction	52-53
4.2	Impedance Analysis of Interconnects Based on Numerical Evaluation of Temperature-Dependent Circuit Parameters	53-56
4.3	Influence of Temperature on Crosstalk Effect	56-66
4.4	Conclusion	66-67
CHAPTER 5	Effect of Armchair and Zigzag Edges on Functional and Dynamic Crosstalk Noise in Coupled Interconnects of ID-MLGNR	68-79
5.1	Introduction	68-69
5.2	Model for Discrete Energy Level in AC- and ZZ-GNR	69
5.3	Analysis of Temperature Dependent Circuit Models	69-73
5.4	Temperature Dependent Crosstalk Analysis	74-79
5.5	Conclusion	79
CHAPTER 6	Temperature-Dependent Frequency-Domain Crosstalk Model for ID-MLGNR and MCB	80-101
6.1	Introduction	80-81
6.2	Circuit Model of Capacitively Coupled Interconnects	81-82
6.3	Frequency-Domain Crosstalk Model	82-89
6.4	Frequency and Time Domain Analysis of Coupled Interconnects	89-95
6.5	Frequency Domain Analysis of CMOS Gate Driven MLGNR Interconnect	95-98
6.6	Frequency Spectrum Analysis of Functional Crosstalk Noise	98-101
6.7	Conclusion	101
CHAPTER 7	Conclusion and Future Scope	102-108
7.1	Introduction	102
7.2	Results Summary	102
7.3	Temperature-Dependent Performance of Single-Line Multilayer Graphene Nanoribbon Interconnect	102-103
7.4	Temperature-Dependent Crosstalk Analysis in Coupled Interconnects of Intercalation Doped Multilayer Graphene Nanoribbon	103-104

7.5	Effect of The Armchair and Zigzag Edges on Functional and Dynamic Crosstalk Noises in Coupled Interconnects of ID-MLGNR	105-106
7.6	Temperature Dependent Frequency-Domain Crosstalk Model for ID-MLGNR and MCB	106
7.7	Main Research Contributions	107
7.8	Future Scope of the Work	108

References……………………………………………………………………………… 109-122

List of Publications………………………………………………………………………… 123

LIST OF TABLES

Sr. No	Table Details	Page No
Table 3.1	*Simulation parameters (2013) [118].*	44
Table 3.2	*Number of SWCNTs and MWCNTs in MCBs (1-4) structures for global level interconnect width = 24 nm and height = 56 nm. Technology node = 14 nm. SWCNT diameter = 1 nm, and MWCNT diameter = 8 nm [98].*	45
Table 3.3	*Percentage delay penalty (D) in four different structures of MCBs due to tunneling effects at* ℓ *= 1000 μm. R- resistance without tunneling effect.* R^T*- resistance with tunneling effect.*	48
Table 3.4	*Percentage of power dissipation penalty for MCB (1-4) relative to MCBW (1-4).*	48
Table 3.5	*Average relative delay improvement for ID-MLGNR based long interconnect (~1mm).*	50
Table 3.6	*A comparative PDP (*$\times 10^{-15}$ *W-s) for ID-MLGNR, MCB (1-4), and Cu interconnects.*	51
Table 4.1	*Interconnect parameters of ID-MLGNR, MCBs 1-4, and Cu at 14 nm technology node, at the global length of 1000 μm. Here U and ID indicate undoped and intercalation-doped MLGNR, respectively.*	55
Table 4.2	*Peak and width of the F-XT induced overshoot, undershoot, and fall glitch in ID-MLGNR, MCB (1-4) and Cu, at interconnect length of 1000 μm, for the temperature variation range 300 K - 500 K.*	61
Table 4.3	*Average relative reduction of crosstalk-induced noise in ID-MLGNR using proposed TD model relative to conventional TI model.*	63
Table 4.4	*Average percentage of reduction in D-XT induced EM-delay (EMD) relative to OM-delay (OMD) for ID-MLGNR based interconnects, for a temperature range of 300 K-500 K and rising pulse on aggressor line (0→1), at interconnect length* ℓ *=1000 μm.*	64

Sr. No	Table Details	Page No
Table 5.1	*Discrete energy of sub-bands.*	70
Table 5.2	*Conducting channels as a function of temperature.*	71
Table 6.1	*Impedance parameters for interconnects of MLGNR (U, AsF_5-doped and $Fecl_3$-doped) and MCB-1 at different temperatures.*	81
Table 6.2	*3-dB Bandwidth and 50% rise time for U-MLGNR, ID-MLGNR (AsF_5-doped and $Fecl_3$-doped), MCB and Cu.*	91

LIST OF FIGURES

Sr. No	Figure Details	Page No
Figure 1.1	*Schematic view of the armchair- and zigzag-GNR made from a 2-D graphene sheet [5].*	1
Figure 2.1	*Formation of sigma and pi bond between Hybrid sp^2 carbon atoms [27].*	8
Figure 2.2	*Armchair (AC) and Zigzag (ZZ) GNRs.*	9
Figure 2.3	*The geometry of TC-MLGNR over the ground plane [40].*	11
Figure 2.4	*The geometry of SC-MLGNR over the ground plane [40].*	11
Figure 2.5	*Process steps for the fabrication of ID-MLGNR [42].*	12
Figure 2.6	*Coupled transmission line configuration [65].*	21
Figure 3.1	*Schematic view of stage-II ID-MLGNRs (graphite). The solid line indicates graphene layers, where layers with black circles indicate intercalate layers between graphene layers [10].*	34
Figure 3.2	*Temperature-dependent ESC model of MLGNR interconnects, where dl is the differential element along the interconnect length ℓ.*	34
Figure 3.3	*MFP in GNR as a function of temperature. Various scattering mechanism viz. optical phonon, acoustic phonon, and surface polar phonon of substrate- h-BN, SiO_2, HfO_2 is considered.*	37
Figure 3.4	*Resistance p.u.l. for (a) TC-MLGNR, (b) SC-MLGNR interconnects [14].*	38
Figure 3.5	*Different spatially arranged structure of MCBs (a) MCB-1 (b) MCB-2 (c) MCB-3 (d) MCB-4 [95].*	40
Figure 3.6	*ESC model of the MCB based interconnect [98].*	40
Figure 3.7	*The geometry of MWCNT above the ground Plane [110].*	41
Figure 3.8	*Variation of interconnect resistance with temperature ranging from 300 K to 500 K. Interconnects based on ID-MLGNR, MCB (1-4) and Cu are considered here at global length =1000 μm. The effect of inter-shell tunneling is considered for all structures of MCB. ID-MLGNR interconnect edges are assumed to be almost specular for the global domain.*	45
Figure 3.9	*Variation of inductance with temperature ranging from 300 K-500 K. Four different structures of MCB, ID-MLGNR, and Cu interconnects are considered here for global length =1000 μm.*	46

Sr. No	Figure Details	Page No
Figure 3.10	*Variation of capacitance with temperature ranging from 300K-500K. Four different structures of MCB, ID-MLGNR, and Cu interconnects are considered here for global length =1000 μm.*	46
Figure 3.11	*Effect of tunneling conductance on the propagation delay of four different structures of MCB interconnects at length = 1000 μm.*	47
Figure 3.12	*Effect of tunneling conductance on the power dissipation of four different structures of MCBs interconnects at length = 1000 μm.*	47
Figure 3.13	*Propagation delay of ID-MLGNR interconnects in comparison to MCB-1, MCB-2, MCB-3, MCB-4 and Cu interconnects.*	49
Figure 3.14	*Power dissipation of ID-MLGNR interconnects in comparison to MCB-1, MCB-2, MCB-3, MCB-4 and Cu interconnects.*	50
Figure 4.1	*Interconnect geometry [118] and its equivalent capacitively coupled DIL configuration [95].*	53
Figure 4.2	*(a) Validation of the number of conducting channels (b) validation of temperature coefficient of resistance.*	57
Figure 4.3	*F-XT induced transient response at different temperatures, for (a) ID-MLGNR and (b) Cu interconnects.*	59
Figure 4.4	*F-XT induced transient response at different temperatures, for (a) MCB-1 (b) MCB- 2 (c) MCB-3 (d) MCB-4.*	59
Figure 4.5	*Peaks of F-XT induced rise glitch at different temperatures.*	60
Figure 4.6	*Width of F-XT induced rise glitch at different temperatures.*	60
Figure 4.7	*The width of the F-XT induced overshoot in ID-MLGNR, as a function of interconnects length, using TD models (MFP=1.31 μm) and TI models (MFP=1.06 μm).*	62
Figure 4.8	*D-XT induced signal delay in ID-MLGNR, MCBs (1-4), and Cu interconnects at different temperatures, at (a) even mode (EM) and (b) odd mode (OM) of aggressor-victim switching at ℓ =1000 μm.*	63
Figure 4.9	*Single-line (SL) and crosstalk-induced (XT) delay of ID-MLGNR, MCB-1, and Cu interconnect, at different temperatures of interconnects. Even mode of aggressor-victim switching is considered for D-XT delay analysis at global length (ℓ =1000μm) of interconnects.*	64

Sr. No	Figure Details	Page No
Figure 4.10	*Crosstalk-induced delay-ratio of ID-MLGNR to MCB-1 at different temperatures and lengths of interconnects. EM switching case: Rise on aggressor (0→1).*	65
Figure 4.11	*The variation in XT-delay for (a) EM (b) OM as a function of the process parameter.*	66
Figure 5.1	*Schematic view (a) undoped, (b) stage-I $FeCl_3$-doped [42], and (c) stage-II AsF_5-doped MLGNR [10]. The solid lines and dots indicate graphene and intercalation dopant layers, respectively. (d) Thermally-aware ESC model of MLGNR interconnects, where dl is the differential element along the interconnect length ℓ.*	70
Figure 5.2	*Net MFP as a function of interconnect temperature for undoped, AsF_5-doped and $FeCl_3$-doped MLGNR interconnects.*	71
Figure 5.3	*The equivalent resistance of MLGNR interconnects as a function of temperature at interconnect length of 1mm and technology node 14 nm.*	72
Figure 5.4	*The equivalent inductance of MLGNR interconnects as a function of temperature at interconnect length of 1mm and technology node 14 nm.*	73
Figure 5.5	*The equivalent capacitance of MLGNR interconnects as a function of temperature at interconnect length of 1mm and technology node 14 nm.*	73
Figure 5.6	*Crosstalk-induced transient response as a function of temperature at the remote end terminal on the victim line in capacitively-coupled DIL configuration for different MLGNR interconnects of type undoped, $FeCl_3$-doped and AsF_5-doped, shown in (a), (b) and (c), respectively with AC-edges, and (d), (e) and (f), respectively with ZZ-edges.*	75
Figure 5.7	*Crosstalk-induced fall-glitch peak on the victim line as a function of temperature.*	76
Figure 5.8	*Crosstalk-induced rise-glitch time duration on victim line as a function of temperature.*	77

Sr. No	Figure Details	Page No
Figure 5.9	*Propagation-delay as a function of temperature for different types of MLGNR interconnects. ℓ =1000 μm.*	78
Figure 5.10	*Crosstalk-induced delay of the capacitively-coupled MLGNR and MCB interconnects at the different temperatures, at even mode of aggressor-victim switching. ℓ =1000 μm.*	78
Figure 6.1	*Circuit model of capacitively coupled interconnects [142].*	82
Figure 6.2	*Absolute frequency response for coupled interconnects of U-MLGNR, ID-MLGNR (AsF_5- and $FeCl_3$-doped), MCB and Cu at ℓ= 10 and 1000 μm.*	89
Figure 6.3	*Absolute frequency response for coupled interconnects of AsF_5 ID-MLGNR at ℓ = 1000 μm at different temperatures.*	91
Figure 6.4	*Absolute frequency response for single and coupled interconnects of AsF_5 ID-MLGNR at ℓ= 1000 μm, at T=300 K.*	92
Figure 6.5	*Time-domain response for coupled interconnects of U-MLGNR, ID-MLGNR (AsF_5- and $FeCl_3$-doped), MCB and Cu at T=300 K.*	92
Figure 6.6	*Time-domain response for coupled interconnects of AsF_5-ID-MLGNR at ℓ= 1000 μm, W=24 nm and different temperatures.*	93
Figure 6.7	*Nyquist plot for coupled interconnects of U-MLGNR, ID-MLGNR (AsF_5- and $FeCl_3$-doped), MCB and Cu at ℓ= 1000 μm, T=300 K.*	94
Figure 6.8	*Nyquist plot for coupled interconnects of AsF_5-ID-MLGNR at ℓ=1000 μm and at different temperatures.*	95
Figure 6.9	*The temperature-dependent ESC circuit of an MLGNR interconnect driven by a CMOS driver with a lumped capacitive load [148].*	96
Figure 6.10	*The absolute frequency response of single interconnect of undoped MLGNR at different interconnect lengths of 5 μm, 500 μm and 2500 μm.*	97
Figure 6.11	*The absolute frequency response of single interconnect of AsF_5 ID-MLGNR at different interconnect lengths of 10 μm and 1000 μm.*	98
Figure 6.12	*Normalized crosstalk noise amplitude as a function of normalized frequency in coupled interconnects of (a) U-MLGNR, MCB and Cu and (b) ID-MLGNR (AsF_5- and $FeCl_3$-doped), at ℓ= 1000 μm, T=300 K.*	99

Sr. No	Figure Details	Page No

Figure 6.13 *Normalized crosstalk noise amplitude as a function of normalized frequency in coupled interconnects of (a)-(f) MLGNR (U, AsF_5- and $FeCl_3$-doped), with AC and ZZ edges, respectively, (g) MCB and (h) Cu, at ℓ= 1000 μm and T = 300 K - 500 K.* 100

LIST OF ABBREVIATIONS

VLSI	Very large scale integration
ICs	Integrating circuits
DSM	Deep submicron
MFP	Mean free path
Cu	Copper
CNT	Carbon nanotube
GNR	Graphene nanoribbon
AC	Armchair
ZZ	Zigzag
MLGNR	Multilayer graphene nanoribbon
ESC	Equivalent single conductor
ID-MLGNR	Intercalation doped MLGNR
PDP	Power delay product
MCB	Mixed carbon-nanotube bundle
DIL	Driver interconnect load
SWCNT	Single-walled carbon nanotube
MWCNT	Multi-walled carbon nanotube
U-MLGNR	Undoped-MLGNR
TC-MLGNRs	Top contact MLGNRs
SC-MLGNRs	Side contact MLGNRs
TD	Temperature dependent
TI	Temperature independent
SR	Surface roughness
CMP	Chemical mechanical planarization

MW	Mandelbrot-Weierstrass
EDP	Energy delay product
BP	Backplane
PCB	Printed circuit board
BWD	Bandwidth density
DV	Delay variation
RI	Repeater inserted
ASL	All-spin-logic
SLGNR	single layer GNR
MLG	Multilayer graphene
CVD	Chemical vapor deposition
EBL	Electron beam lithography
AFM	Atomic force microscopy
MTL	Multi-conductor transmission line
Di-SC-MLGNR	Dielectric inserted SC-MLGNR
DFF	D flip-flop
TTF	Time-to-fail
RF	Radio-frequency
MTLT	Multiconductor transmission line technique
MCF	Miller-coupling factor
FDTD	Finite difference time domain
VM	Voltage mode
CM	Current-mode
TSVs	Through-silicon vias
NDP	Noise-delay-product

NBWR	Noise-bandwidth-ratio
RTIM	Reduced thickness interconnect model
CNTFET	Carbon nanotube field-effect transistor
US-FDTD	Unconditionally stable FDTD
Di-SC-MLGNR	Dielectric inserted SC-MLGNR
FIT	Failure in time rate
CHC	Channel hot carrier
SSR	Substrate surface roughness
SWB	Bundled SWCNTs
MWB	Bundled MWCNTs
SPP	Surface polar-phonon
RT	Room temperature
GIC	Graphite intercalation compounds
GNRFETs	Graphene nanoribbon FETs
F-XT	Functional-crosstalk
D-XT	Dynamic- crosstalk
EM	Even mode
OM	Odd mode
EMD	EM delay
OMD	OM delay
SL	Single line
XT	Crosstalk-induced
FFT	Fast Fourier technique

LIST OF SYMBOLS

E_G	Bandgap
p	Edge roughness or edge scattering probability
N	Number of carbon rings
W	Interconnect width
a	Length of carbon bonds in graphene
$\sigma_{in-plane}$	In-plane conductivity
σ_c	C-axis conductivity
E_F	Fermi energy
δ_{sr}	Surface roughness of the underlying dielectric materials
V_S	Voltage ramp
R_S	Thevenin resistance in series,
R_V	Linear resistance
H	Interconnect thickness
d	Dielectric thickness
ε_r	Permittivity of the dielectric
n	Total number of layers in MLGNR
δ	Average interlayer distance between the GNR layers
ℓ	Interconnect length
R_c	Contact resistance
$R_q(T)$	Quantum contact resistance
R_{mc}	Imperfect metal-contact resistance
$\hat{r}_s(T)$	Scattering resistance
$R_{j,mc}$	Imperfect metal-contact resistance of the j^{-th} layer

$R_{j,q}$,	Quantum contact resistance '$R_q(T)$' of the j-th layer
$N_{ch}(T)$	Number of conducting channels
n_c	Conduction sub-bands
n_v	Valence sub-bands
E_j	Highest (lowest) energy of the j-th valance (conduction) sub-bands
k_B	Boltzmann's constant
T	Temperature
λ_{eff}	Electron MFP
h	Planck's constant
q	Electron charge
$\lambda_{\mathrm{AC}}(T)$	Temperature-dependent MFP in graphene due to acoustic phonons
$\lambda_{ABS}^{OP}(T)$	MFP due to absorption of optical phonons
$\lambda_{EMS}^{OP}(T)$	MFP due to emission of optical phonons
ρ_m	Mass density of graphene
v_s	Speed of acoustic phonons
N_s	Concentration of 2-D electron gas in graphene
D_{AC}	Acoustic deformation potential
$\mathcal{V}_f$	Fermi velocity
$\hbar\omega_{OP}$	Optical phonon energy
D_{OP}	Optical deformation potential
$N_{OP,AB}$	Phonon occupation numbers given by Bose–Einstein statistics for absorption processes
$N_{OP,EM}$	Phonon occupation numbers given by Bose–Einstein statistics for emission processes
λ_i^{SPP}	Electron MFP in graphene due to surface polar phonons scatterings

β	Separation between the graphene and substrate
z_0	Vander Waals distance between the polar substrate and GNR
F_i^2	Magnitude of the polarization field called Froehlich coupling
$\hbar\omega_{SO,i}$	Surface polar phonon energy
λ_{net}^{SPP}	Net MFP due to surface polar phonons
λ_i	MFP of the $i^{\text{-th}}$ sub-band in GNR related to scattering at its edges
λ_D	MFP associated with scattering due to defects
n_p	Carrier concentration
ρ_c	C-axis resistivity
$R_{SC\text{-}MLGNR}(T)$	Total resistance of SC-MLGNR
$\hat{l}_k(T)$	Kinetic inductance
$\hat{l}_e$	Magnetic inductance
c_q	Quantum capacitance
c_m	Coupling capacitance
$\hat{c}_q(T)$	Equivalent quantum capacitance
$\hat{c}_e$	Electrostatic capacitance
$C(T)$	Total equivalent temperature-dependent capacitance
$L(T)$	Total equivalent temperature-dependent inductance
W_P	Width of the MWCNT bundle
H_P	Thickness of the MWCNT bundle
D_i	Diameter of a particular shell *i* in MWCNT
$n_{\text{MWCNT}-\text{BUNDLE}}$	Total number of MWCNTs in the bundle
N_{total}	Total number of CNTs in a given structure of MCB
n_{HM}	Number of columns in the bundle
n_{WM}	Number of rows in the bundle

D_P	Maximum outer diameter of isolated MWCNT
y_{ILD}	Height of the bundle from the ground
$n_{\text{SWCNT−BUNDLE}}$	Total number of SWCNTs in the bundle
R_{ti}	Inter-shell tunneling resistance
$R_{BUNDLE}^{X}(T)$	Resistance of MWCNT/SWCNT bundle
$L_{BUNDLE}^{X}(T)$	Inductance of MWCNT/SWCNT bundle
$C_{BUNDLE}^{X}(T)$	Capacitance of MWCNT/SWCNT bundle
C_{CSM}	Coupling capacitance between the bundles of SWCNT and MWCNT
S_{S-M}	Spacing between the two equivalent bundles
α	Temperature coefficient of resistance
ρ_0	Resistivity of *Cu*
C_c	Coupling capacitance between interconnects
$R_{ESC}(T)$	Equivalent resistance
$L_{ESC}(T)$	Equivalent inductance
$C_{ESC}(T)$	Equivalent capacitance
E_m	Discrete energy levels
C_L	Load capacitance
$\boldsymbol{V}$	Voltage vector
$\boldsymbol{I}$	Current vector
$\boldsymbol{Z}$	Impedance matrices
$\boldsymbol{Y}$	Conductance matrices
$\boldsymbol{R_D}$	Driver resistance matrix
$\boldsymbol{C_l}$	Load capacitance matrix
$\boldsymbol{H}$	Input/output transfer function matrix for the two-coupled lines
f_C	Cut-off frequency

CHAPTER 1

INTRODUCTION AND PROBLEM STATEMENTS

1.1 INTRODUCTION

Interconnect plays a crucial role in evaluating the operational speed and total power consumption of very large scale integration (VLSI) circuits. In the deep submicron (DSM) regime, the scaling of technology has increased both the device density and interconnect density, and consequently, current density due to reduction in the lateral and vertical dimensions of on-chip interconnects. This leads to a significant increase in coupling effects in parallel interconnects. However, the approach of the scaling limit to the mean-free-path (MFP) of interconnect material has led to the grain boundary, surface-scattering, diffusive surface scattering, and electro-migration in currently in-use interconnect material; copper (*Cu*). Consequently, the interconnect resistance is increased, and the performance of advanced VLSI interconnect is degraded. Hence, to alleviate this problem, a new alternative is required.

In the past several years, much experimental and theoretical progress in material science have reported that the most optimistic alternative for existing interconnect material (e.g. copper) turns out to be carbon-nanomaterials for future interconnects of advanced IC technology [1]-[5]. Carbon nanomaterials have extraordinary physical properties that make them exciting prospects for a variety of applications in microelectronics/nanoelectronics [6]. Particularly in the nanoelectronics area, carbon nanotube (CNTs) and graphene nanoribbons (GNRs) have aroused a lot of interest in their applications as metallic interconnects due to their extraordinary electrical, thermal, and mechanical properties [7]–[10]. To use CNT in realistic high-speed IC applications, material properties such as the bandgap (E_G) have to be precisely controlled. Although, the presence or absence of a bandgap is a strong function of its chirality [11], and there is currently no straightforward way to control the CNT chirality during its growth. Compared to cylindrical CNTs, GNRs with planar structure can be grown through a silicon-compatible, transfer-free, and *in situ* process [12] thus having no alignment, chirality, and transfer-related issues as encountered by CNT-based circuits [13]. Additionally, from the aspect of large-scale fabrication, it is evident that GNR can be easily controlled or adjusted horizontally in comparison with CNTs. Under such circumstances, GNRs are more suitable than CNTs for building up horizontal interconnects as they are more compatible with the conventional lithography [14].

Unique physical properties of GNR such as extremely high current-carrying capabilities (attributed due to strong sp^2 bonds), long MFP leading to large electrical conductance, and high thermal conductivity makes it strongly capable to provide better interconnect performance than that of *Cu* [5], [15]. The GNRs constitute of graphene sheets. Graphene is a two-dimensional structure with a hexagonal array arrangement of carbon atoms. GNRs are obtained by Nanopatterning 2-D graphene sheets down to narrow ribbons with width $< 50\ nm$. Figure 1.1 shows the schematic view of GNRs made from a 2-D graphene sheet. Based on the edge shape, as indicated in Figure 1.1 with bold black lines, GNRs are classified as an armchair (AC) and zigzag (ZZ) GNRs [5].

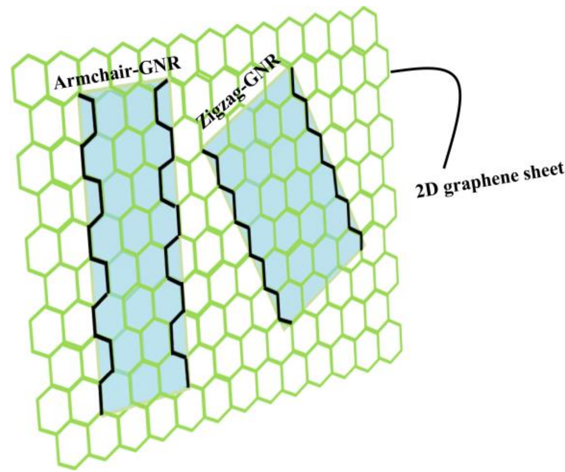

Figure 1.1 Schematic view of the armchair- and zigzag-GNR made from a 2-D graphene sheet [5].

Multilayer graphene nanoribbon (MLGNR) is a potential candidate in nanoscale VLSI interconnects. Based on an equivalent single-conductor (ESC) model, this work presents a temperature-dependent study of the distributed circuit parameters and signal transmission performance of intercalation-doped MLGNR (ID-MLGNR) interconnect in terms of delay, power dissipation, power-delay-product (PDP), crosstalk-induced effects (noise and delay) and frequency-domain behavior at the global domain of interconnects. The interconnect performance of ID-MLGNR is also compared with that of the mixed carbon-nanotube bundle (MCB) and copper (*Cu*), at the 14 *nm* technology node. To explore the reliability issues in the coupled interconnects of ID-MLGNR, a comprehensive analysis of the impact of temperature on the crosstalk performance of ID-MLGNR is performed.

Further, a detailed analysis emphasizing the impact of GNR's edge shape in an armchair (AC) and zigzag (ZZ) structures on crosstalk performance by considering undoped and doped (intercalated with AsF_5 and $FeCl_3$) MLGNR interconnects is presented. A capacitively-coupled driver-interconnect-load (DIL) line configuration is employed to analyze both the functional and dynamic crosstalk at 14 *nm* technology node for global interconnects.

The works reported in the literature have accurately analyzed the performance of optimized MLGNR interconnects in comparison to single-walled carbon nanotube (SWCNT) bundle, isolated multi-walled carbon nanotube (MWCNT) and conventional *Cu* interconnects while taking into account its Fermi energy, edge specularity, interlayer conductance and intercalation doping [19],[21],[22],[56],[57]. However, these works paid less attention to an important parameter that undeniably affects the performance of these interconnects i.e. the effect of temperature variation. Previously, doped MLGNRs have been investigated for single-line propagation-delay, frequency response and bandwidth analysis [23],[24],[30],[31],[43]-[46]. It is reported that crosstalk between coupled interconnects influences their functionality and reliability [56]-[58], [60]-[64]. In the last few decades, to explore the performance of MLGNR as an interconnect material, enormous research and development activities have been dedicated [12]-[77].

However, a detailed study reveals that the focus of the work done is on two aspects. First, the performance of a single doped MLGNR interconnect was evaluated without considering the coupling effect between interconnects. Second, the coupled interconnects of only undoped-MLGNR (U-MLGNR) were considered.

1.2 PROBLEM STATEMENTS

For the accurate evaluation of the crosstalk performance in coupled MLGNR interconnects, the following three essential facts must be taken into account. First, is the feasibility of interconnect fabrication. The known experiments have reported that top-contact (TC)-MLGNRs can be fabricated easily than side-contact (SC)-MLGNRs [22]. Second, the impact of crucial process parameters. The detailed analysis of interconnects beyond 45 *nm* technology node reveals that the temperature of the metals increases due to the cumulative effect of increased resistivity, current density, and the number of global metal-layers. Hence, for designing next-generation interconnects, the thermal issue is a predetermined design criterion. Third, the influence of the physical structure of interconnect on its performance. For instance, for interconnect width beyond 10 *nm*, metallic AC-GNRs possess more significant conductivity as compared to that of ZZ-GNRs. This work presents the temperature-dependent performance evaluation of TC-MLGNRs (undoped, doped) considering both AC and ZZ edged GNRs, and compared it with that of the MCB. The work presented in this thesis meets the following objectives.

1. Development of the temperature-dependent circuit parameters of side-contact and top-contact based MLGNR interconnects.
2. Development of the temperature-dependent crosstalk model of coupled MLGNR interconnects with the application of DIL (driver-interconnect-load).
3. Analysis of the temperature-dependent crosstalk and frequency spectrum, using the developed model, in coupled MLGNR interconnects at 14 *nm* technology node.
4. Comparison of the temperature-dependent and temperature-independent crosstalk analysis in coupled MLGNR interconnects at 14 *nm* technology node.
5. Validation of the temperature-dependent crosstalk analysis in coupled MLGNR interconnects with coupled mixed carbon nanotubes bundle interconnects at 14 *nm* technology node.

1.3 ORGANIZATION OF THESIS

This work mainly presents the detailed analysis of the impact of interconnect temperature, edge roughness (p), edge shape in GNR and intercalation doping on performance matrices of MLGNR interconnect in single-line configuration (viz. propagation delay, power dissipation, and power-delay-product), and in coupled-line configuration (viz. crosstalk-induced delay, crosstalk-induced noise, bandwidth, and stability). The interconnect performance of MLGNR is also compared with that of MCB and *Cu*. The work in this thesis is organized in the following chapters.

Chapter 1 introduces the introduction, objectives and organization of the thesis work.

Chapter 2 summarizes the previous studies conducted to analyze the performance of undoped and doped single MLGNR interconnect in terms of propagation delay, power dissipation, and PDP. In coupled-line configuration how crosstalk-induced effects influence the switching delay, reliability, and stability of MLGNR interconnects, is discussed in detail. Besides, previous investigations in concern to the effect of the process parameters, structural parameters (like MLGNR edge-shape), intercalation doping in MLGNR on its interconnect performance are presented.

Chapter 3*:* In this chapter, the temperature-dependent circuit parameters of side contact and top contact based MLGNR interconnects are derived by considering different types of scattering mechanism. A temperature-dependent analysis of the signal transmission performance of single ID-MLGNR in terms of propagation delay, power dissipation, and power-delay products at the global domain of interconnects is performed based on an equivalent single-conductor (ESC) model of intercalation-doped MLGNR (ID-MLGNR) interconnect. A similar analysis is carried out for MCB interconnects and copper (*Cu*) interconnects and the obtained results are compared with ID-MLGNR interconnects at the 14 *nm* technology node**.** In the present analysis, a stage-II arsenic pentafluoride (AsF_5) ID-MLGNR with nearly specular edges (p=1) and four different structures of MCB viz. MCBs (1-4) with and without tunneling effects are considered. A comparative analysis of the SPICE simulation results, obtained for about 1*mm* long interconnects of ID-MLGNR, MCBs (1-4) and *Cu,* under the influence of temperature variation from 300 K to 500 K is performed.

Chapter 4: This chapter explores the temperature-dependent performance evaluation due to crosstalk in coupled interconnects of ID-MLGNR. The crosstalk performance of ID-MLGNR is investigated in terms of crosstalk-induced noise and crosstalk-induced delay under different switching conditions of the aggressor and victim. Other metallic interconnect materials viz. MCB and *Cu* are also analyzed similarly. The temperature-dependent crosstalk performance of ID-MLGNR is compared with that of MCB and *Cu*, at different temperatures from 300 K to 500 K. Further, considering the temperature-dependent (TD) and temperature-independent (TI) models, the variation of the time duration of crosstalk-induced overshoot at victim's output is also studied at different interconnect lengths of ID-MLGNR.

Chapter 5 presents a detailed analysis that emphasizes the impact of GNRs edge shape i.e. AC and ZZ, on crosstalk performance of undoped and doped (intercalated with AsF_5 and $FeCl_3$) MLGNR interconnects, considering the temperature variation from 300 K to 500 K. A capacitively coupled driver-interconnect-load (DIL) line configuration is employed to analyze both the functional and dynamic crosstalk at 14 *nm* technology node for global interconnects (~1 *mm*). The crosstalk performance of MLGNR interconnects, under the influence of edge shape, is compared with that of MCB interconnects. The impact of AC and ZZ edge shape in GNR is also studied on the propagation delay of undoped and doped single MLGNR interconnect.

Chapter 6 presents an analytical frequency-domain model for the coupled interconnects of MLGNR and MCB. The proposed model is based on a temperature-dependent equivalent single conductor (ESC) model, which provides physical insight into the transient behavior of coupled interconnects i.e., the derived input-output transfer function of the aggressor line under dynamic switching conditions can be used to analyze its bandwidth, delay and stability performance. The transfer function of the capacitively coupled interconnects is derived using the fourth-order pade's approximations. Using the transfer function, the bandwidth and step response for undoped and AsF_5-doped MLGNR interconnects are analyzed. Based on the Nyquist stability criterion, the stability of undoped and doped MLGNR is analyzed and compared with their MCB counterparts. Further, the temperature-dependent, frequency-domain behavior of the capacitively coupled interconnects under functional switching conditions is also studied.

Finally, chapter 7 summarizes the research work based on undoped - and ID-MLGNR in the preceding chapters, and briefly concludes the study done. A few suggestions regarding the future work that can be done to alleviate the current in use interconnect problems are given here.

CHAPTER 2

PROSPECTS OF MLGNR AS NEXT GENERATION ON-CHIP INTERCONNECTS: A REVIEW

2.1 INTRODUCTION

The realistic scenario with global on-chip interconnects in deep submicron (DSM) technology nodes is unfavorable for the high-speed ICs. At the global level, an increase in the interconnect cross-sectional area reduces its resistance, whereas an increase in the interconnect length makes it more resistive, and thus increase the interconnect delay. Additionally, the growing density of on-chip interconnects and reduction in chip-size results in the crosstalk effects even in the non-adjacent interconnects. The geometry and material of interconnect and the adopted technology node are the key factors that enhance the crosstalk effect. As technology scales into the DSM regime, the interconnect dimension approaches to mean-free-path (MFP), and it leads to the grain boundary, surface-scattering, diffusive surface scattering, and electro-migration effects in existing interconnect material; copper(*Cu*) [7]. As a result, *Cu* resistivity increases, causing degradation in its interconnect performance in terms of propagation delay, power dissipation [16], and crosstalk [17]. Hence, to alleviate these problems, a new alternative is required. Unlike *Cu* with MFP ~ 40 *nm* [7], CNT and GNR with large MFP (~ 1 μm) are two recently proposed carbon-nanomaterials consisting of one of the physically available carbon allotropes-graphene [18]. Between these two carbon-based nanomaterials (CNTs and GNRs), GNRs are found to be more compatible with conventional lithography techniques (due to their planar structure). Therefore, the most promising alternative to *Cu* interconnects in the DSM regime turns out to be GNR based interconnects [10], [19]. The present literature reviews the performance of currently-in-use *Cu* interconnects, recently proposed doped (D) and undoped (U) MLGNR, and MCB based interconnects, at DSM technology nodes. Like crosstalk, the temperature is also reported to affect the performance of interconnects significantly in a configuration of single line and coupled lines. Therefore, under the influence of varying temperature, the performance of these on-chip interconnects is studied in single-line and coupled-line configuration, for performance matrices viz. propagation delay, power dissipation, PDP, crosstalk-induced effects, stability and bandwidth.

2.2 COPPER (Cu) AS ON-CHIP INTERCONNECTS

The resistivity of on-chip *Cu* interconnects is increased due to size effects, and further worsens with surface roughness (SR). Through efficient fabrication techniques like chemical mechanical planarization (CMP), the roughness of the top and bottom surface of *Cu* interconnects can be controlled to a large extent. However, it is difficult to control sidewall roughness, which leads to an increase in the capacitance and, consequently, to an increase in interconnect delay. Kumar *et al.* [20] characterize the scale-independent natural SR in *Cu* interconnects through an efficient approach based on Mandelbrot-

Weierstrass (MW) fractal function. SR affects the parasitics of interconnect and hence their performance matrices, thereby, the signal integrity of interconnect is affected. It is noted that as the technology scales from 45 *nm* to 13 *nm*, the resistance of rough *Cu* interconnect increases by 2.6×, and the capacitance and the inductance increase by 13% and 37% as technology shrinks from 45 *nm* to 7 *nm*. Additionally, the 5× and 5.7× increase in propagation delay and energy-delay-product (EDP), respectively is observed with technology scaling from 45 *nm* to 7 *nm*.

The authors in [21] extended their study to quantitatively evaluate the effects of SR in on-chip *Cu* interconnects at several GHz frequency regimes, based on the backplane (BP) and printed circuit board (PCB) approach. It is noted that 50 *cm* long BP interconnects at 100 GHz exhibited the 2.5× and 2.6× larger delay and energy budget, respectively due to SR. Whereas, with PCB interconnects these penalties respectively are 2.5× and 2.6×. Besides, SR also increased the computational overheads required in simulating the BP and PCB interconnects.

The influence of SR in on-chip *Cu* interconnects is more prominent at sub-22 *nm* technology nodes due to size effects, grain-boundary and surface-boundary scatterings. To benchmark the performance of *Cu* interconnects, it is of utmost importance to consider its realistic SR profile. The authors in [22] first studied the effects of crosstalk in on-chip global *Cu* interconnects with realistic SR profile at sub-22 *nm*, i.e., 13 *nm* and 7 *nm* technology nodes. It is reported that the insertion of an optimum number of repeaters in rough *Cu* interconnects can improve their crosstalk performance. It is revealed that FINFET driven rough *Cu* interconnects exhibit the increase of 17× and 9× in their worst-case crosstalk delay and power dissipation, respectively as the technology node shrinks to 7 *nm*.

Additionally, SR causes a bandwidth density (BWD) reduction of 17× for global *Cu* interconnects. Encouragingly, at a 7 *nm* technology node, through repeater insertion the crosstalk delay and PDP are observed to improve by 85% and 99%. However, at a 13 *nm* technology node, the penalties in the performance matrices of rough *Cu* interconnects are noted to marginal. These findings signify the degraded performance of rough *Cu* interconnects with technology scaling from 13 *nm* to 7 *nm*.

The scaling of technology has resulted in the scaling of interconnect dimensions. However, due to increased device density, the density of *Cu* interconnects is increased in the DSM region. The combined temperature of interconnects and on-chip devices may exceed up to 600 K in high temperatures ICs. Previously, studies have been carried out to study the effects of temperature variation on the delay variation (DV) of the local, intermediate, and repeater-inserted (RI) global interconnects of *Cu*, at technology node 32 *nm* [23]. Not only the resistance of interconnects, but the resistance of drivers or repeaters is also a strong function of temperature. However, studies reveal that interconnects with the local and intermediate number of layers exhibit negligible temperature-dependent DVs. For interconnects at the local and intermediate level, the temperature-dependent resistance of drivers alone can results in respective DVs of -33% and -28% at 50 K, and 240% and 232% at 600 K. Moreover, for unit-RI and cascaded-RI global interconnects, the respective temperature-dependent DVs are -23% and -38% at 50 K, and 116% and 200% at 600 K.

The performance of *Cu* interconnects has also been analyzed for all-spin-logic (ASL) [24]. The ASL *Cu* interconnects are found more energy-efficient and faster at the local level rather than at the global level. This is because of the smaller resistance and high injection efficiencies offered by them. Further, it is indicated that spin-relaxation-length is longer in Al than in *Cu*. Therefore, at the global level, even Al interconnects due to their shorter delay and lower EDP can outperform *Cu* interconnects.

Numerous theoretical and experimental investigations as in [20]-[24] regarding the dismal performance of scaled *Cu* interconnects with realistic roughness profiles force the researchers to look for a potential and reliable alternative to *Cu* for future DSM technology nodes. Graphene nanoribbon based interconnects have emerged as a possible solution to this key interconnect problem.

2.3 MLGNR AS ON-CHIP INTERCONNECTS

GNRs exhibit a ballistic transport of charge carriers that consists of a long MFP ~ 1 μm at $T = 300$ K, linear increase in its electrical conductivity beyond $T = 300$ K, high thermal conductivity (~ 3×10^3 - 5.3×10^3 W. m^{-1}. K^{-1}) and large current density (~ 10^9 A. cm^{-2}), and thereby are highly suitable for interconnect applications [25], [26]. GNR poses its amazing electronic properties to its honeycomb lattice carbon network, in which 2s, $2p_x$, and $2p_y$ orbitals hybridize are arranged in such a way that each sp^2 hybridized carbon atom is bonded to its three neighbors by strong sp^2 or "sigma" bonds and has a pi orbital [27], as shown in Figure 2.1.

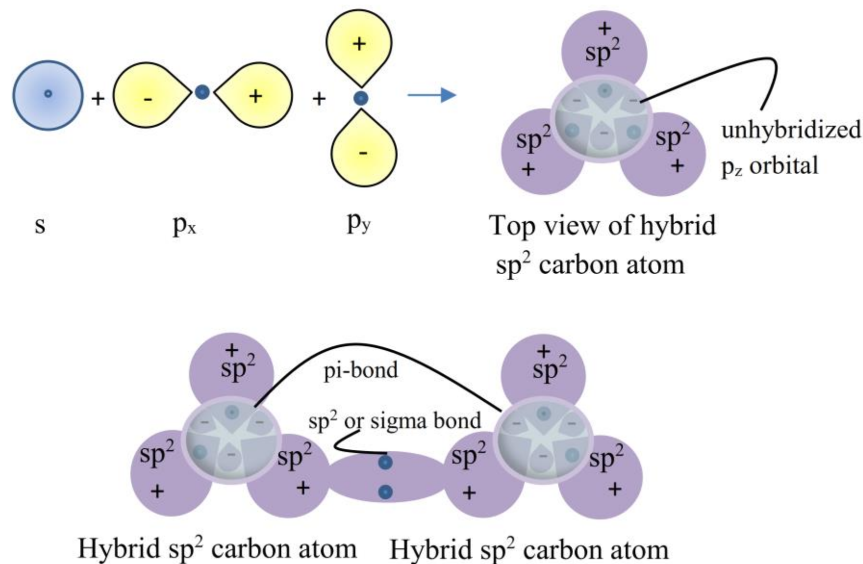

Figure 2.1 Formation of sigma and pi bond between Hybrid sp^2 carbon atoms [27].

The basic building structure for 1-D GNR is graphene. GNR is obtained by cutting 2-D graphene in a few nanometers wide planar ribbons whose edges can be of armchair (AC) or zigzag (ZZ) shape, as shown in Figure 2.2.

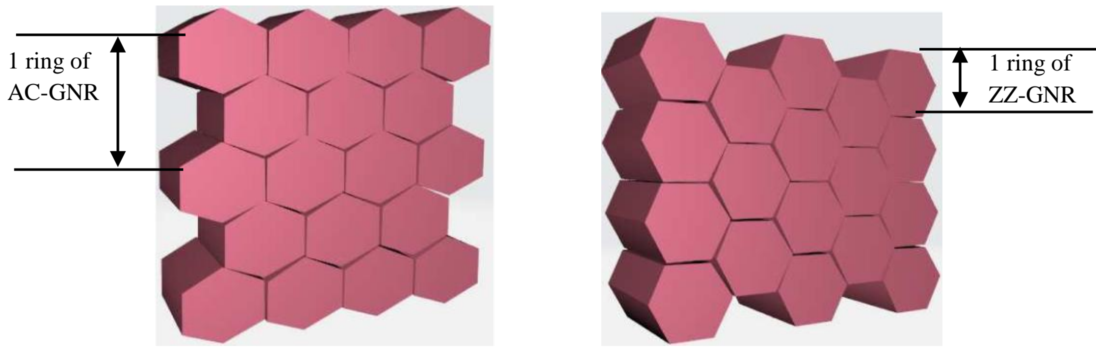

Figure 2.2 Armchair (AC) and Zigzag (ZZ) GNRs.

It is indicated that due to the nature of honeycomb lattice of graphene, the number of carbon rings (*N*) of AC-GNR and ZZ-GNR are related as [28], [29]

$$N \text{ of AC-GNR} = \sqrt{3}\, N \text{ of ZZ-GNR (for identical width)}$$

The AC-GNRs are either metallic or semiconducting based upon the number of hexagonal carbon rings (*N*) along its width. Depending on *N* along the width, with $N=3m-1$ or $3m+2$, AC-GNR is Metallic. With $N=3m$ or $3m+1$, AC-GNR is semiconducting, where *m* is an integer. The bandgap of AC-GNR is an inverse function of its width [25],[30]. However, only the metallic nature of GNRs is essential for its use as interconnect material [31]. Whereas ZZ-GNRs are always metallic irrespective of *N*. For a given width *W*, the number of carbon rings can be calculated as $W = \cos 30^{o}(N-1)\, a$. Where *a* is the length of carbon bonds in graphene and is equal to 0.142 *nm*. Naeemi *et al.* were the first to introduce the compact physics-based model for both AC and ZZ GNRs [11].

2.3.1 Fabrication challenges and Key issues in GNR interconnect

For the performance evaluation of MLGNR based interconnects, the essential fact that must be taken into account is its fabrication feasibility. Previously, a few researches have been conducted and confirmed the possibility of fabricating both the SC-MLGNR and TC-MLGNR based interconnects. However, production of MLGNR with desired sharp edge shape of GNRs (e.g. AC and ZZ) is a challenging task.

The most commonly used techniques to produce GNRs include electron-beam patterning of individual graphene sheets [32] or unzipping carbon nanotubes with plasma etching methods that require ultra-high vacuum systems [33]. These techniques produce GNRs of good quality, however, with very low yield. To overcome these issues, the authors in [34] introduced a new facile fabrication process to synthesize GNR thin films on any substrate. To obtain the GNR films, *Cu* nanoparticles were grown on graphene films by RF sputtering. It was observed that adherence of *Cu* nanoparticles on flat graphene surface was good, whereas on graphene wrinkles and ridges, it was negligible. *Cu* nanoparticles were then etched in nitric acid, which resulted in the removal of flat graphene flakes to large extent. Only ridges and wrinkles were left behind as individual GNRs. The fabricated GNRs (with high yield) were

of two categories, i.e., wide GNR (obtained from planar ridges) and narrow and straight GNRs (obtained from vertical wrinkles), that exhibited the outstanding electrical conductivity of pristine graphene.

Politou *et al.* [35] fabricated the multilayer graphene ribbons (MLGR), with ribbon width of 5 µm, 20 µm and 80 µm, using the photolithography and oxygen plasma etching method. For MLGR, the metal contacts were formed using photolithography followed by metal lift-of. Both TC- and SC-MLGR were fabricated using a 50 *nm* thick Pd as contact metal to form the low-resistive metal contact. The fabrication of TC-MLGR required an additional oxygen plasma etching step after the second lithography step. Both the TC- and SC-MLGR with graphene-Pd contact demonstrated the low contact resistivity.

The physical structure of interconnect have significant effect on its performance. For instance, for interconnect width beyond 10 *nm*, metallic AC-GNRs possess more significant conductivity as compared to that of ZZ-GNRs. Hence, the feasibility to fabricate GNRs with atomically sharp edges is important for various graphene applications because these edges significantly affect the overall electronic properties. Chang *et al.* [36] introduced a new technique to create complex graphene nanostructures (e.g. GNRs with atomically sharp ZZ or AC-edges) using AFM-induced self-folding. The presence of dangling bonds at the edges of the patterned or etched GNRs causes the chemical instability. However, using this technique, GNRs were fabricated without affecting the physical properties of graphene. The folded GNRs were created by controlled AFM scan of the 2-D graphene sheet with a normal force sufficient to overcome the interfacial adhesion. The lateral force microscopy (LFM) was used to confirmed the atomically sharp ZZ or AC-edges of folded GNRs.

Akiba *et al.* [37] proposed the "etching-precipitation" method to produce MLG with wide range of graphene layers. In this method, graphene obtained from Fe-C films (50 or 100 *nm* in thickness) is grown on SiO_2 substrate at 650 °C with different carbon concentrations (15–30 at.%). The etching process removed Fe from the Fe-C film, leaving carbon directly on SiO_2. It is observed that the layer-number of MLG is tunable for a wide range of ~10–40 layers by varying the carbon concentrations and the film thicknesses of the initial Fe-C films.

In addition to fabrication challenges, there are several fundamental issues in GNRs. These issues are as follows:

- ***Edge scattering*****:** it reduces the effective electron MFP in GNR, while there is no such issue in CNTs.
- ***MFP*****:** The MFP in single layer GNRs (SLGNRs) at room temperature is about 1 *µm* and whereas it is reduced to 419 *nm* in MLGNR [10]. As the number of layers in MLGNR increases, it turns to graphite and inter-sheet electron hopping also reduces its conductivity per layer.
- ***Interlayer interaction*****:** Interaction between the layers of GNR modifies its band structure (in neutral graphite a band overlap of 0.04 eV is generated). A nonzero band gap is exhibited by

ZZ-GNR because of the staggered potential sub-lattice from magnetic ordering upon the consideration electron spin that reduces the conductance.

Although it has been reported that by cutting the graphene along certain crystallographic directions AC and ZZ GNR can be potentially produced using nanoparticle, but this approach is uncontrollable (as the diameter and moving direction of particles cannot be controlled accurately).

MLGNRs, a stacked structure of GNRs, are preferred over SLGNRs for VLSI interconnect applications. It is due to their large intrinsic conductance as compared to SLGNRs. MLGNR structures are termed as top contact (TC) and side contact (SC) depending on the contact of metal with topmost graphene layer or with all the layers of MLGNR, respectively [38]. As shown in Figure 2.3, in TC-MLGNR interconnect the coupling of metallic contacts is done only with its topmost layer. While in SC-MLGNR physical connection of all the layers with the contacts is formed, shown in Figure 2.4. It is reported that TC-MLGNR interconnects have inferior performance in comparison to SC-MLGNR interconnects due to the difference in physical connections [14], [39]. On the other hand, the fabrication of SC-MLGNR is a big challenge to achieve, while that of TC-MLGNR is easier [10], [14].

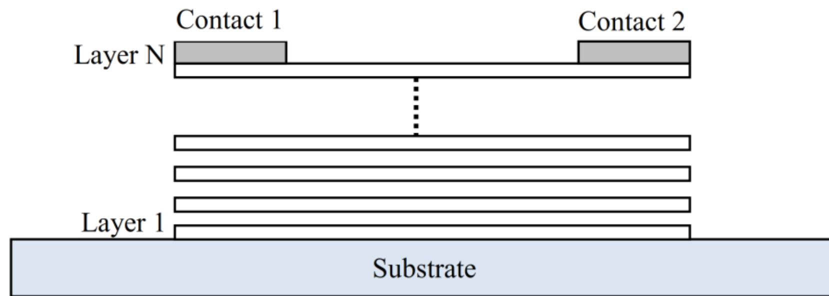

Figure 2.3 The geometry of TC-MLGNR over the ground plane [40].

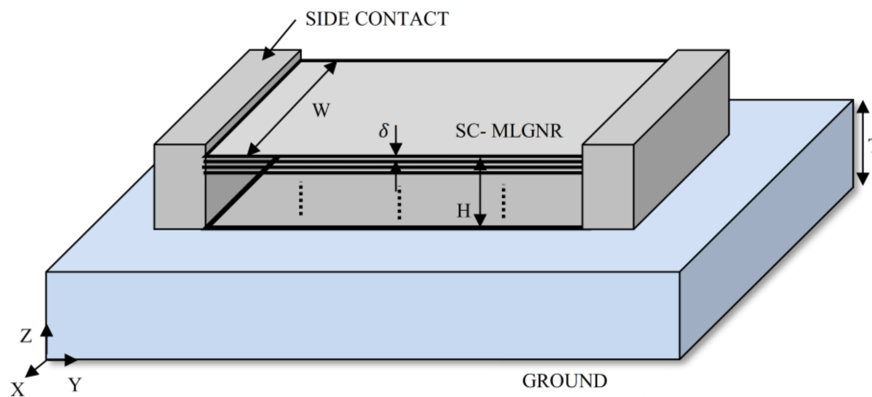

Figure 2.4 The geometry of SC-MLGNR over the ground plane [40].

2.3.2 Intercalation doping in GNR

MLGNRs are considered a potential interconnect material. In U-MLGNR there is an interlayer spacing of approximately 0.34 *nm*. This gives rise to interlayer interactions that consequently reduce the MFP,

in-plane conductivity, and normal plane (or c-axis) conductivity of U-MLGNR [10]. To alleviate these problems, U-MLGNR is doped with donor or acceptor impurities (e.g., Li, $FeCl_3$, AsF_5), and is termed as intercalation doped MLGNR (ID-MLGNR) [10],[41],[42]. The intercalation is a process of controlled insertion of an intercalate layer between the graphene layers. The susceptible Van der Waals bonding between graphene layers makes it viable to intercalate. The level of intercalate concentration can be indicated by the stage index (or stage number) of intercalated MLGNR [43].

For MLGNR interconnects, intercalation doping is inevitable as it can increase the in-plane conductivity, c- axis conductivity, and Fermi energy up to 30×, 7×, and 3×, respectively [41]. Previously the authors in [10],[41] proposed the intercalation doping in MLGNR with the intercalate compound of *arsenic pentafluoride* (AsF_5) and *lithium* (Li). They reported the significant improvement in conductance and delay performance of ID-MLGNR over undoped MLGNR. J. Jiang *et al.* [42] have synthesized the high-performance MLGNR with *ferrous chloride* ($FeCl_3$) intercalation doping. The authors have grown the multilayer graphene (MLG) by chemical vapor deposition (CVD) on the *Cu*-Ni catalyst subsequently transferred it on SiO_2 substrate, as shown in Figure 2.5. The MLG was further patterned into MLGNR by electron beam lithography (EBL). Subsequently, the MLGNRs were intercalation-doped with $FeCl_3$ (acceptor intercalate) at 360°C. The c-axis thickness of $FeCl_3$ ID-MLGNR measured by atomic force microscopy (AFM) was noted to be 10 *nm* – 12 *nm*.

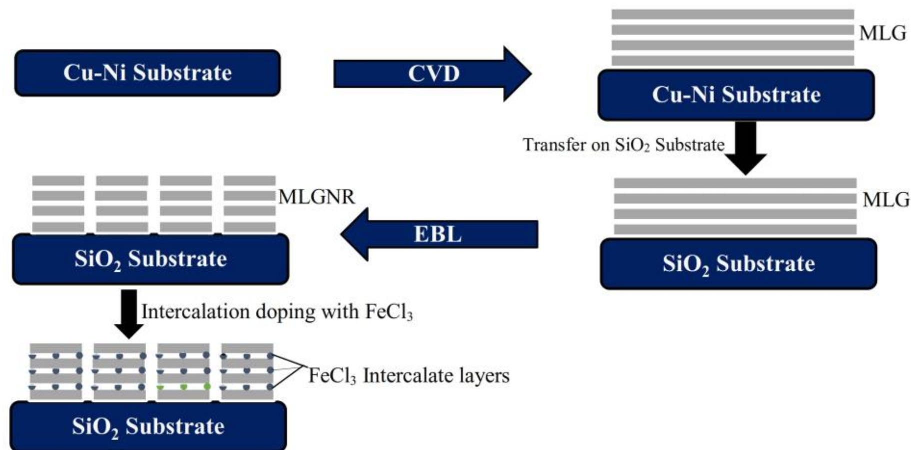

Figure 2.5 Process steps for the fabrication of ID-MLGNR [42].

2.4. PERFORMANCE OF MLGNR INTERCONNECT

2.4.1 Single line interconnect performance

2.4.1.1 *Doped and undoped MLGNR*

Neeami *et al.* [11] first proposed a physics-based ESC model for AC- and ZZ-SLGNR interconnects and benchmarked the conductance of SLGNRs against those of CNTs and *Cu*. They reported that for interconnect applications, GNRs not necessarily required to be of a metallic type; a semiconducting variety can also work equally or better. This report implies that chirality control is no longer an issue

with GNR interconnects. However, edge roughness can severely deteriorate their interconnect performance in comparison to *Cu*.

Later on, as an extension of their work in [11], they proposed the physical models for the effective resistance of TC-MLGNR interconnects in [38]. They considered the influence of finite interlayer resistive coupling in GNRs on the total resistance of TC-MLGNR. The effective resistance in TC-MLGNRs is noted as a non-linear function of the number of layers due to the presence of non-zero c-axis resistivity, which initially decreases and then gets saturated beyond a few layers. The effects of interlayer resistive coupling (termed as screening) are found a bottleneck in the performance improvement of MLGNR over SLGNR. However, interconnect doping can compensate for these effects. Further studies regarding performance metrics of MLGNR interconnects like delay and EDP reveal that these performance metrics primarily depend on edge scattering probability and dimensions of MLGNR interconnects. Furthermore, for a MLGNR interconnect to demonstrate a better delay and EDP performance than *Cu* interconnect, the edges of GNRs must be perfectly specular.

Rai *et al.* [9], analyzed the influence of interlayer resistance due to c-axis resistivity as well as imperfect metal-contact resistance, and Fermi-energy on the propagation delay, power dissipation and PDP performance of MLGNR interconnect while taking into account the inductive and capacitive coupling between the layers of MLGNR. Despite the presence of interlayer resistance, an increase in Fermi-energy improves the performance of global level MLGNR interconnects. It is because, at the global level, the in-plane resistance dominates the interlayer resistance in estimating the overall resistance of MLGNR interconnects, whereas at the local level governing interlayer resistance deteriorates its performance. However, irrespective of interconnect length, MLGNR based interconnects found to outperform *Cu* if the effects of interlayer resistance are neglected

For providing physical insights into the transient conduct of the MLGNR interconnects, the authors in [14] presented the analytical time-domain models for both SC- and TC-MLGNR. In this work, the authors developed the closed-form equations for the delay and EDP in MLGNR interconnects based on a second-order transfer function derived using standard Elmore delay formulation. It is reported that for the TC-MLGNR to have a performance that is comparable or improved than that of the SC-MLGNR, the key parameters to be considered are Fermi energy, conductance and interconnect width. The deployment of optimum TC-MLGNR may lead to the avoidance of fabrication challenges in SC-MLGNR. In terms of delay, EDP, frequency response and step response, the optimum TC-MLGNR demonstrates better performance than SC-MLGNR and optical interconnects.

The variations in process-induced parameters like the width of interconnect, interlayer spacing, MFP, dielectric thickness, dielectric constant and intercalate doping concentration can affect the delay performance of MLGNR interconnects. Based on a multi-conductor transmission line (MTL) model and Monte Carlo approach, these investigations were carried out by Reddy *et al.* in [44]. The authors considered the nominal values and previously predicted variations of these process parameters to analyze the performance of the global interconnects of AsF_5-D-MLGNR. Favorably, among all the

process parameters considered in the presented study, variation in only MFP is found to affect the delay variation in MLGNR interconnects significantly, rest causes an insignificant variation of less than 3%. Interlayer dielectric insertion can improve the performance of MLGNR interconnects. The researchers reveal this fact in [45] through the performance evaluation of dielectric inserted SC-MLGNR (Di-SC-MLGNR), which based on the computation of interconnect performance matrices like delay, EDP, BWD and the ratio of BWD/EDP. Based on their analytical models, developed for scattering rate, mobility, and MFP, it is found that carrier transport in MLGNR is a strong function of the dielectric attributes viz. its surrounding environment and sample quality. A Di-SC-MLGNR with a clean dielectric sample is reported to have a MFP > 1μm. The carrier mobility, and scattering rate also exhibited the improvement by an order of magnitude. It is noted that the insertion of graphene compatible HfO_2 resulted in the 2× and a 35% increase in the EDP and BWD, respectively, in comparison to *Cu*. Further, the performance comparison between Di-SC-MLGNR and optical interconnects based on EDP and BWD demonstrates the competing performance of Di-SC-MLGNR interconnect at the global level.

The interconnect performance of MLGNR is benchmarked against that of *Cu*, not only based on theoretical circuit-level investigations employing analytical and physics-based compact models [9],[11],[14],[38],[44],[45] but also based on the realistic circuit and system-level studies as in [46].

Chenyun Pan *et al.* [46] investigated a 32-bit adder and an ARM Cortex-M0 processor for the realistic circuit and system level, respectively, performance evaluation of MLGNR interconnects. It is indicated that for the MLGNR interconnects to be advantageous than *Cu* the critical parameters criterion must be met. The critical parameters identified at the device-level that affect MLGNR delay and EDP performance are the supply and threshold voltage, whereas, at the circuit-level, these are the length and width of interconnects. Replacement of *Cu* interconnects with that of MLGNR in a 32-bit ARM core processor resulted in 15% and 22% improvements in its clock frequency and EDP, respectively. In the MLGNR based 32-bit adder, the upgrades in delay and EDP are 40% and 70% than its *Cu* based counterparts.

Where most of the researchers [9],[11],[14],[38],[44]-[46] focused their research on performance evaluation of MLGNR interconnects while following different aspects to study its signal transmission characteristics, there a few of them also worked on studying the performance of MLGNR as power interconnects. One such analysis is performed in [47].

The authors developed the delay fault model for TC- and SC-MLGNR based power interconnects, employing the PTM HP model for technology node 16 *nm* [47]. The development of this model was based on the design of a negative edge triggered master-slave D flip-flop (DFF). A cascaded chain of 12 inverters was considered to drive the DFF. To analyze the IR-drop induced delay in the designed DFF (based on MLGNR), the derived scattering parameter-dependent and temperature-dependent resistance of MLGNR is used to model the segments of power interconnects between the inverters. The SC-MLGNR is found highly efficient in suppressing the IR-drop induced delay in the DFF circuit than TC-MLGNR and *Cu*. It is demonstrated that regardless of interconnect length, the highest number of

DFF stages supported by SC-MLGNR is ~ 3-4× and ~ 1-1.5× more than that by TC-MLGNR and *Cu*, respectively, at chip operating temperatures of 233 K, 300 K, and 378 K, that too without any delay fault.

The conductivity of a realistic MLGNR (U-MLGNR) interconnects suffers due to three reasons. Firstly, it is due to additional carrier scatterings that include intersheet electron hopping. Secondly, it is due to reduced carrier MFP from edge scatterings. The third reason for the reduced conductivity is due to the bandgap opening for sub-20 nm width [42]. To overcome these challenges in U-MLGNR interconnects intercalation doping is inevitable. The intercalation of U-MLGNR increases its in-plane conductivity ($\sigma_{in-plane}$), c-axis conductivity (σ_c) and Fermi energy (E_F) [10], [42].

These findings force the researchers to focus their research on the performance evaluation of D-MLGNR interconnects rather than U-MLGNR one to find its potential applications for future VLSI interconnects. A few recent works [41], [42], [48], [49] based on this perspective are discussed in detail here.

Xu *et al.* [10] were the first to propose the AsF_5 ID-MLGNR interconnects. The authors, based on the theoretical investigation, proved that ID-MLGNR could beat the resistivity of *Cu*. Later on, Nishad *et al.* [48] analyzed the influence of AsF_5 intercalation doping on delay, EDP and BWD of TC-MLGNR interconnect. It is indicated for interconnect lengths < 20 μm, among *Cu*, U-TC-MLGNR and AsF_5 D-TC-MLGNR based global interconnects least resistance is associated with *Cu*, whereas beyond this, AsF_5-doped TC-MLGNR leads. Further, with undoped structure TC-MLGNR could not compete *Cu* for the delay, EDP and BWD. However, with AsF_5 intercalation doping TC-MLGNR performs much better than *Cu* in terms of these performance metrics.

Besides AsF_5, the authors in their other work [41], to estimate MLGNR performance improvement as on-chip interconnects, in particular at the local level, investigate the influence of Li-intercalation in MLGNR. First, to obtain the reduced delay and EDP in MLGNR, thickness of MLGNR is optimized. It is observed that respective values of delay and EDP in MLGNR are lower than *Cu*, by 1.37 × and 2.5 × with diffusive edges, 1.9 × and 4.1 × with specular edges. This suggests that like AsF_5-intercalated MLGNR, Li-intercalated MLGNR can be a better substitute to *Cu* for interconnect applications at DSM technology nodes.

Scaling in MLGNR width causes more roughness on its edges that, consequently, reduce the MFP due to edge scattering and, thereby, the effective resistance in MLGNR is increased. Considering these facts, Kumar *et al.* [49] analyzed the performance of D-MLGNR interconnect in terms of delay, power dissipation, and bandwidth. With specular edges, in D-MLGNR interconnects (edge scattering probability, $p = 0$) significant reductions of 86.13% and 43.72% are noted in the overall delay and power dissipation, respectively as compared to *Cu* interconnects. Also, the reported bandwidth improvement in fully specular D-MLGNR is 4× than *Cu* at both the intermediate and global levels of interconnects lengths. Further, the wider, thicker, and highly doped global MLGNR interconnect demonstrates higher system stability. For a narrow width MLGNR interconnect, as p increases from 0 to 1, the propagation delay increases, whereas system stability improves.

Jiang *et al.* [42], for the first time, synthesized the D-MLGNR interconnects through a 45 min CVD process. The stage-I $FeCl_3$-doped MLGNR on SiO_2 substrate exhibited a delay (*p. u. l.*) improvement of 20% than *Cu* with optimized interconnect dimensions (width < 20 *nm*, thickness ~ 12 *nm*). It is noted that this delay improvement in D-MLGNR is obtained with only 14 layers, which is much less than predicted earlier (about 80) [46] to achieve a delay improvement of 30% in MLGNR interconnect on SiO_2 substrate w.r.t. *Cu*. Further, it is reported that under a DC stress = 200 MA/cm^2 and temperature = 475 K, the time-to-fail (TTF) for D-MLGNR interconnect (with width 21.6 *nm* and 68.6 *nm*) exceeds 7 hrs, whereas the TTF for U-MLGNR is only 1.8 hrs and 5.2 hrs at widths 20.6 *nm* and 73.5 *nm*, respectively. These findings marked the outstanding reliability of stage-I $FeCl_3$ doped MLGNR interconnects.

Parallel to MLGNR, other carbon nanomaterials like MWCNT have also been proposed as a potential substitute for *Cu* based interconnects. A few kinds of researches, as in [50], have analyzed the performance of MLGNR vs. MWCNT to find the best alternative to *Cu* interconnects. A rough-edged MLGNR and a densely packed bundle of MWCNTs are considered at technology node 22 *nm*. For accurate analyses of the propagation delay and area in both MLGNR and MWCNT interconnects at the local and global level, an analytical FDTD and real-time simulation approach are considered. It is found that a fewer number of MWCNTs in the bundle can provide an equivalent propagation delay as in MLGNR, for lengths below 200 μm. However, beyond this interconnect length, MLGNR even with rough edges outperforms the bundled MWCNTs. Moreover, at the global level, the area required by the rough-edged MLGNR is 97.98% less in comparison to the MWCNT bundle. Hence, MLGNR, even with rough edges, can compete for MWCNT for global interconnects applications.

2.4.1.2 *Temperature-dependent performance*

High-performance ICs exhibit a significant variation in its performance over the temperature range 300-450 K [16]. These temperature variations severely affect the delay of the signal propagating along interconnects and hence, influence the performance of interconnects. A detailed analysis in *Cu* wires reveals that beyond 45 *nm*, with technology scaling the cumulative impact of reduced resistivity, thermal conductivity and an increasing number of metal-layer for global level has raised the temperature of *Cu* interconnects. Many researchers have proposed the graphene-based nanomaterial viz. MLGNR as a potential alternative to *Cu*. IC often operates at a temperature much beyond room temperature (300 K), therefore, to use these proposed interconnect materials in future VLSI IC applications, it is essential to develop the thermal model of these interconnects for the accurate estimation of their temperature profile and to study their behavior at the high on-chip operating temperatures beyond 300 K [17].

Earlier, many researchers have investigated the influence of temperature on the key interconnect matrices of MLGNR, i.e., resistance, inductance, capacitance, propagation delay, power dissipation, PDP, EDP in single-line configuration [51]-[53].

Das *et al.* [51] developed the thermally aware analytical time-domain models for SC-MLGNR and TC-MLGNR interconnects at technology node 16 *nm*. They also presented the interlayer capacitive model for TC-MLGNR interconnects. Interlayer capacitance in TC-MLGNR severely deteriorates its performance than *Cu*. Further, delay analysis reveals that along with the presence of interlayer capacitance, an increase in interconnect length and chip-operating temperature stimulate this deterioration in TC-MLGNR interconnects. However, intercalation doping can improve the delay performance of TC-MLGNR by enhancing its interlayer conductance. Crosstalk analysis in TC-MLGNR, SC-MLGNR, and *Cu* interconnects reveals that among these interconnects, least crosstalk noise and overshoot/undershoot is obtained in SC-MLGNR.

MLGNR interconnects, in addition to their signal transmission characteristics, have also been studied for its applicability as power interconnects. The work in [52] studied the influence of temperature on the performance of MLGNR based power interconnects and compared it with that of *Cu*. The power supply voltage drop (IR- drop) is analyzed, at technology node 16 *nm,* for temperature variations from 150 K to 450 K. It is observed that MLGNR interconnect exhibits approximately 2-5× less temperature-dependent resistance variation than *Cu* interconnects. Also, the propagation-delay and IR-drop in MLGNR interconnects are respectively ~1.5-3× and ~1.5-3.5× lower than in *Cu* interconnects.

Interlayer interactions in MLGNR result in interlayer resistance or c-axis resistivity. In SC-MLGNR, metal contact formed with each layer makes it equally potential hence, only in-plane resistance considered in the overall resistance. However, in TC-MLGNR, the contact formed with only the topmost layer results in higher potential at topmost layers as compared to other layers that cause dominating interlayer resistance, and therefore, affects their interconnect performance, in particular, at the local level.

Considering these facts, Bhattacharya *et al.* [53] critically examined the interconnect performance of SC-MLGNR and TC-MLGNR at local interconnect lengths while accommodating the impact of different temperatures (i.e., 233 K, 300 K, and 378 K) and line-widths (11 *nm*, 16 *nm*, and 22 *nm*), and compared it with that of *Cu*. For this analysis, they performed delay and repeater optimization based on the wire-sizing technique. Based on repeaters optimization technique, it is found that repeaters required in SC-MLGNR are approximately 3-6× and 2-3× less than in TC-MLGNR and *Cu*, respectively. The estimation of propagation delay as a function of line-width, line-length and chip operating temperature reveals that the SC-MLGNR achieves the maximum delay reduction of 73× w.r.t. TC-MLGNR at line-width and line–length of 22 *nm* and 10 μm, respectively, and at two chip operating temperatures of 233 K and 300 K. The same findings in *Cu* w.r.t. to TC-MLGNR are 6× at line-widths 16 and 22 *nm*, line-length 10 μm, and at temperature 300 K.

2.4.1.3 *Frequency-dependent Analysis*

Technology scaling has adversely affected the propagation delay of VLSI circuits due to the increased value of resistivity as the cross-sectional dimension shrunk down. Higher resistivity of conventional

interconnects as Al and *Cu* attribute to the enhanced grain and surface scattering effects. Moreover, at the high operating frequency, electro-migration induced adverse effects becomes prominent for these thinner interconnects. In high frequency (GHz) application of ICs, issues like skin effects, proximity effects, crosstalk severely degrades the performance of conventional interconnects. Various studies have predicted the potential applicability of MLGNR as interconnects, but lacks in its high-frequency characterization. So far, graphene has been demonstrated for its high-frequency applications merely in few analog ICs (e.g., RF voltage amplifier and RF receiver) [54]. Hence, it is essential to investigate the frequency-dependent crosstalk performance of recently proposed MLGNR interconnects to estimate their performance in high-frequency ICs applications [49].

Earlier, the input/output transfer function of a single U-MLGNR interconnect is approximated based on the Fourth-order pade's approximation [55]. However, they neglected the resistances introduced by the CMOS driver and imperfect metal contacts. Later on, based on the ESC model, Nishad *et al.* [14] derived a generic expression of a second-order transfer function for estimating the delay in SC- and TC-MLGNR interconnects in the single-line DIL configuration. However, again the negligence of driver parameters (resistance and capacitance) is noted that may lead to inaccurate estimation of delay in MLGNR interconnects. Accommodating the driver parameters, Majumder *et al.* [56] presented the improved frequency domain analytical model to accurately estimate the frequency response and bandwidth analysis in a single interconnect line of U-MLGNR, and compared it with MWCNT. The model is based on ABCD parameters of a distributed transmission line. Employing this model, compared with MWCNT, a bandwidth improvement of 10× and 4× is noted in MLGNR at local and global interconnects lengths, respectively.

The authors further in [49], performed a comprehensive analysis of bandwidth and relative stability in single interconnect of D-MLGNR while considering the impact of edge-roughness in narrow GNRs. The reported bandwidth improvement in fully specular D-MLGNR is 4× than *Cu* at both the intermediate and global levels of interconnects lengths. Further, the wider, thicker, and highly doped global MLGNR interconnect demonstrates higher system stability. For a narrow width MLGNR interconnect, as p increases from 0 to 1, the propagation delay increases, whereas system stability improves.

The work in [57] mainly focuses on the relative stability analysis of SC-MLGNR, TC-MLGNR, and *Cu* as a function of length and width of interconnect, based on bode plots. The authors considered the D-MLGNR, but they did not explicitly include the impact of doping in their developed model rather than taking an arbitrary doping concentration of 0.3 eV and interlayer spacing of 0.34 *nm* for D-MLGNR interconnects. As stated earlier, intercalation doping in MLGNR affects its in-plane conductivity, c-axis conductivity, Fermi-energy, and interlayer spacing. Therefore, for the accurate evaluation of stability analysis in D-MLGNR interconnects, these physical parameters must be taken into account. CVD GNR exhibits constant characteristic impedance at a high frequency that can be exploited for its use in radio frequency interconnect applications [54].

Incorporating the improved physical parameters of doped interconnects, the authors in [58] presented the thermally-aware radio-frequency (RF) model to analyze the performance of single interconnects of doped (AsF_5-, $FeCl_3$-, and Li-doped) TC-MLGNR. A temperature-dependent MFP model and ABCD parameter based MTL model demonstrated the RF model for D- and U-TC-MLGNR and pristine SC-MLGNR. It is noted that intercalation-doping improves the temperature-dependent RF performance of TC-MLGNR even than to pristine SC-MLGNR. Investigations reveal that global interconnects of D-TC-MLGNR can operate up to several MHz, whereas for semi-global operating frequency, operating frequency up to few GHz is identified. Moreover, the bandwidth of D-TC-MLGNR further improves with specular edges.

The SR of the underlying dielectric materials, δ_{sr}, can influence the transport properties and, consequently, the performance of supported MLGNR. Sanaeepur *et al.* [59] first investigated the impact of SR of different dielectrics (viz. silicon dioxide (SiO_2), boron nitride (BN), and silicon carbide (SiC)) and edge roughness of GNRs on delay and bandwidth performance of MLGNR interconnects. It is observed that delay and bandwidth performance of perfectly specular (i.e. $p = 0$) MLGNR interconnects grown on SiC substrate ($\delta_{sr} = 10$ pm) is better than *Cu* interconnects, compared to that on SiO_2 ($\delta_{sr} = 170$ pm), and BN ($\delta_{sr} = 70$ pm) substrates. Further, perfectly specular MLGNR interconnects can exhibit higher bandwidth than *Cu* with identical dimensions only when $\delta_{sr} < 62$ (54) for local (intermediate or global) lengths. That implies, with an existing SR of SiO_2, MLGNR interconnects could not beat the delay and bandwidth performance of *Cu*.

The performance of U-MLGNR interconnects also improves by inserting the high-k dielectric materials between its layers. The authors in [45] demonstrated the improved time-domain propagation delay and PDP performance of HfO_2 dielectric inserted MLGNR interconnects. Later on, Xu *et al.* [60], based on the time- and frequency-domain model demonstrated that global interconnects of MLGNR with the insertion of $SrTiO_3$ can achieve the maximum propagation delay reduction up to 12.746 *ns* at interconnect length of 4000 *μm.* Additionally, the 3-dB BW improvement of more than 4× is also observed than its U-MLGNR counterparts at a technology node of 7.5 *nm*.

The authors in [61] analyzed the thermal stability of MLGNR vs. *Cu* interconnects for the THz frequency range. It is noted that for frequency > 10^{12} Hz, SC-MLGNR interconnects are highly thermally stable than TC-MLGNR and *Cu*, at interconnect length of 10 *μm* and at chip operating temperatures 233 K, 300 K, and 378 K. Later on, coupled interconnects of MLGNR were analyzed for crosstalk stability, based on the step response, Nyquist stability, and Nichols stability criterion [62], [63], [64]. In [62], bandwidth, stability, and step response in inductively and capacitively coupled interconnects of MLGNR are analyzed based on the Nichols stability criterion. It is noted that longer MLGNR interconnects with strong capacitive coupling and weak inductive coupling exhibits higher stability at the victim's near-end output, whereas, for these interconnects, the stability reduces at the victim's far-end output. Also, the stability of the near-end and far-end output of the victim line improves with the decrease in line width. Further, the wider and short MLGNR interconnects achieve a bandwidth improvement with weak capacitive coupling and strong inductive coupling.

The stability analysis of MLGNR interconnects presented in [62] was limited to the functional crosstalk only (i.e., for the switched aggressor and quite victim line). Qian *et al.* [63] further worked for stability analysis of dynamic crosstalk in MLGNR interconnects based on the distributed transmission line model using ABCD parameter matrices. They studied in detail the influence of line switching modes (i.e., in-phase and out-phase) and design parameters (viz. wire length, wire width, inter-wire space, Fermi-energy, and backscattering probability) on the relative stability and crosstalk in adjacent interconnects of MLGNR and *Cu* at technology node 14 *nm*. The crosstalk stability analyses reveal that the presence of miller capacitance in the equivalent capacitance of coupled interconnects, switched in out-phase mode, makes them more stable than that switched in in-phase mode and even than a single interconnects. Moreover, the stability enhancement in interconnects can be achieved by increasing their length and edge roughness, and by reducing their width, inter-wire space, and Fermi-energy.
The crosstalk stability analyses of MLGNR interconnects carried out earlier in [62], [63] primarily based on the ESC Model of MLGNR. However, these models excluded the critical impacts of the distributive nature of MLGNR interconnects, screening effect, substrate ionized impurity effect, tunneling effect, the magnetic and electrostatic coupling between the layers of MLGNR. Considering these parameters and employing a multiconductor transmission line technique (MTLT), Fotoohi *et al.* [64], presented a compact matrix model for inductively and capacitively coupled interconnects of MLGNR. The MTLT model and Nyquist stability criterion were used to analyze the stability of MLGNR interconnect at different interconnect lengths and at different technology nodes 10, 14, and 22 *nm*. The distributed nature of interconnects implies the number of distributive blocks between the lumped elements present at the two ends of interconnects. It is noted that the output response converges with the increase in block number. Employing the MTL technique, a reduction of 3.5× and 3.2× is obtained in the Nyquist response w.r.t. Sixth-order pade's approximation and FDTD based ESC models, respectively. Further, it is demonstrated that an increase in interconnect length and technology node enhances the stability of MLGNR interconnects.

2.4.2 Crosstalk in adjacent interconnect lines

2.4.2.1 *Key parameters affecting crosstalk*

For global and intermediate interconnects, upper metal layers use wide wires frequently. These low resistive lines exhibit significant inductive effects, which forced the designers of the new generation's VLSI technology to model interconnects as distributed RLC transmission lines. The parallel running of these RLC transmission lines induce significant inductive and capacitive coupling effects. So, one of the critical impacts to be considered while designing is crosstalk. With the growing interconnect density and reduction in chip-size, even non-adjacent interconnects exhibit significant coupling effects. The geometry of interconnect, the distance between them, and the transition time of the input signal are the prime factors that enhance the coupling effect. Crosstalk affected interconnect line is called the victim,

and interconnect line that induces crosstalk on victim line is termed as the aggressor. If the crosstalk-induced overshoot and undershoot voltage exceeds the threshold voltage of the CMOS gate (as interconnect driver), it causes the false switching of interconnect. Accurate prediction of crosstalk waveform shape and noise peak in a DIL system is a crucial design concern [65], [66].

Coupled transmission lines

Figure 2.6 shows two coupled interconnect lines, where line one is switched (aggressor), and line two is quiet (victim). A voltage ramp V_S replaces the CMOS driver for an active line with a Thevenin resistance in series R_S, and for a quiet line, a linear resistance R_V (grounded) replaces the driver. At the far end, a lumped capacitive load modeled the interconnect receiver.

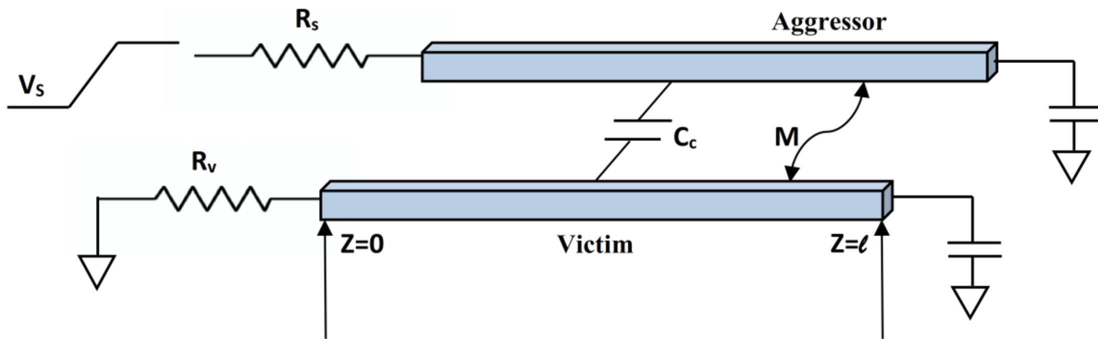

Figure 2.6 Coupled transmission line configuration [65].

Kaushik *et al.* developed the alpha-power law model [67] of MOS transistor in CMOS driver. This CMOS driver is used to analyze crosstalk in capacitively and inductively coupled distributed RLC interconnect. Based on the developed model, they analyzed the transient analysis of crosstalk noise. Earlier crosstalk was analyzed based on the assumption of CMOS driver operating in a linear region, represented by a linear resistance. The fact that the MOS transistor in CMOS gate behaves partially linearly and partially non-linearly (in saturation) was neglected. A CMOS is accurately modeled as a linear resistance when the transistor operates in the linear region of its characteristics. However, when the transistor operates in saturation mode, a current source in parallel with a high resistance is used for approximate modeling of the CMOS [66]. Research work performed on the crosstalk analysis of MLGNR so far is covered in the following literature [39], [40], [68], [69]-[87].

2.4.2.2 *Crosstalk in doped and undoped MLGNR interconnects*

Jiang-Peng Cui *et al.* [68] analyzed the transient response of the MLGNR, employing an ESC model (this model considered interlayer capacitive and inductive coupling in MLGNR), to study its signal transmission characteristics. The input-output transfer function derived using fourth-order pade's

approximation predicted the output voltage waveforms at 14 and 22 *nm* technology nodes. They also predicted the output voltage waveforms in edge-coupled MLGNR interconnects based on the partial differential equations (for decoupled lines) for common and differential modes of waveform propagation. The transient response of edge-coupled MLGNR observes to improve as the Fermi energy increases to a value of 0.21 eV for both active and quiescent lines at 14 and 22-*nm*. The crosstalk analysis in capacitively and inductively coupled MLGNR interconnects shows that at $|E_F|$= 0.21 and 0.4 eV, the ESC resistance of MLGNR interconnects is smaller than that of *Cu*, the *p.u.l.* inductance decreases and the *p.u.l.* capacitance is negligibly affected at both 14 *nm* and 22 *nm* technologies.

Wen-Sheng Zhao *et al.* [40] performed the comparative study of the distributed parameters and transmission characteristics of SC-MLGNR, TC-MLGNR, MWCNT and *Cu* interconnects at 13.4 *nm* and 21 *nm* technology nodes. They found that conducting channels of metallic MLGNR varies linearly with its Fermi-energy and line width. For local interconnect length, smaller resistance in interconnects of SC-MLGNR is reported in comparison to that of TC-MLGNR. The estimated value of propagation delay shows that MLGNR has improved transmission performance than MWCNT at an intermediate level of interconnect, but inferior at global length. They characterized the crosstalk for tri-MLGNR at an intermediate interconnect level. The crosstalk analysis demonstrated the improved crosstalk performance of MLGNR interconnect, with rough edges, over *Cu* with technology scaling.

K. Narasimha Reddy *et al.* [69], analyzed the dynamic crosstalk in global MLGNR interconnects using RLC based two-coupled lines bus architecture. It is found that with an increase in interconnect length from 100 *μm* to 500 *μm* the crosstalk-delay increases, and there is a more rapid increment in out-phase delay in comparison to in-phase delay. The fact behind this effect is the miller-coupling factor (MCF) that mainly influences the coupling capacitance C_{CM} between coupled lines. It is indicated that, when two lines switch in the same direction (in-phase), MCF=0, i.e., best case-delay, and when two lines switch in the opposite direction (out-phase), MCF=2 , i.e., worst case-delay. The out-phase crosstalk delay worsens the performance of global interconnects at high-speed VLSI technology nodes. However, with a large number of layers in MLGNR a % improvement of 4.75 and 18.04 is noted in-phase and out-phase delay, respectively, in comparison to with lesser ones.

M. Sahoo *et al.* [70] investigated the impact of line-resistance variations on crosstalk-induced delay and crosstalk-induced noise in fully specular ID-MLGNR, for semi-global and global interconnect length at 11 *nm* and 8 *nm* technology nodes. The crosstalk is analyzed in capacitively coupled aggressor-victim-aggressor configuration. It is noted that the % variation in signal transmission delay is almost equal to that of line-resistance, whereas the % variation in peak-noise voltage is observed 0.25 to 0.5 times to that of line resistance. The effect of line resistance variation is found less on the interconnect delay of MLGNR. Finally, they demonstrated that fully specular, intercalation doped and ZZ-edged MLGNRs are more advantageous to *Cu* interconnects, if the line-resistance variation is concerned, for advanced IC technology.

The authors in [71] presented the FDTD-based accurate and efficient model for crosstalk analysis in the coupled interconnects of MLGNR. They proposed a model for precise estimation of voltage and current

at any particular point of interconnect. Employing this model, an average error of < 2 % occurred in estimating the crosstalk-induced noise peak voltage and crosstalk-induced delay. They considered two-coupled MLGNR interconnect architecture for the analysis of functional crosstalk and dynamic crosstalk at interconnect length of 100 μm. They also present the model extension to analyze 3-coupled interconnects lines. Later on, the same authors, in [72], proposed a crosstalk model based on width dependent MFP for accurate estimation of the crosstalk-induced performance of MLGNR. They studied the impact of width dependent MFP on dynamic crosstalk, for both in-phase and out-phase switched interconnect lines.

The work in [39] explored the dynamic crosstalk performance of MLGNR interconnects employing a distributed circuit model based on the ESC model. The authors studied the impact of two critical parameters, i.e., edge specularity and Fermi-level on crosstalk in capacitively and inductively coupled configuration of MLGNR interconnects, at global length. Through this analysis, they demonstrated that the effect of diffusive edge on crosstalk delay performance of MLGNR reduces with the increase in interconnect width. Additionally, it was observed that delay performance of SC-MLGNR interconnects is superior to that of TC-MLGNR at local length rather than at global length due to its dominating interlayer- resistance at local length.

Yash Agrawal *et al.* developed a unified model for *Cu* and MLGNR interconnects based on finite difference time domain (FDTD) technique [73]. The voltage-mode (VM) and current-mode (CM) signaling scheme are employed to analyze the performance of interconnects. They studied the effects of edge roughness and Fermi-energy in capacitively and inductively coupled interconnects of MLGNR at the 32 *nm* technology node. It is found that, at identical interconnect dimensions and operating conditions, interconnects of MLGNR outperform their *Cu* counterparts in terms of propagation delay, power dissipation, energy dissipation and crosstalk noise. It is also indicated that the CM and VM signaling scheme are best suited for delay-oriented and power-oriented designs, respectively, for local and intermediate interconnects length. However, for interconnects of global lengths, the CM signaling scheme is better than the VM signaling scheme. Besides, MLGNR interconnects with a significant value of specularity constant and high Fermi-energy exhibits low propagation delay. Further, the crosstalk analysis in MLGNR interconnects reveals that low values of crosstalk-induced noise peak and crosstalk delay are obtained with CM signaling than with VM signaling.

The authors in [74] compared the performance of MLGNR as well as MWCNT based interconnects and through-silicon vias (TSVs) with that of *Cu*. They remarked the superior crosstalk delay performance of both MLGNR and MWCNT interconnects than *Cu*. It is also noted that a higher number of conducting channels in MLGNR interconnects results in a smaller value of crosstalk delay than in MWCNT. Further, the authors presented a review of the performance of TSVs based on *Cu*, MLGNR, and MWCNT. This review reveals that, at higher operating frequencies and current density, the key factors that limit the consistent performance of *Cu*-based TSVs are electro-migration, crosstalk noise, and skin effects. Moreover, MLGNR and MWCNT are marked as suitable materials for high-performance TSVs.

Sahoo and Rahaman [75] investigated the crosstalk effects in MLGNR interconnects, based on ABCD parametric approach, to predict their performance at few DSM technology nodes (11 and 8 *nm*). For this investigation, they considered both U- and D-MLGNR with GNR edges in a zigzag shape. At 8 *nm* technology node, the values of worst-case crosstalk delay for perfectly specular D-MLGNR interconnect are found about 4% (at interconnect length of 1*mm*) and 7% (at interconnect length of 5 *mm*) lower than that in *Cu* interconnects. However, worst-case crosstalk noise marginally reduces in both D- and U-MLGNR than its value in *Cu*. Moreover, the crosstalk noise is found unaffected with technology scaling.

The work in [76] focuses on thickness optimization of AsF_5 ID-MLGNR interconnects for crosstalk delay, crosstalk noise, noise-delay-product (NDP), noise-bandwidth-ratio (NBWR), EDP and PDP, at technology node of 8 *nm,* for different values of specularity constant, p = 0, 0.8, 1. The optimized thickness based on the minimization of crosstalk-delay, NDP, NBWR and EDP of ID-MLGNR (at p = 0, 1) found to 25 *nm* and 100 *nm* for semi-global and global interconnects lengths, respectively. A higher crosstalk noise peak observed in ID-MLGNR than in *Cu*. However, as far as the area and width of crosstalk noise concern, the performance of ID-MLGNR is found better than *Cu*. The PDP analysis, irrespective of interconnects lengths, resulted in an optimized thickness of 100 *nm* for perfectly specular MLGNR interconnect.

A comparative analysis of crosstalk-effects in MLGNR and MWCNT interconnect in ternary ICs is performed at a technology node of 10 *nm* and 7 *nm* [77]. For accurate crosstalk analysis, in the coupled 5-line and 7-line architecture, the effects of adjacent aggressors on an actively and passively shielded victim line are considered. In a 5-line architecture at 7 *nm*, the crosstalk delays in MLGNR are 54%, 56%, and 49% lower than in MWCNTs for active, passive and unshielded lines respectively. These improvements obtained in the case of power dissipation are 49%, 36% and 36%. Furthermore, crosstalk noise areas in MLGNR diminish by 25% and 72% to its values in MWCNT in the case of passive and active line shielding, respectively. Additionally, MLGNR interconnects are noted to have more technological advantages than MWCNT with technology scaling from 10 *nm* to 7 *nm*.

The research works carried out in [78],[79] have studied the influence of the physical dimension of MLGNR interconnects on its crosstalk performance.

The work in [78] analyzed the influence of interconnect spacing and technology scaling on crosstalk performance of nearly diffusive coupled MLGNR interconnects of global length at 14 *nm* technology. For this analysis, they presented a modified MTL model, which improved by incorporating two important physical parameters of interconnect, i.e., length and inter-line spacing. It is indicated that at a specific technology node, delay reduces with the increase in interconnect spacing from 5 to 20 *nm*. The crosstalk delay and crosstalk noise reduce by 45% and 9% with technology scaling from 32 *nm* to 14 *nm*.

Bhattacharya *et al.* [79] presented a reduced thickness interconnect model (RTIM) for MLGNR to diminish the crosstalk effects. The crosstalk delay and crosstalk noise are analyzed in RTIM based SC- and TC-MLGNR (i.e., SC- and TC-RMLGNR) interconnects, and the results are compared with ITRS

based *Cu* and SC- and TC-MLGNR interconnects. The crosstalk-induced delay in SC-RMLGNR reduces to about 1.02 to 2.36× in comparison to *Cu*, whereas in TC-RMLGNR, these reductions are about 1.58 to 1.95×. Furthermore, the effects of crosstalk noise, i.e., rise/fall glitches and overshoot/undershoot, are found less in both the SC- and TC-RMLGNR than *Cu*.

Previously crosstalk effects in MLGNR interconnects have been studied based on different types of repeaters insertion like FinFET and carbon nanotube field-effect transistor (CNTFET), different techniques like FDTD and unconditionally stable FDTD (US-FDTD) at various DSM technology nodes [80],[81].

The authors in [80] have analyzed the effects of FinFET and CNTFET based repeaters insertion on the crosstalk performance of AC and ZZ-edged MLGNR interconnects, at different interconnects lengths, employing a 3-line architecture. It is found that the crosstalk delay in MLGNR interconnects much reduces with CNTFET repeaters than with FinFET. However, power consumption in FinFET repeaters in driving the MLGNR and *Cu* interconnects is slightly less than in CNTFET. The crosstalk delay reductions in MLGNR are 47.47%, 30.91% and 20.65% with CNTFET and 41.54%, 34.57% and 19.71% with FinFET, in comparison with *Cu*, at interconnects lengths of 100, 500, and 1000 μm, respectively. Regardless of the FinFET or CNTFET repeater insertion, both AC and ZZ-edged MLGNR interconnects demonstrated better crosstalk delay and noise reduction at the local/semi-global level than at the global level.

Mekhla *et al.* [81] developed an US-FDTD method to accurately analyze the crosstalk effects in coupled interconnects of dielectric inserted SC-MLGNR (Di-SC-MLGNR), SC-MLGNR and *Cu*. The US-FDTD method found 1.5× faster than the FDTD method in concern to CPU runtime. Moreover, Di-SC-MLGNR demonstrates better crosstalk delay reduction compared to SC-MLGNR and *Cu.*

The authors in [62],[82],[83],[84] studied the crosstalk in coupled interconnects of doped and U-MLGNR interconnects from the perspective of gate oxide reliability and stability for future VLSI interconnect applications.

In the presented work [82], the authors studied the crosstalk effects to analyze the gate oxide reliability in U-MLGNR interconnects in comparison to that of *Cu* and MWCNT. The analysis is carried out at technology node 16 *nm,* and crosstalk is evaluated in terms of near/far end noise and overshoot/undershoot. To estimate the influence of overshoot/undershoot, a critical parameter, i.e., gate oxide failure-in-time rate (FIT) is investigated. The crosstalk analysis revealed that the lowest far-end overshoot/undershoot area obtained in MLGNR interconnects implied small gate oxide FIT and hence signifies its higher gate oxide reliability than both *Cu* and MWCNT. Moreover, channel-hot-carrier (CHC) reliability is found deficient in MLGNR due to the higher near-end overshoot/undershoot peaks obtained in it as compared to that in *Cu* and MWCNT.

A similar study as in [82] was carried out for U- and D-MLGNR interconnects at specularity constant, $p = 0, 0.8, 1$ in [83], based on ABCD matrix parameter approach, at technology nodes 11 and 8 *nm*. It is found that perfectly specular ($p = 1$), D-MLGNR outperforms U-MLGNR and *Cu* in terms of gate

oxide reliability. The gate oxide failure rate in the perfectly specular (p =1), D-MLGNR interconnects estimated to ~ 240 × and ~ 790 × less than in *Cu* at 11 and 8 *nm* technology node, respectively.
The U-MLGNR interconnects also have been investigated for their bandwidth, stability, and step time responses [62]. For this analysis, the transfer function matrix for inductively and capacitively coupled interconnects of MLGNR is derived. The longer and narrow MLGNR due to their rapidly damping step response are found more stable at their near-end output, whereas longer and wider MLGNR due to the hike in maximum overshoot becomes unstable at their far end output. Besides, the effects of the increase in coupling capacitance observed positive for near-end stability and adverse for far-end stability, whereas the reverse is seen with the increase of inductive coupling. Furthermore, increase either in interconnect length or in capacitive coupling causes the bandwidth reduction. In contrary to this, increase either in interconnect width or in inductive coupling causes the bandwidth improvement.
The effects of substrate surface roughness (SSR) on crosstalk delay and stability in coupled interconnects of U-MLGNR have also studied [84]. The different types of dielectric materials viz. SiO_2, BN, SiC with their RMS value of SSR 'δ_{SSR}' equal to 10, 50 and 170 pm, respectively, are considered. It is found that regardless of interconnect length (i.e., local or global), the 50% crosstalk delay in MLGNR interconnects increases with an increase in δ_{SSR} and edge scattering probability (p) of MLGNR. Further, the crosstalk delay in MLGNR interconnects in comparison to *Cu* interconnects obtained larger on SiO_2 substrate but smaller on BN and SiC. It is indicated that better crosstalk performance of MLGNR interconnects than *Cu*, on SiO_2 substrate, can be achieved either by using a perfectly flattened dielectric surface or by increasing doping concentration (Fermi-energy) in MLGNR. Moreover, an increase in SSR improves the stability in MLGNR interconnects than in *Cu*.

2.4.2.3 *Temperature-dependent crosstalk*

Bhattacharya *et al.* [85] studied the influence of temperature on crosstalk performance (in terms of delay and noise) of diffusive edged MLGNR interconnects. The crosstalk delay analysis reveals that % delay variation in MLGNR interconnects with the increase in temperature (233-278 K) as well as interconnects length (from 10-100 *μm*) are small in comparison to that in *Cu* interconnects. As far as crosstalk-noise is concerned, at near-end of the victim line, the noise voltage variation for MLGNR is less than for *Cu* at all the temperature and interconnects lengths considered under the study. While at the victim's far end, the noise voltage in both MLGNR and *Cu* becomes insensitive to temperature. Moreover, MLGNR interconnects noted to more thermally stable than their *Cu* counterparts do.
Rai *et al.* [31] were the first to present the temperature-dependent ESC model for MLGNR interconnects. They analyzed the performance of single as well as coupled interconnects of MLGNR at technology node 22 *nm*, and compared it with that of *Cu* interconnects. It is indicated that propagation delay and power dissipation in a 1 *mm* long single interconnect of MLGNR is low than in *Cu* at different temperatures beyond room temperature (i.e., 300 K to 500 K). In the coupled interconnects configuration, a lower value of temperature-dependent crosstalk delay and noise is observed in MLGNR

than in *Cu,* which attributes to the lower resistance and ground capacitance of the former. Further, based on their developed temperature-dependent model, an average % improvement (over an interconnect length from 200 to 1000 μm) of 37.24 and 19.59 in propagation delay and power dissipation, respectively, is observed in MLGNR in comparison to the conventional temperature-independent model. Employing the developed model, a significant reduction of 35% is also obtained in the width of the victim output pulse which signifies the improved gate oxide reliability of MLGNR interconnect with rising interconnect temperature.

The work presented in [86] is the extension of authors prior research on crosstalk effects in coupled interconnects of MLGNR at sub 10 *nm* technology nodes in [77], considering influences of process parameters (i.e., the width of interconnect, interlayer spacing, Fermi-energy, dielectric thickness, and MFP) and temperature in the present study. Crosstalk effects variation (i.e., variation in delay, noise area, and power) in the presence of all process parameters increases with the increase in interconnect length at both technology node 7 and 10 *nm*. If compared, these variations found significant as the technology node shrinks from 10 *nm* to 7 *nm* at any interconnect lengths and becomes more prominent as the interconnect length approaches from local to global level. Further, among the various process parameters, the MFP and interconnect width are found leading factors in estimating these variations. On average, the noted values of delay, power and noise area variations are 65 ps (135 ps), 0.4 μW (0.57 μW) and 6 V-ps (12 V-ps), respectively at 10 *nm* (7 *nm*). The variation trend of crosstalk delay and noise area, with the rise in temperature from 200 K to 450 K, is to increase. The noted values of maximum variations of these two parameters are 57 ps (118 ps) and 6 V-ps (9V-ps) at 300 K $< T \leq$ 450 K and 6 ps (12 ps) and 0.5 V-ps (1V-ps) at 200K $\leq T <$ 300 K, at technology node 10 *nm* (7 *nm*).

Recently, Das *et al.* [87] developed the temperature-dependent distributed T-network model and gate oxide reliability model for MLGNR interconnects. They analyzed the temperature-dependent crosstalk overshoot/undershoot and its effects on gate oxide reliability in terms of gate oxide FIT for different variants of MLGNR, viz., U-SC-MLGNR, TC-MLGNR (U, AsF_5-doped, Li-doped, and $FeCl_3$-doped). The gate oxide FIT in *Cu* is found to increase with the rise in chip operating temperature from 233 K to 450 K and lengths of interconnects, whereas, gate oxide FIT in U-SC-MLGNR and D-TC-MLGNR remain almost insensitive to the variations of these two parameters (i.e., IC temperature and interconnect length). These findings in U-SC-MLGNR and D-TC-MLGNR obtained due to their smaller resistance and larger ground capacitance. The D-TC-MLGNRs also demonstrates the better gate oxide reliability than U-TC-MLGNR.

After the extensive literature review on the crosstalk analysis of MLGNR interconnects, it is noted that although MLGNR interconnects has been investigated for crosstalk using different bus architecture, DIL configurations incorporating inductive and capacitive coupling and process parameters but these investigations paid less attention to the studies of the effect of temperature variation on crosstalk performance in ID-MLGNR interconnects. Viewing the eminent performance of ID-MLGNR interconnect among the SWB, MWB, and *Cu* interconnects, it becomes of utmost importance to explore the impact of crucial process parameters like temperature on its crosstalk performance that could plague

its promising interconnect performance. Besides that, frequency-domain analysis in coupled interconnects of ID-MLGNR needs investigations for its high-frequency application.

2.5 INTERCONNECT PERFORMANCE OF OTHER GRAPHENE-BASED MATERIALS

The approach of VLSI industries in the DSM regime aids in achieving the goals of fast and multitasking electronic devices and systems in the submicron regimes. However, this approach has led to the dismal performance of scaled *Cu* interconnects due to critical issues arisen as a result of technology scaling (viz. electro-migration, size effects, etc.). The constrained performance of *Cu* interconnects for existing and emerging technology nodes, as discussed earlier in [20]-[24], expectedly be the prime bottleneck in achieving this future industrial goal, and hence demands the introduction of radical change in the design and technology of on-chip interconnects. Responding to these demands, researchers, besides MLGNR, have proposed numerous novel and innovative interconnects materials like CNTs and its other compositions (viz. bundled SWCNTs and bundled MWCNTs).

Though these two compositions of CNT, i.e., bundled SWCNTs (SWB) and bundled MWCNTs (MWB), are presently under theoretical and experimental investigations for their potential interconnects applications [88]-[90]. However, reportedly, the fabrication of both SWB and MWB possessing several constraints [91],[92]. The produced CNT bundles are neither alone of SWCNTs nor alone of MWCNTs, but the mixtures of two. Besides, not all the CNTs within the bundle are of metallic types. The chirality control, diameter-control and formation of metal contacts with each SWCNT or with each shell of MWCNT are some challenging task confronted in the growth of SWB and MWB. Hence, several researchers have introduced the MCB, with either specific or random arrangements of SWCNTs and MWCNTs within the bundle [93]-[99].

The best structure of MCB is that in which CNTs at the center serve as the excellent conductor, and those at the extreme boundary (periphery) provide the shielding from adjacent MCBs. A metallic SWCNT or a large diameter MWCNT with each shell contacted with metal can serve as a good conductor, whereas, a semiconducting SWCNT or a small diameter MWCNT with only outermost shell contacted with metal can serve as a good insulator. This structural arrangement of CNTs within MCB could suppress the capacitive as well as inductive crosstalk in coupled interconnects of MCBs [93].

Majumder *et al.* [94] first introduced the analytical modeling of MCB following the random distribution of CNTs within a bundle. Considering the normal distribution of CNTs having different diameters within MCB, the propagation delay, power dissipation and crosstalk-induced delay are analyzed. In estimating the output voltage waveform of MCB, employing the MTL and ESC models, a deviation of about 5.6% in the later w.r.t. former is observed. The crosstalk delay analysis in capacitive-coupled interconnect lines of MCBs reveals that for tube densities ranging from 10^9-10^{12} tubes/cm^2, at global interconnect length, the crosstalk delay significantly reduces for higher tubes densities in a bundle. Besides that, it is investigated that in estimating the propagation delay an average error of 2.44% is obtained using the simplified ESC model rather than using the MTL approach.

The same authors, further in [95], proposed the different structures of MCBs with the spatial and random distribution of SWCNTs and MWCNTs within it, and compared the interconnect performance of randomly structured MCB with that of specifically structured MCB. It is noted that the MCB structure (addressed as 'MCB-VI' by the authors), in which MWCNTs works as peripheral shield and SWCNTs works as centrically placed conductors demonstrates the best interconnect performance in terms of propagation delay and crosstalk delay. On average, in 'MCB-VI', the propagation delay and crosstalk delay reduces by 80% and 82.8%, respectively, in comparison to that in randomly structured MCB.

The MCB structures proposed in [95] were further analyzed in [96] for their interconnect performance in comparison to SWB, MWCNT, MWB, and *Cu*, at a technology node of 32 *nm*. The computed results further marked the outstanding performance of MCB interconnects than their SWB, MWCNT, MWB and *Cu* counterparts. Like, in the propagation delay of MCB, as interconnect length varies from 500 μm - 2500 μm, an average reduction of 60%, 40%, 22% and 69% is observed as compared to that of SWB, MWCNT, MWB and *Cu*. These % reductions in the power dissipation are 49%, 45%, 36% and 60% and in the worst-case crosstalk delay are 39%, 25%, 15%, and 59%. This implies the MCB interconnect is a better alternative to *Cu* interconnect than SWB, MWCNT and MWB.

The sensitivity of interconnect performance to process variation becomes more pronounced with the scaling of feature size. Majumder *et al.* [97] presented a compact analytical model for randomly structured MCB interconnects, and reported the impact of process-induced variations on MCB single-line delay performance. For this analysis, the process parameters considered are temperature, the metallic ratio of CNTs, metal-CNT contact resistance, and the bundle area. It is observed that densely packed MCB interconnects are more immune to process-induced variation than SWB and MWB. This is because the CNT (of different diameters) count is higher in densely packed MCB than in SWB and MWB, which implies its higher conductance, and thereby lower propagation delay.

The tunneling conductance and inter-shell capacitive coupling in MWCNTs have a significant impact on its delay and power dissipation, consequently, on the interconnect performance of MCB. Considering these facts, the authors in [98] analyzed the effects of temperature-dependent crosstalk-noise in capacitively coupled interconnects of MCBs at a technology node of 22 *nm*. Four different structures of MCBs with spatial arrangements, i.e., MCB 1-4, were analyzed. The computed results reveal that over the temperature variation from 300 K to 500 K, the MCBs, regardless of its structure and tunneling effects, exhibit lower crosstalk-induced noise at the victim's far end as compared to *Cu* interconnects. Further, the lowest peaks of crosstalk-induced noise are observed with MCB-2, and the smallest duration of that is noted with MCB-1. Interestingly, the presence of the tunneling conductance and inter-shell capacitive coupling improves the immunity of the victim line to crosstalk-induced noise at its far-end.

Based on the FDTD method, the work in [99] presented time and memory-efficient model to accurately analyze the temperature-dependent crosstalk effects in MCB interconnects. They exploited the concept that the number of CNTs of a specific diameter, within MCB, follows a Gaussian distribution. Employing the proposed model, an in-depth analysis of in-phase and out-phase crosstalk-induced delay,

and crosstalk-induced noise peak and time duration is performed, under different switching conditions as well as at different temperatures. It is observed that the performance of MCB interconnects deteriorates with the rise in temperature. Further, through the execution of various test cases, it is demonstrated that the proposed model is highly efficient in estimating the crosstalk effects in MCB interconnects, with percentage error within 1% for all the test cases.

A literature survey on CNT bundles leads to the conclusion that although MCB has been analyzed for signal transmission performance (in terms of delay, power dissipation, and PDP), temperature-dependent crosstalk performance, and stability performance. However, the interconnect performance of MCB is yet to be compared with a graphene-based potential alternative to *Cu*, i.e., MLGNR to find the best alternative to *Cu* for future high technology ICs.

2.6 CONCLUSION

The presented literature has reviewed the performance of currently being used *Cu* interconnects, recently proposed U-MLGNR, ID-MLGNR and MCB based interconnects, at various DSM technology nodes, in terms of propagation delay, power dissipation, PDP and EDP in single-interconnect configuration, and dynamic crosstalk, functional crosstalk and frequency-domain behavior of coupled-interconnects configuration.

The study of numerous theoretical and experimental works in the available literature reveals that the performance of scaled *Cu* interconnects with realistic roughness profiles is degraded in terms of delay, power dissipation and crosstalk. Graphene nanoribbon based interconnects have emerged as a possible solution for these key interconnect problems.

Although the research work carried out by various researchers, reveal that the performance metrics of single MLGNR interconnect (viz. delay, power dissipation, PDP and EDP) primarily depend on its edge scattering probability, Fermi-energy, conductance and dimensions of interconnect. Many researchers have investigated the influence of temperature as well as process-induced parameters like the width of interconnect, interlayer spacing, MFP, dielectric thickness and dielectric constant on the aforementioned performance matrices of U-MLGNR interconnects in single-line configuration. A few researchers have also analyzed the performance of ID-MLGNR vs. U-MLGNR and MWCNT to find the best alternative to *Cu* interconnects. However, reportedly, no studies have been made to analyze the impact of temperature on the performance of ID-MLGNR interconnects, and to comparatively analyze the temperature-dependent behavior of both MLGNR and MCB based interconnects which have been proposed for their potential interconnect applications in the DSM regime.

From a detailed literature study on crosstalk-induced noise and delay in coupled interconnects of MLGNR, it is noted that the crosstalk performance of MLGNR interconnects improves over SWB, MWB and *Cu* interconnects, with the increase in its edge-specularity, number of layers in MLGNR, Fermi energy, and technology scaling. A fewer works has also reported the influence of variation in line-resistance, temperature and process parameters (i.e., the width of interconnect, interlayer spacing,

Fermi-energy, dielectric thickness, and MFP) on crosstalk effects variation (i.e., variation in delay, noise area, and power) in two or more than two coupled interconnects of U-MLGNR. The coupled interconnects of ID-MLGNR have also been studied for temperature-dependent crosstalk noise and its effects on gate oxide reliability.

However, after the extensive literature review on the crosstalk analysis of MLGNR interconnects, it is noted that although MLGNR interconnects has been investigated for crosstalk using different bus architecture, DIL configurations incorporating inductive and capacitive coupling and process parameters but these investigations paid less attention to the studies of the effect of temperature variation on crosstalk performance (in terms of both crosstalk-induced noise and delay) in ID-MLGNR interconnects. Moreover, it is worth noting that despite the predictions of outstanding performance of ID-MLGNR in single line configuration, most of the available literature paid less attention to the performance evaluation of ID-MLGNR in coupled interconnect lines.

Further, a few researchers investigated the impact of GNR's edge shape on the interconnect performance of MLGNR. However, two important aspects were neglected. First, the performance of a single doped MLGNR interconnect was evaluated without considering the coupling effect between the interconnects. Second, the coupled interconnects of only U-MLGNR were considered. For the accurate evaluation of the crosstalk performance in coupled MLGNR interconnects, the three imperative facts viz. feasibility of interconnect fabrication, the impact of crucial process parameters and the influence of the physical structure of interconnect on its performance, must be taken into account.

Furthermore, investigations have been carried out on temperature-dependent frequency-domain performance of single interconnect of U-MLGNR and ID-MLGNR, and temperature-independent frequency-domain performance of coupled interconnects of U-MLGNR. Hence, there is need to investigate the temperature-dependent frequency-domain performance of coupled interconnects of ID-MLGNR to estimate their performance in high-frequency ICs applications, under the influence of temperature variations.

Several theoretical and experimental investigations have proved that ID-MLGNR is the strongest contender for future VLSI interconnects among another graphene-based interconnects (i.e. purely metallic SWB, MWB) due to its key advantages of easy fabrication and intercalation doping. However, to date, no such study is reported that has compared the crosstalk performance of ID-MLGNR with another graphene-based potential interconnect material i.e. MCB.

CHAPTER 3

TEMPERATURE DEPENDENT PERFORMANCE OF SINGLE-LINE MULTILAYER GRAPHENE NANORIBBON INTERCONNECT

3.1 INTRODUCTION

High-performance ICs often operate at a temperature much beyond room temperature (300 K) and have a great variation in its performance with the variation in temperature. These temperature variations can significantly affect the signal propagating along the recently proposed interconnect materials (CNTs and GNRs) [16], [31], [98].

In the past, J. Cui *et. al* [68] analyzed the MLGNR interconnects for signal transmission characteristics at 14 and 22 *nm* technology nodes. Particularly, the effects of the Fermi level of MLGNR on the time delay of the transmitted rectangular pulse have been examined. W. S. Zhao *et. al* [40] compared the signal transmission performance of TC-MLGNR and SC-MLGNR interconnects. Additionally, the resistivity of MLGNR interconnects was compared with the densely packed SWNT bundle, isolated MWNT and *Cu*. Nishad *et. al* [14] proposed the optimization of TC-MLGNR interconnects to enhance their performance than *Cu* interconnects and to achieve comparable performance with SC-MLGNR interconnects.

The works reported in the literature [14], [39], [40], [68] have accurately analyzed the superior performance of MLGNR interconnects in comparison to SWCNT bundle, isolated MWCNT and *Cu* interconnects. Earlier, Kumar *et al.* [49] analyzed the power and delay performance of ID-MLGNR interconnects. The authors in [41] analyzed and compared the delay and EDP of ID-MLGNRs, U-MLGNR and *Cu* interconnect. They demonstrated ID-MLGNRs as potential candidates for local interconnect applications. For the performance evaluation of MLGNR interconnects, the key factors that can affect its performance i.e., Fermi energy, edge specularity, interlayer conductance, and intercalation doping have been taken into account, but avoiding a crucial process parameter i.e. the effect of varying operating temperature in ICs.

Reportedly, no studies have been made to comparatively analyze the temperature-dependent (TD) behavior of both MLGNR and MCB based interconnects which have been proposed for their potential interconnect applications in the DSM region. Therefore, there is a need to address temperature-dependent circuit models for accurate estimation of TD signal transmission delay and power dissipation in ID-MLGNR interconnects in comparison to MCB interconnects.

This chapter presents the TD circuit modeling and the performance analysis in terms of propagation delay, power dissipation and PDP of ID-MLGNR interconnects, at the global domain of interconnects, over a temperature range from 300 K-500 K. In section 3.2, based on the ESC model, analytical TD models to extract the interconnect parameters of MLGNR and MCB are presented. In section 3.3, incorporating ITRS 2013 update at 14 *nm* technology node, the TD impedance of MLGNR interconnect

is analyzed for a temperature variation over a range from 300 K-500 K and is compared with that of MCBs exhibiting tunneling effects and *Cu* interconnects. In section 3.4, firstly the effect of the tunneling conductance on the propagation delay and power dissipation in four different structures of MCBs, i.e., MCB (1-4) is reported. Further, conclusions are drawn based on the numerical evaluation of delay and power dissipation in MCBs structures considering with and without tunneling conductance effect within a temperature range from 300 K-500 K. Subsequently, based on the T-spice simulations, the global-length ID-MLGNR interconnects are analyzed for the TD delay, power dissipation and PDP performance in comparison to MCB 1-MCB 4 (considering tunneling effect) and *Cu* based interconnects of identical dimensions, over the temperature range from 300 K-500 K. Conclusions are finally drawn in section 3.5.

3.2 TEMPERATURE DEPENDENT ESC MODELS OF MLGNR INTERCONNECTS

3.2.1 Equivalent RLC models of MLGNR interconnects

This section presents an accurate analytical temperature-dependent model based on the geometrical and physical parameters of MLGNR. The cross-sectional geometry of stage-II ID-MLGNR interconnect, with a width (W), thickness (H), and dielectric thickness (d) is shown in Figure 3.1. The permittivity of the dielectric is represented by ε_r. The total number of layers 'n' in MLGNR is obtained by using the formula given as

$$n = 1 + \text{int}\left[\frac{H}{\delta}\right] \tag{3.1}$$

Where 'int' indicates integer value and δ is the average interlayer distance between the GNR layers and is defined as $\delta = (S_1 + S_2)/2$ [10]. The corresponding values of S_1 and S_2 (Figure 3.1) are assumed to be 0.335 *nm* and 0.815 *nm*, respectively, and the average layer spacing between two adjacent graphene layers is 0.575 *nm* for stage-II AsF_5 ID-MLGNR. The stage-II AsF_5 intercalated graphite (p-type) can have an in-plane conductivity of 0.63 $(\mu\Omega\ .\text{cm})^{-1}$. The increased layer spacing of 0.575 *nm* in AsF_5 intercalated MLGNR as compared to the interlayer-layer spacing of 0.34 *nm* in undoped MLGNR results in the increase of MFP [10]. Figure 3.2 presents the equivalent temperature-dependent circuit model of MLGNR interconnects. MLGNR is viewed in the form of a stacked arrangement of SLGNRs [31]. Therefore, to derive the ESC circuit parameters of MLGNR, ESC circuit parameters of SLGNR can be used [40].

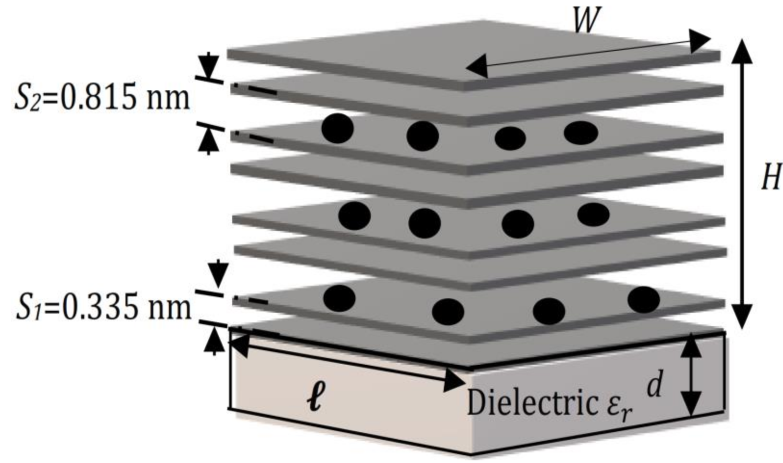

Figure 3.1 Schematic view of stage-II ID-MLGNRs (graphite). The solid line indicates graphene layers, where layers with black circles indicate intercalate layers between graphene layers [10].

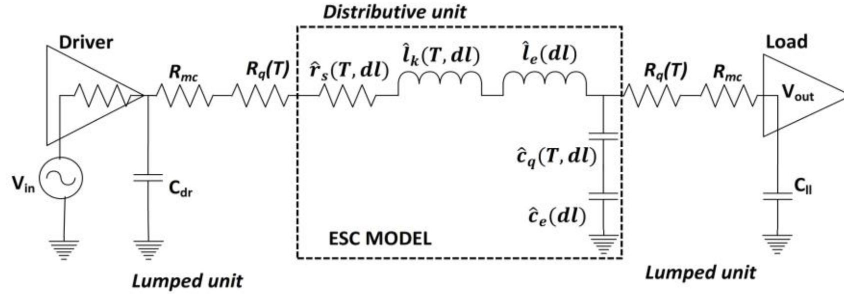

Figure 3.2 Temperature-dependent ESC model of MLGNR interconnects, where *dl* is the differential element along the interconnect length ℓ.

Interconnect line parameters i.e. resistance, capacitance and inductance are the main elements of the ESC model. The TD behavior of MLGNR interconnects mainly relies on the resistance which is a function of temperature [16]. The temperature-dependence of the resistance arises due to the temperature-dependence of the electron scattering MFP with acoustic phonons at low-bias [100]. The resistance of SLGNR per-unit-length (*p.u.l.*) is classified as (i) contact resistance 'R_c' which includes quantum contact resistance '$R_q(T)$', and imperfect metal-contact resistance 'R_{mc}' and (ii) scattering resistance '$\hat{r}_s(T)$'. The contact resistance (R_c) of MLGNR is expressed by [16]

$$R_c = \left[\sum_{j=1}^{n}\left(R_{j,mc}/2 + R_{j,q}/2\right)^{-1}\right]^{-1} \tag{3.2}$$

Where $R_{j,mc}$ is the imperfect metal-contact resistance of the j^{-th} layer, which is fabrication dependent. It has a typical value of about 20 KΩ [68]. $R_{j,q}$, represent quantum contact resistance '$R_q(T)$' of the $j^{\text{-th}}$ layer [11]. $R_q(T)$ takes into accounts the effect of spin- and sub-lattice degeneracy of carbon-atoms and is expressed as in Equation (3.3) [14],

$$R_q(T) = \frac{h/2e^2}{N_{ch}(T)} = \frac{12.9\ K\Omega}{N_{ch}(T)} \tag{3.3}$$

The number of TD conducting channels '$N_{ch}(T)$' is obtained by considering the contributions of all the conduction subbands 'n_c' and valence subbands 'n_v', given as [11], [40], [68], [101],

$$N_{ch}(T) = \sum_{j=0}^{n_c}\left(1 + e^{\frac{E_j - E_F}{k_B T}}\right)^{-1} + \sum_{j=0}^{n_v}\left(1 + e^{\frac{E_j + E_F}{k_B T}}\right)^{-1} \tag{3.4}$$

Where E_j denotes the highest (lowest) energy of the j-th valance (conduction) sub-bands. E_F, k_B, and T are the Fermi-energy, the Boltzmann's constant, and the temperature, respectively.

If interconnect length 'ℓ' is larger than the electron MFP (λ_{eff}), its scattering resistance is taken into account. The *p.u.l.* distributive scattering resistance $\hat{r}_s(T)$ for SLGNR is given by [40].

$$\hat{r}_s(T) = \frac{h}{2q^2.\lambda_{eff}(T).N_{ch}(T)} \tag{3.5}$$

The impact of temperature on the impedance parameters i.e. resistance, inductance, and capacitance of GNR interconnects can be understood by the temperature-dependent conducting channels $N_{ch}(T)$. However, for electrical and thermal modeling of GNR resistance, understanding the influence of various electron-phonon scattering mechanisms is of much importance. The primary sources of scattering at finite temperature, in GNR, are due to 1) acoustic, 2) non-polar optical phonons, and 3) surface polar phonons of the substrate. Using Matthiessen's rule, the value of temperature-dependent TD effective MFP for electrons in SLGNR interconnects is given by $\lambda_{eff}\ (T)$.

$$\lambda_{eff}\ (T) = \ [1/\lambda_{AC}(T) + \ 1/\lambda_{OP}\ (T) + \textstyle\sum_i (1/\lambda_i^{\mathrm{SPP}})]^{-1} \tag{3.6),}$$

The TD MFP in graphene due to acoustic phonons '$\lambda_{\mathrm{AC}}(T)$' can be obtained from the acoustic phonon mobility as in [102], and is given by Equation (3.7). The MFP due to scatterings by optical phonons is obtained by considering two components; $\lambda_{ABS}^{OP}(T)$ and $\lambda_{EMS}^{OP}(T)$ that represent the absorption or emission of optical phonons respectively [31], as expressed in Equation (3.8),

$$\lambda_{AC}(T) = \frac{\rho_m(\hbar \mathcal{V}_f v_s)^2}{\sqrt{\pi.n}D_{AC}^2 \kappa_B T} \tag{3.7),}$$

$$\lambda_{ABS}^{OP}(T) = \frac{\rho_m \hbar\omega_{OP}(\mathcal{V}_f)^2}{\sqrt{\pi N_S}D_{OP}^2 N_{OP,AB}\left(1 + \frac{\omega_{OP}}{\mathcal{V}_f\sqrt{\pi.n}}\right)} \qquad \lambda_{EMS}^{OP}(T) = \frac{\rho_m \hbar\omega_{OP}(\mathcal{V}_f)^2}{\sqrt{\pi N_S}D_{OP}^2 N_{OP,EM}\left(1 - \frac{\omega_{OP}}{\mathcal{V}_f\sqrt{\pi.n}}\right)} \tag{3.8}$$

Where the mass density of graphene ρ_m = 7.6× 10^{-7} kg/m^2, the speed of acoustic phonons v_s= 20 km/s. N_s is the concentration of 2-D electron gas in graphene and D_{AC} is the acoustic deformation potential, and the values of these parameters can be obtained in [103]. $\mathcal{V}_f$ is the Fermi velocity ≈ 8×10^5 m/s. Typical values of optical phonon energy, $\hbar\omega_{OP}$~160 meV and optical deformation potential D_{OP}~(1-4)×10^9 eV/cm are used in literature [102]. $N_{OP,AB}$ and $N_{OP,EM}$ are the phonon occupation numbers given by Bose–Einstein statistics for absorption and emission processes, respectively, and can be calculated as $N_{OP} = 1/(e^{(\omega_{OP}\hbar)/(k_B T)} - 1)$.

Besides acoustic and optical phonon, the polar nature of the substrate causes the surface polar-phonon (SPP) scatterings in graphene. The SPP produces an electric field that interacts with the electrons on the nearby graphene. This type of scattering is prominent in the case of the graphene and carbon nanotubes, as the vertical dimensions of these materials are negligible (~ Van der Waals distance). The electron MFP, λ_i^{SPP} in graphene limited due to SPP scatterings is given as [104],

$$\lambda_i^{SPP} = \sqrt{\frac{\beta}{\hbar\omega_{SO,i}}\frac{\hbar V_f}{e^2}\frac{eV_f}{F_i^2}\frac{exp(\hbar_0 z_0)}{N_{SPP,i}}\frac{\hbar\sqrt{\pi}}{e}} \tag{3.9}$$

Where the separation between the graphene and substrate $\beta \approx 0.153 \times 10^{-4}e$V, the Vander Waals distance between the polar substrate and GNR $z_0 \approx 3.5$ Å, $\hbar_0 \approx [(2\hbar\omega_{SO,i}\hbar^{-1}V_f{}^{-1})^2 + \chi n]^{1/2}$and $\chi \approx 10.5$. F_i^2, denotes the magnitude of the polarization field called Froehlich coupling. Surface polar phonon energy '$\hbar\omega_{SO,i}$' is obtained from the bulk longitudinal optical phonons. It is indicated that the temperature dependency of λ_i^{SPP} is given by the SPP phonon occupation number $N_{SPP,i} \approx \kappa_B T/\hbar\omega_{SO,i}$.

As shown in Figure 3.3, at a high-temperature limit beyond room temperature (RT) 300 K, MFP due to acoustic phonon, optical phonon, and SPP scattering decreases with the rise in temperature from 300 K-500 K. Nominal variation in the MFP associated with acoustic phonon (λ_{AC}) is due to the high temperature and the low-field mobility of charge carriers [102]. Exponential behavior of λ_{OP} is attributed to the $N_{OP,AB}$ and $N_{OP,EM}$. Additionally, it can be observed that at high temperatures (≥ 300 K), MFP is mainly contributed by optical phonon. As can be seen in the case of λ_{net}^{SPP}, depending on the type substrates (i.e., hexagonal Boron Nitride (h-BN), silicon dioxide (SiO_2) and hafnium dioxide (HfO_2)) and at carrier concentration$n = 5 \times 10^{11}$cm^{-2}, the best value of $\lambda_{net}^{SPP} \approx 900\ nm$ is extracted using h-BN substrate while the least value of $\lambda_{net}^{SPP} \approx 30\ nm$ is obtained using HfO_2 substrate. While with SiO_2 substrate, it is 190.3 *nm* at room temperature [103] and falls with the rise in temperature varying from 300 K-500 K.

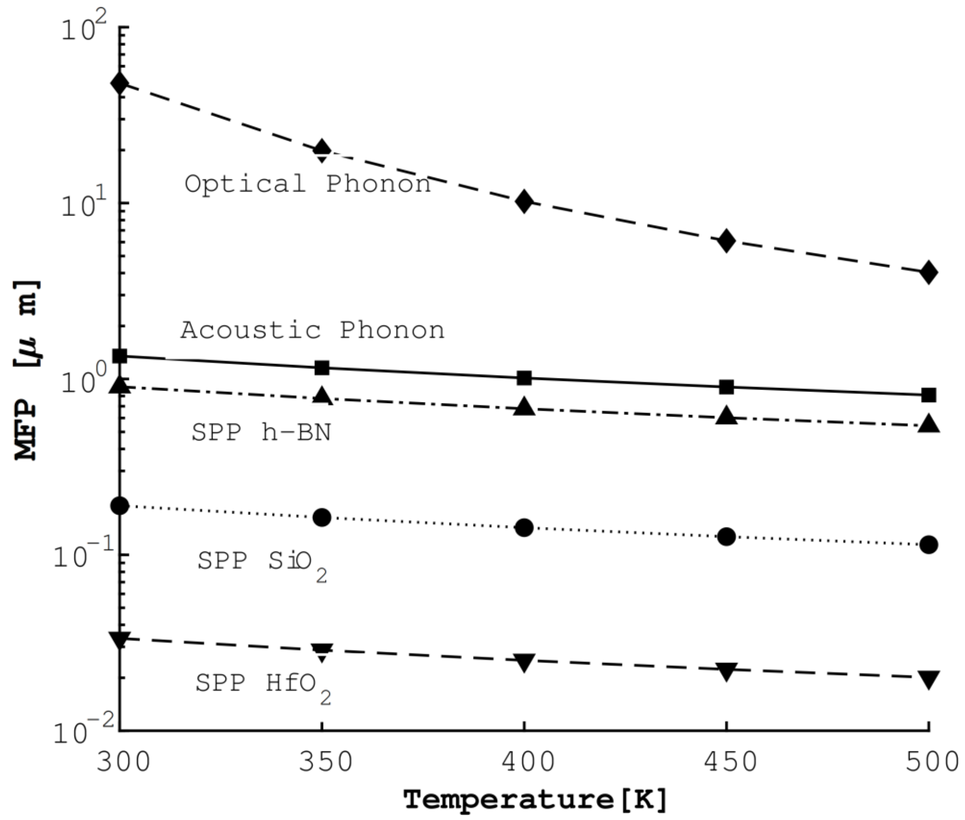

Figure 3.3 MFP in GNR as a function of temperature. Various scattering mechanism viz. optical phonon, acoustic phonon, and surface polar phonon of substrate- h-BN, SiO_2, HfO_2 is considered.

It is indicated that most of the GNRs fabricated reportedly in the last few years are found with rough (or diffusive) edges [11]. Additionally, in most of the literature, a typical value of the MFP due to defects is taken as $1\mu m$ for the performance evaluation of the different variants of MLGNR (for instance doped and undoped MLGNR), which is impractical. Hence, to evaluate the realistic interconnect performance of MLGNR, the TD ESC model of MLGNR is further improved by including the scattering effects due to edge roughness and defects in GNR. To achieve the aim, the formulation for $\lambda_{eff}\,(T)$ for electrons in SLGNR interconnect, as given in Equation (3.6), is extended to include the MFP associated with scatterings due to the rough edges and defects present in GNR.

The modified expression for $\lambda_{eff}\,(T)$ is given as

$$\lambda_{eff}{}'(T) = \lambda_{eff}\,(T) + \lambda_i + \lambda_D \qquad (3.10),$$

The MFP 'λ_i'of the i-th sub-band in GNR related to scattering at its edges [40] is expressed as,

$$\lambda_i = \frac{W}{1-p}\sqrt{\left(\frac{2WE_F}{ihv_F}\right)^2 - 1} \qquad (3.11)$$

Where p is edge specularity. For fully specular edges in GNR, its value is unity, and for fully diffusive edges, it is taken as zero. The MFP associated with scattering due to defects 'λ_D' of AsF_5 ID-MLGNR can be obtained using $\sigma_{in-plane}$ and n_p. Where $\sigma_{in-plane}$ indicates in-plane conductivity and n_p denotes carrier concentration [10]. λ_D is formulated as

$$\lambda_D = \frac{\sigma_{in-plane}}{2q^2}.\frac{h^2 v_F}{\pi}.\frac{1}{|E_F|}\text{; where } k_B T \ll |E_F| \quad (3.12),$$

Using simplified tight-binding model, E_F can be expressed as [10],

$$E_F = hv_F\sqrt{\frac{n_p.\delta}{4\pi}} \quad (3.13),$$

E_F has been optimized for TC-MLGNR to meet its performance with SC-MLGNR over the local domain of interconnect length (10 nm – 100 nm) [14], [48]. The values of $\sigma_{in-plane}$ and σ_c (c-axis conductivity) are found to be 0.63 × 10^6 $(\Omega.\text{cm})^{-1}$ and 0.24 $(\Omega.\text{cm})^{-1}$, respectively for AsF_5 (stage index-II) ID-MLGNR [41], [65], [71].

It is reported that SC-MLGNR can provide smaller resistance than TC-MLGNR for short interconnect length. However, the perpendicular resistance between adjacent layers in TC-MLGNR decreases with the increasing length of interconnects that makes its resistance and performance comparable to SC-MLGNR [14], [39]. In this work, to evaluate the performance of global level interconnects, TC-MLGNR (ZZ-edged) with the reported fabrication feasibility is considered. The resistive networks shown in Figure 3.4 (a) and (b) are used to evaluate the resistance of TC-MLGNR and SC-MLGNR, respectively.

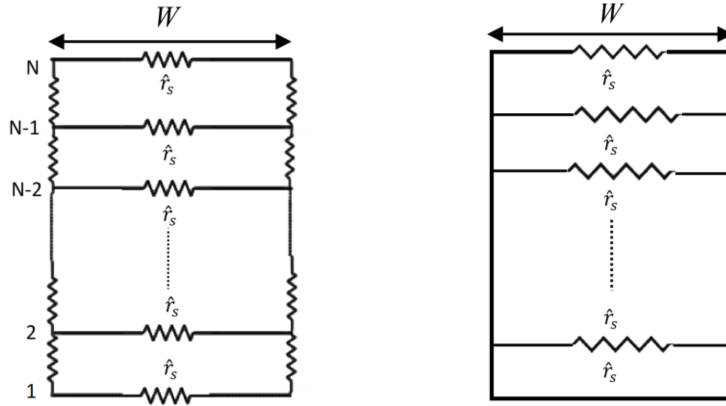

Figure 3.4 Resistance *p.u.l.* for (a) TC-MLGNR , (b) SC-MLGNR interconnects [14].

The *p.u.l.* total scattering resistance 'R' of TC-MLGNR [14], is given as

$$R = R_{N-1} = \left[\frac{1}{\hat{r}_{s(N)}+R_Y} + \frac{1}{\hat{r}_{s(N-1)}}\right]^{-1} \quad (3.14a),$$

where $R_Y = \rho_c\delta/W.\ell$ and $\hat{r}_{s(N)} = \hat{r}_s$ at the Nth layer. ρ_c is the c-axis resistivity. W and ℓ are the width and length of MLGNR interconnect, respectively. Here $\hat{r}_s(N) = \hat{r}_s(N-1) = \hat{r}_s(N-2) = \cdots = \hat{r}_s(2) = \hat{r}_s(1) = \hat{r}_s$. The total resistance of TC-MLGNR is as follows

$$R_{TC\text{-}MLGNR}(T) = 2R_c + R.\ell = 2\left[\sum_{j=1}^{n}\left(R_{j,mc}/2 + R_{j,q}/2\right)^{-1}\right]^{-1} + \left[\frac{1}{\hat{r}_{s(N)}+R_Y} + \frac{1}{\hat{r}_{s(N-1)}}\right]^{-1}.\ell \quad (3.14b),$$

Equation (3.15) expresses the total resistance of SC-MLGNR

$$R_{SC\text{-}MLGNR}(T) = 2R_c + \frac{\hat{r}_s(T)}{n}.\ell = 2R_C + \sum_k\left(\frac{h.\ell}{2e^2.n.\ \lambda_{eff,k}(T).N_{ch}(T)}\right) \quad (3.15)$$

The total inductance of MLGNR interconnect is given by the series addition of two types of inductances: (i) kinetic inductance and (ii) magnetic inductance. The kinetic inductance '$\hat{l}_k(T)$' represents the kinetic energy of the electrons and is a function of $N_{ch}(T)$.Whereas, the magnetic inductance '$\hat{l}_e$' is due to the stored energies of charge carriers in the magnetic field [105]. The *p.u.l.* the kinetic and magnetic inductances of MLGNR are expressed in Equation (3.16) [31], [49]. Where d is the height of MLGNR interconnects above the ground plane.

$$\hat{l}_k(T) = \frac{h}{4\,e^2 v_F\, n\, N_{ch}}\ , \quad \hat{l}_e = \frac{\mu_0 d}{W} \tag{3.16}$$

Two types of capacitance are defined for MLGNR: (i) quantum capacitance and (ii) electrostatic capacitance. The quantum capacitance (c_q) is due to the stored electrostatic energy in charge carriers. As stated by the Pauli Exclusion principle, the possibility to add the electrons into the 1-D conductor depends on the available quantum state at a level higher than the Fermi energy level [105]. The expression for *p.u.l.* quantum capacitance can be obtained by equating the required energy to an effective capacitance. The electrostatic capacitance is defined as the capacitance between the bottom-most layer of MLGNR and ground due to the electric field induced between them [105],

The *p.u.l.* coupling capacitance 'c_m' and *p.u.l.* equivalent quantum capacitance '$\hat{c}_q(T)$' (using recursive scheme) [40] is given as

$$c_m = \varepsilon_0 W \tag{3.17a}$$

$$\hat{c}_q(T) = c_{rec}^n \tag{3.17b}$$

$$c_{rec}^1 = c_q(T) = \frac{4e^2 N_{ch}(T)}{h v_F} \tag{3.17c}$$

$$c_{rec}^i = \left(\frac{1}{c_{rec}^{i-1}} + \frac{1}{c_m}\right)^{-1} + c_q(T) \qquad , i \in [2, n] \tag{3.17d}$$

The analytical expression for the distributed *p.u.l.* electrostatic capacitance '$\hat{c}_e$' can be obtained from [14]. The total equivalent TD capacitance '$C(T)$' including electrostatic capacitance '$\hat{c}_e$', quantum capacitance '$\hat{c}_q\,(T)$' and the total equivalent TD inductance '$L(T)$' in MLGNR interconnect are given by Equations (3.18) and (3.19), respectively,

$$C(T) = (\,\hat{c}_q(T)^{-1} + \hat{c}_e^{-1}\,)^{-1} \tag{3.18}$$

$$L(T) = (\hat{l}_k(T) + \hat{l}_e) \tag{3.19}$$

3.2.2 ESC modeling of MCB with the spatial arrangement

In this work, four different structures of MCBs [106] have been considered, where SWCNT and MWCNT are arranged differently as MCB-1, MCB-2, MCB-3, and MCB-4, respectively, shown in Figure 3.5. W_P and H_P denote the width and thickness of the MWCNT bundle, respectively. The novel structure of MCB i.e. MCB-1, where SWCNTs are in a central position and MWCNTs at the periphery, is shown in Figure 3.5 (a). Figures 3.5 (b) and (c) show that MWCNTs and SWCNTs share an equal

half area of a bundle with the horizontal and vertical arrangement in MCB-2 and MCB-3, respectively. MCB-4 has SWCNTs at the periphery with the central location of MWCNTs, as depicted in Figure 3.5 (d).

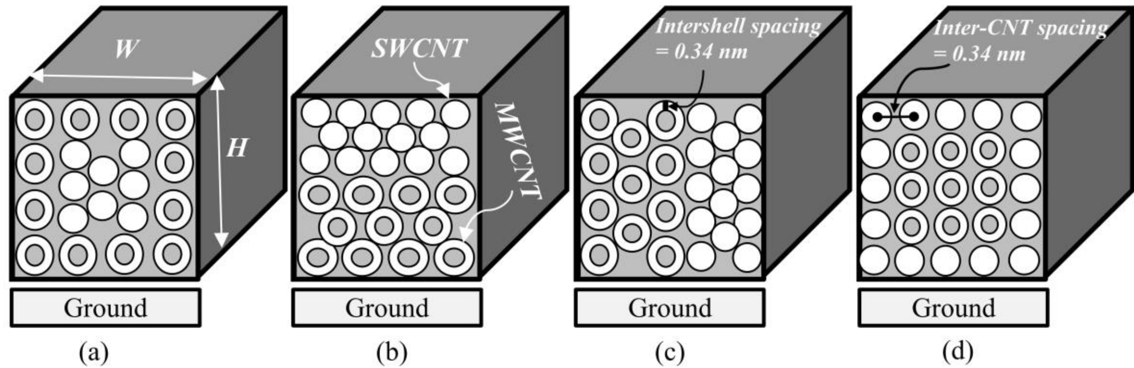

Figure 3.5 Different spatially arranged structure of MCBs (a) MCB-1 (b) MCB-2 (c) MCB-3 (d) MCB-4 [95].

The hierarchy of spatially arranged MCB (1-4) structures is based on the concept that the ESC model of the MCB consists of an ESC model of the MWCNT-bundle and the SWCNT-bundle, as shown in Figure 3.6, where $R^X_{BUNDLE}(T), L^X_{BUNDLE}(T)$ and $C^X_{BUNDLE}(T)$ denote the impedance parameters of bundles. Superscript X indicates M, S for MWCNT and SWCNT, respectively. The ESC model of MW/SW-CNTs is based on the multiconductor transmission line theory [107].

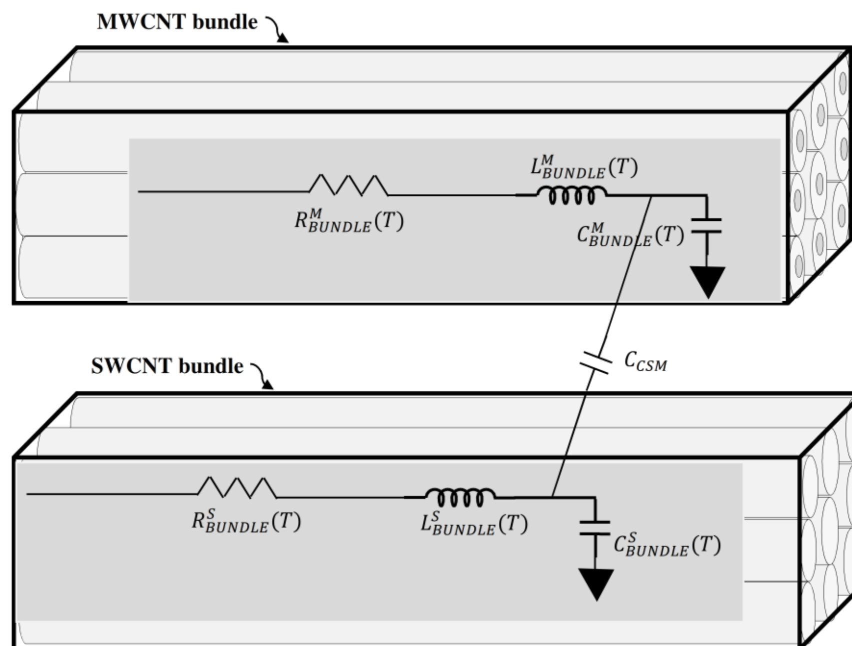

Figure 3.6 ESC model of the MCB based interconnect [98].

The modeling of interconnect parameters of the MCB interconnect, using the ESC model, is based on the total number of the conducting channels [108]. The conducting channels of MWCNT/SWCNT are

modeled as a function of temperature and shell/tube diameter, assuming 1/3 SWCNT or MWCNT's shells as metallic [95]. Number of conducting channels for an isolated SWCNT with diameter *d* or for any particular shell with a diameter D_i in MWCNT is expressed as

$$N_i(D_i,T) \approx \begin{cases} A.T.D_i + B & D_i > d_T/T \\ 2/3 & D_i < d_T/T \end{cases} \quad (3.20),$$

Where A = 6.12 × 10^{-4} nm^{-1} K^{-1} and B =1.275. Based on the thermal energy of electrons and the gap between the sub-bands d_T ≈1300 nm.K at T=300 K [109]. The total number of conducting channels in MCB is obtained by the summation of conducting channels N_i of each MWCNT and SWCNT in the bundle [95] as

$$N_{total} = \sum_{i=1}^{n_{\text{MWCNT-BUNDLE}}} . \left(\sum_{j=1}^{p} N_i(D_j,T)\right) + \sum_{i=1}^{n_{\text{SWCNT-BUNDLE}}} N_i(d) \quad (3.21),$$

The total number of CNTs in any of the given structures of MCBs (1-4) can be obtained by adding the number of SWCNTs and MWCNTs in the MCB bundle [98]. The number of MWCNT in the bundle is expressed as [95],

$$n_{\text{MWCNT-BUNDLE}} = \left\{ \begin{matrix} n_{WM} * n_{HM} - \left(\frac{n_{HM}}{2}\right) \text{ for } n_{HM} \text{ is even} \\ n_{WM} * n_{HM} - \left(\frac{n_{HM}-1}{2}\right) \text{ for } n_{HM} \text{ is odd} \end{matrix} \right\} \quad (3.22),$$

$$n_{WM} = \left\lfloor \frac{W_P - D_P}{S_{C-C}} \right\rfloor \quad , \; n_{HM} = \left\lfloor \frac{H_P - D_P}{S_{C-C}} \right\rfloor . \quad (3.23)$$

Where n_{HM} and n_{WM} represent the number of columns and rows in the bundle, respectively, and $n_{\text{MWCNT-BUNDLE}}$ is the total number of MWCNTs in the bundle. As shown in Figure 3.7, D_P is the maximum outer diameter of isolated MWCNT, with a *p* number of shells. y_{ILD} is a symbolic presentation for the height of the bundle from the ground.

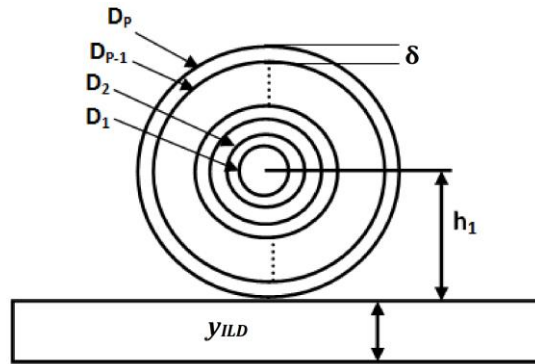

Figure 3.7 The geometry of MWCNT above the ground Plane [110].

The total number of SWCNTs in the bundle given by $n_{\text{SWCNT-BUNDLE}}$ can be determined using Equations (3.22) and (3.23), by replacing outer-shell diameter term D_P of the MWCNTs, with diameter

d of the SWCNT. For both SWCNTs and MWCNT, an inter-tube/inter-shell spacing of 0.34 *nm* is considered here [111].

The electrical resistance for an isolated SWCNT or i^{th} shell in MWCNT is expressed by Equation (3.24). It constitutes of intrinsic or fundamental quantum resistance of CNT in the ballistic region 'R_{Qi}', CNT-metal contact resistance 'R_{Ci}' and distributed scattering resistance 'R_{Si}' for non-ballistic region i.e. $\ell > \lambda_{eff,i}$ [16], [100].

$$R_{shell,i}(T) = R_{Qi} + R_{Si}.\ell + R_{Ci} = \frac{h}{2.e^2.N_i(D_i,T)} + \frac{h}{2.e^2.N_i(D_i,T)}.\frac{\ell}{\lambda_{eff,i}(T)} + R_{ci} \quad (3.24),$$

In addition to $N_i(D_i, T)$, temperature-dependence of $R_{shell,i}(T)$ mainly comes from $\lambda_{eff,i}(T)$ which is the MFP of electrons and is proportional to the diameter of each SWCNT/MWCNT for $T_0 = 100$ K [112], [113], as expressed in Equation (3.25)

$$\lambda_{eff,i}(T) = 890\frac{D_i.T_0}{T-2T_0} \quad (3.25)$$

Multiple shells in MWCNTs are separated with a Vander Waals gap and do interact with each other. This inter-shell interaction induces a tunneling conductance between adjacent shells. Several researchers have proved its existence [114]. The resistance of an isolated MWCNT, that includes the resistance of all the shells *i* = 1, 2, 3…p and inter-shell tunneling resistance 'R_{ti}' is obtained by the recursive function $R = R_N^{rec}$ and is given by Equation (3.26). Where R_{ti}, computed using conductivity normalized to shell interval $\sigma \sim 0.3(\mu\Omega.cm^2)^{-1}$ is $\approx 0.106\ K\Omega/D_i(\mu m)$ [114].

$$R_{MWCNT}(T) = \begin{cases} R_i^{rec} = \left(\left(R_{i-1}^{rec} + R_{t(i-1)}\right)^{-1} + (R_{shell,i})^{-1}\right)^{-1} i \in [2, N] \\ R_1^{rec} = R_{shell,1} \end{cases} \quad (3.26)$$

The inductance of SWCNT/MWCNT is given by the series addition of the kinetic inductance induced by the electric field within and between the tubes, and magnetic inductance depending on the current loop induced by SWCNT/MWCNT [105]. For an isolated MWCNT, the *p.u.l.* kinetic inductance '$\hat{l}_k(T)$' and the *p.u.l.* magnetic inductance 'l_m' are obtained as in Equation (3.27). Where *h* (= 6.63 × 10^{-34} m^2 kg/s) is the Planck's constant, $L_e^{\prime p,p}$ is the *p.u.l.* magnetic inductance of the external p^{th} shell, and h_1 is the height of the isolated CNT above the ground plane [107].

$$\hat{l}_k(T) = \frac{\frac{h}{2e^2(v_f)} \approx 16.1\ nH/\mu m}{2\sum_{j=1}^{p} N_i(D_j,T)\ p}, \ l_m = L_e^{\prime p,p} = \frac{\mu_0}{2\pi}\cosh^{-1}\left(\frac{D_p/2+h_1}{D_p/2}\right) \quad (3.27)$$

The total capacitance in isolated MWCNT is obtained by taking *p.u.l.* quantum capacitance '$\hat{C}_Q(T)$' in series to the *p.u.l.* electrostatic capacitance 'C_E' for each conducting channel [115]. $\hat{C}_Q(T)$ of isolated MWCNT can be obtained using a recursive function while taking into account mutual capacitance, due to intershell interaction in MWCNT [114]. However, $\hat{C}_Q(T)$ is much larger than the 'C_E', hence can be ignored. The *p.u.l.* electrostatic capacitance 'C_E' can be obtained as in Equation (3.28). Where $C_e^{p,p}$ is the *p.u.l.* electrostatic capacitance of the external p^{th} shell [116].

$$C_E = C_e^{p,p} = \frac{2\pi\epsilon_0\epsilon_r}{\cosh^{-1}\left(\frac{D_p/2+h_1}{D_p/2}\right)} \quad (3.28)$$

The *p.u.l.* resistance, kinetic inductance, magnetic inductance, and the electrostatic capacitance of an isolated SWCNT can be obtained using Equations (3.24-3.26), Equation (3.27), and Equation (3.28), respectively, taking the unit shell of an isolated MWCNT. The equivalent bundle parameters $R_{BUNDLE}^{X}(T), L_{BUNDLE}^{X}(T)$ and $C_{BUNDLE}^{X}(T)$ for MWCNT/SWCNT can be obtained by dividing the impedance parameters of its corresponding isolated unit with $n_{\text{XWCNT-BUNDLE}}$.

Based on the aforementioned analysis regarding the modeling of temperature-dependent circuit parameters, *p.u.l.* equivalent circuit parameters for the ESC model of MCB are given by Equation (3.29). C_{CSM} given by Equation (3.30), is the coupling capacitance between the bundles of SWCNT and MWCNT [102], [117]. Where S_{S-M}, is the spacing between the two equivalent bundles and *D* is the average diameter of MWCNTs and SWCNTs.

$$R^{MIXED}(T) = (1/R_{BUNDLE}^{M}(T) + 1/R_{BUNDLE}^{S}(T))^{-1} \quad (3.29a),$$

$$L^{MIXED}(T) = L_{BUNDLE}^{M}(T) + L_{BUNDLE}^{S}(T) \quad (3.29b),$$

$$C^{MIXED}(T) = ((C_{CSM} + C_{BUNDLE}^{S}(T))^{-1} + (C_{BUNDLE}^{M}(T))^{-1})^{-1} \quad (3.29c),$$

$$C_{CSM} = \frac{\pi\varepsilon_0\varepsilon_r}{\cosh^{-1}(S_{S-M}/D)} \quad (3.30)$$

To estimate the performance of *Cu* interconnects accurately under varying temperatures, *Cu* interconnect is replaced by a solid metal of the same dimensions. The following temperature-dependent, low-bias resistance formula can be used for *Cu* [31], [98].

$$R(T) = R_0[1 + \alpha(T - T_0] \quad (3.31)$$

Where $\alpha = 0.00339K^{-1}$ is the temperature coefficient of resistance at *T*=300 K. The resistance $R_0 = \rho_0.\ell/(W.h_1)$, where ρ_0 is the resistivity of *Cu* at *T*=300 K. The analytical expressions for inductance and capacitance of *Cu* interconnects can be obtained in [98].

3.3 TEMPERATURE DEPENDENT IMPEDANCE ANALYSIS FOR NEARLY SPECULAR ID-MLGNR, FOUR DIFFERENT STRUCTURES OF MCB AND *Cu* INTERCONNECTS

In this section, incorporating ITRS-2013 updates for 14 *nm* technology node as shown in Table 3.1, the temperature-dependent impedance (resistance, capacitance, and inductance) of ID-MLGNR (ZZ-edged) interconnects is analyzed for a temperature variation range 300 K-500 K and compared with that of MCB (1-4) (with consideration of tunneling effect) and *Cu* interconnects.

MLGNR interconnects are considered to perfectly specular (i.e., specularity constant *p* = 1), stage-II AsF_5 intercalation-doped with an interlayer spacing of 0.585 *nm*. Further, in this work, the temperature-dependent performance of AsF_5 ID-MLGNR interconnects is evaluated, in terms of power dissipation,

single-line propagation delay and PDP, over a temperature range 300 K-500 K. The work presented is focused on AsF_5 ID-MLGNR, as AsF_5 was one of the fabricated graphite intercalation compounds (GIC) with tremendous stage-II in-plane conductivity of 0.63 $(\mu\Omega\text{-cm})^{-1}$ and Fermi energy (E_F) of 0.6 eV [119], [120]. Chen Xu *et al.* [10] was the first to propose AsF_5 intercalation doping for neutral/undoped MLGNR interconnects and theoretically estimated the superior resistivity of stage-II AsF_5 ID-MLGNR interconnects than *Cu* interconnects. Earlier, a few experimental works have been reported on GNR but they have either focused on few-layer graphene (unsuitable for interconnect application) [121] or on undoped MLGNR(with poor electrical conductivity $\sim 0.026\ (\mu\Omega.cm)^{-1}$ [122].

Table 3.1 Simulation Parameters (2013) [118].

	Technology Node	14 nm
Local interconnects	Width, W(nm)	16
	Aspect ratio, A/R (wire)	2.1
	Height, H (nm)	34
	Aspect ratio, A/R (Via)	2.1
	Y_{ILD} Thickness, $h1$ (nm)	34
	ρ_{Cu}($\mu\Omega$-cm)	6.84
Intermediate interconnects	Width, W(nm)	16
	Aspect ratio, A/R (wire)	2.1
	Height, H (nm)	34
	Aspect ratio, A/R (Via)	1.9
	Y_{ILD} Thickness, $h1$ (nm)	30.4
	ρ_{Cu}($\mu\Omega$-cm)	6.84
Global Interconnects	Width, W(nm)	24
	Aspect ratio, A/R (wire)	2.34
	Height, H (nm)	56
	Aspect ratio, A/R (Via)	1.5
	Y_{ILD} Thickness, $h1$ (nm)	36
	ρ_{Cu}($\mu\Omega$-cm)	5.69
	Effective dielectric constant, ε_r	2.48
Minimum sized gate	C_L(fF)	0.065
	R_{dr}(KΩ)	18.33
	C_{dr}(fF)	0.030

For MCBs: SWCNT diameter d =1 *nm*, MWCNT inter-shell spacing= 0.34 *nm*, inter-CNT spacing for SWCNT/MWCNT bundle present in MCBs = 0.34 *nm* [98]. The number of SWCNTs and MWCNTs in MCBs (1-4) structures, for global level interconnect width W = 24 *nm* and height H= 56 *nm*, is tabulated in Table 3.2. To evaluate the ultimate potential of bundled MWCNT interconnect, the outermost diameter of MWCNT 'D_p' is set equal to the minimum width of interconnect (at technology node of 14 *nm*), with an innermost/outermost diameter ratio (i.e. D_p/D_1) equal to 0.5 [114], [123]. However, as MCBs are complex structures of bundled MWCNTs and SWCNTs, hence for the sake of simplicity in calculating the equivalent circuit parameters of the MCB interconnects considering inter-shell interactions and tunneling conductance of MWCNTs, MWCNT diameter is assumed to equal to 8 *nm* [98]. Additionally, in support of this assumption, it has been indicated that for larger diameter the

resistivity of global level MWCNT interconnect becomes smaller, and hence, counteracted the negative effect of decreasing the number of MWCNTs [114].

Table 3.2 Number of SWCNTs and MWCNTs in MCBs (1-4) structures for global level interconnect width = 24 *nm* and height = 56 *nm*. Technology node = 14 *nm*. SWCNT diameter = 1 *nm*, and MWCNT diameter = 8 *nm* [98].

MCB structure	No. of SWCNT	No. of MWCNT
MCB-1	345	16
MCB-2	752	9
MCB-3	736	7
MCB-4	666	10

As illustrated in Figure 3.8, the resistance of interconnects i.e. ID-MLGNR, MCB-1, MCB-2, MCB-3, MCB-4 and *Cu* increase with the rise in temperature due to the positive temperature coefficient of resistance for metals. The resistance of ID-MLGNR at any specific temperature, in the range from 300 K to 500 K, is small in comparison to four different structures of MCBs and *Cu* at the global domain of interconnects. The small resistance of ID-MLGNR interconnect is justified because of (i) large value of the Fermi-energy ~ 0.6 eV and (ii) increased MFP due to reduced interlayer scattering achieved by AsF_5 intercalation doping [10] that is not feasible in the cylindrical structure of CNTs (constituting the MCB structures). This suggests that, in the context of reduced propagation delay and power dissipation of ICs, compared with MCBs and *Cu* interconnects, ID-MLGNR interconnects are more promising.

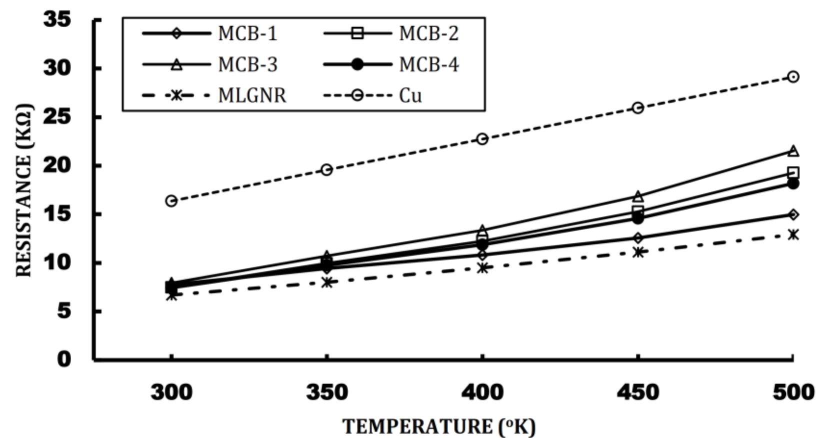

Figure 3.8 Variation of interconnect resistance with temperature ranging from 300 K to 500 K. Interconnects based on ID-MLGNR, MCB (1-4) and *Cu* are considered here at global length =1000 μm. The effect of inter-shell tunneling is considered for all structures of MCB. ID-MLGNR interconnect edges are assumed to be almost specular for the global domain.

The variation of inductance with temperature, ranging from 300 K to 500 K, is shown in Figure 3.9. As the inductance of *Cu* is not a function of temperature, hence, a constant line is obtained in this case. The capacitance of a single-line interconnect is a key factor in the determination of delay and power dissipation. The variation of capacitance with temperature is shown in Figure 3.10. Capacitance increases with a rise in temperature, but due to its weak dependence on TD channels, the obtained curves

are almost straight. Moreover, the capacitance of ID-MLGNR interconnects is small as compared to all structures of MCBs and *Cu*.

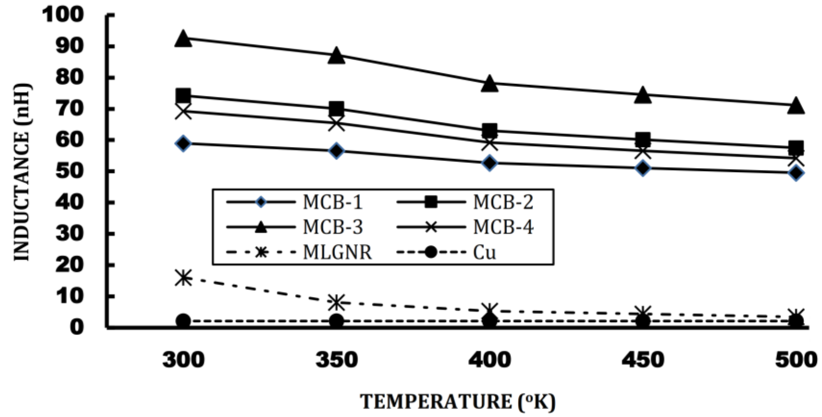

Figure 3.9 Variation of inductance with temperature ranging from 300 K-500 K. Four different structures of MCB, ID-MLGNR, and Cu interconnects are considered here for global length =1000 μm.

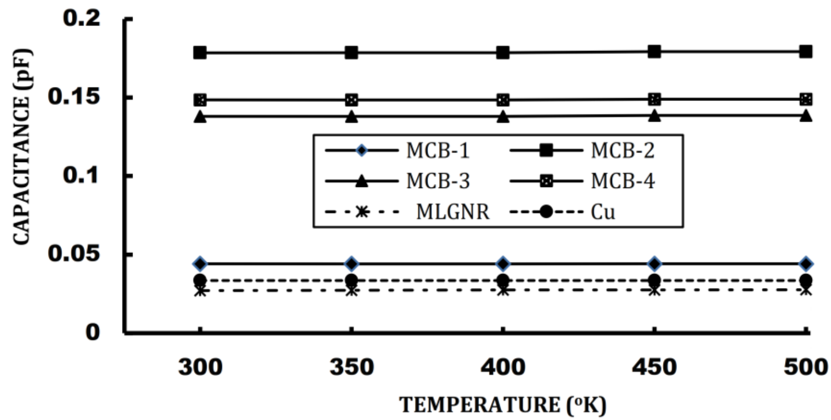

Figure 3.10 Variation of capacitance with temperature ranging from 300K-500K.Four different structures of MCB, ID-MLGNR, and Cu interconnects are considered here for global length =1000 μm.

3.4 TEMPERATURE DEPENDENT PERFORMANCE ANALYSES

3.4.1 Effect of tunneling conductance on MCB performance

MCBs are constituted of SWCNTs and MWCNTs. The tunneling conductance of MWCNTs has a significant impact on its delay and power dissipation, consequently, on MCB interconnect performance. In driver-interconnect-load (DIL) configuration (Figure 3.2), the interconnect line can be represented by an MCB interconnect whose equivalent temperature-dependent circuit model is given by Figure 3.6, the driver is actuated by a CMOS gate and load is actuated by the lumped capacitive load (C_L). The parameters R_{dr} and C_{dr} are the resistance and capacitance of the driver, respectively. The values of the

driver and load parameters (viz. C_L, R_{dr} and C_{dr}) and dimensional parameters of MCB interconnect, required for simulation purpose, is obtained from Table 3.1.

Figure 3.11 and Figure 3.12 demonstrate the effect of tunneling conductance on propagation delay and power dissipation of MCBs (1-4) interconnects, respectively. For this analysis, MCB structures are considered with and without tunneling effect and a temperature variation range from 300 K to 500 K is taken. Here MCB indicates structures with tunneling effect and MCBW indicates structures without consideration of tunneling effect. In context to propagation delay and power dissipation, MCB-1 outperforms the MCB-2, MCB-3 and MCB-4 due to its smaller impedance parameters (viz., resistance (R), inductance (L) and capacitance (C)) in comparison to MCBs (2-4) structures as demonstrated in Figures 3.8, 3.9 and 3.10, respectively.

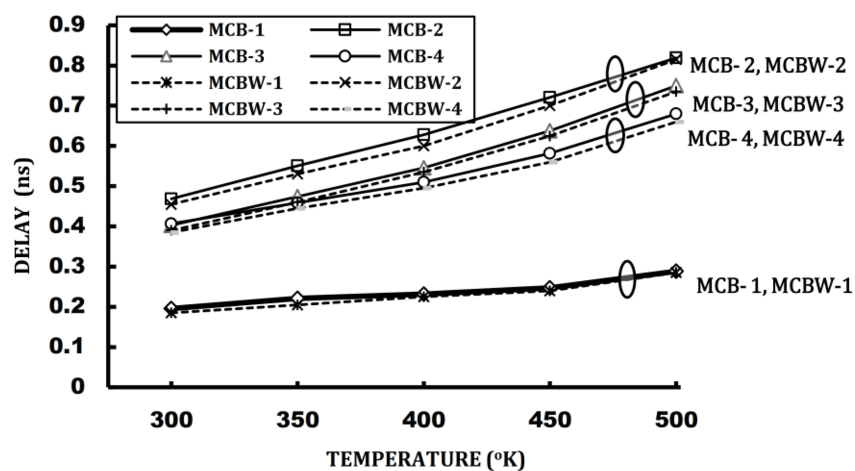

Figure 3.11 Effect of tunneling conductance on the propagation delay of four different structures of MCB interconnects at Length = 1000 μm.

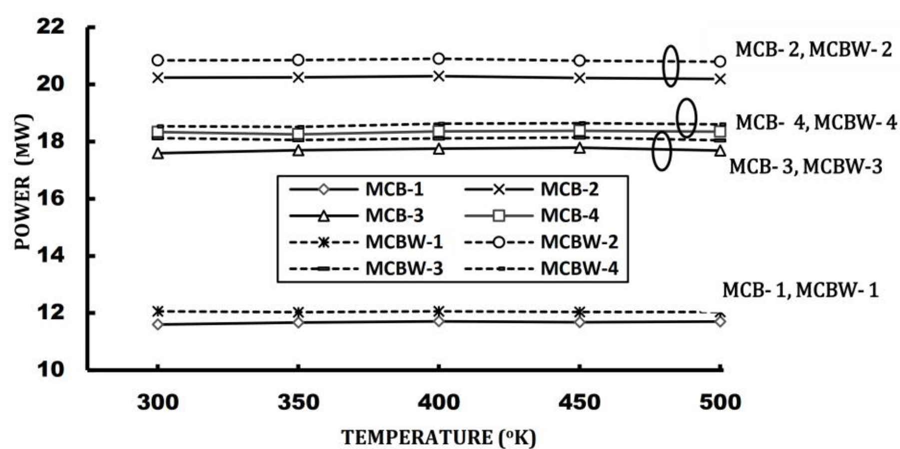

Figure 3.12 Effect of tunneling conductance on the power dissipation of four different structures of MCBs interconnects at Length = 1000 μm.

It has also been indicated that in comparison to MCBs (1-4), the performance of MCBWs (1-4) are observed to superior in terms of power dissipation and signal delay, over a temperature range from 300 K to 500 K. This performance improvement in MCBWs is attributed to the smaller resistance of these structures due to the avoidance of tunneling resistance that is otherwise considered in series with the in-plane shell resistance of MWCNTs present in the structure of MCBs, as shown in Table 3.2. Moreover, Table 3.3 and Table 3.4 also show the percentage penalty in signal transmission delay and power dissipation results, respectively, for MCBs (1-4) due to tunneling effect (of MWCNT) in comparison to results obtained without considering this effect i.e. for MCBWs (1-4), at the global length of 1000 μm over a temperature range from 300 K to 500 K.

Table 3.3 Percentage delay penalty (D) in four different structures of MCBs due to tunneling effects at ℓ = 1000 μm. R- resistance without tunneling effect. R^T- resistance with tunneling effect.

	MCB-1			MCB- 2			MCB- 3			MCB- 4		
T(K)	**R**	**R^T**	**D (%)**	**R**	**R^T**	**D (%)**	**R**	**R^T**	**D (%)**	**R**	**R^T**	**D (%)**
300	7.70	7.75	**5.47**	7.17	7.19	**2.91**	7.91	7.93	**3.20**	7.42	7.44	**5.37**
350	9.39	9.44	**7.43**	9.54	9.57	**3.82**	10.68	10.71	**3.02**	9.72	9.76	**2.91**
400	10.76	10.81	**2.91**	11.75	11.78	**4.50**	13.32	13.35	**1.96**	11.82	11.86	**2.91**
450	12.55	12.58	**2.91**	14.67	14.70	**2.91**	16.86	16.88	**1.96**	14.57	14.60	**3.77**
500	14.91	14.98	**2.91**	18.47	18.53	**0.47**	21.48	21.54	**1.96**	18.13	18.18	**2.91**
Average			**4.32**			**2.92**			**2.42**			**3.58**

Table 3.4 Percentage of power dissipation penalty for MCB (1-4) relative to MCBW (1-4).

	MCB-1	MCB-2	MCB-3	MCB-4
T(K)	**Power (%)**	**Power (%)**	**Power (%)**	**Power (%)**
300	3.81	2.91	2.94	1.07
350	2.96	2.92	1.95	1.41
400	2.91	2.92	1.97	1.42
450	2.95	2.91	1.96	1.43
500	2.76	2.91	1.96	1.43
Average	**3.08**	**2.91**	**2.16**	**1.35**

It can be seen from Table 3.3 that best-delay structure i.e. MCB-1 has the largest and significant penalty of 4.3% in concern to delay performance as compared to MCBs (2-4) structures. Similar findings are obtained in case of the power dissipation performance of MCB (1-4) shown in Table 3.4, where this penalty is 3.08 % for MCB-1.

3.4.2 Temperature-dependent delay, power dissipation and PDP analysis for ID-MLGNR, MCB and *Cu* based interconnects

The global interconnect delay has been the biggest challenge yet to achieve by the semiconductor industry. While the nominal gate delay and local interconnect delay traditionally decreases with technology scaling, global interconnect delay increases [124]. It has been observed that the conductance

of graphene nanoribbon FETs (GNRFETs) exhibits a poor variation even over a temperature range 0 - 2000 K [125]. Whereas, Wan Sick Hwang *et. al* [126] experimentally measured the drain current 'I_D' as a function of gate bias 'V_{GS}' at different temperatures, and demonstrated that low-temperature conduction in GNRFET is dominated by the band to band tunneling [127], whereas at 300 K and above, conduction is dominated by thermionic emission. This indicates that like GNR based interconnect, the conductance of GNRFET is a strong function of temperature. However, the present work is focused on the temperature-dependent performance evaluation of interconnects.

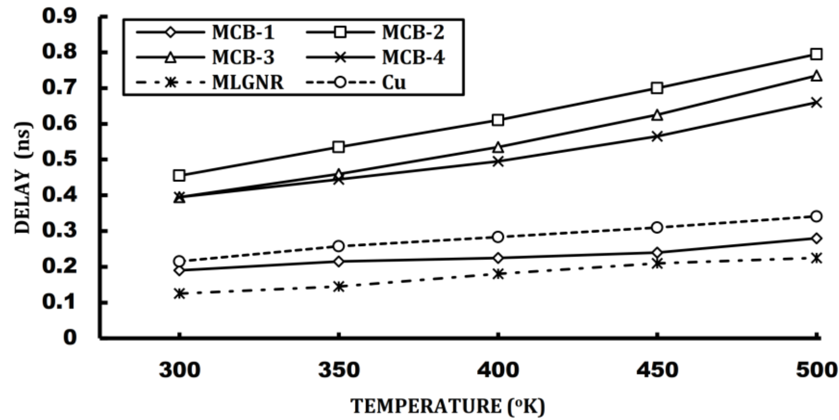

Figure 3.13 Propagation delay of ID-MLGNR interconnects in comparison to MCB-1, MCB-2, MCB-3, MCB-4 and *Cu* interconnects.

In this subsection, the effect of temperature on the delay of 1000 μm (at global domain) long ID-MLGNR interconnect is analyzed in comparison with that of MCBs (1-4) and *Cu* interconnects, over a temperature range 300 K-500 K. For simulation, all technological parameters for ID-MLGNR, MCBs and *Cu* interconnects, at 14 *nm* technology node, are tabulated in Table 3.1. In this analysis, MCBs structures with tunneling effects are considered. It can be seen from Figure 3.13 that propagation delay of all the three interconnects with identical dimensions is increasing with the rise in temperature, but ID-MLGNR interconnect exhibits the smallest delay as compared to that of MCBs (1-4) and *Cu* interconnects.

It is known that delay of global-length interconnects is largely impacted by interconnect resistance since large drivers (driver size of 100 times the minimum size of the driver, is used in this work) are used to drive these interconnects [124]. Hence, global ID-MLGNR interconnects with their minimum resistance in comparison to other two global interconnects (MCBs and *Cu*), as indicated in section 3.3, possess lower interconnect delay for temperature variations ranging from 300 K to 500 K. On average, a relative temperature-dependent delay improvement of 23.78% and 37.66% is observed with ID-MLGNR interconnect in comparison with the best-delay structure of MCB (MCB-1) and *Cu* interconnects, respectively, as depicted in Table 3.5.

Table 3.5 Average relative delay improvement for ID-MLGNR based long interconnect (~1*mm*).

Temperature (K)	Delay improvement w.r.t. MCB-1 (%)	Delay improvement w.r.t. *Cu* (%)
300	34.21	41.92
350	32.55	43.63
400	20.00	36.50
450	12.50	32.20
500	19.64	34.06
Average improvement	23.78	37.66

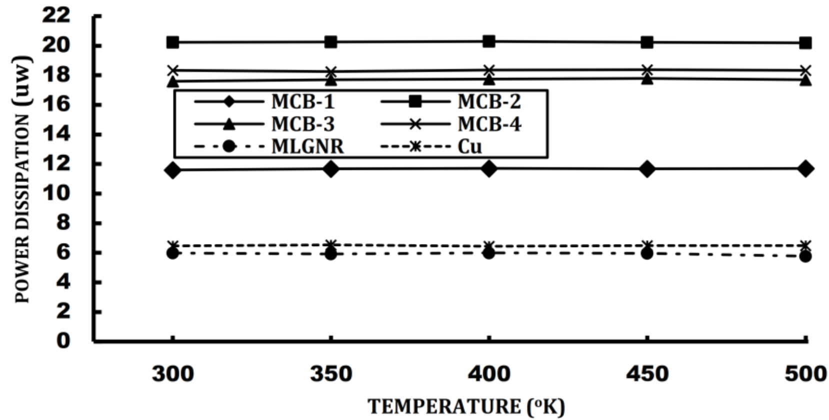

Figure 3.14 Power dissipation of ID-MLGNR interconnects in comparison to MCB-1, MCB-2, MCB-3, MCB-4 and *Cu* interconnects.

Figure 3.14 shows that nearly specular, global level (~1000 *μm*) ID-MLGNR interconnect dissipates minimum power in comparison to MCBs (1-4) and *Cu* interconnects, at any specific temperature over a temperature range from 300 K-500 K. It is mainly because of the minimum capacitance associated with global-length ID-MLGNR interconnects in comparison to MCBs and *Cu* based interconnects, at any specific temperature from 300 K to 500 K. Hence, ID-MLGNR interconnects with their small capacitance can reduce the power dissipation at the global level.

A comparative PDP analysis, as tabulated in Table 3.6, demonstrates the lowest PDP for ID-MLGNR based global interconnects at any specific temperature over a range from 300 K to 500 K. It is justified by the lowest delay and power dissipation in ID-MLGNR as compared to other two interconnects (MCBs and *Cu*). MCB structures with tunneling effects are considered for this PDP analysis. Although MCB-1 exhibits the smallest PDP among its other three structures (MCB-2, MCB-3, MCB-4), this is inferior to *Cu*. This is due to the large power dissipated in MCBs than *Cu*, as shown in Figure 3.14.

Table 3.6 A comparative PDP (×10^{-15} W-s) for ID-MLGNR, MCB (1-4), and *Cu* interconnects.

T(K)	ID-MLGNR	MCB-1	MCB-2	MCB-3	MCB-4	*Cu*
300	0.747	2.204	9.205	6.949	7.243	1.390
350	0.859	2.509	10.831	8.143	8.122	1.680
400	1.079	2.634	12.376	9.497	9.087	1.825
450	1.254	2.802	14.156	11.116	10.383	2.006
500	1.298	3.276	16.051	13.002	12.106	2.211

3.5 CONCLUSION

For the global level (~1000 μm) interconnects, a comparable temperature-dependent performance is investigated for stage-II AsF_5 ID-MLGNR with nearly specular edges and MCB interconnects in terms of signal transmission delay, power dissipation and PDP at 14 *nm* technology node. It has been indicated that mixed CNT bundles (MCBWs) with non-consideration of the tunneling effect outperform mixed CNT bundles with tunneling effect (MCBs). Among MCBs (1-4), possessing a tunneling conductance effect, MCB-1 is demonstrated to have the least propagation delay and power dissipation. The SPICE simulation results reveal that for global interconnects, ID-MLGNR has lower propagation delay and power dissipation than MCBs (1-4) with tunneling effects and conventional *Cu* based interconnects, over a temperature range from 300 K– 500 K. On average, a relative delay improvement of 23.78% and 37.66% is observed for AsF_5 intercalated-MLGNR interconnects in comparison to the best-delay structure of MCBs i.e. MCB-1 and *Cu* interconnects, respectively, over a temperature ranging from 300 K to 500 K. The lowest average PDP value of 1.0474×10^{-15} W-s is also reported for ID-MLGNR based global interconnects. This suggests that, in the context of reduced propagation delay, power dissipation and PDP compared with MCBs and *Cu* interconnects, nearly specular global-length ID-MLGNR interconnects are more promising.

CHAPTER 4

TEMPERATURE DEPENDENT CROSSTALK ANALYSIS IN COUPLED INTERCONNECTS OF INTERCALATION DOPED MULTILAYER GRAPHENE NANORIBBON

4.1 INTRODUCTION

It is reported that with increasing density of on-chip devices, crosstalk effects in adjacent-interconnects have critically arisen the reliability issues in interconnects [65]. However, the research works carried out previously only had focused on the performance evaluation of potential ID-MLGNR in non-adjacent (uncoupled) interconnect applications [14], [39], [40], [41], [49], [68].

Later on, after understanding the crucial impact of crosstalk in coupled interconnects, a few researchers worked primarily to predict the crosstalk performance of one of the promising interconnect materials: MLGNR. Zhao *et al.* [40] investigated the impact of edge-specularity and technology scaling on crosstalk-delay and crosstalk-noise voltage of U-MLGNR. Qian *et al.* [39] performed the dynamic-crosstalk analysis of U-MLGNR interconnects incorporating the parameters viz. edge-specularity and Fermi level. Further, based on the FDTD technique, numerical evaluation of the crosstalk effects in U-MLGNR interconnects is performed [71]. From the discussion mentioned above, it is worth noting that despite the predictions of outstanding performance of ID-MLGNR in single line configuration [14], [39], [40], [41], [49], [68], most of the available literature [39], [40], [71] paid less attention to the performance evaluation of ID-MLGNR in coupled interconnect lines.

The impact of temperature variations is significantly reported to affect the crosstalk performance of the coupled interconnects. It is because there is a great variation (300 K-450 K) in the temperature of high-performance ICs [16]. Hence, both crosstalk and the thermal issues come out to be predestined design criterion for the design of future nanoscale interconnects.

In recent years, both MLGNRs and MCBs based interconnects are investigated for temperature-dependent crosstalk performance at DSM technology nodes [31], [86], [87], [98], [99]. Rai *et al.* first developed the temperature-dependent ESC model for MCBs based interconnects. They analyzed the impact of temperature variations on crosstalk-induced noise in four different structures of MCBs [98]. It was found that the tunneling effect in MCB aids in reducing the crosstalk noise effects as the temperature rises from 300 K to 500 K. In [99], temperature-dependent crosstalk-noise and delay in MCB interconnect were analyzed based on the finite-difference time-domain (FDTD) method. It was demonstrated that the FDTD method is highly efficient in accurately estimating the crosstalk effects in MCB with an error of less than 1%. For MLGNR, the impact of temperature variation on the crosstalk performance was studied in [31], considering its undoped type. Das *et al.* [87] developed a thermally-aware gate oxide reliability model to analyze the effects of crosstalk-induced noise on the performance

of ID-MLGNR, U-MLGNR and *Cu* interconnects. They demonstrate that ID-MLGNR interconnects are highly efficient in suppressing the crosstalk-induced noise effects compared to their U-MLGNR and *Cu* counterparts, and thereby possess more gate-oxide reliability. The authors in [86] analyzed the impact of variation in temperature and process parameters on the crosstalk effects in U-MLGNR at sub-10 *nm* technology nodes. It was indicated that the MFP and the interconnect width are the dominating process parameter in determining the crosstalk effect variations. Also, the crosstalk induced delay and noise area are increased with the rise in temperature from 200 K to 450 K.

Several theoretical and experimental investigations have proved that ID-MLGNR is the strongest contender for future VLSI interconnects among another graphene-based interconnects (i.e. purely metallic SWCNT bundle and MWCNT bundle) [10],[42],[77] due to its key advantages of easy fabrication and intercalation doping. However, to date, no such study is reported that has compared the crosstalk performance of ID-MLGNR with another graphene-based potential interconnect material i.e. MCB.

Based on a temperature-dependent ESC model, improved by incorporating the scatterings due to defects in the existing model, this work presents a more realistic and detailed analysis of the influence of temperature-variation on crosstalk-induced noise voltage and the crosstalk-induced time delay in AsF_5 ID-MLGNR (AC-edged) interconnects. For the first time, a comparative analysis of the temperature-dependent crosstalk performance of ID-MLGNR and MCB (with 4 different structures) interconnects is performed to explore the best alternative to *Cu*. Moreover, the influence of variation in the process parameter i.e. MFP, interlayer spacing, and Fermi energy is investigated on the crosstalk-induced time delay in ID-MLGNR. It is to be noted that the stage–II AsF_5 ID-MLGNR is considered here rather than $FeCl_3$ ID-MLGNR due to its higher values of $\sigma_{in-plane}$ (~ 0.63 × 10^6 $(\Omega\text{-cm})^{-1}$) and E_F (~ 0.6 eV) [43],[128]-[130].

4.2 IMPEDANCE ANALYSIS OF INTERCONNECTS BASED ON NUMERICAL EVALUATION OF TEMPERATURE-DEPENDENT CIRCUIT PARAMETERS

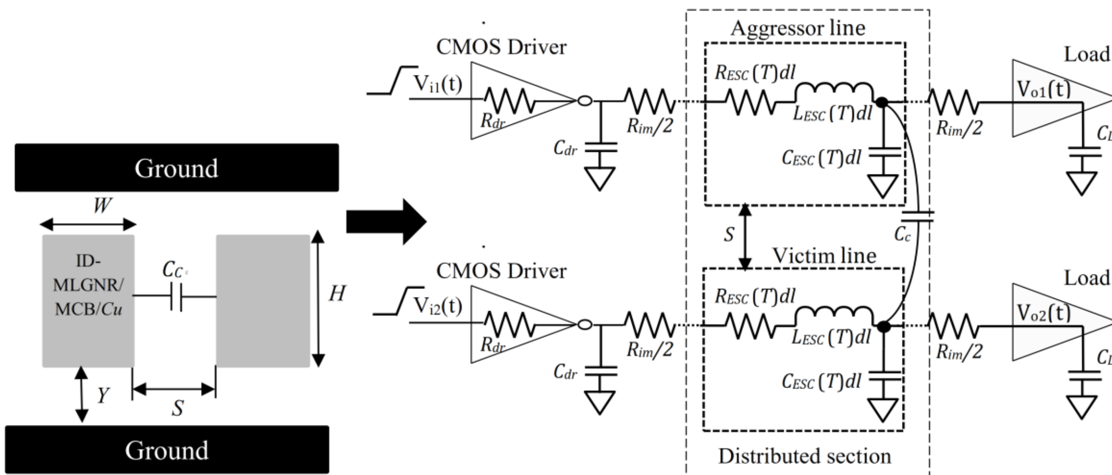

Figure 4.1 Interconnect geometry [118] and its equivalent capacitively coupled DIL configuration [95].

Figure 4.1 shows the geometry of coupled interconnects and their equivalent DIL setup. In capacitively coupled lines, one is referred to as the victim, and another as the aggressor [95]. The equivalent temperature-dependent circuit model of either ID-MLGNR or MCB or *Cu* represents each of the two lines. In DIL configuration, for each interconnect line, the driver is actuated by a CMOS and load is actuated by the lumped capacitive load (C_L). The parameters R_{dr} and C_{dr} are the resistance and capacitance of the driver, respectively.

Given in Figure 4.1, the *p.u.l.* ESC impedance parameters for a MLGNR interconnect, i.e., $R_{ESC}(T)$, $L_{ESC}(T)$, and $C_{ESC}(T)$ can be obtained using the Equations (3.14(b)), (3.18) and (3.19), respectively, as re-written below

$$R_{ESC}(T) = R_{TC-MLGNR}(T) \quad (4.1),$$

$$L_{ESC}(T) = L(T) = (\hat{l}_k(T) + \hat{l}_e) \quad (4.2),$$

$$C_{ESC}(T) = C(T) = (\, \hat{c}_q(T)^{-1} + \hat{c}_e^{-1}\,)^{-1} \quad (4.3)$$

The coupling capacitance between interconnects 'C_c' mainly depends on the spacing (*S*) between the victim and aggressor lines. The value of *S*=24 *nm* is taken in the present analysis. C_c can be expressed for MLGNR [68] as given in Equation (4.4). Where the terms $C_{[BCP]}$ and $C_{[CP]}$ are defined as the capacitance to ground of the bottom side of each GNR and coupling capacitance between two coplanar GNRs, respectively [68].

$$\frac{C_c}{\varepsilon_0 \varepsilon_r} = \frac{0.5}{1+(S/(Y+H))^2} C_{[BCP]}\left(\frac{H}{S/2}, \frac{2Y}{S/2}\right) + \left[\frac{0.87}{1+\left(\frac{S}{2(Y+H)}\right)^2}\right] C_{[CP]}(W/S) \quad (4.4)$$

The *p.u.l.* ESC impedance parameters (i.e., $R_{ESC}(T)$, $L_{ESC}(T)$, and $C_{ESC}(T)$) for a MCB interconnect can be determined using Equations (3.29a)-(3.29c), respectively. The coupling capacitance between adjacent interconnects (C_c) based on MCBs can be obtained in [98]. The *p.u.l.* impedance parameters, i.e., *R, L, C* and C_c for adjacent *Cu* interconnects are obtained using the expressions available in [31], [98].

The quantitative values of equivalent circuit parameters of interconnects based on ID-MLGNR, MCB with four different structures (i.e. MCBs 1-4) and *Cu* for global interconnect length (~ 1 *mm*) at 14 *nm* technology node, at different temperatures within the interval 300 K-500 K, are tabulated in Table 4.1.

Table 4.1 Interconnect parameters of ID-MLGNR, MCBs 1-4, and *Cu* at 14 *nm* technology node, at the global length of 1000 μm. Here U and ID indicate undoped and intercalation-doped MLGNR, respectively

Circuit Parameters	T(K)	MLGNR		MCBs STRUCTURES				
		U	ID	1	2	3	4 4	*Cu*
$R_{ESC}(T)$ (KΩ)	300	22.94	6.01	7.15	7.19	7.90	7.45	16.37
	350	24.92	7.20	9.44	9.57	10.70	9.76	19.56
	400	27.13	8.52	10.81	11.78	13.35	11.86	22.75
	450	29.59	9.99	12.57	14.69	16.87	14.59	25.95
	500	32.27	11.59	14.98	18.52	21.53	18.19	29.14
$L_{ESC}(T)$ (nH)	300		13.61	58.97	74.24	92.64	69.25	2.12
	350		9.07	56.59	70.02	87.21	65.45	2.12
	400		7.42	52.68	63.06	78.27	59.19	2.12
	450		5.83	51.03	60.14	74.51	56.56	2.12
	500		4.80	49.57	57.54	71.17	54.22	2.12
$C_{ESC}(T)$ (pF)	300		0.027	0.044	0.178	0.138	0.139	0.030
	350		0.027	0.044	0.178	0.138	0.139	0.030
	400		0.028	0.044	0.178	0.138	0.139	0.030
	450		0.028	0.044	0.179	0.139	0.139	0.030
	500		0.028	0.044	0.179	0.139	0.139	0.030
C_C (fF)			53.34	72.59	72.59	72.59	72.59	72.59

The dimensional baseline parameters of interconnect are acquired from the latest (ITRS-2013) [118] and are listed in Table 3.1. Intercalation doping mainly affects E_F and $\lambda_{eff}{}'(T)$ in MLGNR based interconnects [10]. Hence, in this analysis, the AsF_5 doping effect is incorporated by taking δ = 0.585 *nm* (stage-II doping) and E_F = 0.6 eV. As indicated in [11], for E_F = 0.2 eV and $W > 10$ *nm*, both semiconducting and metallic AC-GNRs exhibit smaller resistivity than ZZ-GNRs (predominantly metallic). However, in particular, for 20 *nm* < *W* < 100 *nm*, semiconducting AC-GNRs possess significantly large resistance than metallic AC-GNRs [131]. In the present analysis, the width (*W*) of the global interconnect (~ 1 *mm*) is considered to be 24 *nm* [118]. Based on the findings as mentioned above, AC-MLGNR is assumed to be metallic to evaluate its ultimate potential for interconnect application. For an MCB, the diameters of SWCNT and MWCNT are 1 *nm* and 8 *nm*, respectively [98]. The inter-shell spacing for an MWCNT is 0.34 *nm*, while the spacing between CNTs within an MCB is 0.34 *nm*.

Employing the temperature-dependent model, the computed value of $\lambda_{eff}{}'$ for AsF_5 ID-MLGNR, at room temperature (300 K), is 1.31μm. However, U-MLGNR exhibits $\lambda_{eff}{}'$ (300 K) of merely 419 *nm*, calculated earlier in [10], using the temperature-independent model. The difference in the values of resistance of AsF_5 ID-MLGNR and U-MLGNR, estimated using their corresponding $\lambda_{eff}{}'$ values can be seen in Table 4.1.

It can be seen noted from Table 4.1 that despite the identical bundle dimensions for MCB (1-4) (bundle width, *W*=24 *nm*, bundle height, *H*=56 *nm*), the equivalent impedance parameters i.e., $R_{ESC}(T)$,

$L_{ESC}(T)$ and $C_{ESC}(T)$ of MCB (1-4) are significantly different. It is indicated that $R_{ESC}(T)$, $L_{ESC}(T)$ and $C_{ESC}(T)$ for an MCB primarily depends on the number and structural arrangement of SWCNTs and MWCNTs within the bundle, and the total number of conducting channels associated with these CNTs [95]. For the specific bundle dimensions, an increase in the number of SWCNTs and/or MWCNTs decreases the $R_{ESC}(T)$ and $L_{ESC}(T)$. Whereas, $C_{ESC}(T)$ mainly depends on the number of SWCNTs or MWCNTs facing the ground. Further, it can be observed from Table 4.1 that among MCB (1-4), the lowest values of $R_{ESC}(T)$, $L_{ESC}(T)$ and $C_{ESC}(T)$ are obtained with MCB-1. This is due to the best structural arrangement of SWCNTs and MWCNTs within an MCB [93], [95], [99].

As depicted in Table 4.1, the resistance increases as the temperature rises for all the three different interconnects viz. ID-MLGNR, MCBs (1-4), and *Cu*. However, the resistance of ID-MLGNR interconnect, over a temperature range 300 K-500 K, is significantly smaller than that of U-MLGNR, MCBs (1-4) and *Cu* interconnects. It is noted that stage-II AsF_5 intercalation doping in MLGNR results in the increase of an average layer spacing from 0.34 *nm* to 0.585 *nm* [10]. This increase in interlayer spacing consequently reduces the interlayer scattering. Hence, a large value of $\sigma_{in-plane}$ (0.63×10^6 $(\Omega\text{-cm})^{-1}$) is obtained for AsF_5-doped stage-II MLGNR. As expressed in Equation (3.12), MFP associated with scattering due to defects, λ_D, is a direct function of $\sigma_{in-plane}$ for a given value of E_F. Therefore, for a given temperature range (300 K-500 K), a large value of λ_{eff}' (~1.31μm at T = 300 K, calculated using Equation (3.10)) alternatively provides a small value of resistance for ID-MLGNR. Note here, the approximated values of the effective MFP in *Cu* and MCB, at T = 300 K, are 40 *nm* and 1μm, respectively [16],[98].

It is investigated that there is a significant reduction in inductance for both ID-MLGNR and MCBs interconnects as the temperature rises. As mentioned earlier that '$L_{ESC}(T)$' (see Equation (4.2)) of these interconnects mainly depends on $\hat{l}_k(T)$ with negligible dependence on $\hat{l}_e$. Further, as expressed in Equation (3.16), that $\hat{l}_k(T)$ is an inverse function of $N_{CH}(T)$. It is noted that as the temperature rises from 300 K to 500 K, $N_{CH}(T)$ increases (will be discussed in Table 5.2 in chapter 5). Hence, the rise in temperature causes a reduction in $L_{ESC}(T)$ for both ID-MLGNR and MCBs interconnects. Note here, the expressions for '$L_{ESC}(T)$' and '$\hat{l}_k(T)$' for an MCB are given in Equations (3.27) and (3.29b). It can be noted from Table 4.1 that C_{ESC}(T) for ID-MLGNR (calculated using Equation 4.3) and MCB (calculated using the Equation 3.29c) negligibly varies with temperature. Since $\hat{c}_e \ll \hat{c}_q(T)$, hence $\hat{c}_q(T)$ contributes negligibly to $C_{ESC}(T)$ [31]. This implies that the values of $C_{ESC}(T)$ for both the ID-MLGNR and MCB are primarily the values of $\hat{c}_e$ (electrostatic or ground capacitance). Hence, the equivalent capacitances of both ID-MLGNR and MCBs are marginally affected by varying the temperature.

4.3 INFLUENCE OF TEMPERATURE ON CROSSTALK EFFECT

Temperature-variation significantly affects both the functional-crosstalk (F-XT) and dynamic- crosstalk (D-XT) in adjacent interconnects [31],[99]. This chapter presents the temperature-dependent performance evaluation of adjacent interconnects of AsF_5 ID-MLGNR, exhibiting a capacitive coupling, in terms of F-XT and D-XT induced noises that explores the reliability of coupled interconnects of ID-MLGNR. The influence of temperature-variation on crosstalk performance of ID-MLGNR interconnects is studied over a temperature range of 300 K-500 K. It is to be noted that till date, a few experimental works have been reported on GNR interconnects, that is either focused on multi-layer graphene with a very small number of layers (practically inappropriate for interconnect applications) [121] or on U-MLGNR (exhibits small electrical conductivity $\sim 0.00048\ (\mu\Omega.cm)^{-1}$ [122],[132]. However, the present work validates the temperature-dependent number of conducting channels and temperature-dependent resistance of ID-MLGNR based on the numerical data in [101] and experimental data in [133], respectively.

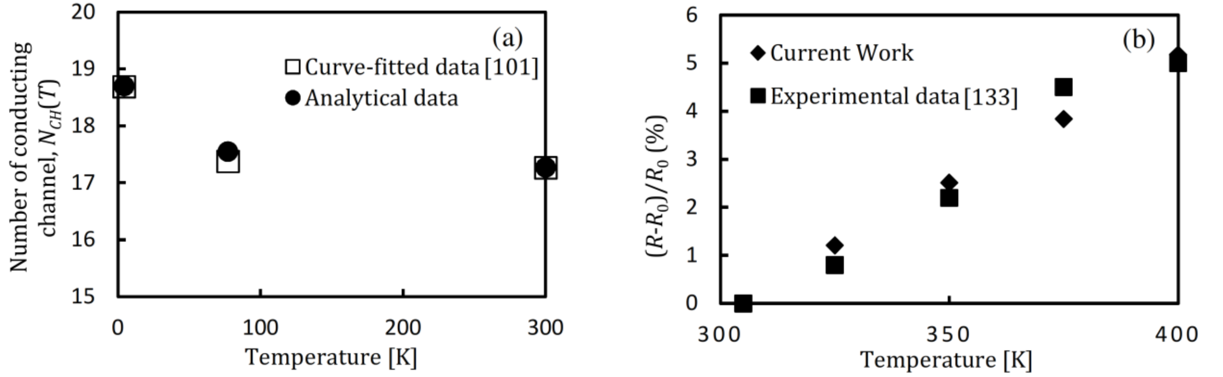

Figure 4.2 (a) Validation of the number of conducting channels (b) validation of temperature coefficient of resistance.

Figure 4.2 (a) compares the number of conducting channels $N_{CH}(T)$ of ID-MLGNR obtained analytically using Equation (3.4) with that evaluated, using the fitting parameters values available in [101], for metallic AC-GNR. It can be observed that the analytical data for $N_{CH}(T)$ shows an excellent agreement with the curve-fitted data in [101]. In Figure 4.2 (b), the temperature coefficient of resistance (TCR) of ID-MLGNR obtained using the expression $(R-R_0)/R_0$ is compared with the experimental data available for TCR in [133]. Where R is calculated using Equation (3.14), and R_0 denotes the value of R at T=300 K. On an average, the analytical results differ by 7.3% since the self-heating effect is neglected in the present analysis. Note here, the experimental data available in [133] is of ferric chloride ($FeCl_3$) ID-MLGNR. For a fair comparison, to evaluate the TCR for ID-MLGNR, the present work has considered the data of synthesized $FeCl_3$ ID-MLGNR obtained in [42], [133].

Crosstalk in coupled interconnects can affect its functionality, reliability and timings in VLSI circuits [65], [95], [134]. Hence, this section begins with a comparative analysis of F-XT noise between ID-

MLGNR, MCBs (1-4) and *Cu* with a global interconnect length of 1 *mm*. Further, this section presents the detailed analysis of D-XT delay for coupled interconnect of ID-MLGNR, MCBs (1-4) and *Cu*, with temperature-dependent circuit parameters estimated by (a) considering intercalation doping effect in MLGNR, and (b) considering inter-shell coupling and tunneling effects in MCB.

Both F-XT and the D-XT noises are analyzed using DIL setup, as shown in Figure 4.1. As stated earlier, each line is represented by its equivalent temperature-dependent circuit model of either ID-MLGNR or MCB or *Cu*.

In DIL configuration (Figure 4.1), the parameters of CMOS driver are obtained from the predictive technology model [135] at a technology node of 14 *nm*. The data required for calculation and simulation purposes is taken from Table 3.1. For CMOS-driver, the driver size is set to 100 times its minimum size. To enhance the efficiency of CMOS driver in driving the interconnect line and to diminish the width of the output noise waveforms, repeaters in DIL configuration have been optimized. It is important to note that the prime objective of this study is to explore the potential of ID-MLGNR as an interconnect for the technology node defined in the DSM region (e.g. 14 *nm*). According to the ITRS projection, the crosstalk performance of the coupled interconnects of ID-MLGNR is predicted and compared with its *Cu* and MCB counterparts.

Figures 4.3 and 4.4 depict the F-XT induced transient responses (or noise pulses) at different temperatures at the remote end of the victim line for ID-MLGNR, *Cu* and MCBs (1-4), respectively. The temperature varies in the range of 300 K-500 K with an interval of 50 K. For the present F-XT analysis, a case of functional switching (i.e., rise glitch) is considered. Under this case, the aggressor line takes a switching transition from logic 0 to logic 1, and the victim line is kept at static 0. It is observed that as the temperature rises, the peak and width of F-XT induced transient responses increase for ID-MLGNR, *Cu* and MCBs (1-4). This is owing to the combined effect of R, L and C of interconnects [31].

Further, it can be observed from Figures 4.3 and 4.4, that the peaks of F-XT noise pulse in ID-MLGNR are lower than that in *Cu* and MCB-1, but higher than that in MCB 2-4. It is justified based on $R_{ESC}(T)$ and $C_{ESC}(T)$ associated with these interconnects. It is indicated that peak of F-XT noise pulse at the far end of the victim line, increases with the increase in $R_{ESC}(T)$ and decreases with the increase in $C_{ESC}(T)$ [82]. Since the $C_{ESC}(T)$ of ID-MLGNR, *Cu* and MCB-1 is comparable as shown in Table 4.1, the peaks in these interconnects are primarily affected by $R_{ESC}(T)$. Among ID-MLGNR, *Cu* and MCB-1, the least resistance is obtained with ID-MLGNR. Hence, the peaks of F-XT noise in ID-MLGNR are low. However, if $R_{ESC}(T)$ and $C_{ESC}(T)$ of ID-MLGNR is compared with that of MCB 2-4, than the relative difference in $C_{ESC}(T)$ of these interconnects is observed to dominate over that in $R_{ESC}(T)$. As mentioned earlier, the higher values of $C_{ESC}(T)$ in MCB 2-4 than in ID-MLGNR, causes the peaks of F-XT noise in MCB 2-4 to fall below that in ID-MLGNR. Further, it is noted that the width of F-XT noise at the far end of the victim line varies inversely to its peak [99]. Hence, the opposite findings are obtained in case of the width of F-XT noise in ID-MLGNR, MCB 1-4 and *Cu*. However, these findings

are in contradiction in the case of *Cu* only. This is due to its highest values of $R_{ESC}(T)$ and the coupling capacitance.

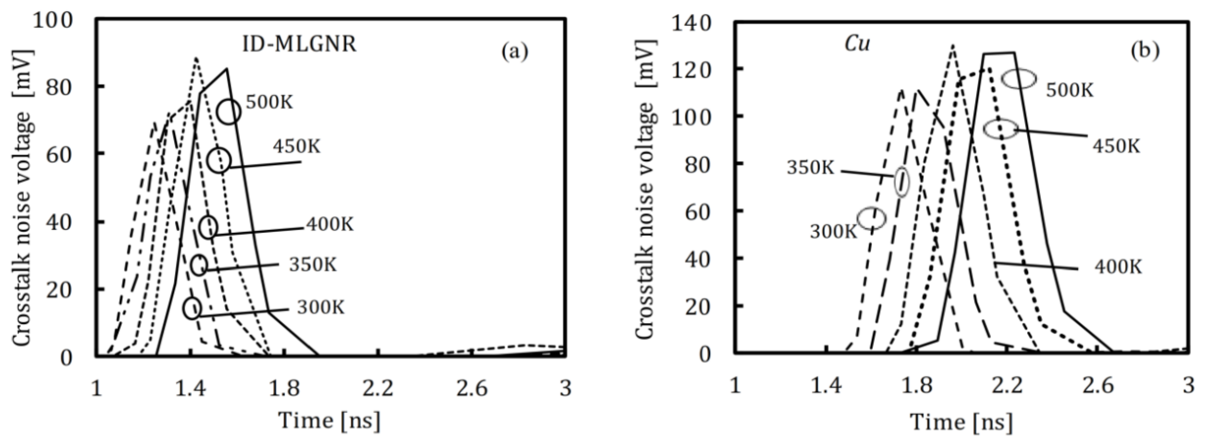

Figure 4.3 F-XT induced transient response at different temperatures, for (a) ID-MLGNR and (b) *Cu* interconnects.

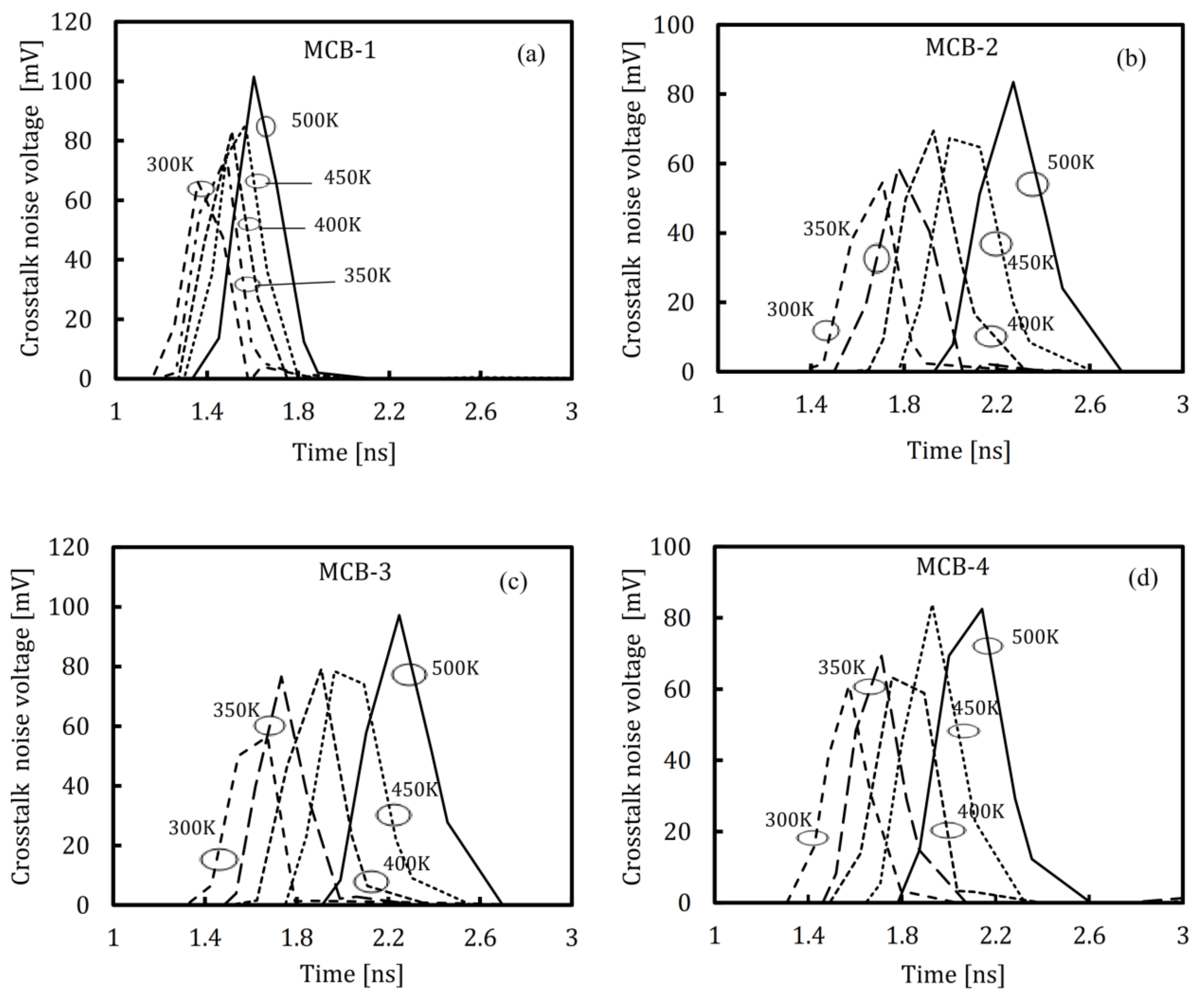

Figure 4.4 F-XT induced transient response at different temperatures, for (a) MCB-1 (b) MCB-2 (c) MCB-3 (d) MCB-4.

The peak and width of the F-XT noise in the coupled interconnects of ID-MLGNR, MCB 1-4 and *Cu* are shown in Figures 4.5 and 4.6, respectively. These results are extracted from Figures 4.3 and 4.4.

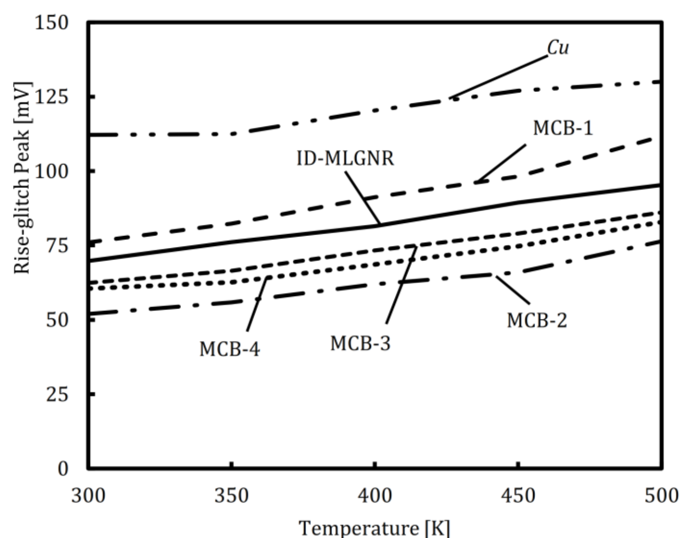

Figure 4.5 Peaks of F-XT induced rise glitch at different temperatures.

Figure 4.5 shows the +ve peaks of F-XT induced rise glitch, at different temperatures, in capacitively coupled interconnects of ID-MLGNR, MCBs and *Cu*. It is noted that the results obtained in case of MCBs (under the case of rise glitch) in the present analysis are in good agreement with the trend followed by MCBs (under the case of fall glitch) in [98] (see "Figure 12 in Ref. 98"), i.e., MCB-1 exhibits the highest crosstalk-induced peak among MCBs (2-4). However, for ID-MLGNR, +ve peak over an entire temperature range (300 K-500 K) is smaller than that of *Cu* and MCB-1, but higher than MCBs (2-4). It is because crosstalk-induced noise is mainly affected by coupling capacitance between adjacent interconnect lines [111], and the coupling capacitance in the ID-MLGNR interconnect is about 26.52% lesser as compared to those in *Cu* and MCB counterparts (see Table 4.1). However, higher +ve noise-peaks in ID-MLGNR, compared to MCBs (2-4), are justified by the impact of ground capacitance. It has been reported that peaks of F-XT induced noise pulses at the remote-end of the victim line in capacitively-coupled interconnects increase with a decrease in ground capacitance [65],[98].

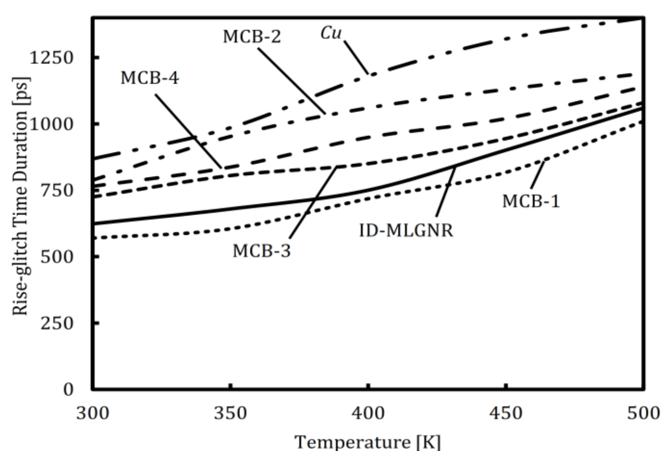

Figure 4.6 Width of F-XT induced rise glitch at different temperatures.

Figure 4.6 shows the width (or time-duration) of F-XT induced rise glitch at different temperatures for ID-MLGNR, MCBs (1-4) and *Cu* based global interconnects. It is observed that the width of the rise-glitch increases as the temperature rises from 300 K to 500 K for all the three types of interconnects. It is noted that a gradual increase in the width of noise pulse is due to the resistance of interconnect that dominates over its inductance and the capacitance as the temperature rises [98]. Due to the minimum line resistance, exhibited by ID-MLGNR at any specific temperature range 300 K-500 K (see Table 4.1), it has small width of rise-glitch as compared to that of *Cu* and MCBs (2-4) interconnects. In comparison to MCBs (2-4), MCB-1 has the smallest width of rise-glitch in opposition to its highest rise-glitch peak

Table 4.2 Peak and width of the F-XT induced overshoot, undershoot, and fall glitch in ID-MLGNR, MCB (1-4) and *Cu*, at interconnect length of 1000 *μm,* for the temperature variation range 300 K - 500 K.

Crosstalk Effect	T(K)	ID-MLGNR	MCBs STRUCTURES				*Cu*
			1	2	3	4	
Overshoot Peak (mV)	300	864	861	849	850	855	905
	350	867	867	854	871	863	906
	400	879	875	864	873	859	912
	450	884	877	874	875	878	921
	500	895	879	879	879	876	923
Overshoot Width (ps)	300	518	741	1030	1200	1030	1270
	350	571	820	1390	1600	1270	1390
	400	672	920	2540	1810	1320	1490
	450	869	935	2910	1850	2310	1710
	500	930	1060	3150	2500	2770	1910
Magnitude of -ve Under Shoot Peak (mV)	300	59	57	75	91	85	95
	350	63	61	76	90	87	97
	400	69	72	75	89	88	111
	450	75	74	75	89	87	113
	500	77	86	78	92	85	121
Undershoot Width (ps)	300	633	956	1450	1230	1250	1250
	350	693	989	1570	1490	1330	1390
	400	710	1020	1700	1530	1500	1480
	450	780	1110	1810	2200	2400	1540
	500	867	1470	2190	2340	2860	1750
Fall-Glitch Peak (mV)	300	739	742	721	706	715	702
	350	736	737	720	704	710	699
	400	729	725	720	703	707	685
	450	723	723	719	702	706	683
	500	720	711	718	701	706	675
Fall-Glitch Width (ps)	300	669	973	1400	1250	1480	1080
	350	738	980	1490	1490	1370	1170
	400	879	1060	1790	1600	1540	1350
	450	970	1310	1950	2320	1720	1470
	500	1130	1530	2460	2500	2000	1530

Table 4.2 shows the numerical values of the peaks and width of F-XT induced overshoot, undershoot and fall glitch at victim's output for ID-MLGNR, MCBs (1-4) and *Cu*. In case of overshoot and undershoot, the aggressor line is switched from logic 0 → logic 1 and logic 1→ logic 0, and the corresponding victim line is held at logic 1 and logic 0, respectively [65]. In case of fall glitch, the aggressor line is switched from logic 1→ logic 0 and the victim line is held at logic 0. Likewise, in the case of rise glitch, the crosstalk-induced overshoot peak of the ID-MLGNR, MCBs (1-4) and *Cu* follows the usual trend of increasing as the temperature rises. Again, the highest peak is observed in *Cu* as compared to ID-MLGNR and MCBs (1-4). On the other hand, both crosstalk-induced fall glitch and undershoot peaks for the three different interconnects fall as the temperature rises from 300 K to 500 K. Here ID-MLGNR interconnects exhibit lower fall glitch and undershoot peak than MCB-1 but higher than that of MCBs (2-4).

The width of crosstalk–induced noise in case of overshoot, fall glitch and undershoot for ID-MLGNR, MCBs (1-4) and *Cu* interconnect follows the usual trend of increasing with the rise in temperature. Encouragingly, ID-MLGNR interconnects exhibit the lowest width of temperature-dependent noise pulse for the cases of overshoot, undershoot, and fall glitch among the three different interconnects.

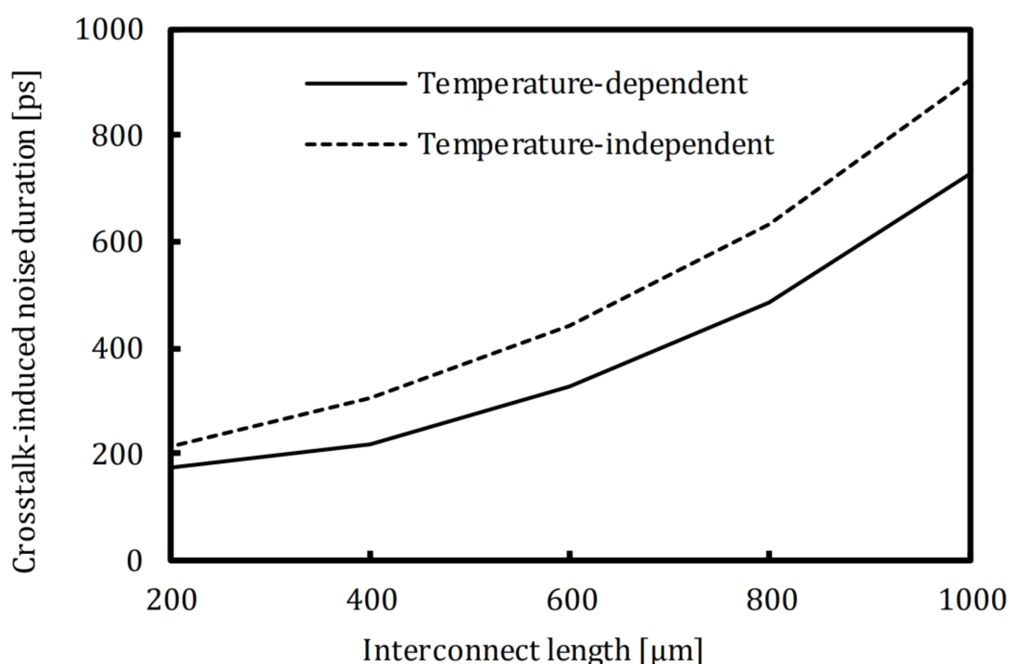

Figure 4.7 The width of the F-XT induced overshoot in ID-MLGNR, as a function of interconnects length, using TD models (MFP=1.31 μm) and TI models (MFP=1.06 μm).

Figure 4.7 shows the variation of the width of F-XT induced overshoot (at the victim's output) in ID-MLGNR at different interconnect lengths, considering temperature-dependent (TD) and temperature-independent (TI) models. For this analysis, the aggressor line is switched from logic 0→1 and the corresponding victim line is held at logic 1. It can be observed that at different interconnect lengths (200 μm-1000 μm), the width of the F-XT induced noise pulse increases with an increase in interconnect length. Here the gradual increase in the width (in case of both TD and TI models) of crosstalk-induced

noise waveforms indicates the dominance of interconnect resistance over its inductance and capacitance with the increase in interconnect length. Moreover, it is noted that the width of the noise pulse obtained using TD models is always less as compared to that obtained using TI models for the entire length of interconnect.

An average relative reduction of about 30.96 % is obtained by accurately estimating the width of crosstalk-induced noise for ID-MLGNR using the TD models w.r.t. TI models, as expressed in Table 4.3. The remarkable reduction in the width of TD crosstalk-induced noise for ID-MLGNR interconnect is attributed to the lower impedance parameters and coupling capacitance associated with it in comparison to that of MCBs and *Cu* interconnects.

Table 4.3 Average relative reduction of crosstalk-induced noise in ID-MLGNR using proposed TD model relative to conventional TI model

Sr No.	Length of interconnect (μm)	% Improved reduction in the crosstalk-noise width
1	200	22.74
2	400	42.17
3	600	34.78
4	800	30.80
5	1000	24.32
Average reduction		30.96

The impact of even mode (EM) and odd mode (OM) switching on D-XT induced delay at the remote end of the aggressor line is shown in Figures 4.8 (a) and (b), respectively. The performance of interconnects is analyzed at the global length of 1000 μm. In the present analysis, two possible cases of simultaneous switching of aggressor and victim lines under EM and OM are considered [65].

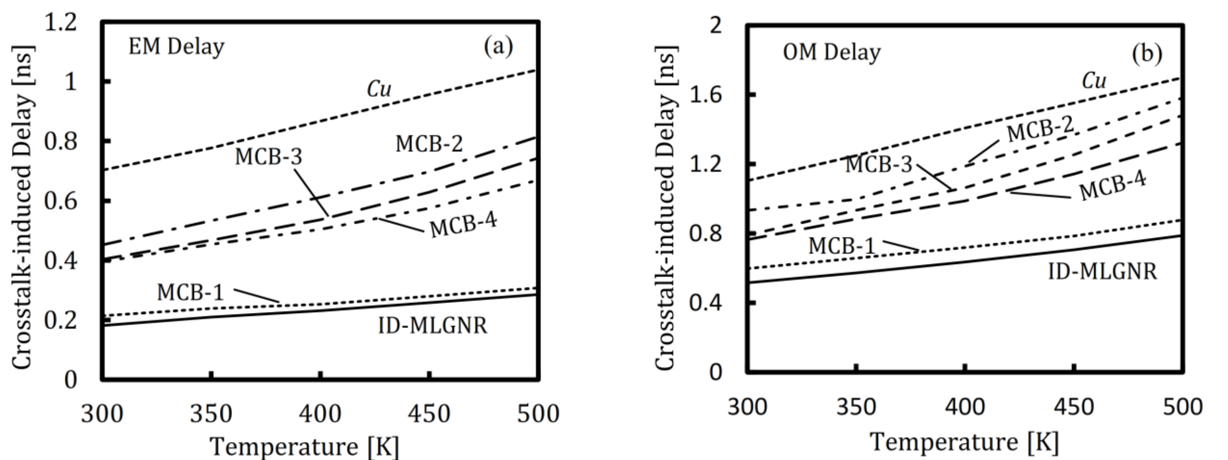

Figure 4.8 D-XT induced signal delay in ID-MLGNR, MCBs (1-4), and *Cu* interconnects at different temperatures, at (a) even mode (EM) and (b) odd mode (OM) of aggressor-victim switching at ℓ =1000 μm.

Where EM of switching implies that both the aggressor and the victim lines take similar transition logic either 1→0 or 0→1. In other words, both the aggressor and the victim lines are switched in-phase. Whereas, OM of switching implies that both the aggressor and the victim lines take an opposite transition logic i.e. if transition logic on the aggressor is 1→0, then transition logic on the victim is 0→1 and vice versa. It is seen that D-XT induced delay is the lowest with ID-MLGNR interconnects in both the EM and OM cases than with MCBs (1-4). This significant reduction in crosstalk-induced delay of ID-MLGNR comes due to the lowest resistance associated with it over a temperature range of 300 K-500 K. Additionally, among all MCBs (1-4), MCB-1 has the best performance in terms of EM and OM crosstalk-delay. The main reason behind this improvement is the lowest value of temperature-dependent impedance parameters associated with MCB-1 (See Table 4.1).

It is noted from Table 4.4 that the overall EM-delay of ID-MLGNR is 63.79 % less in comparison to its OM-delay. This is because, in capacitively coupled interconnects, the time-of-flight required by the voltage step to arrive at the remote end of the aggressor line is less for EM than for OM. Hence, the EM voltage-step arrives earlier at the remote end of the interconnect than the OM voltage-step [65]. Additionally, over a temperature range of 300 K-500 K, ID-MLGNR is observed to have an average relative EM-delay reduction of 10.21% and 73.21% compared to MCBs (MCB-1) and *Cu* interconnects, respectively. On the other hand, a significant average OM-delay reduction of 11.8% and 54.09% is also obtained in ID-MLGNR as compared to that for MCB-1 and *Cu*, respectively.

Table 4.4 Average percentage of reduction in D-XT induced EM-delay (EMD) relative to OM-delay (OMD) for ID-MLGNR based interconnects, for a temperature range of 300 K-500 K and rising pulse on aggressor line (0→1), at interconnect length ℓ =1000 μm

T(K)	EMD relative to OMD of ID-MLGNR	EM-Delay(ns)		OM-Delay(ns)	
		MCB-1	*Cu*	MCB-1	*Cu*
300	64.82	15.33	74.18	13.70	53.30
350	63.37	12.17	73.03	13.15	54.20
400	63.55	8.55	73.29	11.66	54.85
450	63.45	7.81	73.02	10.26	54.53
500	63.77	7.19	72.52	10.20	53.58
Av. % reduction	63.79	10.21	73.21	11.80	54.09

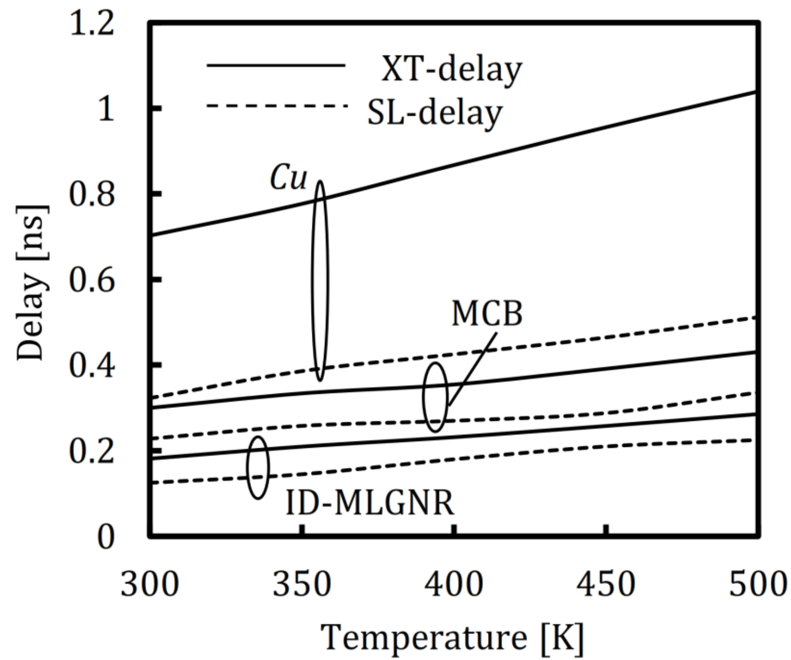

Figure 4.9 Single-line (SL) and crosstalk-induced (XT) delay of ID-MLGNR, MCB-1, and *Cu* interconnect, at different temperatures of interconnects. Even mode of aggressor-victim switching is considered for D-XT delay analysis at global length (ℓ =1000μm) of interconnects.

Figure 4.9 shows single-line (SL) and crosstalk-induced (XT) delays of ID-MLGNR, MCB-1 and *Cu* based long interconnects at different temperatures. XT-delay of these interconnects is observed to be high compared to SL-delay, which reflects the effect of coupling on interconnects. Moreover, regarding SL and XT-delays, ID-MLGNR interconnects are demonstrated to outperform the best delay structure of MCBs, i.e., MCB-1 (see Figure 4.8) and *Cu* based counterparts consistently over a temperature range 300K-500K.

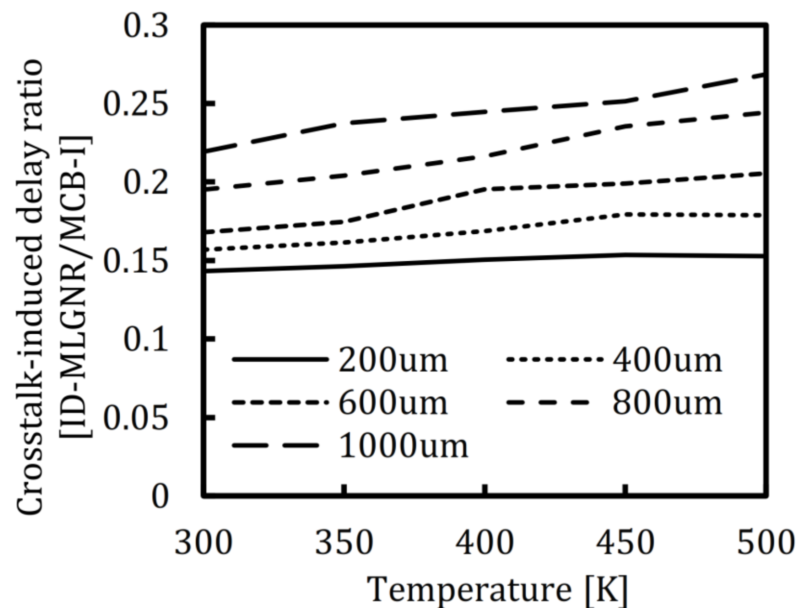

Figure 4.10 Crosstalk-induced delay-ratio of ID-MLGNR to MCB-1 at different temperatures and lengths of interconnects. EM switching case: Rise on aggressor (0→1).

Figure 4.10 shows the crosstalk-induced delay ratio of ID-MLGNR to MCB-1 interconnects for varying temperatures and lengths of coupled interconnects under EM switching conditions. The crosstalk-induced delay ratio of ID-MLGNR to MCB-1 is found to be less than unity. This is due to the lower crosstalk-induced delay possessed by ID-MLGNR than MCB-1 interconnects, as demonstrated in Figure 4.10. It is also noted that the delay ratio increases with the rise in temperature as well as with the increase in interconnect length. This is because the delay of interconnects is primarily influenced by their TD resistance [31],[98].

Besides temperature variation, variation in process parameters depending upon the techniques used to synthesize and pattern the GNRs can also affect the crosstalk performance of ID-MLGNR. It is reported that Van der Waals force between the layers (δ) of MLGNR can vary up to ±10%, and consequently, the number of layers (n) in ID-MLGNR [44]. In addition, the Fermi energy of dopant atoms can vary the Fermi level (E_F) of MLGNR by ±10%, and thereby its number of conducting channels (N_{CH}). It is also indicated that $\lambda_{eff}'(T)$ in MLGNR (see Equation 3.10) incorporating the MFP associated with scatterings due to optical phonons, acoustic phonons, defects and edge roughness can vary up to ±17% [86]. Considering these process parameters (i.e. δ, E_F, and $\lambda_{eff}'(T)$), the % variation in EM and OM crosstalk-induced delay in coupled interconnects of $1mm$ long ID-MLGNR is shown in Figures 4.11 (a) and (b), respectively.

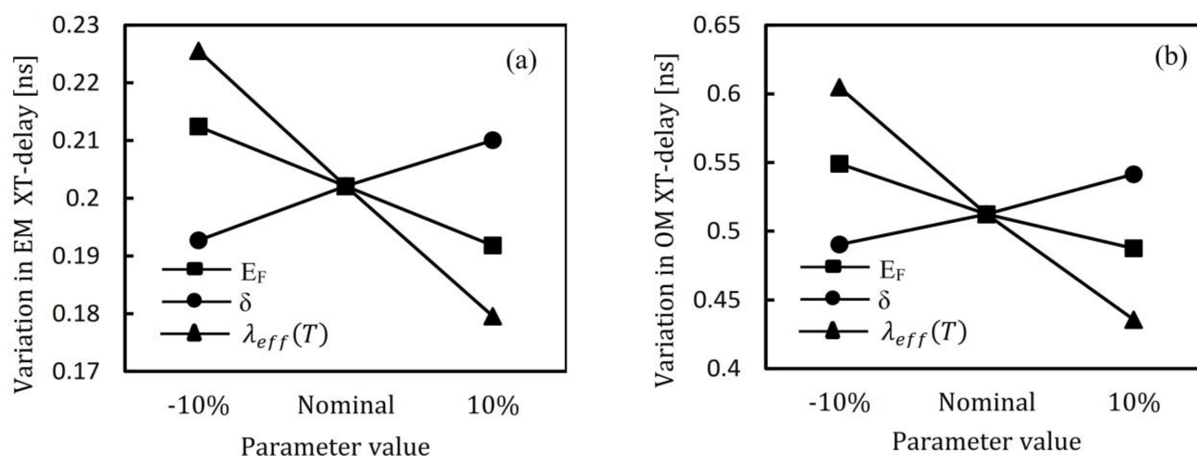

Figure 4.11 The variation in XT-delay for (a) EM (b) OM as a function of the process parameter.

It can be observed from Figures 4.11 (a) and (b) that increasing the E_F and $\lambda_{eff}'(T)$ cause to reduce the EM and OM D-XT delay. This is because D-XT delay in global level interconnects is mainly dominated by $R_{ESC}(T)$ [86]. The increase in both E_F (consequently, in N_{CH}) and $\lambda_{eff}'(T)$ reduces the $R_{ESC}(T)$, and therefore, D-XT delay decreases. On the other hand, an increase in δ, reduces the D-XT delay due to a reduced value of n. The average variation in EM D-XT delays due to the variation in E_F, δ and $\lambda_{eff}'(T)$ is found to be 21 ps, 17 ps, and 46 ps, respectively. In the case of the OM D-XT delay, these variations are found to be 62 ps, 51 ps, and 169 ps. These findings reveal that, in addition to the

temperature, MFP is a crucial process parameter whose variation can severely deteriorate the crosstalk performance of ID-MLGNR.

4.4 CONCLUSION

The temperature-dependent ESC model is employed in the DIL configuration of capacitively coupled ID-MLGNR interconnects to perform the crosstalk analysis at the global interconnect length (~1000µm). The comparisons are performed with MCB and *Cu*-based interconnects. It is found that in terms of crosstalk-induced noise peaks, over a temperature range 300K-500K, ID-MLGNR outperforms both the MCB-1 and *Cu.* This is because the value of coupling capacitance associated with ID-MLGNR is small as compared to with MCBs and *Cu*. However, crosstalk-induced noise pulses are less wide in MCB-1 than in ID-MLGNR and *Cu*. This is due to the effect of ground capacitance associated with these interconnects. Moreover, ID-MLGNR with nearly specular edges, at the global interconnect dimension, exhibits a lower crosstalk-induced delay as compared to its MCBs-1 and *Cu* counterparts owing to larger MFP and lower values of impedance parameters. It is also observed that ID-MLGNR possess a significant reduction in odd mode crosstalk-induced delay of 54.09% and 11.8%, in comparison to *Cu* and MCBs (MCB-1) interconnects, respectively. Further, it is found that a ±17% variation in MFP causes a significant average variation in the odd mode crosstalk delay of ID-MLGNR. This implies the viable application of ID-MLGNR as global interconnects for the DSM technology node.

CHAPTER 5

EFFECT OF ARMCHAIR AND ZIGZAG EDGES ON FUNCTIONAL AND DYNAMIC CROSSTALK NOISE IN COUPLED INTERCONNECTS OF ID-MLGNR

5.1 INTRODUCTION

It is indicated that the number of conducting channels (N_{ch}) in MLGNR along with its dependence on the temperature (T), width (W), and Fermi-energy (E_F) are also the function of the discrete energy levels (E_m) in both ZZ and metallic AC-GNRs [31]. The 'N_{ch}' is obtained by considering the contributions of all the conduction sub-bands 'n_c' and valence subbands 'n_v', in GNR [11], [40], [68], [101]. However, only those sub-bands whose $E_m \leq E_F$ are populated and contribute to conduction, rest do not. According to the modified tight-binding model, all the subbands in both ZZ and metallic AC-GNRs are not degenerative. Hence, a non-zero bandgap does exist in them. Theoritically, the ZZ-GNRs are predominantly metallic. However, in reality, a bandgap is induced in it because of the staggered sublattice potential from magnetic ordering once electron spin is considered. The bandgap of ZZ-GNR increases with decreasing wire width 'W' (nm) [11].

Considering these facts about the AC and ZZ-GNRs, a few researchers previously, have investigated undoped MLGNRs for single-line propagation-delay, frequency response and bandwidth performance [56], [44]. Single line delay of doped TC-MLGNR is evaluated and compared with that of doped SC-MLGNR considering both AC and ZZ edges of GNRs [14]. It is noted that doped TC-MLGNR with optimized thickness in the case of ZZ-edge has the best delay performance as a function of interconnect length. Further, knowing the fact that crosstalk between coupled interconnects influences their functionality and reliability [136], Ziang-Peng Cui *et al.* examined the crosstalk-induced delay in undoped TC-MLGNR [68]. W. S. Zhao *et al.* investigated the crosstalk effects in undoped SC-MLGNR with AC-edges [40]. V. R. Kumar *et al.* analyzed the crosstalk delay performance of doped MLGNR and compared it with that of MWCNT [74]. The same authors in another work analyzed the power, delay and bandwidth performance of SC-MLGNR (undoped and doped), taking into account both smooth and diffusive edges [49]. In [39], it is reported that the crosstalk-induced delay in coupled SC-MLGNR interconnects is small as compared to coupled TC-MLGNR interconnects.

Though the work done in [14], [39],[40],[44],[49],[56],[68],[74],[136] took into account the impact of GNR's edge shape while evaluating the interconnect performance of MLGNR, two important aspects were neglected. First, the performance of a single doped MLGNR interconnect was evaluated without considering the coupling effect between the interconnects. Second, the coupled interconnects of only U-MLGNR were considered. For the accurate evaluation of the crosstalk performance in coupled MLGNR interconnects, the following three essential facts must be taken into account. First, the known experiments have verified that TC-MLGNRs can be fabricated easily than SC-MLGNRs [39]. Second, the detailed analyses of interconnects beyond 45 *nm* technology node reveal that the temperature of the

metals increases due to the cumulative effect of increased resistivity, current density and the number of global metal-layers [31], [98], [138]. Hence, for designing next-generation interconnects, the thermal issue is a predetermined design criterion. Third, for interconnect width beyond 10 nm, metallic AC-GNRs possess more significant conductivity as compared to those of ZZ-GNRs [11]. This chapter presents the temperature-dependent functional and dynamic crosstalk analyses in TC-MLGNRs (undoped, AsF_5-doped and $FeCl_3$-doped) considering both AC and ZZ edged GNRs, and compared it with that of MCB.

5.2 MODEL FOR DISCRETE ENERGY LEVEL IN AC- AND ZZ-GNR

The number of conducting channels '$N_{ch}(T)$' is expressed in Equation (3.4). It is rewritten as

$$N_{ch}(T) = \sum_{m=0}^{n_c}\left[1 + \mathrm{e}^{\frac{E_m - E_F}{k_B T}}\right]^{-1} + \sum_{m=0}^{n_v}\left[1 + \mathrm{e}^{\frac{E_m + E_F}{k_B T}}\right]^{-1} \quad (5.1),$$

The discrete energy levels in both ZZ and metallic-AC GNRs are expressed in Equations (5.2) and (5.3), respectively. Where E_m denotes the highest energy of the mth valance subband. It also represents the lowest energy of the mth conduction subband. In Equations (5.2) and (5.3), h is the Planck's constant and $v_F = 8 \times 10^5$ m/s is the Fermi velocity, W denotes the width of the interconnect. a_0 is the carbon-carbon atom distance, $c = 0.12$ and $t = 2.7$ eV. Note here that all subbands whose $E_m \leq E_F$ are populated and provide one conduction channel [11].

$$E_0 = \frac{0.933}{2(W+1.5)}, \ m=0; \ E_m = \frac{hv_F}{2W}|m + 1/2|, \ m \neq 0 \qquad \text{ZZ-GNR} \quad (5.2),$$

$$E_0 = \frac{3\sqrt{3}a_0 ct/2}{W+\sqrt{3}a_0}, \ m=0; \ E_m = \frac{hv_F}{2W}|m|, \ m \neq 0 \qquad \text{AC-GNR} \quad (5.3)$$

5.3 ANALYSIS OF TEMPERATURE DEPENDENT CIRCUIT MODELS

In this section, the temperature-dependent circuit models of MLGNR (undoped, $FeCl_3$-doped, and AsF_5-doped) interconnects considering both the metallic-AC and ZZ GNRs are analyzed at the temperature range 300 K-500 K. The geometry of different types of MLGNR interconnect i.e., undoped, stage-I $FeCl_3$-doped and stage-II AsF_5-doped is shown in Figure 5.1. Where W and H denote the width and thickness of MLGNR interconnect, and Y denotes the dielectric thickness with effective dielectric constant represented by ε_r. The total number of layers (n) in three different types of MLGNR is obtained as n= 1+int [H/S_x], where x=1, 2, 3 [39]. The term S_1=0.335 nm and S_2= 0.815 nm denote the spacing between two adjacent graphene layers [10]. S_3 is the average interlayer distance between GNR layers for stage-II AsF_5 ID-MLGNR and is defined as $S_3 = (S_1 + S_2)/2$. The temperature-dependent ESC model of MLGNR interconnects is presented in Figure 5.1(d), and as described earlier in chapter 3.

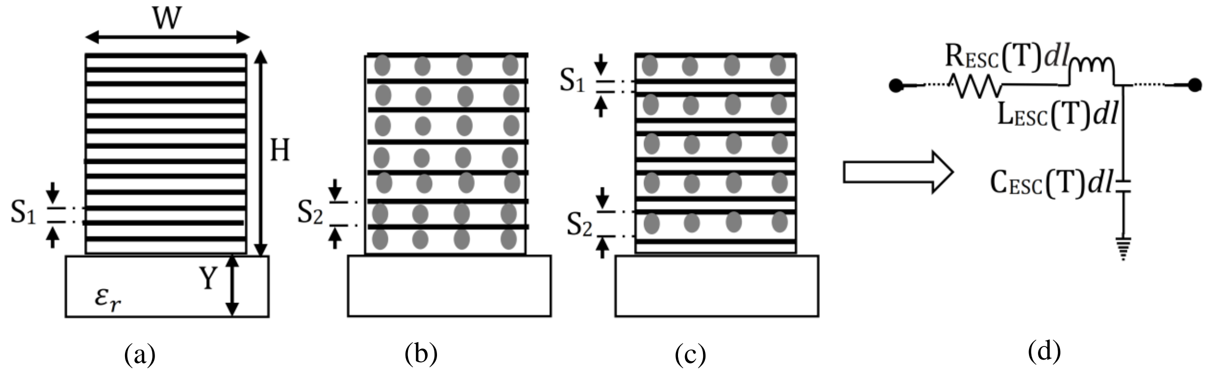

Figure 5.1 Schematic view (a) undoped, (b) stage-I $FeCl_3$-doped [42], and (c) stage-II AsF_5-doped MLGNR [10]. The solid lines and dots indicate graphene and intercalation dopant layers, respectively. (d) Thermally-aware ESC model of MLGNR interconnects, where *dl* is the differential element along the interconnect length ℓ.

The dimensional and physical parameters are taken from the latest (ITRS-2013) [118], and are given in Table 3.1. The present analysis is executed for $1mm$ long interconnect. As indicated in [11], for $W > 10\ nm$ and $E_F = 0.2$ eV, metallic AC-GNR exhibits larger conductivity than ZZ-GNR. Therefore, in the present analysis, the effects of both the intercalation doping and chirality (AC and ZZ) are considered to evaluate the MLGNR's ultimate potential for interconnect design.

Table 5.1 Discrete energy of sub-bands

Sub-bands index (m)	0	1	2	3	4	5	6	7	8	9	10
E_m (AC-GNR)	0.05	0.07	0.14	0.20	0.28	0.34	0.41	0.48	0.55	0.62	0.69
E_m (ZZ-GNR)	0.03	0.10	0.17	0.24	0.31	0.38	0.45	0.52	0.59	0.65	0.72

Table 5.1 lists the discrete energy of sub-bands for both the ZZ and AC-GNRs, calculated using Equations (5.2) and (5.3), respectively. It is seen that bandgap, $2E_0$, in ZZ-GNR is less than that in AC-GNR. However, for a given index of sub-bands, the discrete energy of AC-GNR is less than that of ZZ-GNR except for sub-band index '0'. As stated earlier, all sub-bands whose $E_m \leq E_F$ are populated and contribute to conduction. This implies that for a given E_F, a greater number of sub-bands in AC-GNR will contribute to conduction than that of ZZ-GNR [11]. This useful feature of AC-GNR is also illustrated in terms of the number of conducting channels (N_{ch}) calculated using Equation (5.1) and is tabulated in Table 5.2. The optimum values of E_F for undoped, AsF_5-doped and $FeCl_3$-doped are 0.2 eV, 0.6 eV and 0.68 eV, respectively [10], [11], [42]. It is noted from Table 5.2 that the N_{ch} increases with the rise in temperature as well as with an increase in E_F.

Table 5.2 Conducting channels as a function of temperature

	$N_{ch}(T)$ of Metallic AC-GNR			$N_{ch}(T)$ of ZZ-GNR		
T(K)	undoped	AsF_5-doped	$FeCl_3$-doped	undoped	AsF_5-doped	$FeCl_3$-doped
300	5.40	17.41	19.20	3.36	15.40	17.15
350	5.40	17.52	19.29	3.44	15.52	17.19
400	5.42	17.64	19.38	3.51	15.63	17.24
450	5.45	17.75	19.49	3.58	15.74	17.30
500	5.49	17.87	19.60	3.65	15.85	17.37

Figure 5.2 illustrates the behavior of MFP with interconnect temperature for doped and undoped MLGNR interconnects. The effects of scattering associated with acoustic phonons, optical phonons, and rough edges of MLGNR interconnects worsens with the rise in interconnect temperature. This consequently results in the reduction of MFP as the interconnect temperature rises from 300 K-500 K.

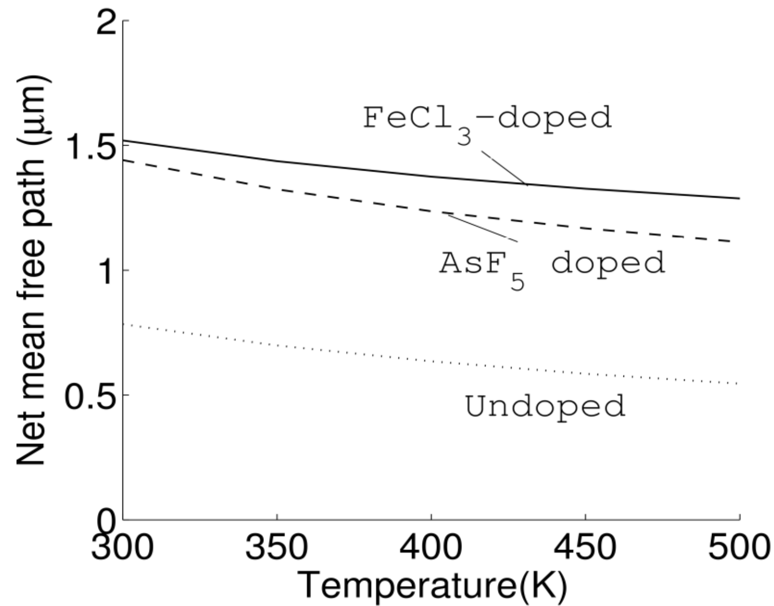

Figure 5.2 Net MFP as a function of interconnect temperature for undoped, AsF_5-doped and $FeCl_3$-doped MLGNR interconnects.

However, intercalation doping can increase the MFP of undoped MLGNR [10]. Experimental measurements also confirmed the rise in MFP of doped MLGNR [42]. It is noted from Section 4.2 that low-bias resistance of MLGNR interconnects is primarily affected by both temperature-dependent number of conducting channels ($N_{ch}(T)$) and temperature-dependent MFP ($\lambda_{eff}{}'(T)$) of charge carriers, whereas inductance and capacitance are the sole functions of the temperature-dependent number of conducting channels.

Figure 5.3 shows the resistance of three different types of MLGNR interconnects as a function of temperature, obtained using Equations (3.1) - (3.14). The increase in the values of resistance of these interconnects with temperature is the reflection of their dominating MFP (see Figure 5.2).

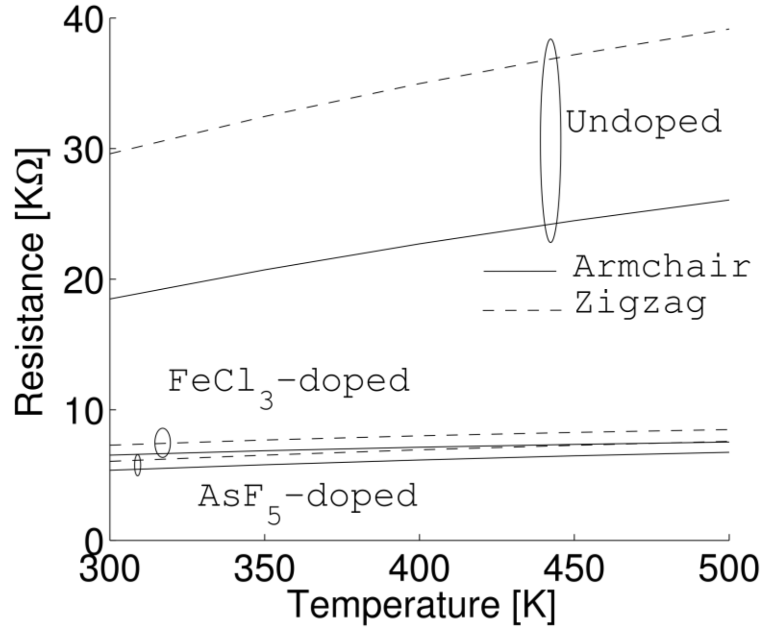

Figure 5.3 The equivalent resistance of MLGNR interconnects as a function of temperature at interconnect length of 1*mm* and technology node 14 *nm*.

The impact of chirality on the resistance of MLGNR interconnects can also be seen. Both the $FeCl_3$-doped and AsF_5-doped MLGNRs are observed to have lower values of resistance compared to undoped MLGNR. It is due to the fact that intercalation-doping mainly impacts the MFP (λ_D) and E_F (see Equations (3.12) and (3.13)) in MLGNR [10] as shown in Figure 5.2. It is indicated that with intercalation doping, the in-plane conductivity of undoped MLGNR increases from 0.026 $(\mu\Omega\text{-cm})^{-1}$ to 0.142 $(\mu\Omega\text{-cm})^{-1}$ for $FeCl_3$-doped and to 0.63 $(\mu\Omega\text{-cm})^{-1}$ for AsF_5-doped, respectively [10], [42]. Note here that despite higher $N_{ch}(T)$ (see Table 5.2) and large MFP (see Figure 5.2) in $FeCl_3$-doped MLGNR as compared to AsF_5- doped MLGNR, at any temperature range from 300 K-500 K, smaller values of resistance are obtained in case of AsF_5-doped MLGNR. It is due to the reason that number of conducting layers (n) that contribute to the overall conductance of MLGNR is large with stage-II AsF_5-doping as compared to that of stage-I $FeCl_3$-doping.

The temperature-dependent inductance of MLGNR is calculated using Equations (3.16) and (3.19). As can be observed from Figure 5.4 that the inductance of MLGNR based interconnects decreases with the rise in temperature. It is because the equivalent inductance of these interconnects is contributed mainly by temperature-dependent kinetic inductance as compared to temperature-independent magnetic inductance.

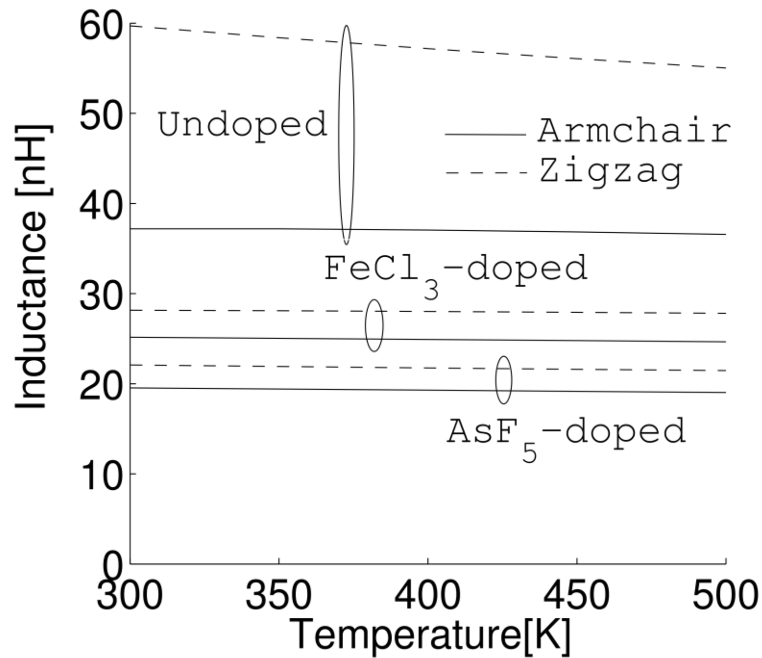

Figure 5.4 The equivalent inductance of MLGNR interconnects as a function of temperature at interconnect length of 1*mm* and technology node 14 *nm*.

Apart from this, as depicted in Figure 5.5, capacitance increases with the rise in temperature. The variations in temperature negligibly affect the equivalent capacitance of MLGNR (see Equations (3.17) and (3.18)). The reason is because that the electrostatic-capacitance (temperature-independent) dominates over quantum-capacitance (temperature-dependent) in equivalent circuit capacitance [31].

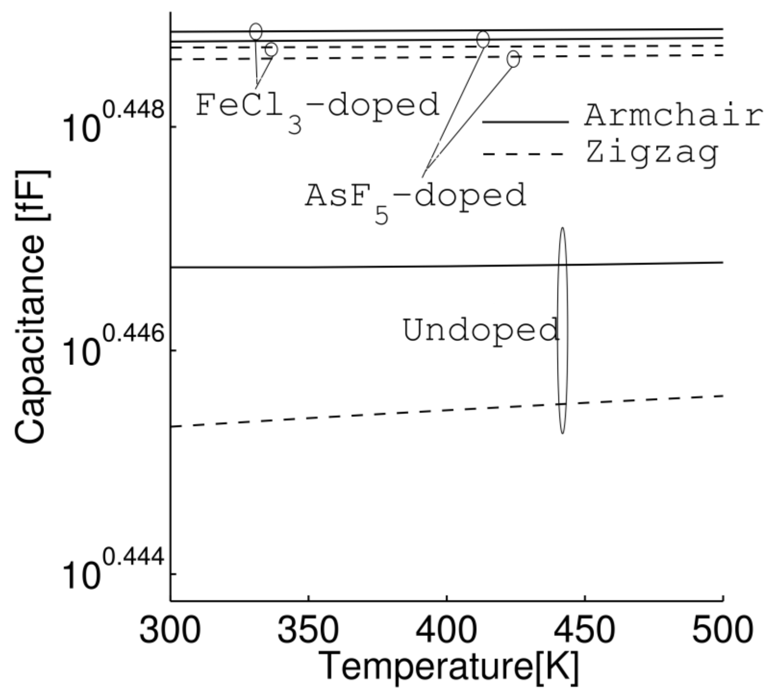

Figure 5.5 The equivalent capacitance of MLGNR interconnects as a function of temperature at interconnect length of 1*mm* and technology node 14 *nm*.

5.4 TEMPERATURE DEPENDENT CROSSTALK ANALYSIS

It is investigated that both the crosstalk-induced noise and delay in coupled interconnects have severely degraded the performance of interconnects [40], [134], [139]. As the interconnect temperature goes beyond room temperature, the crosstalk worsens [31]. Hence, while taking into account the temperature variation from 300 K to 500 K, this section analyses the impact of intercalation doping and chirality on both the functional and dynamic crosstalk in capacitively coupled interconnects of MLGNR. To evaluate the ultimate performance of TC-MLGNR, 1*mm* long global interconnect is considered [14].

Both the functional and dynamic crosstalk are analyzed using the DIL setup, shown in Figure 4.1 of chapter 4. The temperature-dependent ESC model of MLGNR represents both the aggressor and victim lines. The parameter C_L is the input capacitance of the terminal gate with its value equal to 0.065fF [68]. A CMOS driver at the 14-*nm* technology node drives each interconnects line with V_{DD} and clock frequency of 0.8 V and 0.1 GHz, respectively. In CMOS-driver, the PMOS to NMOS width ratio (w_p/w_n) is taken as 2:1 and the size of the NMOS transistor is set to be 100× the minimum size of the transistor. The driver transistors in Nano regime are modeled by high performance Predictive Technology model (PTM) [47]. Repeater optimization is first attained to enhance the drive capability and reduce the time duration of the output pulse. Previously, many researchers have studied the effect of the driver and repeater insertion on the performance of coupled interconnects in terms of delay and crosstalk [140]-[143]. In [140], it was observed that the crosstalk-induced noise peaks increase with the increase in the PMOS transistor width. The dependency of the short circuit current on the width of the driver transistors was also studied by Kaushik *et al.* [141]. It was observed that the short channel current depends on the width of the driver and becomes significant in the case of large drivers. The work reported in [142] shows that repeater insertion not only reduces the crosstalk-induced delay but also crosstalk-induced peaks in coupled interconnects. Kumar *et al.* [143] proposed an accurate and time-efficient model for dynamic crosstalk analysis. However, their analysis included the non-linear effects of the CMOS driver.

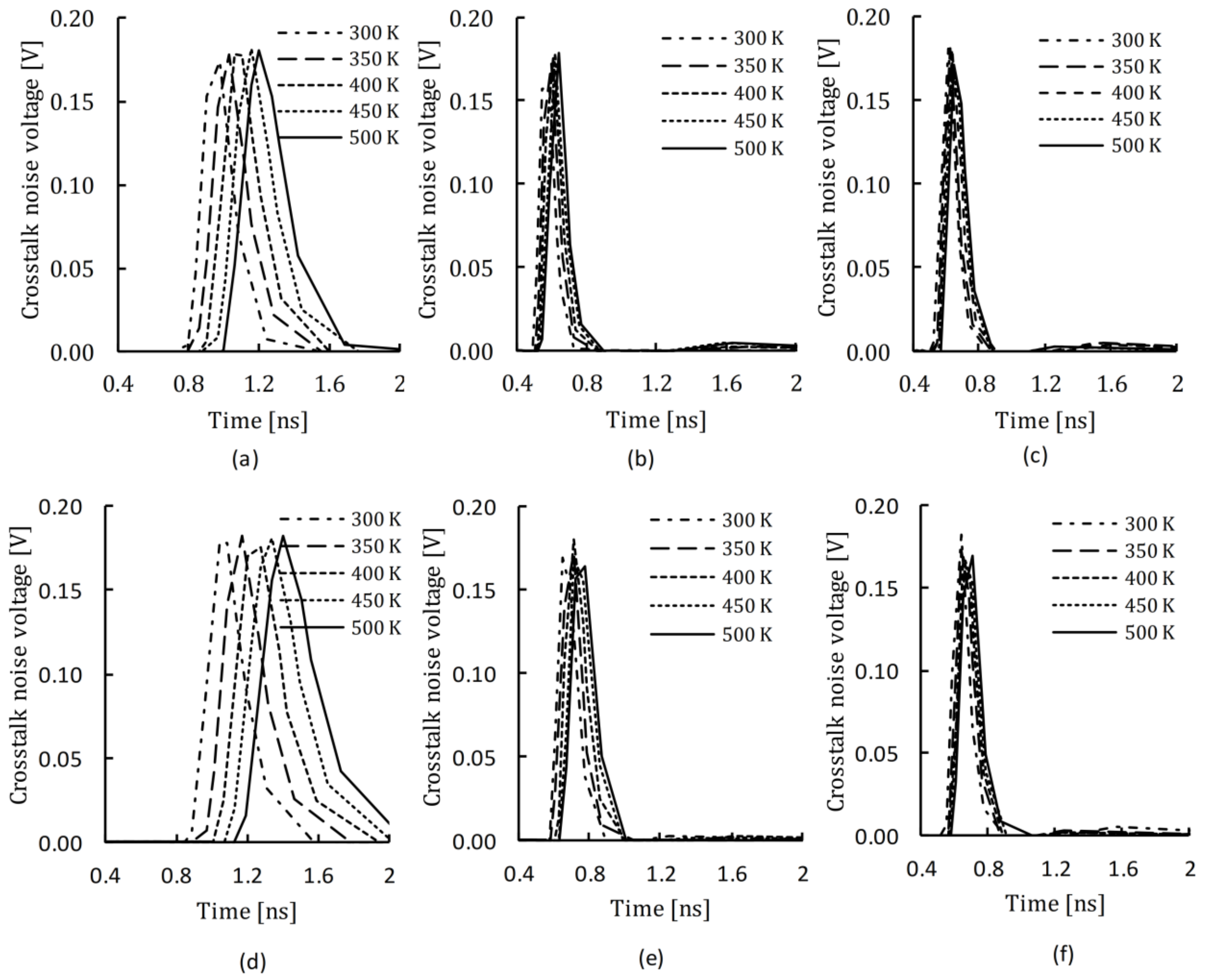

Figure 5.6 Crosstalk-induced transient response as a function of temperature at the remote end terminal on the victim line in capacitively-coupled DIL configuration for different MLGNR interconnects of type undoped, $FeCl_3$-doped and AsF_5-doped, shown in (a), (b) and (c), respectively with AC-edges, and (d), (e) and (f), respectively with ZZ-edges.

Figure 5.6 (a-f) shows the variation of the functional crosstalk-induced transient responses as a function of temperature at the remote end of the victim line for MLGNR (undoped, AsF_5-doped and $FeCl_3$-doped) with both the AC and ZZ edges. These results are obtained under functional switching (fall-glitch), i.e., the aggressor is switched from logic 1 to logic 0, and the victim is held at logic 1. It is seen that with the rise in temperature from 300 K to 500 K, the noise peaks of crosstalk-induced transient responses fall while the time-duration of transient responses increases for all the different types of MLGNR interconnects. It is justified by the combined effect of interconnect's resistance, inductance and capacitance [98]. It is also observed that over a temperature range from 300 K to 500 K, undoped MLGNR has a wider crosstalk-induced noise pulse compared to that of both the doped MLGNRs. It is due to the large value of resistance associated with undoped MLGNR.

Based on the results plotted in Figure 5.6, crosstalk- induced noise peaks and their time duration are shown in Figures 5.7 and 5.8, respectively.

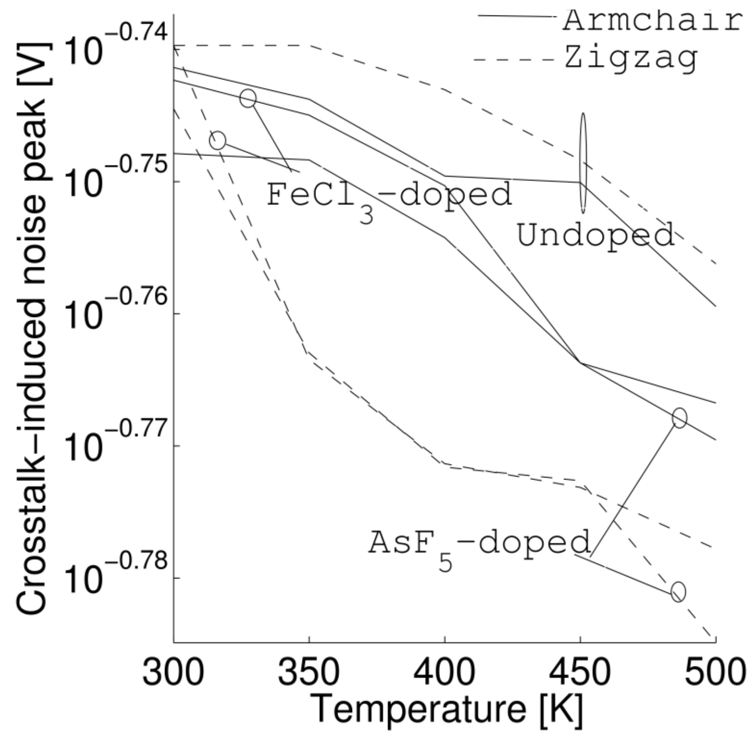

Figure 5.7 Crosstalk-induced fall-glitch peak on the victim line as a function of temperature.

For both the doped MLGNRs, +ve peaks over an entire temperature range (300 K-500 K) are observed to be smaller in comparison to that of undoped MLGNR, as shown in Figure 5.7. It is also noted that +ve peak in coupled MLGNR interconnects with AC-edges, at any specific temperature within the range from 300 K-500 K, is larger than those with ZZ-edges. It is due to the prime contribution of inductance and capacitance than resistance (see Figures 5.4 and 5.5). It is reported that the combined effects of the decrease in the inductance and increase in the capacitance of interconnects result in an overall reduction in the crosstalk-induced +ve peak [65]. High crosstalk-induced noise voltage peaks obtained in the case of undoped MLGNR interconnect can exceed the safe voltage limit across the dielectric (oxide), which consequently leads to dielectric breakdown [136].

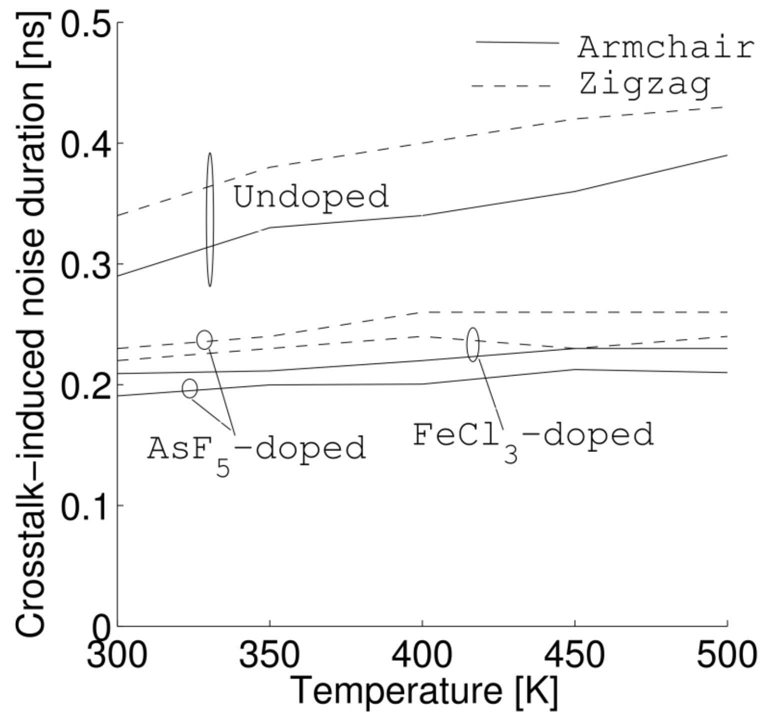

Figure 5.8 Crosstalk-induced rise-glitch time duration on victim line as a function of temperature.

From Figure 5.8, it is seen that the time duration of fall-glitch is increasing with the rise in temperature from 300 K to 500 K for both the doped and undoped MLGNRs. It is reported that a gradual increase in time duration is primarily accompanied by the temperature-dependent line resistance than capacitance and inductance [98]. As the small value of resistance is exhibited by both the doped-MLGNRs at any specific temperature range 300 K-500 K, therefore, the doped-MLGNRs have a lower duration of fall-glitch in comparison to that of undoped MLGNR interconnects. The impact of chirality (AC and ZZ) can also be seen clearly on the time-duration of crosstalk-induced fall glitch.

Figure 5.9 shows the impact of intercalation doping and chirality on the propagation delay of MLGNR interconnects. For this analysis, a single-line bus architecture is considered. It can be seen that the propagation delay of all the three types of MLGNR interconnects (undoped, AsF_5-doped and $FeCl_3$-doped) with both the AC and ZZ-edges increases with the rise in temperature. However, the doped MLGNR interconnects (in particular with AC-edges) exhibit smaller delays as compared to undoped MLGNR interconnects. It is noted that delay in global-length interconnects is mainly affected by interconnect resistance since large drivers (driver size of 100 times the minimum size of the driver has been used in present work) are used to drive these interconnects [31]. Hence, doped-MLGNR interconnects (AC-edges), with their minimum resistance (see Figure 5.3) in comparison to other MLGNR interconnects (undoped MLGNR with both the AC and ZZ-edges and doped MLGNR with ZZ-edges), for temperature within the interval 300 K-500 K (as indicated in Section 5.3), possess lower propagation delay. Also, the results of MLGNR are compared to the best structure of MCBs, i.e., MCB-1 (as noted earlier in chapter 3 and 4) at the same technology node (~ 14 *nm*). It can be noted that both

the doped MLGNR (with the AC and ZZ-edges) kept their advantage in terms of superior delay performance than MCB-1.

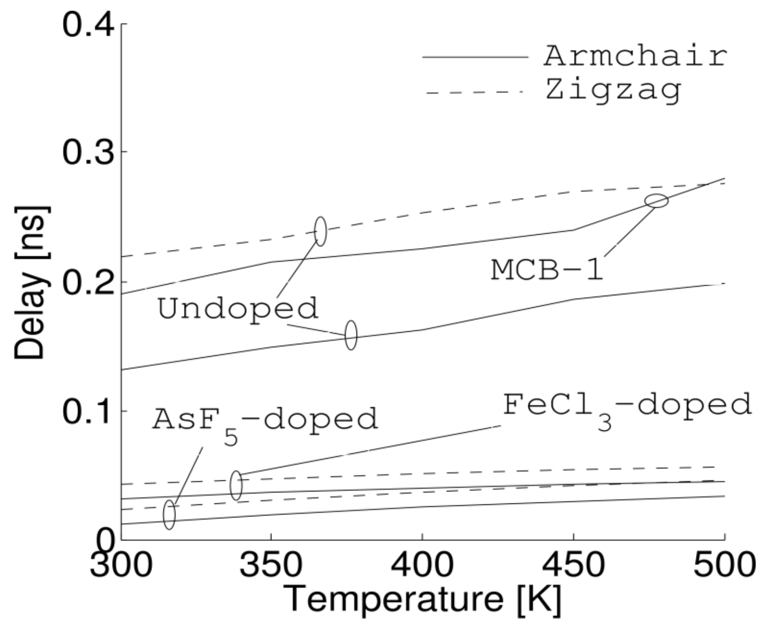

Figure 5.9 Propagation-delay as a function of temperature for different types of MLGNR interconnects. ℓ =1000 μm.

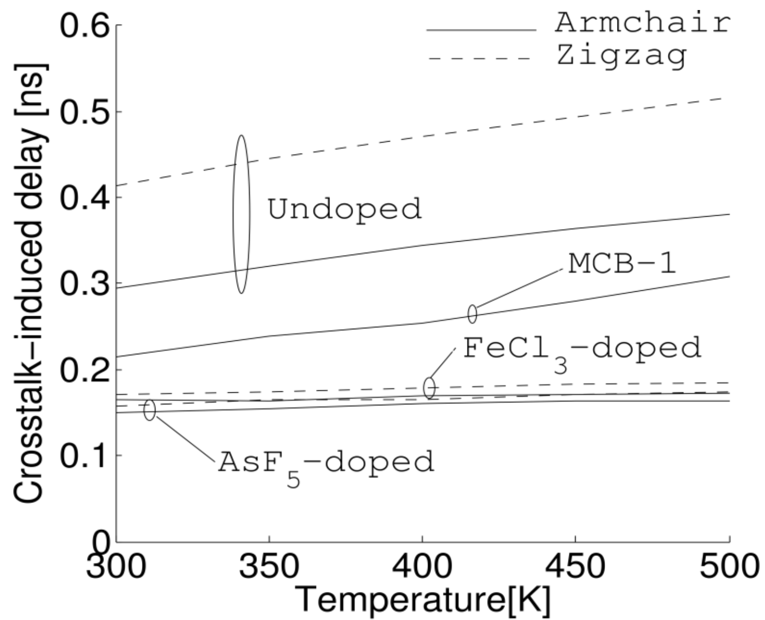

Figure 5.10 Crosstalk-induced delay of the capacitively-coupled MLGNR and MCB interconnects at the different temperatures, at even mode of aggressor-victim switching. ℓ =1000 μm.

The temperature-dependent crosstalk-induced delay at the remote end of the aggressor line, in coupled MLGNR and MCB (MCB-1) interconnects, is shown in Figure 5.10. The corresponding values of the circuit parameters i.e., R, L, C, and C_C for coupled interconnects based on MCB are calculated using the appropriate expressions available in the literature [95]. These results are obtained under dynamic

switching, i.e., the aggressor is switched from logic 0 to 1, and the victim is switched in phase with the aggressor, i.e., from logic 0 to logic 1 [136]. It has been seen that the similar findings are obtained in case of crosstalk-induced delay as compared to the propagation delay obtained through a single line. But the effect of capacitive coupling can be seen in terms of the magnitude of crosstalk-induced delay. It has been further noted that the lowest crosstalk-induced delay is observed with ID-MLGNR interconnects than that of undoped MLGNR and MCB interconnects. It is because of the lowest resistance exhibited by ID-MLGNR interconnects (see Figure 5.3).

5.5 CONCLUSIONS

Detailed analyses that emphasize the impact of GNRs edge shape i.e. AC and ZZ, on crosstalk performance of undoped and doped (intercalated with AsF_5 and $FeCl_3$) MLGNR interconnects is performed. It is found that over a temperature range of 300 K-500 K, lower values of peaks and time duration of crosstalk-induced noise are obtained in doped MLGNRs as compared to undoped MLGNR with ZZ and AC-edges, respectively. This signifies that doped MLGNR is less prone to oxide damage as compared to undoped MLGNR and is more reliable. Further, the smaller values of propagation delay and crosstalk-induced delay are obtained with doped MLGNR (in particular with AC-edges) as compared to undoped MLGNR and MCB. It is attributed to the combined effect of intercalation doping and the high conductivity of AC-edge MLGNRs. The results also reveal that the doped MLGNR gives better performance than undoped counterparts in terms of switching speed. Hence, the doped MLGNR with AC-edges can be a strong contender for high-speed interconnect applications in the deep sub-micron regime.

.

CHAPTER 6

TEMPERATURE DEPENDENT FREQUENCY-DOMAIN CROSSTALK MODEL FOR ID-MLGNR AND MCB

6.1 INTRODUCTION

It is investigated that the crosstalk in adjacent (or coupled) interconnects of MLGNR and MCB affects the reliability and functionality [14], [31], [98], [137]. The operating temperature of the IC can worsen the crosstalk performance of coupled MLGNR and MCB interconnects. Various theoretical and experimental investigations have proven the deteriorated impact of interconnect temperature on the performance of U-MLGNR and MCB interconnects [14], [31], [98], [137]. This is because of the dependence of their impedance parameters on temperature.

Previously, the models presented in [14], [49], [55], [137], [144] accurately analyzed the frequency response and bandwidth performance of U-MLGNR, ID-MLGNR and CNTs interconnects in non-adjacent (or isolated) interconnect configuration. Fathi *et al.* [144] presented an accurate analytical method to analyze the time-domain response of CNT interconnects in the DIL configuration. They studied the impact of metal-contact resistance on the step-response, in particular, on a 50% propagation delay. Based on a similar approach, as in [144], the effects of different Fermi levels, widths and lengths of MLGNR interconnects were studied on their absolute frequency response and relative stability (using Nyquist stability criterion) [55], [137]. The authors in [14], used their proposed novel analytical model to analyze the absolute frequency response of SC- and TC-MLGNR interconnects for different Fermi energies. However, they neglected the driver and load parameters in their model. Later on, as an improvement, the equivalent single conductor (ESC) model presented in [56] accurately considered the driver and load parameters, and analyzed the bandwidth and frequency response of MLGNR interconnect in comparison to MWCNT counterparts at different domain of interconnect lengths (viz. local, semi-global and global). It is revealed that MLGNR interconnect outperforms MWCNT interconnect significantly in terms of bandwidth performance at both the local and global lengths of interconnect. The authors in [145] comparatively analyzed the propagation delay and relative stability of MLGNR and MWCNT interconnects. It is observed that dominating effect of capacitance in MWCNT interconnect makes it relatively more stable than MLGNR interconnect at local lengths. Whereas, stability of MLGNR and MWCNT is comparable at both the semi-global and global lengths of interconnect. Further, Kumar *et al.* [49] analyzed the performance of ID-MLGNR interconnects in frequency- and the time-domain responses of ID-MLGNR interconnects for different Fermi energies, lengths, widths and doping fraction.

However, the frequency response and bandwidth performance of coupled interconnects of ID-MLGNR still need more investigations. In chapter 3, a temperature-dependent ESC model has been developed based on temperature-dependent impedance parameters of the interconnect. Employing the developed

temperature-dependent ESC model, this chapter presents a new analytical model to analyze the frequency-domain response in capacitively-coupled interconnects of ID-MLGNR and MCB, that incorporates the effects of intercalation doping in MLGNR and inter-shell tunneling resistance in MCB. The derived transfer function is employed to analyze and compare the bandwidth performance of MLGNR (U, AsF_5-doped and $FeCl_3$-doped) and MCB interconnects using the DIL configuration at 14 *nm* technology node. Moreover, a 50% rise time computed using step response is also studied for these interconnects. Further, the temperature-dependent frequency spectrum in coupled interconnects of MLGNR (U, AsF_5-doped and $FeCl_3$-doped) and MCB is also analyzed, using a 64-point fast Fourier technique (FFT).

6.2 CIRCUIT MODEL OF CAPACITIVELY COUPLED INTERCONNECTS

The circuit model of capacitively coupled interconnects of MLGNR/MCB in a DIL configuration which is based on the ESC model is presented earlier in chapter 3. Based on the ITRS projection at the 14 *nm* technology node (Table 3.1) physical and dimensional parameters of interconnect and driver transistors are extracted. Using the obtained ITRS interconnect parameters and the expressions for $R_{ESC}(T)$, $C_{ESC}(T)$ and $L_{ESC}(T)$ as in chapter 3, the impedance parameters for interconnects of MLGNR (U, AsF_5, and $FeCl_3$) and MCB at different temperatures are calculated, and are tabulated in Table 6.1.

Table 6.1 Impedance parameters for interconnects of MLGNR (U, AsF_5-doped and $Fecl_3$-doped) and MCB-1 at different temperatures.

Impedance Parameter	T (K)	U-MLGNR	AsF_5- MLGNR	$FeCl_3$- MLGNR	MCB
R(KΩ)	300	2.64	0.77	0.93	0.97
	350	2.96	0.83	0.98	1.18
	400	3.24	0.88	1.02	1.35
	450	3.49	0.92	1.05	1.57
	500	3.72	0.96	1.08	1.87
L(nH)	300	5.31	2.79	3.59	7.37
	350	5.31	2.77	3.58	7.07
	400	5.29	2.75	3.56	6.58
	450	5.26	2.74	3.54	6.38
	500	5.22	2.72	3.52	6.19
C(fF)	300	2.3430	2.3737	2.3751	5.5197
	350	2.3430	2.3738	2.3751	5.5198
	400	2.3431	2.3739	2.3752	5.5198
	450	2.3433	2.3741	2.3753	5.5231
	500	2.3436	2.3742	2.3754	5.5231

In the present analysis, a global interconnect length 'ℓ' of 1000 μm and width 'W' of 24 *nm* is considered. MLGNR of a metallic-AC chirality is considered [11]. The values of Fermi energy 'E_F' for U, AsF_5 and $FeCl_3$ MLGNRs are 0.2 eV, 0.6 eV and 0.68 eV, respectively (given earlier in chapter 5). The constituting elements of MCB, i.e., SWCNTs and MWCNTs are assumed to have diameters of 1 *nm* and 8 *nm*, respectively [98]. For the present analysis, the MCB structure, which has been proposed

previously as the best structure in terms of crosstalk-noise performance, is considered [93], [98], [99] (in the present work labeled as MCB-1). It can be noted from Table 6.1 that $C_{ESC}(T)$ increases with the rise in the temperature as it is directly proportional to N_{ch}. Whereas, $L_{ESC}(T)$ being the inverse function of N_{ch} decreases with the rise in temperature. Further, it can be noted that among the impedance parameters $R_{ESC}(T)$, $C_{ESC}(T)$ and $L_{ESC}(T)$, $R_{ESC}(T)$ is dominantly affected by the temperature. This is due to the dependence of $R_{ESC}(T)$ on both N_{ch} and λ_{eff} that causes a significant increase in its value with the rise in temperature [98], [99]. Moreover, among the four different interconnects (i.e., U-, AsF_5-doped and $FeCl_3$-doped MLGNR and MCB), lowest values of $R_{ESC}(T)$, $C_{ESC}(T)$ and $L_{ESC}(T)$ are obtained with AsF_5-doped MLGNR interconnect that indicates its improved bandwidth performance [55], [49].

6.3 FREQUENCY-DOMAIN CROSSTALK MODEL

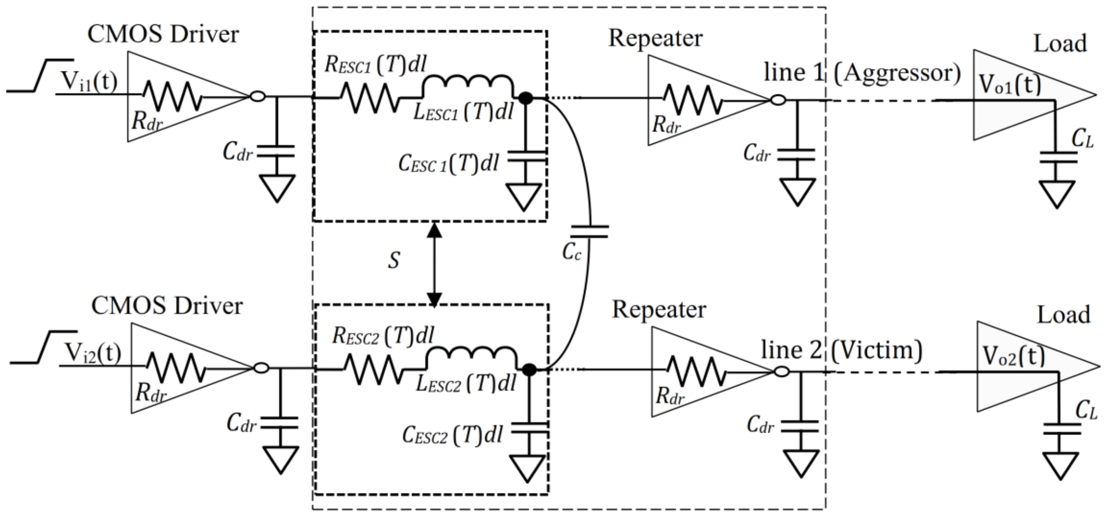

Figure 6.1 Circuit model of capacitively coupled interconnects [142].

In Figure 6.1, each distributed RLC line can be modeled as a transmission line [142]. To derive the transfer function of the capacitively-coupled configuration in Figure 6.1, at first, the derivation of total transmission line parameter matrices is required. The *p.u.l* interconnect parameters of the two-coupled lines are the 2 × 2 symmetric matrices of the resistance, inductance and the capacitance, i.e., ***R***, ***L*** and ***C***, respectively, and are expressed as

$$\boldsymbol{R} = \begin{bmatrix} R_{ESC1}(T) & 0 \\ 0 & R_{ESC2}(T) \end{bmatrix} \quad (6.1a),$$

$$\boldsymbol{L} = \begin{bmatrix} L_{ESC1}(T) & 0 \\ 0 & L_{ESC2}(T) \end{bmatrix} \quad (6.1b),$$

$$\boldsymbol{C} = \begin{bmatrix} C_{ESC1}(T) + KC_C & -KC_C \\ -KC_C & C_{ESC2}(T) + KC_C \end{bmatrix} \quad (6.1c)$$

Where K is the switching factor. The values of K=0 and 1 denote the even-mode and odd-mode switching conditions under dynamic crosstalk, respectively. The telegrapher equations in terms of the voltage vector $\boldsymbol{V}$ and the current vector $\boldsymbol{I}$ [146] can represent the two-coupled transmission lines, i.e.,

$$\frac{d}{dl}\begin{pmatrix}\boldsymbol{V}\\ \boldsymbol{I}\end{pmatrix} = -\begin{pmatrix}\boldsymbol{0} & \boldsymbol{Z}\\ \boldsymbol{Y} & \boldsymbol{0}\end{pmatrix}\begin{pmatrix}\boldsymbol{V}\\ \boldsymbol{I}\end{pmatrix} \quad (6.2)$$

Where $\boldsymbol{Z} = \boldsymbol{R}+s\boldsymbol{L}$ and $\boldsymbol{Y} = s\boldsymbol{C}$. $\boldsymbol{Z}$ and $\boldsymbol{Y}$ are the *p.u.l* impedance and conductance matrices, respectively.

The closed-form solutions of the transfer function of two-coupled interconnect lines can be obtained based on the decoupled model in [146]. Decoupling of these coupled interconnect lines is achieved by performing a linear transformation of $\boldsymbol{V}$ and $\boldsymbol{I}$, i.e., $\boldsymbol{V} = \boldsymbol{M}\widehat{\boldsymbol{V}}$ and $\boldsymbol{I} = \left(\boldsymbol{M}^{\boldsymbol{T}}\right)^{-1}\widehat{\boldsymbol{I}}$. For the interconnect lines with identical circuit parameters and length, i.e.

$$R_{ESC1}(T) = R_{ESC2}(T) = R_{ESC}(T) \quad (6.3a),$$

$$L_{ESC1}(T) = L_{ESC2}(T) = L_{ESC}(T) \quad (6.3b),$$

$$C_{ESC1}(T) = C_{ESC2}(T) = C_{ESC}(T);\ \ell_1 = \ell_2 \quad (6.3c),$$

the matrix $\boldsymbol{M}$ as in [146] is given by,

$$\boldsymbol{M} = \begin{bmatrix}\sqrt{2}/2 & \sqrt{2}/2\\ \sqrt{2}/2 & -\sqrt{2}/2\end{bmatrix} \quad (6.4)$$

Two decoupled interconnect lines, in terms of the voltage vector $\widehat{\boldsymbol{V}}$ and the current vector $\widehat{\boldsymbol{I}}$ is described by

$$\frac{d}{dl}\begin{pmatrix}\widehat{\boldsymbol{V}}\\ \widehat{\boldsymbol{I}}\end{pmatrix} = -\begin{pmatrix}\boldsymbol{0} & \widehat{\boldsymbol{Z}}\\ \widehat{\boldsymbol{Y}} & \boldsymbol{0}\end{pmatrix}\begin{pmatrix}\widehat{\boldsymbol{V}}\\ \widehat{\boldsymbol{I}}\end{pmatrix} \quad (6.5)$$

Where $\widehat{\boldsymbol{Z}} = \boldsymbol{M}^{-1}\boldsymbol{Z}\left(\boldsymbol{M}^{\boldsymbol{T}}\right)^{-1}$ and $\widehat{\boldsymbol{Y}} = \boldsymbol{M}^{\boldsymbol{T}}\boldsymbol{Y}\boldsymbol{M}$. Using Equations (6.1), (6.4) and (6.5), the matrices $\widehat{\boldsymbol{Z}}$ and $\widehat{\boldsymbol{Y}}$ are simplified as

$$\widehat{\boldsymbol{Z}} = \begin{bmatrix}R_{ESC}(T) + sL_{ESC}(T) & 0\\ 0 & R_{ESC}(T) + sL_{ESC}(T)\end{bmatrix} \quad (6.6),$$

$$\widehat{\boldsymbol{Y}} = \begin{bmatrix}sC_{ESC}(T) & 0\\ 0 & s(C_{ESC}(T) + 2C_C)\end{bmatrix} \quad (6.7),$$

Note here, both $\widehat{\boldsymbol{Z}}$ and $\widehat{\boldsymbol{Y}}$ are diagonal. Two coupled lines, therefore, decoupled into two independent lines [147]. The characteristic impedances (Z_1, Z_2) and propagation coefficients (θ_1, θ_2) of the two interconnect lines are the elements of the diagonal matrices $\sqrt{\widehat{\boldsymbol{Z}}\,.\,\widehat{\boldsymbol{Y}}^{-1}}$ and $\sqrt{\widehat{\boldsymbol{Z}}\,.\,\widehat{\boldsymbol{Y}}}$, respectively, and are obtained as,

$$Z_1 = \sqrt{(R_{ESC}(T) + sL_{ESC}(T))/sC_{ESC}(T)} \quad (6.8a),$$

$$Z_2 = \sqrt{(R_{ESC}(T) + sL_{ESC}(T))/s(C_{ESC}(T) + 2C_C)} \quad (6.8b),$$

$$\theta_1 = \sqrt{\left(R_{ESC}(T) + sL_{ESC}(T)\right).sC_{ESC}(T)} \quad (6.8c),$$

$$\theta_2 = \sqrt{\left(R_{ESC}(T) + sL_{ESC}(T)\right).s(C_{ESC}(T) + 2C_C)} \quad (6.8d),$$

Applying the ABCD parameter concept to Equation (6.5), the relationship between the voltage and the current vector at the driver side (or near-end) i.e. $\widehat{\boldsymbol{V}}_{\boldsymbol{D}}$, $\widehat{\boldsymbol{I}}_{\boldsymbol{D}}$ and at the load side (or far end) i.e. $\widehat{\boldsymbol{V}}_{\boldsymbol{R}}$, $\widehat{\boldsymbol{I}}_{\boldsymbol{R}}$ is obtained as

$$\begin{bmatrix} \widehat{\boldsymbol{V}}_{\boldsymbol{D}} \\ \widehat{\boldsymbol{I}}_{\boldsymbol{D}} \end{bmatrix} = \begin{bmatrix} \widehat{\boldsymbol{A}}_{\boldsymbol{D}} & \widehat{\boldsymbol{B}}_{\boldsymbol{D}} \\ \widehat{\boldsymbol{C}}_{\boldsymbol{D}} & \widehat{\boldsymbol{D}}_{\boldsymbol{D}} \end{bmatrix} \begin{bmatrix} \widehat{\boldsymbol{V}}_{\boldsymbol{R}} \\ \widehat{\boldsymbol{I}}_{\boldsymbol{R}} \end{bmatrix} \quad (6.9)$$

Where $\widehat{\boldsymbol{A}}_{\boldsymbol{D}}$, $\widehat{\boldsymbol{B}}_{\boldsymbol{D}}$, $\widehat{\boldsymbol{C}}_{\boldsymbol{D}}$ and $\widehat{\boldsymbol{D}}_{\boldsymbol{D}}$ are the ABCD parameter of decoupled lines and are expressed by

$$\widehat{\boldsymbol{A}}_{\boldsymbol{D}} = \text{diag}\ (\cosh \theta_1, \cosh \theta_2), \quad (6.10a),$$

$$\widehat{\boldsymbol{B}}_{\boldsymbol{D}} = \text{diag}\ (Z_1 .\ \sinh \theta_1, Z_2 .\ \sinh \theta_2), \quad (6.10b),$$

$$\widehat{\boldsymbol{C}}_{\boldsymbol{D}} = \text{diag}\ (\sinh \theta_1/ Z_1, \sinh \theta_2/ Z_2), \quad (6.10c),$$

$$\widehat{\boldsymbol{D}}_{\boldsymbol{D}} = \text{diag}\ (\cosh \theta_1, \cosh \theta_2) \quad (6.10d)$$

By performing a linearization of $\widehat{\boldsymbol{V}}$ and $\widehat{\boldsymbol{I}}$ i.e., $\widehat{\boldsymbol{V}} = \boldsymbol{M}^{-1}\boldsymbol{V}$ and $\widehat{\boldsymbol{I}} = \boldsymbol{M}^{T}\boldsymbol{I}$, the ABCD parameter matrices of coupled interconnect lines are

$$\begin{bmatrix} \boldsymbol{V}_{\boldsymbol{D}} \\ \boldsymbol{I}_{\boldsymbol{D}} \end{bmatrix} = \begin{bmatrix} \boldsymbol{A}_{\boldsymbol{D}} & \boldsymbol{B}_{\boldsymbol{D}} \\ \boldsymbol{C}_{\boldsymbol{D}} & \boldsymbol{D}_{\boldsymbol{D}} \end{bmatrix} \begin{bmatrix} \boldsymbol{V}_{\boldsymbol{R}} \\ \boldsymbol{I}_{\boldsymbol{R}} \end{bmatrix} \quad (6.11)$$

Where $\boldsymbol{A}_{\boldsymbol{D}} = \boldsymbol{M}\widehat{\boldsymbol{A}}_{\boldsymbol{D}}\boldsymbol{M}^{-1}$, $\boldsymbol{B}_{\boldsymbol{D}} = \boldsymbol{M}\widehat{\boldsymbol{B}}_{\boldsymbol{D}}\boldsymbol{M}^{T}$, $\boldsymbol{C}_{\boldsymbol{D}} = \left(\boldsymbol{M}^{T}\right)^{-1}\widehat{\boldsymbol{C}}_{\boldsymbol{D}}\boldsymbol{M}^{-1}$ and $\boldsymbol{D}_{\boldsymbol{D}} = \left(\boldsymbol{M}^{T}\right)^{-1}\widehat{\boldsymbol{D}}_{\boldsymbol{D}}\boldsymbol{M}^{T}$.

The boundary conditions for the two coupled lines are $\boldsymbol{V_D} = \boldsymbol{V_{in}} - \boldsymbol{R_D}.\boldsymbol{I_D}$ and $\boldsymbol{I_R} = s\boldsymbol{C_l}.\ \boldsymbol{V_R}$. Where the driver resistance matrix $\boldsymbol{R_D}$ and the load capacitance matrix $\boldsymbol{C_l}$ are

$$\boldsymbol{R}_{\boldsymbol{D}} = \begin{bmatrix} R_{dr} & 0 \\ 0 & R_{dr} \end{bmatrix}; \boldsymbol{C}_{\boldsymbol{l}} = \begin{bmatrix} C_L & 0 \\ 0 & C_L \end{bmatrix} \quad (6.12)$$

Using the boundary conditions, Equation (6.11) is further simplified to obtain the following Equations

$$\boldsymbol{V_{in}} - \boldsymbol{R_D}.\boldsymbol{I_D} = \boldsymbol{A_D}.\boldsymbol{V_R} + s\,\boldsymbol{B_D}\boldsymbol{C_l}.\ \boldsymbol{V_R}, \quad (6.13),$$

$$\boldsymbol{I_D} = \boldsymbol{C_D}.\ \boldsymbol{V_R} + s\,\boldsymbol{D_D}.\ \boldsymbol{C_l}.\ \boldsymbol{V_R} \quad (6.14),$$

Solving Equations (6.13) and (6.14) for $\boldsymbol{V_R}$ and $\boldsymbol{V_{in}}$

$$\boldsymbol{V_R}/\boldsymbol{V_{in}} = \boldsymbol{H} = [\boldsymbol{A_D} + s\,\boldsymbol{B_D}\boldsymbol{C_l} + \boldsymbol{R_D}\boldsymbol{C_D} + s\,\boldsymbol{R_D}\boldsymbol{D_D}.\ \boldsymbol{C_l}]^{-1} \quad (6.15),$$

Where $\boldsymbol{H}$ is the input/output transfer function matrix of the order of 2×2 for the two-coupled lines. The matrix $\boldsymbol{H}$ is further simplified as given below

$$\boldsymbol{H} = \begin{bmatrix} M_1 & M_2 \\ M_3 & M_4 \end{bmatrix}^{-1} = \frac{1}{M_1M_4 - M_2M_3}\begin{bmatrix} M_4 & -M_2 \\ -M_3 & M_1 \end{bmatrix} \quad (6.16),$$

$$M_1 = \frac{R_{dr}\, sinh\theta_1}{2Z_1} + \frac{R_{dr}\, sinh\theta_2}{2Z_2} + \frac{cosh\theta_1}{2} + \frac{cosh\theta_2}{2} + \frac{sR_{dr}\, C_L cosh\theta_1}{2} + \frac{sR_{dr}\, C_L cosh\theta_2}{2} + \frac{sC_LZ_1 sinh\theta_1}{2} + \frac{sC_LZ_2 sinh\theta_2}{2} \quad (6.17a),$$

$$M_2 = \frac{R_{dr}\, sinh\theta_1}{2Z_1} - \frac{R_{dr}\, sinh\theta_2}{2Z_2} + \frac{cosh\theta_1}{2} - \frac{cosh\theta_2}{2} + \frac{sR_{dr}\, C_L cosh\theta_1}{2} - \frac{sR_{dr}\, C_L cosh\theta_2}{2} + \frac{sC_LZ_1 sinh\theta_1}{2} - \frac{sC_LZ_2 sinh\theta_2}{2} \quad (6.17b),$$

$$M_3 = \frac{R_{dr}\, sinh\theta_1}{2Z_1} - \frac{R_{dr}\, sinh\theta_2}{2Z_2} + \frac{cosh\theta_1}{2} - \frac{cosh\theta_2}{2} + \frac{sR_{dr}\, C_L cosh\theta_1}{2} - \frac{sR_{dr}\, C_L cosh\theta_2}{2} + \frac{sC_LZ_1 sinh\theta_1}{2} - \frac{sC_LZ_2 sinh\theta_2}{2} \quad (6.17c),$$

$$M_4 = \frac{R_{dr}\, sinh\theta_1}{2Z_1} + \frac{R_{dr}\, sinh\theta_2}{2Z_2} + \frac{cosh\theta_1}{2} + \frac{cosh\theta_2}{2} + \frac{sR_{dr}\, C_L cosh\theta_1}{2} + \frac{sR_{dr}\, C_L cosh\theta_2}{2} + \frac{sC_LZ_1 sinh\theta_1}{2} + \frac{sC_LZ_2 sinh\theta_2}{2} \quad (6.17d)$$

The terms M_1-M_4 of the transfer function matrix in Equation (6.17) can be simplified using the linear parametric terms for $sinh\theta_1/Z_1$, $sinh\theta_2/Z_2$, $cosh\theta_1$ and $cosh\theta_2$, (i.e., using 4th or higher-order expansion of hyperbolic functions), as given below

$$M_1 = M_4 = 1 + s\left[(R_{ESC}(T) + R_{dr})C_L + (C_{ESC}(T) + C_C) \times \left(R_{dr} + \frac{R_{ESC}(T)}{2!}\right)\right]$$

$$+s^2\left[\frac{R_{ESC}(T)C_{ESC}(T)^2R_{dr}}{2 \times 3!} + L_{ESC}(T)C_L + \frac{R_{ESC}(T)(C_{ESC}(T) + C_C)^2R_{dr} + R_{ESC}(T)^2(2C_{ESC}(T) + C_C)C_L}{2 \times 3!} + (C_{ESC}(T) + C_C) \times \left(\frac{L_{ESC}(T)}{2!} + \frac{R_{ESC}(T)R_{dr}C_L}{2!}\right) + \frac{R_{ESC}(T)^2(C_{ESC}(T)^2 + (C_C)^2)}{4!}\right]$$

$$+s^3\left[\frac{L_{ESC}(T)C_{ESC}(T)^2R_{dr}}{2\times 3!}+\frac{R_{ESC}(T)^2C_{ESC}(T)^3R_{dr}+R_{ESC}(T)^3C_{ESC}(T)^2C_L}{2\times 5!}+(C_{ESC}(T)+C_C)\right.$$

$$\times\left(\frac{2R_{ESC}(T)L_{ESC}(T)C_L}{3!}+\frac{L_{ESC}(T)R_{dr}C_L}{2!}\right)+\frac{L_{ESC}(T)(C_{ESC}(T)+2C_C)^2R_{dr}}{2\times 3!}$$

$$+\frac{R_{ESC}(T)^2(C_{ESC}(T)+2C_C)^3R_{dr}+R_{ESC}(T)^3(C_{ESC}(T)+2C_C)^2C_L}{2\times 5!}+\frac{2R_{ESC}(T)L_{ESC}(T)C_{ESC}(T)^2}{2\times 4!}$$

$$+\frac{R_{ESC}(T)^3C_{ESC}(T)^3}{2\times 6!}+\frac{R_{ESC}(T)^2C_{ESC}(T)^2R_{dr}C_L}{2\times 4!}+\frac{2R_{ESC}(T)L_{ESC}(T)(C_{ESC}(T)+2C_C)^2}{2\times 4!}$$

$$\left.+\frac{R_{ESC}(T)^3(C_{ESC}(T)+2C_C)^3}{2\times 6!}+\frac{R_{ESC}(T)^2(C_{ESC}(T)+2C_C)^2R_{dr}C_L}{2\times 4!}\right]$$

$$+s^4\left[\frac{R_{ESC}(T)L_{ESC}(T)C_{ESC}(T)^2(C_{ESC}(T)+2C_C)R_{dr}+R_{ESC}(T)^2L_{ESC}(T)C_{ESC}(T)^2C_L}{5!}\right.$$

$$+\frac{(C_{ESC}(T)R_{dr}+R_{ESC}(T)C_L)R_{ESC}(T)^3C_{ESC}(T)^3}{2\times 7!}+\frac{R_{ESC}(T)^2C_{ESC}(T)^2L_{ESC}(T)C_L}{2\times 5!}$$

$$+\frac{R_{ESC}(T)L_{ESC}(T)(C_{ESC}(T)+2C_C)^3R_{dr}+R_{ESC}(T)^2L_{ESC}(T)(C_{ESC}(T)+2C_C)^2}{5!}$$

$$+\frac{((C_{ESC}(T)+2C_C)R_{dr}+R_{ESC}(T)C_L)R_{ESC}(T)^3(C_{ESC}(T)+2C_C)^3}{2\times 7!}+\frac{L_{ESC}(T)^2(C_{ESC}(T)+C_C)C_L}{3!}$$

$$+\frac{R_{ESC}(T)^2(C_{ESC}(T)+2C_C)^2L_{ESC}(T)C_L}{2\times 5!}+\frac{L_{ESC}(T)^2C_{ESC}(T)^2}{2\times 4!}+\frac{3R_{ESC}(T)^2L_{ESC}(T)C_{ESC}(T)^3}{2\times 6!}$$

$$+\frac{2R_{ESC}(T)L_{ESC}(T)C_{ESC}(T)^2R_{dr}C_L}{2\times 4!}+\frac{R_{ESC}(T)^3C_{ESC}(T)^3R_{dr}C_L}{2\times 6!}+\frac{L_{ESC}(T)^2(C_{ESC}(T)+2C_C)^2}{2\times 4!}$$

$$+\frac{3R_{ESC}(T)^2L_{ESC}(T)(C_{ESC}(T)+2C_C)^3}{2\times 6!}+\frac{R_{ESC}(T)^4(C_{ESC}(T)^4+(C_{ESC}(T)+2C_C)^4)}{2\times 8!}$$

$$\left.+\frac{2R_{ESC}(T)L_{ESC}(T)(C_{ESC}(T)+2C_C)^2R_{dr}C_L}{2\times 4!}+\frac{R_{ESC}(T)^3(C_{ESC}(T)+2C_C)^3R_{dr}C_L}{2\times 6!}\right]$$

(6.18),

$$-M_2=-M_3=s\left[\left(R_{dr}+\frac{R_{ESC}(T)}{2!}\right)C_C\right]$$

$$+s^2\left[-\frac{R_{ESC}(T)C_{ESC}(T)^2R_{dr}}{2\times 3!}+\frac{R_{ESC}(T)R_{dr}(C_{ESC}(T)+2C_C)^2+2R_{ESC}(T)^2C_CC_L}{2\times 3!}\right.$$

$$-\frac{R_{ESC}(T)^2C_{ESC}(T)^2}{2\times 4!}+\frac{L_{ESC}(T)C_C}{2!}+\frac{R_{ESC}(T)^2(C_{ESC}(T)+2C_C)^2}{2\times 4!}$$

$$\left.+\frac{R_{ESC}(T)(C_{ESC}(T)+C_C)R_{dr}C_L}{2!}\right]$$

$$+s^3\Bigg[-\frac{L_{ESC}(T)C_{ESC}(T)^2R_{dr}}{2\times 3!}-\frac{R_{ESC}(T)^2C_{ESC}(T)^3R_{dr}+R_{ESC}(T)^3C_{ESC}(T)^2C_L}{2\times 5!}$$

$$+\frac{(L_{ESC}(T)(C_{ESC}(T)+2C_C)^2R_{dr}+3R_{ESC}(T)L_{ESC}(T)C_CC_L)}{2\times 3!}$$

$$+\frac{(R_{ESC}(T)^2(C_{ESC}(T)+2C_C)^3R_{dr}+R_{ESC}(T)^3(C_{ESC}(T)+2C_C)^2C_L)}{2\times 5!}$$

$$-\frac{R_{ESC}(T)L_{ESC}(T)C_{ESC}(T)^2}{4!}-\frac{R_{ESC}(T)^3C_{ESC}(T)^3}{2\times 6!}-\frac{R_{ESC}(T)^2C_{ESC}(T)^2R_{dr}C_L}{2\times 4!}$$

$$+\frac{R_{ESC}(T)L_{ESC}(T)(C_{ESC}(T)+2C_C)^2}{4!}+\frac{R_{ESC}(T)^3(C_{ESC}(T)+2C_C)^3}{2\times 6!}$$

$$+\frac{L_{ESC}(T)(C_C)R_{dr}C_L}{2!}+\frac{R_{ESC}(T)^2(C_{ESC}(T)+2C_C)^2R_{dr}C_L}{2\times 4!}\Bigg]$$

$$+s^4\Bigg[-\frac{\big((C_{ESC}(T)+2C_C)R_{dr}+R_{ESC}(T)C_L\big)R_{ESC}(T)L_{ESC}(T)C_{ESC}(T)^2}{5!}$$

$$-\frac{R_{ESC}(T)^3C_{ESC}(T)^4R_{dr}+R_{ESC}(T)^4C_{ESC}(T)^3C_L}{2\times 7!}-\frac{R_{ESC}(T)^2C_{ESC}(T)^2L_{ESC}(T)C_L}{2\times 5!}$$

$$+\frac{\big((C_{ESC}(T)+2C_C)R_{dr}+R_{ESC}(T)C_L\big)R_{ESC}(T)L_{ESC}(T)(C_{ESC}(T)+2C_C)^2}{5!}$$

$$+\frac{R_{ESC}(T)^3(C_{ESC}(T)+2C_C)^4R_{dr}+R_{ESC}(T)^4(C_{ESC}(T)+2C_C)^3C_L}{2\times 7!}$$

$$+\frac{L_{ESC}(T)^2C_CC_L}{3!}+\frac{R_{ESC}(T)^2(C_{ESC}(T)+2C_C)^2L_{ESC}(T)C_L}{2\times 5!}-\frac{L_{ESC}(T)^2C_{ESC}(T)^2}{2\times 4!}$$

$$-\frac{3R_{ESC}(T)^2L_{ESC}(T)C_{ESC}(T)^3}{2\times 6!}-\frac{R_{ESC}(T)^4C_{ESC}(T)^4}{2\times 8!}$$

$$-\frac{R_{ESC}(T)L_{ESC}(T)C_{ESC}(T)^2R_{dr}C_L}{4!}-\frac{R_{ESC}(T)^3C_{ESC}(T)^3R_{dr}C_L}{2\times 6!}$$

$$+\frac{L_{ESC}(T)^2(C_{ESC}(T)+2C_C)^2}{2\times 4!}+\frac{3R_{ESC}(T)^2L_{ESC}(T)(C_{ESC}(T)+2C_C)^3}{2\times 6!}$$

$$+\frac{R_{ESC}(T)^4(C_{ESC}(T)+2C_C)^4}{2\times 8!}+\frac{R_{ESC}(T)L_{ESC}(T)(C_{ESC}(T)+2C_C)^2R_{dr}C_L}{4!}$$

$$+\frac{R_{ESC}(T)^3(C_{ESC}(T)+2C_C)^3R_{dr}C_L}{2\times 6!}\Bigg]$$

(6.19),

The denominator term of the transfer function matrix ($H_D = M_1M_4 - M_2M_3$) as in Equation (6.16) can be simplified in terms of fourth-order pade's approximation as $H_D=1+B_0s+B_1s^2+B_2s^3+B_3s^4$

Where $B_0 = R_{ESC}(T)(2C_L + C_2) + 2R_{dr}(C_2 + C_L)$

$$B_1 = (R_{ESC}(T)^2 + R_{dr}^2 + 2R_{ESC}(T)R_{dr})\,{C_L}^2 + 2R_{dr}C_LC_2\ \times\big(R_{dr} + 2R_{ESC}(T)\big) + C_{ESC}(T)C_1R_{dr}$$

$$\times\big(R_{dr} + R_{ESC}(T)\big) + \frac{R_{ESC}(T)R_{dr}}{3!}\big(C_{ESC}(T)^2 + {C_1}^2\big) + \frac{R_{ESC}(T)^2C_L}{3!}\times(4C_{ESC}(T) + C_1)$$

$$+\frac{R_{ESC}(T)^2}{4!}\left(C_{ESC}(T)^2+{C_1}^2\right) \quad +\frac{R_{ESC}(T)^2 C_1}{2!\times 2!}\left(2C_L+C_{ESC}(T)\right)+L_{ESC}(T)(C_2+2C_L)$$

$$B_2=L_{ESC}(T){C_L}^2(2R_{ESC}(T)+R_{dr})+(C_{ESC}(T)+C_1)\times\left(\frac{R_{ESC}(T)C_{ESC}(T)C_1R_{dr}^2}{3!}+\frac{R_{ESC}(T)^3{C_L}^2}{3!}\right.$$

$$\left.+\frac{R_{ESC}(T)^3C_{ESC}(T)C_1}{2!\times 4!}\right)+L_{ESC}(T)R_{dr}C_L\left(3C_1+C_{ESC}(T)\right)+R_{ESC}(T)^2R_{dr}C_L\left({C_1}^2+\frac{C_{ESC}(T)^2}{3!}\right)$$

$$+\frac{5R_{ESC}(T)^2C_{ESC}(T)C_1R_{dr}C_L}{3!}+[C_{ESC}(T).R_{dr}+R_{ESC}(T)C_L]\left[\frac{2L_{ESC}(T)(C_1+C_2)}{3!}+\frac{R_{ESC}(T)^2C_1}{4!}\right.$$

$$\left.\times(2C_{ESC}(T)+C_1)+\frac{R_{ESC}(T)^2C_{ESC}(T)^2}{5!}+\frac{4R_{ESC}(T)C_2R_{dr}C_L}{3}\right]+(R_{ESC}(T)L_{ESC}(T)C_1)$$

$$\times\left(\frac{4C_L}{3}+\frac{C_{ESC}(T)}{2!}\right)$$

$$+[R_{dr}C_1+R_{ESC}(T)C_L]\left[\left(\frac{2L_{ESC}(T)}{3!}+\frac{2R_{ESC}(T)R_{dr}^2C_LC_1}{3!}+\frac{2R_{ESC}(T)^2R_{dr}C_L^2}{3!}\right)\right.$$

$$\times(C_{ESC}(T)+C_1)+\left(\frac{R_{ESC}(T)^2(10C_{ESC}(T)+C_1)}{5!}+\frac{R_{ESC}(T)C_L}{3!}\right)C_1+\frac{R_{ESC}(T)^2C_{ESC}(T)^2}{4!}$$

$$\left.+\frac{R_{ESC}(T)L_{ESC}(T)C_{ESC}(T)C_L}{2!}+\frac{2L_{ESC}(T)R_{dr}C_L^2}{2!}\right]+\left(\frac{2R_{ESC}(T)L_{ESC}(T)}{4!}+\frac{2R_{ESC}(T)^2R_{dr}C_L}{4!}\right)({C_1}^2$$

$$+C_{ESC}(T)^2)$$

$$+\frac{R_{ESC}(T)^3}{6!}({C_1}^3+C_{ESC}(T)^3+R_{ESC}(T)C_2R_{dr}^2C_L^2$$

$$B_3=[C_{ESC}(T).R_{dr}+R_{ESC}(T)C_L]\times\left[R_{ESC}(T)L_{ESC}(T)\left(\frac{2{C_1}^2}{4!}+\frac{C_{ESC}(T)}{3!}\left(\frac{C_{ESC}(T)}{10}+C_1\right)\right)\right.$$

$$\left.+\frac{R_{ESC}(T)^3{C_1}^2}{3!\times 4!}(C_{ESC}(T)+C_1/5)+\frac{R_{ESC}(T)^3C_{ESC}(T)^2}{2!\times 5!}\times\left(\frac{C_{ESC}(T)}{21}+C_1\right)\right]+L_{ESC}(T)C_L(C_1+C_2)$$

$$\times\left(\frac{2C_{ESC}(T)R_{dr}^2}{3!}+\frac{L_{ESC}(T)}{3!}\right)$$

$$+R_{ESC}(T)^2C_L(C_{ESC}(T)+2C_2)\left(\frac{L_{ESC}(T)C_1}{4!}+\frac{C_{ESC}(T)C_1R_{dr}^2}{4!}+\frac{R_{ESC}(T)C_1R_{dr}C_L}{4!}\right)$$

$$+R_{ESC}(T)^2C_{ESC}(T)^2C_L\left(\frac{L_{ESC}(T)}{5!}+\frac{R_{ESC}(T)R_{dr}C_L}{5!}+\frac{C_{ESC}(T)R_{dr}^2}{5!}\right)+R_{ESC}(T)L_{ESC}(T)R_{dr}{C_L}^2$$

$$\times\left(C_1+\frac{2C_{ESC}(T)}{3!}\right)+L_{ESC}(T)^2{C_L}^2+\frac{R_{ESC}(T)^3{C_1}^3R_{dr}C_L}{5!}$$

$$+R_{ESC}(T)L_{ESC}(T)C_1C_L\left(\frac{2R_{ESC}(T)C_L}{3!}+\frac{7C_1R_{dr}}{3!}\right)$$

$$+R_{ESC}(T)L_{ESC}(T)C_{ESC}(T)C_L\left(\frac{2R_{ESC}(T)C_L}{3!}+\frac{C_1R_{dr}}{2!}+\frac{C_{ESC}(T)R_{dr}}{3!}\right)+R_{ESC}(T)^3C_{ESC}(T)C_1R_{dr}C_L$$

$$\times\left(\frac{26C_1}{3!\times 5!}+\frac{C_{ESC}(T)}{3!\times 3!}\right)$$

$$+\left[R_{dr}C_1+R_{ESC}(T)C_L\right]\left[\frac{2R_{ESC}(T)L_{ESC}(T){C_1}^2}{5!}+R_{ESC}(T)^3\left(\frac{{C_1}^3}{7!}+\frac{C_{ESC}(T){C_1}^2}{2!\times 5!}\right.\right.$$

$$\left.\left.+\frac{C_{ESC}(T)^2C_1}{3!\times 4!}+\frac{C_{ESC}(T)^3}{6!}\right)+R_{ESC}(T)L_{ESC}(T)C_{ESC}(T)\left(\frac{2C_{ESC}(T)}{4!}+\frac{C_1}{3!}\right)\right]$$

$$+\left[R_{dr}^2C_LC_1+L_{ESC}(T)C_L\right.$$

$$\left.+R_{ESC}(T)R_{dr}C_L^2\right]\times\left[\frac{2L_{ESC}(T)C_1}{3!}+L_{ESC}(T)C_{ESC}(T)+R_{ESC}(T)^2\left(\frac{{C_1}^2}{5!}+\frac{C_{ESC}(T)C_1}{2!\times 3!}+\frac{C_{ESC}(T)^2}{4!}\right)\right]$$

$$+L_{ESC}(T)^2C_1\left(\frac{C_1}{4!}+\frac{C_{ESC}(T)}{4}\right)+\frac{3R_{ESC}(T)^2L_{ESC}(T){C_1}^3}{6!}$$

$$+R_{ESC}(T)^4\left(\frac{{C_1}^4}{8!}+\frac{C_{ESC}(T){C_1}^3}{2!\times 6!}+\frac{C_{ESC}(T)^2{C_1}^2}{4!\times 4!}\right.$$

$$\left.+\frac{C_{ESC}(T)^3C_1}{2!\times 6!}\right)+\frac{3R_{ESC}(T)^2L_{ESC}(T)C_{ESC}(T)C_1}{2!\times 4!}\left(C_1+C_{ESC}(T)\right)+\left[2R_{ESC}(T)R_{dr}C_L\right]$$

$$\times\left[L_{ESC}(T)\left(\frac{2{C_1}^2}{4!}+\frac{C_{ESC}(T)C_1}{2!}+\frac{2C_{ESC}(T)^2}{4!}\right)\right.$$

$$\left.+R_{ESC}(T)^2\left(\frac{{C_1}^3}{6!}+\frac{C_{ESC}(T){C_1}^2}{2!\times 4!}+\frac{C_{ESC}(T)^2C_1}{2!\times 4!}+\frac{C_{ESC}(T)^3}{6!}\right)\right]$$

$$+\left[R_{dr}^2C_L^2\right]\left[L_{ESC}(T)\left(\frac{C_1}{2!}+\frac{C_{ESC}(T)}{2!}\right)+R_{ESC}(T)^2\left(\frac{{C_1}^2}{4!}+\frac{C_{ESC}(T)C_1}{4}+\frac{C_{ESC}(T)^2}{4!}\right)\right]$$

Where $C_1=C_{ESC}(T)+2C_C$ and $C_2=C_{ESC}(T)+C_C$. (6.20)

6.4 FREQUENCY AND TIME DOMAIN ANALYSIS OF COUPLED INTERCONNECTS

In this section, the frequency- and the time-domain responses of different interconnects are studied using the proposed model. The frequency-domain behaviour of interconnects can also be studied using their frequency spectrum [17]. The bandwidth, delay and stability of capacitively coupled interconnect

are analyzed under odd-mode dynamic switching conditions, i.e., in coupled configuration (Figure 6.1), both the aggressor and the victim lines are simultaneously switched in out-of-phase condition. For example, the aggressor line switches from logic 0 →1, and the victim line switches from logic 1→ 0 or vice-versa.

In the present analysis, different kinds of MLGNR (i.e., U-MLGNR, ID-MLGNR (AsF_5- and $FeCl_3$-doped)), MCB and *Cu* interconnects are considered. The bandwidth performance of these interconnects is analyzed using the absolute frequency response. Figure 6.2 shows the absolute frequency response at the far end of the aggressor line in the DIL configuration of coupled interconnects of U-MLGNR, ID-MLGNR (AsF_5- and $FeCl_3$-doped), MCB and *Cu* at interconnect lengths ℓ = 10 and 1000 μm.

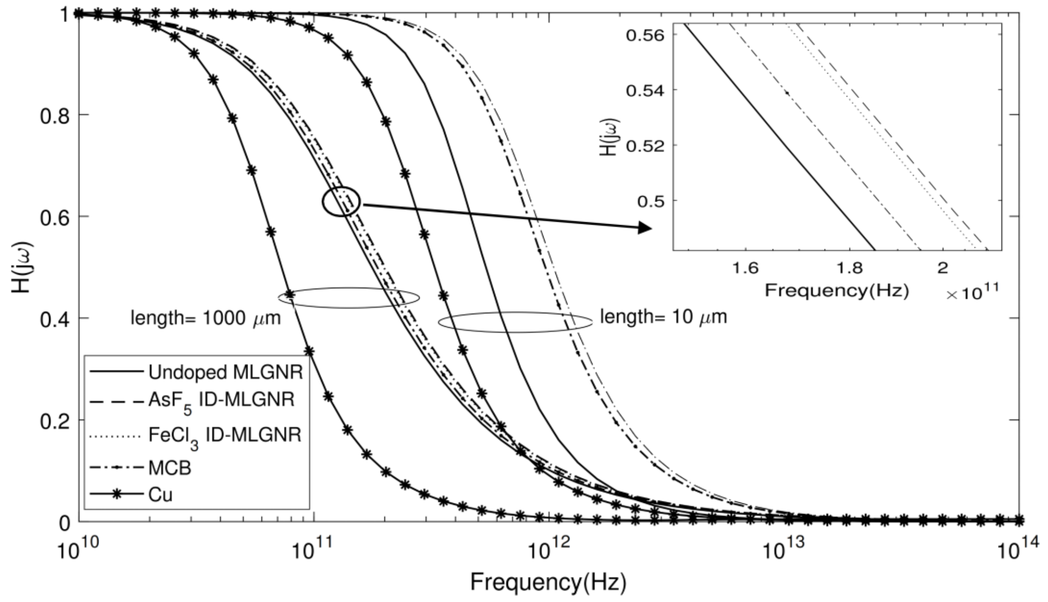

Figure 6.2 Absolute frequency response for coupled interconnects of U-MLGNR, ID-MLGNR (AsF_5- and $FeCl_3$-doped), MCB and *Cu* at ℓ= 10 and 1000 μm.

It is observed that irrespective of the type of interconnect, the 3-dB bandwidth (BW) reduces with an increase in the interconnect length. This is due to the fact that the values of $R_{ESC}(T)$ and $C_{ESC}(T)$ are the direct functions of interconnect length. Therefore, the 3-dB BW of interconnects (viz. an inverse function of the product: $R_{ESC}(T)$. $C_{ESC}(T)$) reduces with the increase in their length. The cut-off frequency 'f_C' of these interconnects can be obtained using the simple formulation as $f_C = 1\ /2\pi\ R_{ESC}(T).C_{ESC}(T)$ [49]. Further, irrespective of the interconnect length, ID-MLGNRs are observed to have much-improved bandwidth performance than that of the U-MLGNR, MCB and *Cu*. This is attributed to the lower values of the $R_{ESC}(T)$ and $C_{ESC}(T)$ obtained in the case of ID-MLGNR (given in Table 6.1). Moreover, satellite projection, at interconnect length ℓ = 1000 μm, shows that AsF_5-doped ID-MLGNR demonstrates a marginal improvement in its bandwidth performance over that of $FeCl_3$-doped ID-MLGNR. Hence, an ID-MLGNR exhibits an improved 3-dB BW in comparison to U-MLGNR, MCB and *Cu* at local (ℓ = 10 μm) and global (ℓ = 1000 μm) domain of interconnect lengths, as tabulated in Table 6.2.

Table 6.2 3-dB bandwidth and 50% rise time for U-MLGNR, ID-MLGNR (AsF_5-doped and $FeCl_3$-doped) MCB and *Cu*.

Type of interconnect	3-dB Bandwidth (GHz) for interconnect length, ℓ, of		50% rise time (ps) for ℓ = 1000 µm
	1000 µm	10 µm	
AsF_5- MLGNR	115.8	727.9	2.29
$FeCl_3$- MLGNR	114.0	727.0	2.32
MCB	107.0	672.8	2.33
U-MLGNR	101.8	394.5	2.34
Cu	52.6	235.2	2.50

Figure 6.3 shows the absolute frequency response for coupled interconnects of AsF_5 ID-MLGNR at ℓ = 1000 μm, at different temperatures within the interval 300 K to 500 K. The 3-dB BW of ID-MLGNR is observed to degrade with the rise in temperature. This is due to the significant increase in the value of $R_{ESC}(T)$ accompanied by the marginal increase in the value of $C_{ESC}(T)$, with the rise in temperature from 300 K-500 K (see Table 6.1).

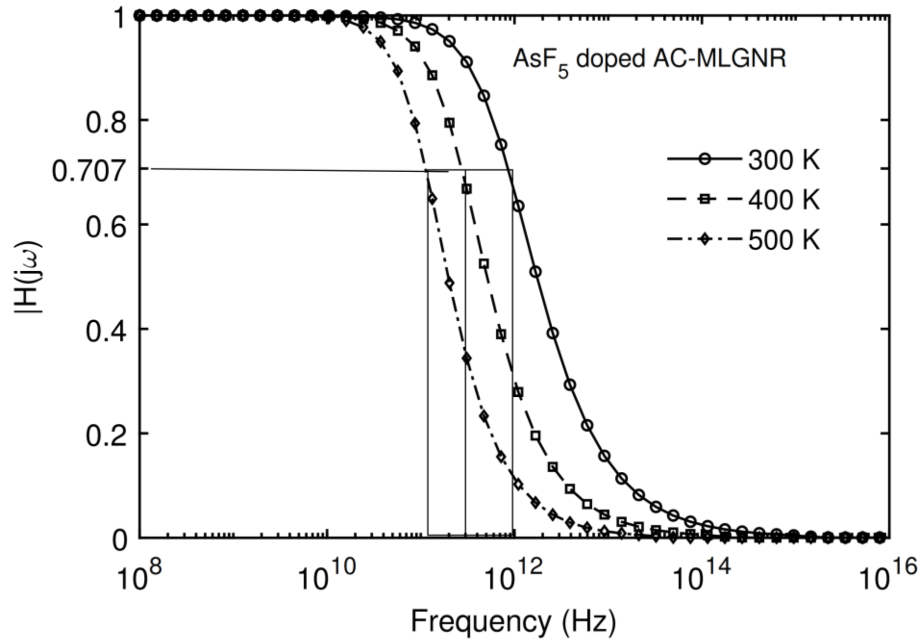

Figure 6.3 Absolute frequency response for coupled interconnects of AsF_5 ID-MLGNR at ℓ = 1000 μm, at different temperatures.

Figure 6.4 shows the absolute frequency response at the far end of 1 *mm* long single and coupled interconnects of AsF_5 ID-MLGNR at T=300 K. The effect of crosstalk in coupled interconnects of ID-MLGNR is evident on its bandwidth performance. With capacitive coupling, a 3-dB BW reduction of 29.3 GHz is noted for ID-MLGNR in comparison to its bandwidth with a single-line configuration.

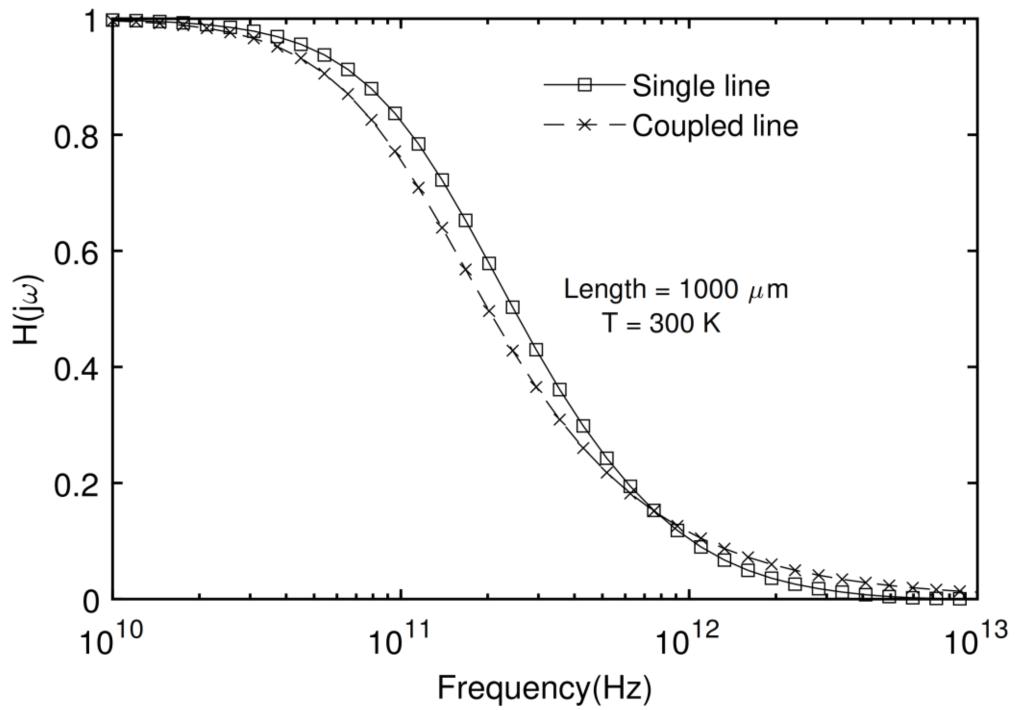

Figure 6.4 Absolute frequency response for single and coupled interconnects of AsF_5 ID-MLGNR at ℓ= 1000 μm, at T=300 K.

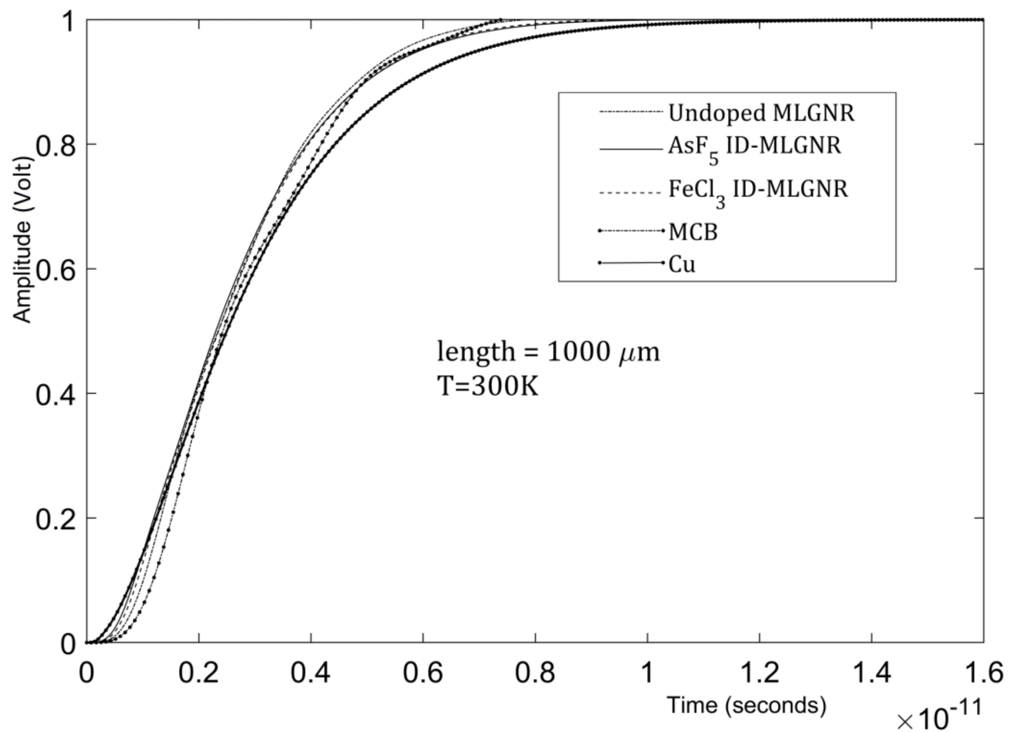

Figure 6.5 Time-domain response for coupled interconnects of U-MLGNR, ID-MLGNR (AsF_5- and $FeCl_3$-doped), MCB and Cu at T=300 K.

Figure 6.5 depicts the time-domain response in terms of step-response at the far end of the aggressor line in capacitively coupled interconnects (in Figure 6.1) of U-MLGNR, ID-MLGNR (AsF_5- and $FeCl_3$-doped), MCB and Cu at interconnect length ℓ = 1000 μm. In the case of ID-MLGNR (AsF_5- and $FeCl_3$-

doped), the 50 % rise time (or propagation delay) of the step response is smaller in comparison to that in the U-MLGNR, MCB and *Cu*, as shown in Table 6.2. Thus, ID-MLGNR demonstrates the smaller propagation delay than the U-MLGNR, MCB and *Cu* for global interconnect length (~ 1 *mm*).

Figure 6.6 shows the time-domain response for 1 *mm* long and 24 *nm* wide coupled interconnects of AsF_5-doped MLGNR at different temperatures within the interval 300 K to 500 K. It is noted that with the rise in the temperature, the N_{ch} in MLGNR interconnects (with fixed length and width) increases, whereas, λ_{eff} decreases [31]. This consequently results in an increase of both $R_{ESC}(T)$ and $C_{ESC}(T)$, and the decrease of $L_{ESC}(T)$. Thereby, the 50 % rise time (or propagation delay) of ID-MLGNR increases with the rise in temperature. To validate the proposed model, the time-domain response of coupled interconnects of ID-MLGNR obtained using the temperature-dependent *R*-model (proposed analytical model) at T = 300 K is compared with that obtained using the temperature-independent *R*-model (analytical model in [63]). It is noted earlier in chapter 4 that equivalent resistance of an MLGNR estimated using the temperature-dependent *R*-model is less than that estimated using the temperature-independent *R*-model. Hence, the 50% rise time (or propagation delay) of ID-MLGNR obtained using the proposed model is less than that using the analytical model (in [63]). The calculated values of rise time using the two models are 2.29 ps and 2.70 ps, respectively.

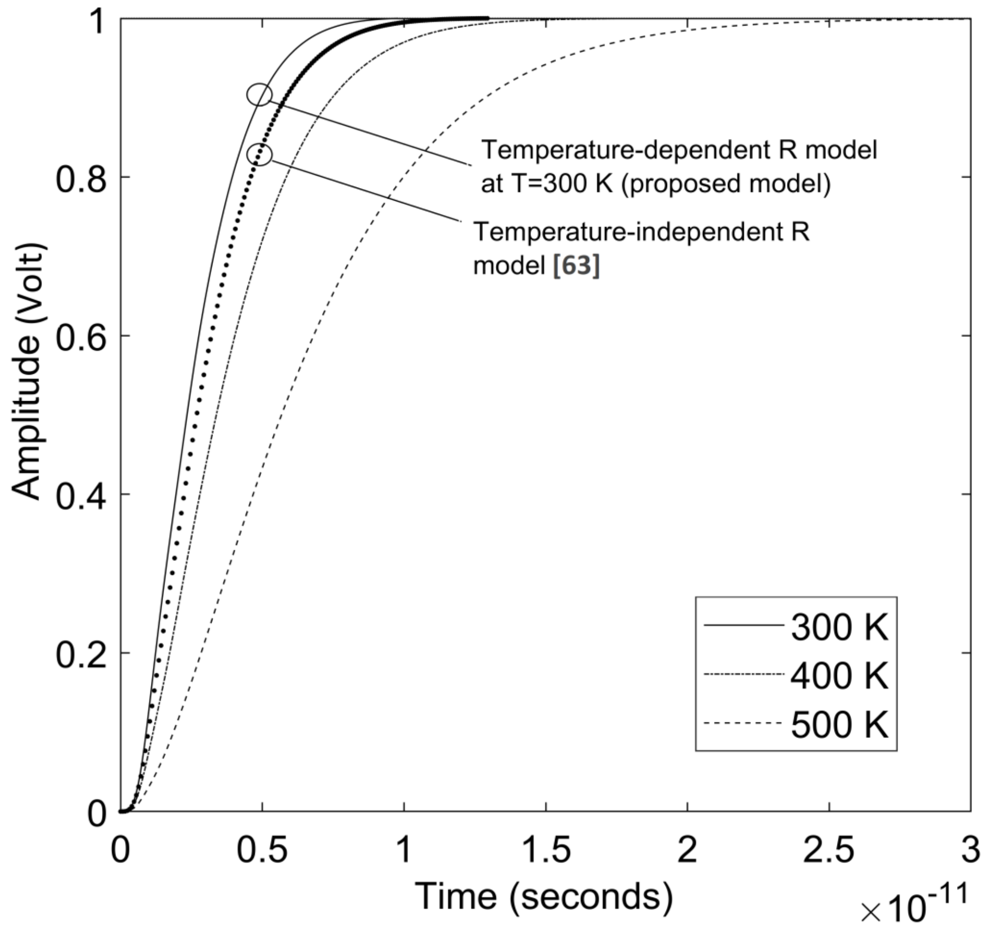

Figure 6.6 Time-domain response for coupled interconnects of AsF_5-ID-MLGNR at ℓ= 1000 μm, W=24 *nm* and different temperatures.

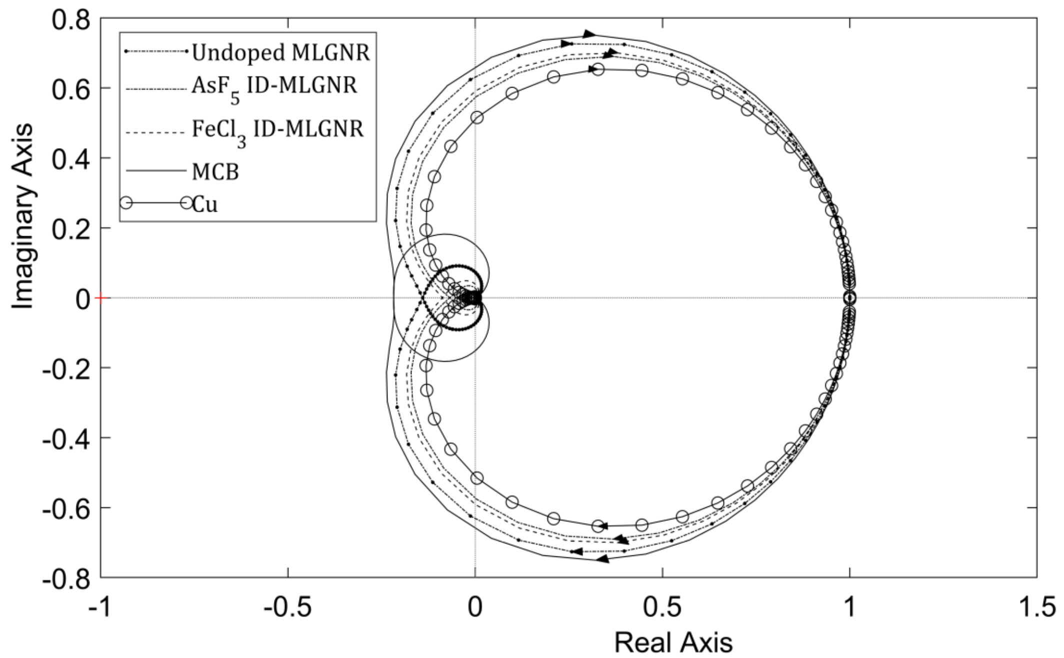

Figure 6.7 Nyquist plot for coupled interconnects of U-MLGNR, ID-MLGNR (AsF_5- and $FeCl_3$-doped), MCB and *Cu* at ℓ= 1000 μm, *T*=300 K.

The relative stability of interconnects is analyzed using the Nyquist plot of the transfer function [49]. In Figure 6.7, Nyquist diagrams for 1 *mm* long coupled interconnects of U-MLGNR, ID-MLGNR (AsF_5- and $FeCl_3$-doped), MCB and *Cu* are plotted at *T* = 300 K. It is indicated that for a system to be stable, the complex point (-1, 0) must be outside of the Nyquist plot, and the stability of the system improves as the distance between the complex point and Nyquist plot increases [49]. That means among the U-MLGNR, ID-MLGNR (AsF_5- and $FeCl_3$-doped), MCB and *Cu*, *Cu* is highly stable. The highest relative stability observed in case of *Cu* interconnect is also justified on the basis of largest rise time obtained for it (as shown in Figure 6.5 and the value given in Table 6.2).

In Figure 6.8 Nyquist diagrams for 1 *mm* long coupled interconnects of AsF_5-ID-MLGNR are plotted at different temperatures, i.e., *T*=300 K, 400 K, and 500 K. It is observed that stability of ID-MLGNR improves with the rise in temperature, i.e., at 500 K. This improvement in the stability with the rise in temperature can be further justified based on rise time plots in Figure 6.6, where it is noted that the rise-time (or propagation delay) of AsF_5-ID-MLGNR interconnect increases with the rise in temperature from 300 K to 500 K. It is indicated that higher the rise time of system implies its improved stability [49]. The stability performance of ID-MLGNR obtained using the temperature-dependent *R*-model (proposed model) at *T*=300 K is also compared with that using the temperature-independent *R*-model (model in [63]). It is found that stability improves with the rise in interconnect resistance (as mentioned earlier that resistance of an MLGNR estimated using the temperature-dependent *R*-model is less than that estimated using the temperature-independent *R*-model). It is also justified on the basis of rise-time (or propagation delay) performance of ID-MLGNR observed in the case of two considered model (see Figure 6.6).

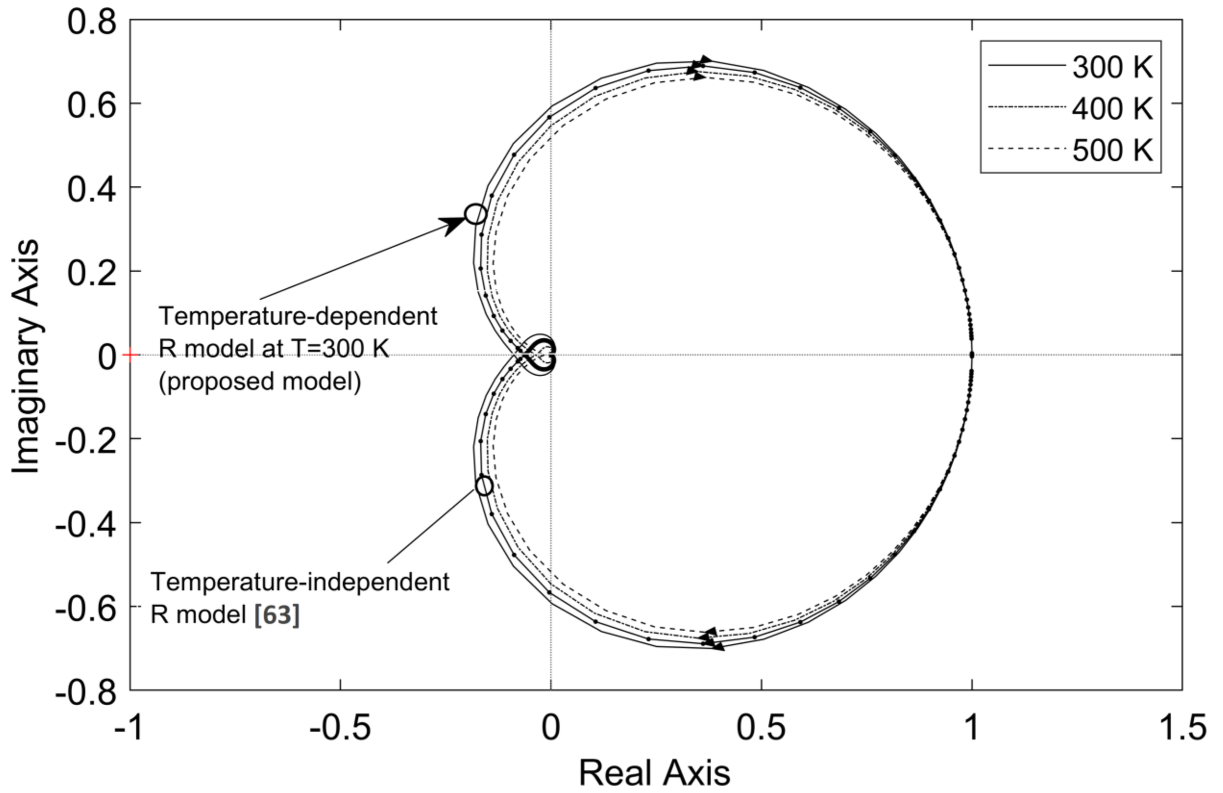

Figure 6.8 Nyquist plot for coupled interconnects of AsF_5-ID-MLGNR at ℓ=1000 μm and different temperatures.

6.5 FREQUENCY DOMAIN ANALYSIS OF CMOS GATE DRIVEN MLGNR INTERCONNECT

The present work (in section 6.4) develops the frequency-domain model of coupled interconnects of MLGNR and MCB under dynamic crosstalk switching conditions of aggressor and victim lines. The transfer function accurately takes into account the parasitics of linear CMOS driver. However, it is indicated that linearization of transistors in CMOS gate leads to an inaccurate estimation of crosstalk results [140],[141]. For accurate estimation of crosstalk, the authors in [140],[141] developed the Alpha Power Law (APL) model of MOS transistor to represent a CMOS driver. It is observed that crosstalk-induced +ve peak noise estimated using APL based CMOS model have nominal average error of 2.97% and maximum error of 7.45% w.r.t. SPICE. While these values, when estimated using linear resistive model, are obtained to be 23.7% and 90%, respectively, which are significantly very high. Since for the CMOS inverter, it is known that the operating regions of the conducting transistors change during the input transition. This change of the operating regions will make the derivation of frequency-domain model of coupled interconnects very complex. However, this work for the first time presents a frequency-domain model for the single interconnect of MLGNR driven by a CMOS gate. For simplicity, the development of the frequency-domain model is achieved with the underlying assumption that the conducting transistors of the driver operate in the triode region for a large portion of the transition time if the line driver has a sufficient current drive capability [148].

Figure 6.9 represents the temperature-dependent ESC circuit of an MLGNR interconnect driven by a CMOS driver with a lumped capacitive load. The figure in the dotted rectangular box represents the simplified equivalent circuit of CMOS driver [148]. The values of the PMOS and NMOS transistor parameters required to calculate drain to source resistance 'R_{ds}' and the diffusion capacitance 'C_{diff}' are obtained from predictive technology model at 14 *nm* technology node. Where C_{diff} denotes the parallel combination of the diffusion capacitance of PMOS and NMOS transistors. The analytical expressions for R_{ds} and C_{diff} can be obtained from "ref [149]".

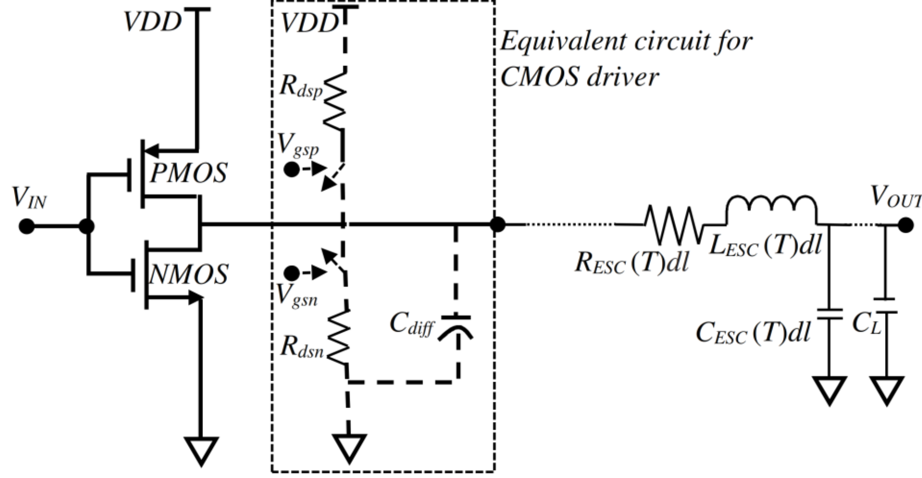

Figure 6.9 The temperature-dependent ESC circuit of an MLGNR interconnect driven by a CMOS driver with a lumped capacitive load [148].

The transfer function of the circuit, shown in Figure 6.9, is obtained as

$$H_{D0} = \frac{1}{1+A_0 s^1+A_1 s^2+A_2 s^3+A_3 s^4} \tag{6.21}$$

Where

$$A_0 = R_{ds}\left(C_{diff} + C_L\right) + R_{im}C_L + \frac{R_{ESC}(T)C_{ESC}(T).\ell^2}{2!} + \left[\left(\frac{R_{im}}{2} + R_{ds}\right)C_{ESC}(T).\ell + R_{ESC}(T).C_L.\ell\right]$$

$$A_1 = R_{ds}C_{diff}R_{im}C_L + \left[\left[R_{ds}\left(C_{diff} + C_L\right) + R_{im}C_L\right]\left[\frac{R_{ESC}(T)C_{ESC}(T).\ell^2}{2!}\right]\right] + \left(\frac{L_{ESC}(T)C_{ESC}(T).\ell^2}{2!} + \frac{R_{ESC}(T)^2C_{ESC}(T)^2.\ell^4}{4!}\right) + \left[\frac{R_{ds}C_{diff}R_{im}C_{ESC}(T).\ell}{2} + \frac{R_{im}{}^2}{4}C_L\,C_{ESC}(T).\ell + L_{ESC}(T).C_L.\ell + R_{ds}C_{diff}C_LR_{ESC}(T).\ell + \frac{R_{ds}C_LR_{im}C_{ESC}(T).\ell}{2} + \left[\left(\frac{R_{im}}{2} + R_{ds}\right)\frac{R_{ESC}(T)C_{ESC}(T)^2\ell^3}{3!}\right] + \left[\frac{R_{ESC}(T)^2C_{ESC}(T)C_L\ell^3}{3!}\right]\right]$$

$$A_2 = \left[R_{ds}C_{diff}R_{im}C_L\right]\left[\frac{R_{ESC}(T)C_{ESC}(T).\ell^2}{2!}\right] + \left[\left[R_{ds}\left(C_{diff} + C_L\right) + R_{im}C_L\right]\left[\frac{L_{ESC}(T)C_{ESC}(T).\ell^2}{2!} + \frac{R_{ESC}(T)^2C_{ESC}(T)^2.\ell^4}{4!}\right]\right] + \left[\frac{2R_{ESC}(T)L_{ESC}(T)C_{ESC}(T)^2\ell^4}{4!} + \frac{R_{ESC}(T)^3C_{ESC}(T)^3.\ell^6}{6!}\right]$$

$$A_3 = 1 + \left[R_{ds}C_{diff}R_{im}C_L\right]\left[\frac{L_{ESC}(T)C_{ESC}(T).\ell^2}{2!} + \frac{R_{ESC}(T)^2C_{ESC}(T)^2.\ell^4}{4!}\right] + \left[R_{ds}\left(C_{diff} + C_L\right) + R_{im}C_L\right]\left[\frac{2R_{ESC}(T)L_{ESC}(T)C_{ESC}(T)^2\ell^4}{4!} + \frac{R_{ESC}(T)^3C_{ESC}(T)^3.\ell^6}{6!}\right]$$

Figure 6.10 shows the absolute frequency response of single interconnect of undoped MLGNR at different interconnect lengths of 5 μm, 500 μm and 2500 μm, using the proposed analytical model and the analytical model in [56] at 14 *nm* technology node. Figure 6.11 shows the absolute frequency response of single interconnect of AsF_5 ID-MLGNR at different interconnect lengths of 10 μm and 1000 μm, using the proposed analytical model and the analytical model (in [56]).

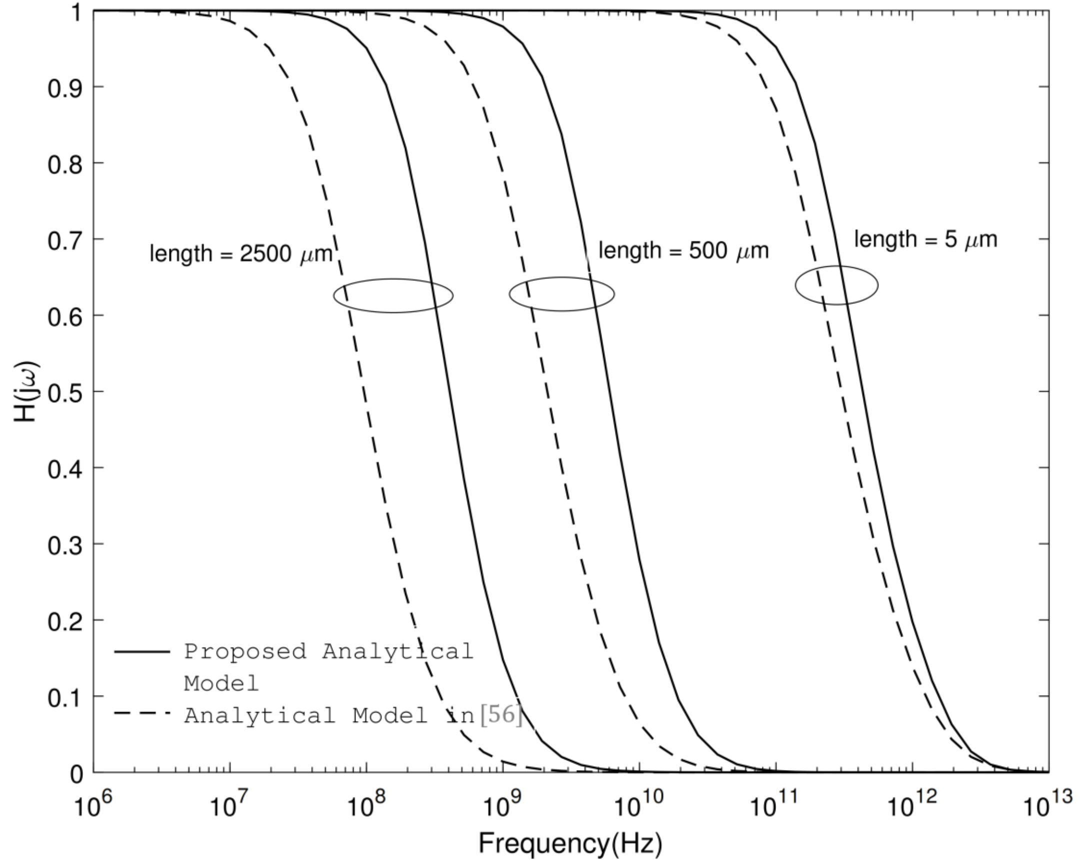

Figure 6.10 The absolute frequency response of single interconnect of undoped MLGNR at different interconnect lengths of 5 μm, 500 μm and 2500 μm.

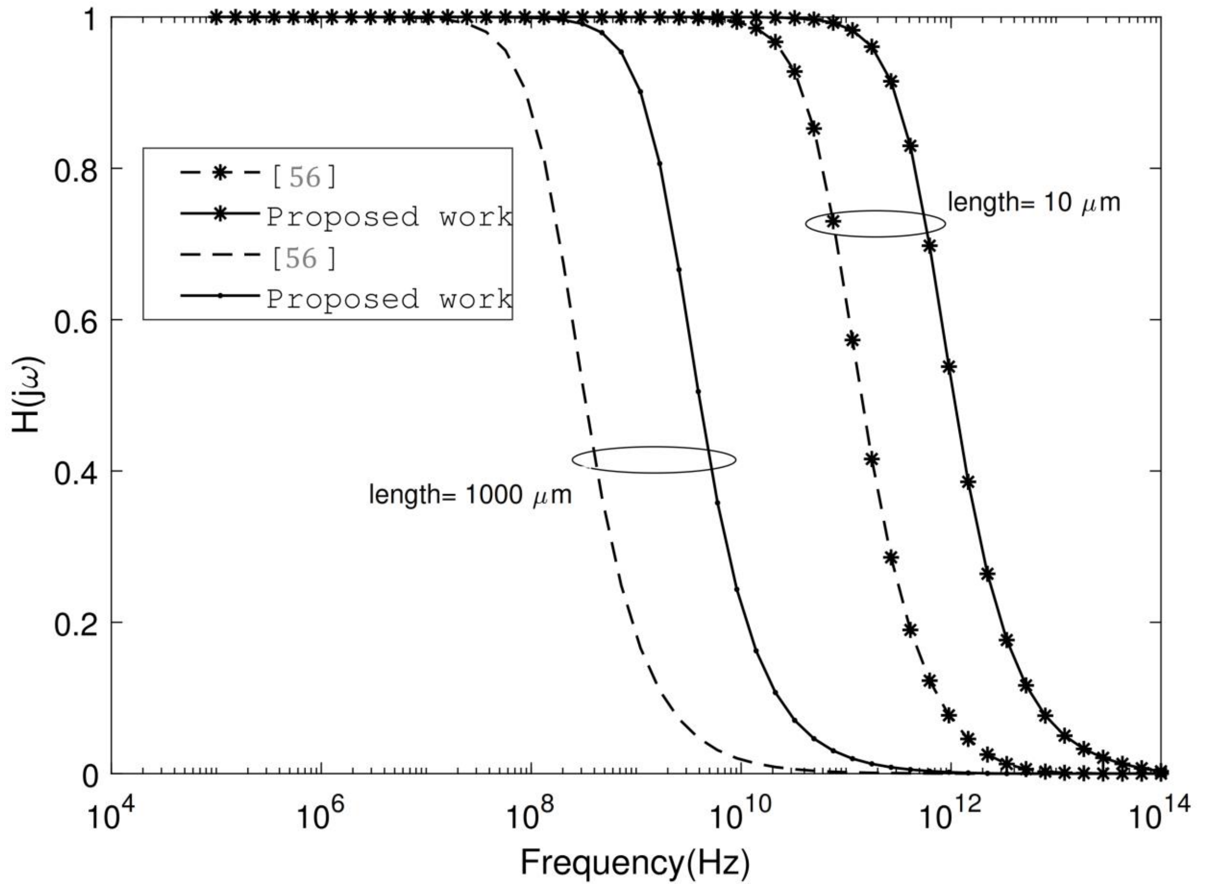

Figure 6.11 The absolute frequency response of single interconnect of AsF_5 ID-MLGNR at different interconnect lengths of 10 *μm* and 1000 *μm*.

It is observed from Figure 6.10 and Figure 6.11 that 3-dB BW of both undoped and AsF_5 ID-MLGNR interconnects improves when driven by an CMOS driver (used in proposed analytical model) rather than by a linear driver (used in analytical model in [56]). It is noted that employing the proposed analytical model, the average improvement in 3-dB BW (in GHz) of a undoped MLGNR is 1.53×, 3.06× and 4.53× at interconnect lengths of 5 *μm*, 500 *μm* and 2500 *μm*, respectively, w.r.t. to values estimated using the analytical model (in [56]). Whereas, in case of AsF_5 ID-MLGNR interconnect (Figure 6.11), these improved values (in GHz) are 7.55× and 12.25× at interconnect lengths of 10 *μm* and 1000 *μm*, respectively.

6.6 FREQUENCY SPECTRUM ANALYSIS OF FUNCTIONAL CROSSTALK NOISE

This section addresses the impact of temperature variation on the frequency spectrum of the functional crosstalk-induced noise waveforms, using the coupled DIL configuration (Figure 6.1), at the 14-*nm* technology node. The functional crosstalk-induced noise waveform is a waveform at the far-end of the crosstalk-affected line (termed as victim line) in the coupled DIL configuration that occurs due to specific switching conditions of the coupled lines [31]. The present analysis is carried out for 1 *mm* long coupled interconnect lines under functional switching (fall-glitch), i.e., the aggressor is switched from

logic 1 to logic 0, and the victim is held at logic 1. A 64-point FFT is used to obtain the frequency components of the victim's output pulse [17].

Figures 6.12 (a) and (b) show the frequency spectrum of the victim's output noise waveforms under functional switching conditions in coupled interconnects of U-MLGNR, MCB, *Cu* and ID-MLGNRs (AsF_5- and $FeCl_3$-doped), respectively, at *T*=300 K. The frequency spectrum amplitudes of the input signal are used to normalize the frequency spectrum amplitudes (along with the y-axis) of the victim's output noise waveforms, while the frequency of the input signal (f_{in} = 0.1 GHz) is used to normalize the output spectrum frequency (along the x-axis).

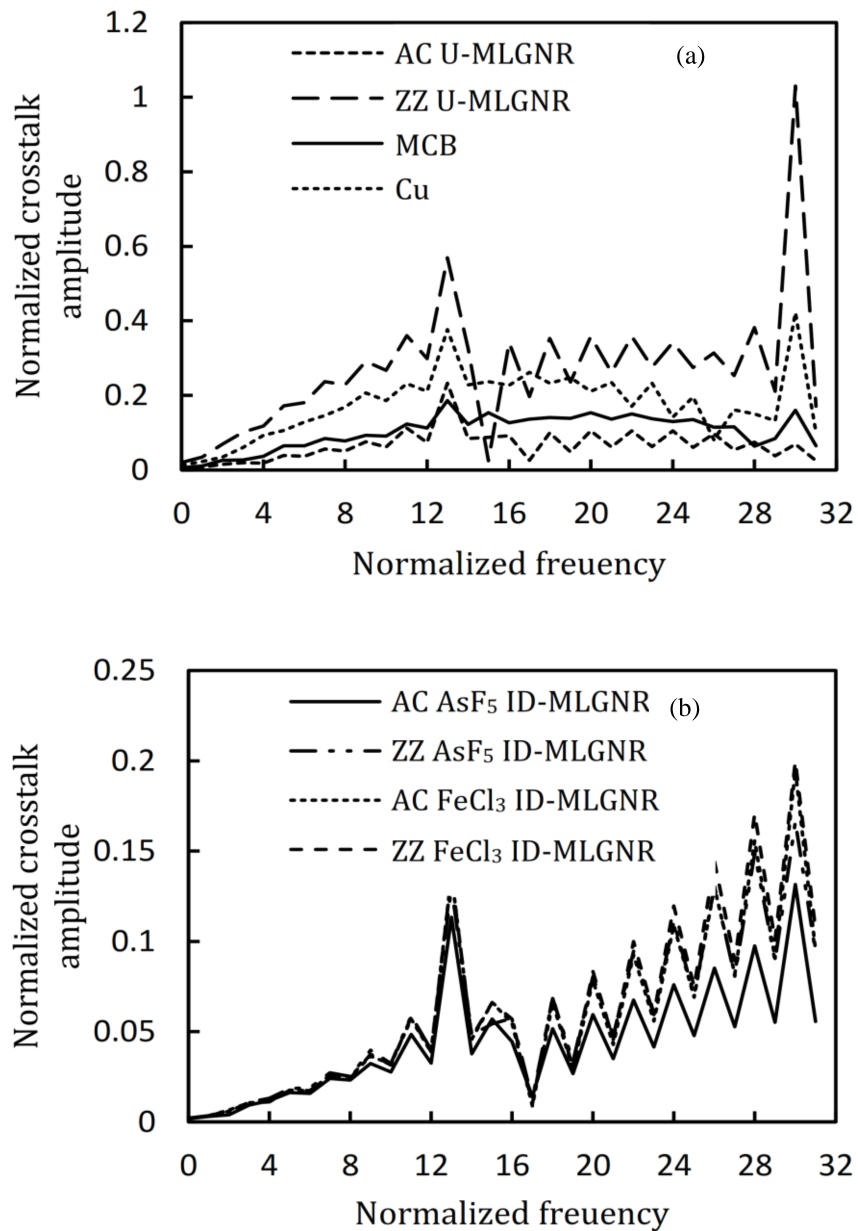

Figure 6.12 Normalized crosstalk noise amplitude as a function of normalized frequency in coupled interconnects of (a) U-MLGNR, MCB and *Cu* and (b) ID-MLGNR (AsF_5- and $FeCl_3$-doped), at ℓ= 1000 μm, *T*=300 K.

In chapter 5, U-, AsF_5- and $FeCl_3$-doped MLGNRs with AC and ZZ edges have been studied for their temperature-dependent crosstalk performance. The present analysis further evaluates the effect of AC and ZZ edge shapes on MLGNR's frequency-domain performance. It is noted from Fig 6.12 (a) that, over the entire normalized frequency domain, among the U-MLGNR, MCB, and *Cu*, the amplitude of noise's frequency spectrum is smallest for U-MLGNR, in particular with AC edges. Similarly, in Figure 6.12 (b), smaller noise amplitude in ID-MLGNRs is noted with AC edges as compared with ZZ edges. Further, the lower amplitude levels of the noise's frequency spectrum are observed in the case of ID-MLGNRs (Figure 6.12 (b)) as compared to U-MLGNR, MCB and *Cu* (Fig 6.12 (a)). This performance improvement of ID-MLGNR, in particular of AsF_5 ID-MLGNR with AC-edges, signifies its best capability to filter out the noise components in the noise waveform at the victim's far end.

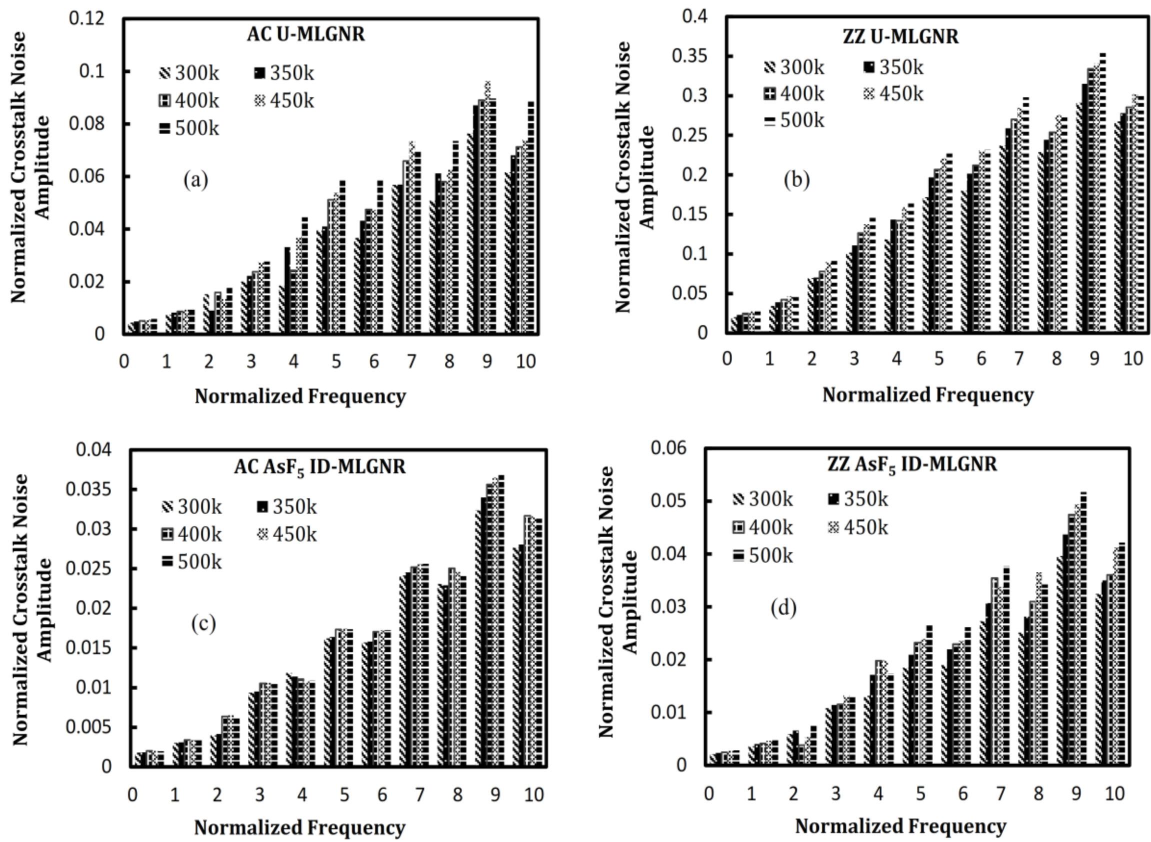

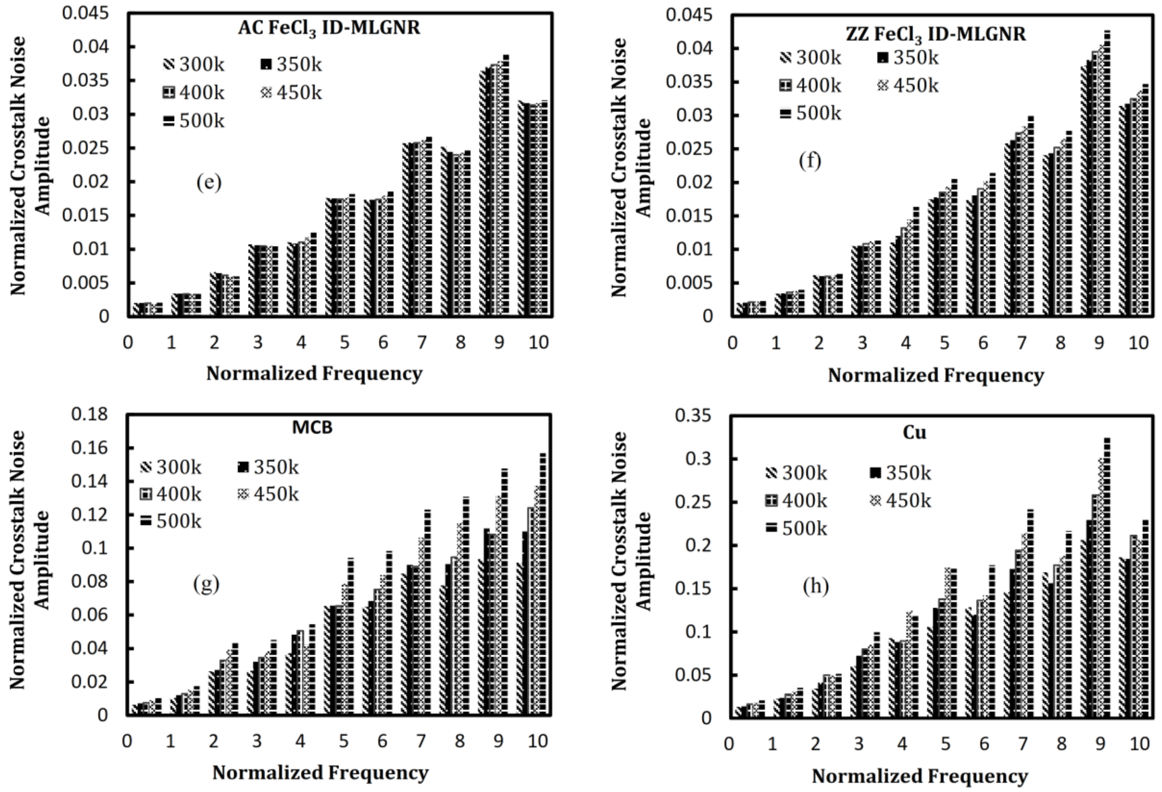

Figure 6.13 Normalized crosstalk noise amplitude as a function of normalized frequency in coupled interconnects of (a)-(f) MLGNR (U, AsF_5- and $FeCl_3$-doped), with AC and ZZ edges, respectively, (g) MCB and (h) *Cu*, at ℓ= 1000 μm and T = 300 K - 500 K.

Figures 6.13 (a)-(h) show the frequency spectrum of the victim's output noise waveforms in coupled DIL configuration of different kinds of MLGNR, MCB and *Cu,* respectively, at different temperatures. It is seen that the amplitude of the noise's frequency spectrum increases with the rise in interconnect temperature. However, AsF_5 ID-MLGNR (AC-edged) kept its advantages, even with the rise in interconnect temperature beyond 300 K, by exhibiting the lowest amplitude of noise's frequency spectrum among all the interconnects considered under present study.

6.7 CONCLUSION

Employing the proposed frequency-domain analytical model under dynamic switching conditions, the bandwidth and delay performance of the capacitively-coupled interconnects of MLGNR (U, $FeCl_3$-doped, and AsF_5-doped), MCB and *Cu* are analyzed, at different chip operating temperatures beyond 300 K, and at local and global levels of interconnect lengths. Bandwidth analysis of the coupled interconnects reveals that AsF_5 ID-MLGNR exhibits the largest bandwidth for both the local and global interconnect length. It is found that 3-dB BW of AsF_5-doped ID-MLGNR improves by 492.7 GHz, at ℓ= 10 μm, and 63.2 GHz at ℓ= 1000 μm in comparison with *Cu*. However, the adverse effect of interconnect temperature on the bandwidth performance of AsF_5-doped ID-MLGNR is observed with the rise in temperature beyond 300 K. The stability analyses of the coupled interconnects reveal that the AsF_5-doped ID-MLGNR interconnect is found more stable than U-MLGNR, $FeCl_3$-doped ID-MLGNR

and MCB interconnects but less stable than *Cu*, and its stability improves with the rise in temperature. Also, a frequency-domain analysis for CMOS-gate-driven single MLGNR interconnect demonstrate that using the proposed CMOS-gate based model, a 3-dB BW improvement of 7.55× and 12.25× is obtained with AsF_5-doped-MLGNR at interconnect lengths of 10 μm and 1000 μm, respectively, w.r.t. to linear resistive model. The frequency-domain analysis under functional switching demonstrates the severe effect of the edge shape (i.e., AC and ZZ) on MLGNR frequency-domain performance. It is noted that the noise-filtering capability of AsF_5-doped ID-MLGNR improves with the AC edge than with the ZZ edge. Hence, AC-edged ID-MLGNR can emerge as a potential and promising material in the DSM regime of VLSI interconnects.

CHAPTER 7

CONCLUSION AND FUTURE SCOPE

7.1 INTRODUCTION

This chapter presents a summary of the complete thesis work. The conclusions are drawn for the results obtained and are given in sections 7.2-7.7. Numerous researchers have proposed ID-MLGNRs as a possible substitute to *Cu* in the high-speed interconnect applications. A few recommendations for the future scope of the work are given in this chapter in section 7.8.

7.2 RESULTS SUMMARY

The approach of VLSI industries to the DSM regime aids in achieving the goals of fast and multitasking electronic devices and systems in the submicron regimes. However, this approach has led to the dismal performance of scaled *Cu* interconnects due to critical issues arisen as a result of technology scaling. The constrained performance of *Cu* interconnects for existing and emerging technology nodes, expectedly be the prime bottleneck in achieving this future industrial goal, and hence demands the introduction of radical change in the design and technology of chip-to-chip interconnects. It has become essential to find a material that is appropriate for potential on-chip interconnect applications to design a high-performance IC. In the past several years, much experimental and theoretical progress has reported that ID-MLGNR as optimistic candidates for future interconnects of advanced IC technology [10], [41], [42], [48], [50], [70], [75], [76], [82].

This work presented a detailed analysis of the influence of temperature on the propagation-delay, power dissipation, PDP, dynamic crosstalk, functional crosstalk, 3-dB BW, stability, and frequency-spectrum in the global interconnects of MLGNR at a technology node of 14 *nm*. The results obtained for MLGNR interconnects are also compared with that of *Cu* and MCB. For the above-said analyses, two important variants of MLGNR, i.e., undoped (neutral) MLGNR and ID-MLGNR (AsF_5-doped and $FeCl_3$-doped) are considered. A DIL configuration is employed, in which interconnect is modeled with a temperature-dependent ESC model. In DIL configuration, for an interconnect line the driver is actuated by a CMOS inverter and load is actuated by the lumped capacitive load (C_L). Further, an analytical frequency-domain model for capacitively coupled interconnects of ID-MLGNR and MCB is developed. The proposed model is used to analyze the bandwidth, delay and stability performance of the coupled interconnects of ID-MLGNR and MCB.

7.3 TEMPERATURE-DEPENDENT PERFORMANCE OF SINGLE-LINE MULTILAYER GRAPHENE NANORIBBON INTERCONNECT

IC often operates at a temperature much beyond room temperature (300 K), which can significantly affect their performance. It is reported that these variations in temperature can also affect the signal

transmission characteristics of MLGNR interconnects [16], [31], [98]. The works reported in the literature [14], [33], [40], [68] have accurately analyzed the superior signal transmission performance of MLGNR interconnects in comparison to SWCNT bundle, isolated MWCNT and *Cu* interconnects. For the performance evaluation of MLGNR interconnects, these authors have taken into account many key factors that can affect its performance (i.e., Fermi energy, edge specularity, interlayer conductance, and intercalation doping), but except for one of the crucial process parameters i.e. the effect of varying operating temperature in ICs. Therefore, to use ID-MLGNR based interconnect materials in future VLSI IC applications, it is essential to develop the thermal model of these interconnects for the accurate estimation of their temperature profile and to study their behavior at the high-performance on-chip operating temperatures beyond 300 K [17].

The presented work developed a temperature-dependent ESC model, which is an improved version of the conventional temperature-independent ESC model. Based on this modified ESC model and incorporating ITRS 2013 update at 14 *nm* technology node, the impact of temperature variations over a range from 300 K-500 K is investigated on the propagation delay, power dissipation and PDP of ID-MLGNR interconnect and is compared with that of MCBs and *Cu* interconnects. In these analyses, a stage-II AsF_5 ID-MLGNR with nearly specular edges and four different structures of MCBs (with and without tunneling effects) are considered.

The SPICE simulation results for global interconnects, high performance predictive technology model, reveal that, for global interconnects, ID-MLGNR has lower propagation delay and power dissipation than MCBs (1-4) with tunneling effects and conventional *Cu* based interconnects over a temperature range from 300 K– 500 K. In the case of MCBs, it is found that MCBWs (with non-consideration of the tunneling effect) outperform MCBs (with tunneling effect), which is due to the absence of tunneling resistance in the former. Among MCBs (1-4), possessing a tunneling conductance effect, MCB-1 is demonstrated to has the least propagation delay and power dissipation. Besides, for AsF_5 ID-MLGNR interconnects, on average, a relative delay improvement of 23.78% and 37.66% is noted in comparison to the best-delay structure of MCBs i.e. MCB-1 and *Cu* interconnects, respectively.

7.4 TEMPERATURE-DEPENDENT CROSSTALK ANALYSIS IN COUPLED INTERCONNECTS OF INTERCALATION DOPED MULTILAYER GRAPHENE NANORIBBON

With the growing density of interconnects, parallel running of adjacent and even non-adjacent interconnects induces inductive and capacitive coupling. These couplings thereby cause the crosstalk effects in coupled interconnects. Taking into account the crucial impact of the crosstalk in coupled interconnects, a few researchers worked primarily to predict the crosstalk performance of MLGNR [39], [40], [71].

Further, like crosstalk, the temperature is also reported to affect the performance of coupled interconnects significantly [16]. Hence, both the crosstalk and the thermal issue were considered

predestined design criteria for the design of future nanoscale interconnects. Most recently, a few researchers have analyzed the temperature-dependent crosstalk performance of both MLGNRs and MCBs based interconnects, at DSM technology nodes [31], [86], [87], [98], [99]. Several theoretical and experimental investigations have proved that ID-MLGNR is the strongest contender for future VLSI interconnects compared to other graphene-based interconnects (i.e. purely metallic SWCNT bundle, MWCNT bundle) [10], [42], [77] due to its key advantages of easy fabrication and intercalation doping. However, to date, no such study is reported that has compared the crosstalk performance of ID-MLGNR with another graphene-based potential interconnect materials i.e. MCB.

Employing a temperature-dependent ESC model which is improved by incorporating the MFP associated with scatterings due to defects in the existing MFP models, this work presents a more realistic and detailed analysis of the influence of temperature-variation on crosstalk-induced noise voltage and the crosstalk-induced time delay in AsF_5 ID-MLGNR (AC-edged) interconnects to explore the reliability issues for these interconnects. For the first time, a comparative analysis of the temperature-dependent crosstalk performance of ID-MLGNR and MCB (with four different structures) interconnects is performed to explore the best alternative to Cu. Note here, that only the stage–II AsF_5 ID-MLGNR is considered here rather than $FeCl_3$ ID-MLGNR due to its higher values of $\sigma_{in-plane}$ (~ 0.63×10^6 (Ω-cm)$^{-1}$) and E_F (~ 0.6 eV) [40]-[43].

The crosstalk analysis carried out for global length (~1000 μm) coupled interconnects of ID-MLGNR, MCB-1 and Cu revealed that in terms of crosstalk-induced noise peaks, over a temperature range 300 K-500 K, ID-MLGNR outperformed both the MCB-1 and Cu. This is because the value of coupling capacitance associated with ID-MLGNR is small as compared to with MCBs and Cu. However, crosstalk-induced noise pulses are found less wide in MCB-1 than in ID-MLGNR and Cu. This is due to the effect of ground capacitance associated with these interconnects. This implies that gate oxide reliability is more with ID-MLGNRs than that with Cu, but gate oxide reliability of ID-MLGNRs is not as good as of MCB-1.

Moreover, ID-MLGNR with nearly specular edges, at the global interconnect dimension, exhibits a lower crosstalk-induced delay as compared to its MCBs-1 and Cu counterparts owing to larger MFP and lower values of impedance parameters. It is also observed that ID-MLGNR possess a significant reduction in odd mode crosstalk-induced delay of 54.09 % and 11.8 % in comparison to Cu and MCBs (MCB-1) interconnects, respectively. Additionally, over a temperature range of 300 K-500 K, ID-MLGNR is observed to have an average relative EM-delay reduction of 10.21% and 73.21% compared to MCBs (MCB-1) and Cu interconnects, respectively. The crosstalk analysis using TD and TI models reveals that the width of the noise pulse obtained using TD models is always less as compared to that obtained using TI models for the entire length of interconnect (200 μm-1000 μm).

7.5 EFFECT OF THE ARMCHAIR AND ZIGZAG EDGES ON FUNCTIONAL AND DYNAMIC CROSSTALK NOISES IN COUPLED INTERCONNECTS OF ID-MLGNR

It is indicated that the shape of GNR's edge plays a key role in the determination of the number of conducting channels (N_{ch}) in MLGNR, and, thereby its conductance [11], [40], [68],[101]. This is justified by the fact that the shape of the GNR edge (AC or ZZ) determines the number of sub-bands present in it. According to the modified tight-binding model, all the subbands in both ZZ and metallic AC-GNR are not degenerative. Thereby, a non-zero bandgap does exist in them. Hence, the theoretical assumption that the ZZ-GNRs are predominantly metallic is in contradiction with the practical scenario with it. In reality, a bandgap is induced in it because of the staggered sublattice potential from magnetic ordering once an electron spin is considered. The bandgap of ZZ-GNRs increases with decreasing wire width W (in *nm*) [11]. Further, as indicated in [11], for $E_F = 0.2$ eV and $W > 10$ *nm*, both semiconducting and metallic AC-GNRs exhibit smaller resistivity than ZZ-GNRs (predominantly metallic). However, in particular, for 20 *nm* $< W <$ 100 *nm*, semiconducting AC-GNRs possess significantly large resistance than metallic AC-GNRs [131]. In the present analysis, the width (W) of the global interconnect (~ 1 *mm*) is considered to be 24 *nm* [118]. Based on the findings as mentioned above, AC-MLGNR is assumed to be metallic to evaluate its ultimate potential for interconnect application.

Knowing these facts about the AC and ZZ-GNRs, the impact of these edge shape in GNR on the interconnect performance of U- and ID-MLGNRs in both single and coupled line configuration is studied in this part of work. Though the work done in [14], [39],[40],[44],[49],[56],[68],[74],[136] took into account the impact of GNR's edge shape while evaluating the interconnect performance of MLGNR, two important aspects were neglected. First, the performance of a single doped MLGNR interconnect was evaluated without considering the coupling effect between the interconnects. Second, the coupled interconnects of only U-MLGNR were considered. For the accurate evaluation of the crosstalk performance in coupled MLGNR interconnects, the following three essential facts are into account. First, the known experiments have verified that TC-MLGNRs can be fabricated easily than SC-MLGNRs [39]. Second, the crucial impact of the operating temperature of ICs [31], [98], [138]. Third, for interconnect width beyond 10 *nm*, metallic AC-GNRs possess more significant conductivity as compared to those of ZZ-GNRs [11].

Incorporating these facts about MLGNR, this work presented the temperature-dependent functional and dynamic crosstalk analyses of TC-MLGNRs (U, AsF_5-doped and $FeCl_3$-doped) considering both AC and ZZ edged GNRs, and compared it with that of MCB. A capacitively-coupled DIL configuration is employed to analyze both the functional and dynamic crosstalk at a 14 *nm* technology node. It is found that over a temperature range of 300 K-500 K, lower values of peaks and time duration of crosstalk-induced noise are obtained in ID-MLGNRs as compared to U-MLGNR with ZZ and AC-edges, respectively. This signifies that ID-MLGNRs are less prone to oxide damage as compared to U-MLGNR and is more reliable.

Further, the smaller values of propagation delay and crosstalk-induced delay are obtained with ID-MLGNR (in particular with AC-edges) as compared to U-MLGNR and MCB. It is attributed to the combined effect of intercalation doping and the high conductivity of AC-edge MLGNRs. The results also reveal that the ID-MLGNR gives better performance than undoped counterparts in terms of switching speed.

7.6 TEMPERATURE DEPENDENT FREQUENCY-DOMAIN CROSSTALK MODEL FOR ID-MLGNR AND MCB

In past, research outcomes in [14], [31], [98], [137] have revealed that crosstalk in adjacent (or coupled) interconnects of MLGNR and MCB affects the reliability and functionality. The operating temperature of the integrated circuit (IC) can worsen the crosstalk performance of these interconnects [14], [31], [98], [137].

In this part of the work, using the developed temperature-dependent ESC model, a new analytical model is developed to analyze the temperature-dependent frequency-domain response in capacitively-coupled interconnects of ID-MLGNR and MCB that incorporates the effect of intercalation doping in MLGNR and inter-shell tunneling resistance in MCB. Employing the proposed frequency-domain analytical model under dynamic switching conditions, the bandwidth and delay performance of the capacitively-coupled interconnects of MLGNR (U, $FeCl_3$-doped and AsF_5-doped) and MCB are analyzed at different chip operating temperatures (beyond 300 K) and at local and global levels of interconnect lengths.

An accurate estimation of 3-dB BW in coupled interconnects revealed that AsF_5 ID-MLGNR exhibits the largest bandwidth for both the local and global interconnect length. It is found that 3-dB BW of AsF_5-doped ID-MLGNR improves by 492.7 GHz at $\ell = 10\ \mu m$, and 63.2 GHz at $\ell = 1000\ \mu m$ in comparison with *Cu*. However, the adverse effect of interconnect temperature on the bandwidth performance of AsF_5-doped ID-MLGNR is observed with the rise in temperature beyond 300 K. The stability analyses of the coupled interconnects reveal that the AsF_5-doped ID-MLGNR interconnect is found more stable than U-MLGNR, $FeCl_3$-doped ID-MLGNR and MCB interconnects but less stable than *Cu*, and its stability improves with the rise in temperature.

Further, a frequency-domain analysis for CMOS-gate-driven single MLGNR interconnect demonstrate that using the proposed CMOS-gate based model, a 3-dB BW improvement of 7.55× and 12.25× is obtained with AsF_5-doped-MLGNR at interconnect lengths of 10 μm and 1000 μm, respectively, with respect to linear resistive model.

Also, the temperature-dependent frequency spectrum of the transient response in coupled interconnects of MLGNR (U, AsF_5-doped, and $FeCl_3$-doped) and MCB is analyzed using a 64-point FFT. The frequency-domain analysis under functional switching demonstrates the severe effect of the edge shape (i.e., AC and ZZ) on MLGNR frequency-domain performance. It is noted that the noise-filtering capability of AsF_5-doped ID-MLGNR improves with the AC edge than with the ZZ edge.

7.7 MAIN RESEARCH CONTRIBUTIONS

- An improved temperature-dependent ESC model, which is improved by incorporating the MFP associated with scatterings due to defects in the existing MFP models, is presented to analytically extract the impedance parameters of both TC-MLGNR and SC-MLGNR.
- Based on this modified ESC model and incorporating ITRS 2013 update at 14 *nm* technology node, the impact of temperature variations over a range from 300 K-500 K is investigated on the propagation delay, power dissipation and PDP of ID-MLGNR (TC) interconnect, and is compared with that of MCBs and *Cu* interconnects.
- Based on a CMOS driven DIL configuration, the influence of temperature-variation on crosstalk-induced noise voltage and the crosstalk-induced time delay in capacitively coupled interconnects of AsF_5 ID-MLGNR (AC-edged) is studied at a 14 *nm* technology node. A comparative analysis of the temperature-dependent crosstalk performance of ID-MLGNR and MCB (with four different structures) interconnects is performed to explore the best alternative to *Cu*.
- Employing the temperature-dependent (TD) and temperature-independent (TI) resistance models, the crosstalk-induced noise is analyzed for ID-MLGNR at different interconnect lengths.
- A detailed analysis to investigate the impact of GNR's edge shape in an AC and ZZ structures on the temperature-dependent functional and dynamic crosstalk performance of TC-MLGNRs (U, AsF_5-doped and $FeCl_3$-doped) interconnects is presented. The results computed are also compared with that of MCB.
- An analytical model is developed to analyze the frequency-domain response of capacitively-coupled interconnects of ID-MLGNR and MCB. Employing the proposed frequency-domain analytical model under dynamic switching conditions, the bandwidth and delay performance of the capacitively-coupled interconnects of MLGNR (U, $FeCl_3$-doped, and AsF_5-doped) and MCB are analyzed at different chip operating temperatures (beyond 300 K) and at local and global levels of interconnect lengths.
- Based on the Nyquist stability criterion, the stability of MLGNR (U, $FeCl_3$-doped and AsF_5-doped) and MCB is also analyzed. For ID-MLGNR, in particular, AsF_5-doped MLGNR interconnects, the stability is analyzed at different temperatures beyond room temperature (300 K).
- The temperature-dependent frequency spectrum of the victim's output noise waveforms (transient response) under functional switching conditions in coupled interconnects of U-MLGNR, MCB, *Cu* and ID-MLGNRs (AsF_5- and $FeCl_3$-doped) is analyzed. The parameters of the frequency spectrum (i.e., amplitude and frequency components) are obtained by writing a script in MATLAB, based on a 64-point FFT technique.

7.8 FUTURE SCOPE OF THE WORK

In the present work, the performance of intercalation-doped TC-MLGNR is analyzed for its delay, power dissipation and PDP, crosstalk-induced delay, crosstalk-induced noise, reliability and 3-dB BW for global level interconnects. Based on these detailed analyses, the presented work has demonstrated that the global interconnects of doped TC-MLGNR rather than MCB, as a substitute to *Cu*, can be a strong contender for high-speed interconnect application in DSM regime. It is further supported by the fact that for the global length of interconnects, the resistance of TC-MLGNR nearly approximates to that of SC-MLGNR. Hence, due to the fabrication complexity to develop SC-MLGNR, the use of TC-MLGNR is highly encouraged. However, as the length of interconnects approaches to the local level i.e., $< 100\ \mu m$, the interlayer resistance in TC-MLGNR dominates, thereby overall resistance in TC-MLGNR exceeds to that in SC-MLGNR. Therefore, at a local level, the performance of TC-MLGNR is compromised. Besides, with the reduction in interconnect width, edge roughness in MLGNR dominates, hence, makes it semiconducting. MLGNR with perfectly specular edges can be produced with atomic precision control. Although, it is a challenging task even for the modern lithography approach, but will be very useful to alleviate the performance limitation of the potential doped MLGNR at local interconnect length.

The presented work, based on the proposed analytical models has theoretically investigated the impact of some of the crucial process parameters like operating temperature, intercalation-doping, chirality (edge-shape) and specularity on the interconnect performance of ID-MLGNR in single as well as coupled DIL configuration. Further, this will be very useful to explore analytically the influence of these and other crucial process parameters (like surface roughness, oxide thickness, doping fraction, etc.) on the performance of this material to confirm its reliable interconnect performance.

REFERENCES

[1] Z. Li, L. Wang, Y. Li, Y. Feng and W. Feng, "Carbon-based functional nanomaterials: Preparation, properties and applications," *Composites Science and Technology*, vol. 179, pp. 10-40, Jul 2019.

[2] N. Choudhary, S. Hwang and W. Choi, "Carbon nanomaterials: a review," *in Handbook of nanomaterials properties*, pp. 709-769, Springer, Berlin, Heidelberg, 2014.

[3] M. S. Dresselhaus, and M. Terrones, "Carbon-based nanomaterials from a historical perspective," *Proceedings of the IEEE*, vol. 101, no. 7, pp. 1522-1535, 2013.

[4] X. Chen, D. Akinwande, K-J. Lee, G. F. Close, S. Yasuda, B. C. Paul, S. Fujita, J. Kong and H-S. P. Wong, "Fully integrated graphene and carbon nanotube interconnects for gigahertz high-speed CMOS electronics," *IEEE Transactions on Electron Devices*, vol. 57, no. 11, pp. 3137-3143, 2010.

[5] H. Li, C. Xu, N. Srivastava and K. Banerjee, "Carbon nanomaterials for next-generation interconnects and passives: Physics, status, and prospects," *IEEE Transactions on electron devices*, vol. 56, no. 9, pp. 1799-1821, 2009.

[6] H. Li, C. Xu and K. Banerjee, "Carbon Nanomaterials: The Ideal Interconnect Technology for Next-Generation ICs," *in IEEE Design & Test of Computers*, vol. 27, no. 4, pp. 20-31, July-Aug 2010.

[7] N. Srivastava and K. Banerjee, "Performance analysis of carbon nanotube interconnects for VLSI applications," *In ICCAD-2005. IEEE/ACM International Conference on Computer-Aided Design*, 2005, pp. 383–390, IEEE.

[8] M. Sahoo and H. Rahaman, "Performance Analysis of Multiwalled Carbon Nanotube Bundles," *In 2013 IEEE XXXIII International Scientific Conference Electronics and Nanotechnology (ELNANO),* 2013, pp. 200-204, IEEE.

[9] M. K. Rai, A. K. Chatterjee, S. Sarkar and B. K. Kaushik, "Performance analysis of multilayer graphene nanoribbon (MLGNR) interconnects," *Journal of Computational Electron*ics, vol. 15, no. 2, pp. 358–366, 2016.

[10] C. Xu, H. Li and K. Banerjee, "Modeling, Analysis, and Design of Graphene Nano- Ribbon Interconnects," *IEEE Transactions on Electron Devices*, vol. 56, no. 8, pp. 1567-1578, Aug. 2009.

[11] A. Naeemi and J. D. Meindl, "Compact physics-based circuit models for graphene nanoribbon interconnects," *IEEE Transactions on Electron Devices*, vol. 56, no. 9, pp. 1822–1833, 2009.

[12] M. R. Choudhury, Y. Yoon, J. Guo and K. Mohanram, "Graphene nanoribbon FETs: Technology exploration for performance and reliability," *IEEE Transactions on Nanotechnol*ogy, vol. 10, no. 4, pp. 727–736, Sep 2011.

[13] J. Guo, M. Lundstrom and S. Datta, "Performance projections for ballistic carbon nanotube field-effect transistors," *Applied Physics Lett*er vol. 80, no. 17, pp. 3192–3194, Apr 2002.

[14] A. K. Nishad and R. Sharma, "Analytical time-domain models for performance optimization of multilayer GNR interconnects," *IEEE Journal of Selected Topics in Quantum Electronics*. vol. 20, no. 1, pp. 17-24, Aug 2013.

[15] V-T. Tran, J. Saint-Martin, P. Dollfus, and S. Volz, "High thermoelectric and electronic performance in graphene nanoribbons by isotope and vacancy engineering," *Materials Today: Proceedings*, vol. 5, no. 4, pp. 10393-10400, Jan 2018.

[16] A. Hosseini and V. Shabro, "Thermally-aware modeling and performance evaluation for single-walled carbon nanotube-based interconnects for future high performance integrated circuits," *Microelectronic Engineering*, vol. 87, no. 10, pp. 1955-1962, 2010.

[17] M. K. Rai and S. Sarkar, "Temperature dependent crosstalk analysis in coupled single-walled carbon nanotube (SWCNT) bundle interconnects," *International Journal of Circuit Theory and Applications*, vol. 43, no. 10, pp. 1367-1378, 2015.

[18] K. I. Bolotin, K. J. Sikes, J. Hone, H. L. Stormer and P. Kim, "Temperature-dependent transport in suspended graphene," *Physical review letters*, vol. 101, no. 9, pp. 096802, Aug 2008.

[19] M. K. Rai, B. K. Kaushik and S. Sarkar, "Thermally aware performance analysis of single-walled carbon nanotube bundle as VLSI interconnects," *Journal of Computational Electronics*, vol. 15, no. 2, pp. 407-419, 2016.

[20] S. Kumar and R. Sharma, "Analytical modeling and performance benchmarking of on-chip interconnects with rough surfaces," *IEEE Transactions on Multi-Scale Computing Systems*, vol. 4, no. 3, pp. 272-284, 2017.

[21] S. Kumar and R. Sharma, "Chip-to-chip copper interconnects with rough surfaces: analytical models for parameter extraction and performance evaluation," *IEEE Transactions on Components, Packaging and Manufacturing Technology*, vol. 8, no. 2, pp. 286-299, 2017.

[22] S. Pathania, S. Kumar and R. Sharma, "Analyzing Crosstalk-Induced Effects in Rough On-Chip Copper Interconnects," *IEEE Transactions on Components, Packaging and Manufacturing Technology*, vol. 9, no. 10, pp. 1984-1992, 2019.

[23] A. Alizadeh, and R. Sarvari, "On temperature dependency of delay for local, intermediate, and repeater inserted global copper interconnects," *IEEE Transactions on Very Large Scale Integration (VLSI) Systems*, vol. 23, no. 12, pp. 3143-3147, 2014.

[24] S-C. Chang, R. M. Iraei, S. Manipatruni, D. E. Nikonov, I. A. Young and A. Naeemi, "Design and analysis of copper and aluminum interconnects for all-spin logic," *IEEE Transactions on Electron Devices*, vol. 61, no. 8, pp. 2905-2911, 2014.

[25] K. Wakabayashi and S. Dutta, "Nanoscale and edge effect on electronic properties of graphene," *Solid State Commun*ication, vol. 152, pp. 1420–1430, 2012.

[26] P. A. Chen, M. H. Chiang and W. C. Hsu, "All-zigzag graphene nanoribbons for planar interconnect application," *Journal of Applied Phys*ics, vol. 122, no. 3, pp. 034301, Jul 2017.

[27] Q-S. Du, P-D. Tang, H-L. Huang, F-L. Du, K. Huang, N-Z. Xie, S-Y. Long, Y-M. Li, J-S. Qiu and R-B. Huang, "A new type of two-dimensional carbon crystal prepared from 1, 3, 5-trihydroxybenzene," *Scientific reports*, vol. 7, no. 1, pp. 1-11, 2017.

[28] A. Maffucci and G. Miano, "Transmission line model of graphene nanoribbon interconnects," *Nanoscience and Nanotechnology Letters,* vol. 5, no. 11, pp. 1207–1216, Nov 2013.

[29] A. Maffucci and G. Miano, "Electrical properties of graphene for interconnect applications," *Applied Sci*ence, vol. 4, no. 2, pp. 305–317, Jun 2014.

[30] Ying-Yu Chen, Amit Sangai, Artem Rogachev, Morteza Gholipour, Giuseppe Iannaccone, Gianluca Fiori and Deming Chen, "A SPICE-compatible model of MOS-type graphene nano-ribbon field-effect transistors enabling gate-and circuit-level delay and power analysis under process variation," *IEEE Transactions on Nanotechnology*, vol. 14, no. 6, pp. 1068-1082, 2015.

[31] M. K. Rai, S. Arora and B. K. Kaushik, "Temperature-dependent modeling and performance analysis of coupled MLGNR interconnects," *International Journal of Circuit Theory and Applications*, vol. 46, no. 2 pp. 299-312, 2018.

[32] X. Liang, Y. S. Jung, S. Wu, A. Ismach, D. L. Olynick, S. Cabrini and J. Bokor, "Formation of bandgap and subbands in graphene nanomeshes with sub-10 nm ribbon width fabricated via nanoimprint lithography," *Nano Letters*, vol. 10, no. 7, pp. 2454-2460, 2010.

[33] D. V. Kosynkin, A. L. Higginbotham, A. Sinitskii, J. R. Lomeda, A. Dimiev, B. K. Price and J. M. Tour, "Longitudinal unzipping of carbon nanotubes to form graphene nanoribbons," *Nature,* vol. 458, no. 7240 pp. 872-876, 2009.

[34] J. Park, A. Akbari-Sharbaf, S. Ezugwu, R. Bauld and G. Fanchini, "Direct synthesis of highly conducting graphene nanoribbon thin films from graphene ridges and wrinkles," *Acta Materialia,* vol. 107, pp. 96-101, 2016.

[35] M. Politou, X. Wu, I. Asselberghs, A. Contino, B. Soree, I. Radu, C. Huyghebaert, Z. Tokei, S. D. Gendt, and M. Heyns, "Evaluation of multilayer graphene for advanced interconnects," *Microelectronic Engineering*, vol. 167, pp. 1–5, 2017.

[36] J. S. Chang, S. Kim, H-J. Sung, J. Yeon, K. J. Chang, X. Li, and S. Kim, "Graphene Nanoribbons with Atomically Sharp Edges Produced by AFM Induced Self-Folding," *small*, vol. 14, no. 47, pp. 1803386, 2018.

[37] S. Akibaa, M. Kosakab, K. Ohashia, K. Hasegawaa, H. Sugimec, and S. Noda, "Direct formation of continuous multilayer graphene films with controllable thickness on dielectric substrates," *Thin Solid Films,* vol. 675, pp. 136–142, 2019.

[38] V. Kumar, S. Rakheja and A. Naeemi, "Performance and energy-per-bit modeling of multilayer graphene nanoribbon conductors," *IEEE transactions on electron devices*, vol. 59, no. 10, pp. 2753-2761, 2012.

[39] L. Qian, Y. Xia and G. Shi, "Study of crosstalk effect on the propagation characteristics of coupled MLGNR interconnects," *IEEE Transactions on Nanotechnology*, vol. 15, no. 5, pp. 810-819, Jun 2016.

[40] W. S. Zhao and W. Y. Yin, "Comparative study on multilayer graphene nano-ribbon (MLGNR) interconnects," *IEEE Transactions on Electromagnetic Compa*tibility, vol. 56, no. 3, pp. 638-646, June 2014.

[41] A. K. Nishad and R. Sharma, "Lithium-intercalated graphene interconnects: Prospects for on-chip applications," *IEEE Journal of the Electron Devices Society*, vol. 4, no. 6, pp. 485-489, 2016.

[42] J. Jiang, J. Kang, W. Cao, X. Xie, H. Zhang, J. H. Chu, W. Liu and K. Banerjee, "Intercalation doped multilayer-graphene-nanoribbons for next-generation interconnects," *Nano letters*, vol. 17, no. 3, pp. 1482-1488, 2017.

[43] J. E. Fischer and T.E. Thompson, "Graphite intercalation compounds," *Physics Today*, vol. 31, pp. 36-45, 1978.

[44] K. N. Reddy, M. K. Majumder and B. K. Kaushik, "Delay uncertainty in MLGNR interconnects under process induced variations of width, doping, dielectric thickness and mean free path," *Journal of Computational Electronics*, vol. 13, no. 3, pp. 639-646, 2014.

[45] A. K. Nishad and R. Sharma, "Performance improvement in SC-MLGNRs interconnects using interlayer dielectric insertion," *IEEE Transactions on Emerging Topics in Computing*, vol. 3, no. 4, pp. 470-482, 2015.

[46] C. Pan, P. Raghavan, A. Ceyhan, F. Catthoor, Z. Tokei and A. Naeemi, "Technology/circuit/system co-optimization and benchmarking for multilayer graphene interconnects at sub-10-nm technology node," *IEEE Transactions on Electron Devices*, vol. 62, no. 5, pp. 1530-1536, 2015.

[47] S. Bhattacharya, D. Das and H. Rahaman, "Analysis of delay fault in GNR power interconnects," *International Journal of Numerical Modelling: Electronic Networks, Devices and Fields*, vol. 31, no. 3, pp. e2308, May 2018.

[48] A. K. Nishad and R. Sharma, "Performance Analysis of AsF_5-intercalated Top-Contact Multi Layer Graphene NanoRibbon Interconnects," *IEEE International Symposium on Nanoelectronic and Information Systems*, IEEE, 2015, pp. 170-174.

[49] V. R. Kumar, M. K. Majumder, N. R. Kukkam and B. K. Kaushik, "Time and frequency domain analysis of MLGNR interconnects," *IEEE Transactions on Nanotechnology*, vol. 14, no. 3, pp. 484-492, 2015.

[50] V. R. Kumbhare, P. P. Paltani, C. Venkataiah, and M. K. Majumder, "Analytical Study of Bundled MWCNT and Edged MLGNR Interconnects: Impact on Propagation Delay and Area," *IEEE Transactions on Nanotechnology*, vol. 18, pp. 606-610, Jun 2019.

[51] W. M. Chanu and D. Das, “Modeling and performance analysis of MLGNR interconnects,” *Journal of Circuits, Systems and Computers*, vol. 27, no. 14, pp. 1850214, 2018.

[52] S. Bhattacharya, D. Das and H. Rahaman, “Analysis of temperature dependent power supply voltage drop in graphene nanoribbon and Cu based power interconnects,” *AIMS Materials Science,* vol. 3, no. 4, pp. 1493-1506, 2016.

[53] S. Bhattacharya, S. Das, A. Mukhopadhyay, D. Das and H. Rahaman, “Analysis of a temperature-dependent delay optimization model for GNR interconnects using a wire sizing method,” *Journal of Computational Electronics*, vol. 17, no. 4, pp. 1536-1548, 2018.

[54] P. D. Nguyen, T. C. Nguyen, A. T. Huynh and E. Skafidas, “High frequency characterization of graphene nanoribbon interconnects,” *Materials Research Express,* vol. 1, no. 3, pp. 035009, 2014.

[55] S. H. Nasiri, M. K. M. Moravvej-Farshi and R. Faez, “Stability analysis in graphene nanoribbon interconnects,” *IEEE Electron Device Lett*ers, vol. 31, no. 12, pp. 1458–1460, Dec 2010.

[56] M. K. Majumder, N. R. Kukkam and B. K. Kaushik, “Frequency response and bandwidth analysis of multi-layer graphene nanoribbon and multi-walled carbon nanotube interconnects,” *Micro & Nano Letters,* vol. 9, no. 9, pp. 557-560, 2014.

[57] S. Bhattacharya, D. Das and H. Rahaman, “Stability analysis in top-contact and side-contact graphene nanoribbon interconnects,” *IETE Journal of Research,* vol. 63, no. 4, pp. 588-596, 2017.

[58] S. Das, D. Das and H. Rahaman, “Electro-thermal RF modeling and performance analysis of graphene nanoribbon interconnects,” *Journal of Computational Electronics,* vol. 17, no. 4, pp. 1695-1708, 2018.

[59] M. Sanaeepur, “Dielectric surface roughness scattering limited performance of MLGNR interconnects,” *IEEE Transactions on Electromagnetic Compatibility,* vol. 61, no. 2, pp. 532-537, 2018.

[60] P. Xu and Z. Pan, “The insertion of high-k dielectric materials in multilayer graphene nanoribbon interconnects for reducing propagation delay and expanding bandwidth,” *Organic Electronics,* vol. 78, pp. 105607, Mar 2020.

[61] S. Das, S. Bhattacharya, D. Das and H. Rahaman, “Thermal Stability Analysis of Graphene Nano-ribbon Interconnect and Applicability for Terahertz Frequency,” *National Academy Science Letters,* pp. 1-5, 2019.

[62] A. Bagheri, M. Ranjbar, S. Haji-Nasiri and Sattar Mirzakuchaki, “Crosstalk bandwidth and stability analysis in graphene nanoribbon interconnects,” *Microelectronics Reliability,* vol. 55, no. 8 pp. 1262-1268, 2015.

[63] L. Qian, Y. Xia, S. Ge, Y. Ye and J. Wang, “Stability analysis for coupled multilayer graphene nanoribbon interconnects,” *Microelectronics journal,* vol. 58, pp. 32-38, Dec 2016.

[64] S. Fotoohi and S. Haji-Nasiri, “Transfer matrix model of multilayer graphene nanoribbon interconnects,” *Microelectronics Reliability,* vol. 79, pp. 193-200, 2017.

[65] K. Agarwal, D. Sylvester and D. Blaauw, “Modeling and Analysis of Crosstalk Noise in Coupled RLC Interconnects,” *IEEE Transactions on computer-aided Design of Integrated Circuits and Systems*, vol. 25, no. 5, pp. 892-900, May 2006.

[66] B. K. Kaushik and S. Sarkar, “Crosstalk analysis for a CMOS-gate-driven coupled interconnects,” *IEEE Transactions on computer-aided Design of Integrated Circuits and Systems,* vol. 27, no. 6, pp. 1150–1154, Jun 2008.

[67] T. Sakuri and A. R. Newton, “Alpha-power law MOSFET model and its applications to CMOS inverter delay and other formulas,” *IEEE Journal of solid-state circuits*, vol. 25, no. 2, pp. 584-594, Apr 1990.

[68] J. Cui, W. Zhao, W. Yin and J. Hu, “Signal Transmission Analysis of multilayer graphene nanoribbons (MLGNR) interconnects,” *IEEE Transactions on Electromagnetic Compatibility*, vol. 54, no. 1, pp. 126–132, 2012.

[69] K. N. Reddy, M. K. Majumder, B. K. Kaushik, S. K. Manhas and B. Anand, “Dynamic crosstalk effect in multi-layer graphene nanoribbon interconnects,” *International Conference on Communications, Devices and Intelligent Systems (CODIS),* Kolkata, 2012, pp. 472-475.

[70] M. Sahoo and H. Rahaman, “Impact of Line Resistance Variations on Crosstalk Delay and Noise in Multilayer Graphene Nano Ribbon Interconnects,” *2014 Fifth International Symposium on Electronic System Design (ISED)*, Surathkal, 2014, pp. 94-98.

[71] V. R. Kumar, B. K. Kaushik and A. Patnaik, “Modeling of crosstalk effects in coupled MLGNR interconnects based on FDTD method,” *IEEE 64th Electronic Components and Technology Conference (ECTC)*, Orlando, FL, 2014, pp. 1091-1097.

[72] V. R. Kumar, B. K. Kaushik and A. Patnaik, "Crosstalk modeling with width dependent MFP in MLGNR interconnects using FDTD technique," *IEEE International Conference on Electron Devices and Solid-State Circuits (EDSSC)*, Singapore, 2015, pp. 138-141.

[73] Y. Agrawal, M. Girish Kumar and R. Chandel, "A Novel Unified Model for Copper and MLGNR Interconnects Using Voltage- and Current-Mode Signaling Schemes," *IEEE Transactions on Electromagnetic Compatibility*, vol. 59, no. 1, pp. 217-227, Feb 2017.

[74] V. R. Kumar, B. K. Kaushik and M. K. Majumder, "Graphene Based On-Chip Interconnects and TSVs: Prospects and Challenges," *IEEE Nanotechnology Magazine*, vol. 8, no. 4, pp. 14-20, Dec 2014.

[75] M. Sahoo and H. Rahaman, "Analysis of crosstalk-induced effects in multilayer graphene nanoribbon interconnects," *Journal of Circuits, Systems and Computers,* vol. 26, no. 06, pp. 1750102, 2017.

[76] B. Kumari and M. Sahoo, "Performance and Power Optimization for Intercalation Doped Multilayer Graphene Nanoribbon Interconnects," *IETE Journal of Research,* pp. 1-10, Jun 2019.

[77] S. G. Hamedani and M. H. Moaiyeri, "Comparative Analysis of the Crosstalk Effects in Multilayer Graphene Nanoribbon and MWCNT Interconnects in Sub-10 nm Technologies," *IEEE Transactions on Electromagnetic Compatibility*, vol. 62, no. 2, pp. 561-570, Apr 2019.

[78] V. R. Kumbhare, P. P. Paltani, and M. K. Majumder, "Impact of Interconnect Spacing on Crosstalk for Multi-layered Graphene Nanoribbon," *IETE Journal of Research,* pp. 1-10, Jul 2019.

[79] S. Bhattacharya, D. Das and H. Rahaman, "Reduced thickness interconnect model using GNR to avoid crosstalk effects," *Journal of computational Electronics,* vol. 15, no. 2, pp. 367-380, 2016.

[80] M. Kaur, N. Gupta and A. K. Singh, "Crosstalk analysis of coupled MLGNR interconnects with different types of repeater insertion," *Microprocessors and Microsystems*, vol. 67, pp. 18-27, 2019.

[81] G. K. Mekala, Y. Agrawal and R. Chandel, "Modelling and performance analysis of dielectric inserted side contact multilayer graphene nanoribbon interconnects," *IET Circuits, Devices & Systems,* vol. 11, no. 3, pp. 232-240, 2017.

[82] D. Das, and H. Rahaman, "Crosstalk and gate oxide reliability analysis in graphene nanoribbon interconnects," *International Symposium on Electronic System Design*, 2011, pp. 182-187, IEEE.

[83] M. Sahoo and H. Rahaman, “Modeling and analysis of crosstalk induced overshoot/undershoot effects in multilayer graphene nanoribbon interconnects and its impact on gate oxide reliability,” *Microelectronics Reliability,* vol. 63, pp. 231-238, 2016.

[84] M. Sanaeepur, “Crosstalk delay and stability analysis of MLGNR interconnects on rough surface dielectrics,” *IEEE Transactions on Nanotechnology,* vol. 18, pp. 1181-1187, 2019.

[85] S. Bhattacharya, D. Das and H. Rahaman, “Analysis of Temperature-Dependent Crosstalk for Graphene Nanoribbon and Copper Interconnects,” *IETE Journal of Research,* pp. 1-12, 2019.

[86] S. G. Hamedani and M. H. Moaiyeri, “Impacts of Process and Temperature Variations on the Crosstalk Effects in Sub-10 nm Multilayer Graphene Nanoribbon Interconnects,” *IEEE Transactions on Device and Materials Reliability,* vol. 19, no. 4, pp. 630-641, 2019.

[87] S. Das, S. Bhattacharya, D. Das and H. Rahaman, “Modeling and analysis of electro-thermal impact of crosstalk induced gate oxide reliability in pristine and intercalation doped MLGNR interconnects,” *IEEE Transactions on Device and Materials Reliability,* vol. 19, no. 3, pp. 543-550, 2019.

[88] A. Alizadeh and Reza Sarvari, “Temperature-dependent comparison between delay of CNT and copper interconnects,” *IEEE Transactions on Very Large Scale Integration (VLSI) Systems,* vol. 24, no. 2, pp. 803-807, 2015.

[89] M. R. Khezeli, M. H. Moaiyeri and A. Jalali, “Analysis of crosstalk effects for multiwalled carbon nanotube bundle interconnects in ternary logic and comparison with Cu interconnects,” *IEEE Transactions on Nanotechnology,* vol. 16, no. 1, pp. 107-117, 2016.

[90] M. R. Khezeli, M. H. Moaiyeri and A. Jalali, “Comparative analysis of simultaneous switching noise effects in MWCNT bundle and Cu power interconnects in CNTFET-based ternary circuits,” *IEEE Transactions on Very Large Scale Integration (VLSI) Systems*, vol. 27, no. 1, pp. 37-46, 2018.

[91] L. Zhu, J. Xu, Y. Xiu, Y. Sun, D. W. Hess and C. P. Wong, “Growth and electrical characterization of high-aspect-ratio carbon nanotube arrays,” *Carbon*, vol. 44, no. 2, pp. 253-258, Feb 2006.

[92] C. L. Cheung, A. Kurtz, H. Park and C. M. Lieber, “Diameter-controlled synthesis of carbon nanotubes,” *The Journal of Physical Chemistry B,* vol. 106, no. 10, pp. 2429-2433, Feb 2002.

[93] S. Subash, J. Kolar and M. H. Chowdhury, "A new spatially rearranged bundle of mixed carbon nanotubes as VLSI interconnection," *IEEE transactions on nanotechnology,* vol. 12, no. 1, pp. 3-12, 2011.

[94] M. K. Majumder, J. Kumar, V. R. Kumar and B. K. Kaushik, "Performance analysis for randomly distributed mixed carbon nanotube bundle interconnects," *Micro & Nano Letters,* vol. 9, no. 11, pp. 792-796, 2014.

[95] M. K. Majumder, B. K. Kaushik and S. K. Manhas, "Analysis of delay and dynamic crosstalk in bundled carbon nanotube interconnects," *IEEE transactions on electromagnetic compatibility,* vol. 56, no. 6, pp. 1666-1673, 2014.

[96] M. G. Kumar, Y. Agrawal, and Rajeevan Chandel, "Carbon Nanotube Interconnects− A Promising Solution for VLSI Circuits," *IETE Journal of Education,* vol. 57, no. 2, pp. 46-64, 2016.

[97] M. K. Majumder, J. Kumar and B. K. Kaushik, "Process-induced delay variation in SWCNT, MWCNT, and mixed CNT interconnects," *IETE Journal of Research,* vol. 61, no. 5, pp. 533-540, 2015.

[98] M. K. Rai, H. Garg and B. K. Kaushik, "Temperature-dependent modeling and crosstalk analysis in mixed carbon nanotube bundle interconnects," *Journal of Electronic Materials,* vol. 46, no. 8 pp. 5324-5337, 2017.

[99] A. Kumar, V. R. Kumar and B. K. Kaushik, "Transient analysis of crosstalk induced effects in mixed CNT bundle interconnects using FDTD technique," *IEEE Transactions on Electromagnetic Compatibility,* vol. 61, no. 5, pp. 1621-1629, 2018.

[100] E. Pop, D. Mann, J. Reifenberg, K. Goodson and H. Dai, "Electro-thermal transport in metallic single-wall carbon nanotubes for interconnect applications," *in Electron Devices Meeting, IEDM Technical Digest. IEEE International*. IEEE, 2005.

[101] S. H. Nasiri, R. Faez and M. K. Moravvej-Farshi, "Compact formulae for number of conduction channels in various types of graphene nanoribbons at various temperatures," *Modern Physics Letters B*, vol. *26*, no. 01, pp. 1150004, 2012.

[102] V. Perebeinos and P. Avouris, "Inelastic scattering and current saturation in graphene," *Physical Review B*, vol. 81, no. 19, pp. 195442, 2010.

[103] S. Rakheja, V. Kumar and A. Naeemi, "Evaluation of the potential performance of graphene nanoribbons as on-chip interconnects," *Proceedings of the IEEE*, vol. 101, no. 7, pp. 1740-1765, 2013.

[104] V. Perebeinos and P. Avouris, "Current saturation and surface polar phonon scattering in graphene," arXiv preprint arXiv:0910.4665, 2009.

[105] P. J. Burke, "Luttinger liquid theory as a model of the gigahertz electrical properties of carbon nanotubes," *IEEE Transactions on Nanotechnology*, vol. 99, no. 3, pp. 129-144, 2002.

[106] M. K. Majumder, B. K. Kaushik and S. K. Manhas, "Analysis of mixed CNT bundle interconnects: Impact on delay and power dissipation," *in 5th International Conference on Computers and Devices for Communication (CODEC)* IEEE, 2012, pp. 1-4.

[107] M. S. Sarto, and A. Tamburrano, "Single-conductor transmission-line model of multiwall carbon nanotubes," *IEEE Transactions on Nanotechnology*, vol. 9, no. 1, pp. 82-92, 2010.

[108] M. K. Majumder, N.D. Pandya, B.K. Kaushik and S.K. Manhas, "Dynamic crosstalk effect in mixed CNT bundle interconnects", *Electronics Letters*, vol. 48 no. 7, Mar 2012.

[109] K. I. Bolotin, K. J. Sikes, J. Hone, H. L. Stormer and P. Kim, "Temperature-dependent transport in suspended graphene," *Physical review letters*, vol. 101, no. 9, pp. 096802, 2008.

[110] M. D'Amore, M. S. Sarto and A. Tamburrano, "Fast transient analysis of next-generation interconnects based on carbon nanotubes," *IEEE Transactions on Electromagnetic Compatibility*, vol. 52, no. 2, pp. 496-503, 2010.

[111] F. Liang, G. Wang and H. Lin, "Modeling of crosstalk effects in multiwall carbon nanotube interconnects," *IEEE Transactions on Electromagnetic Compatibility*," vol. 54, no. 1, pp. 133-139, 2012.

[112] A. Naeemi and J. D. Meindl, "Compact physical models for multiwall carbon-nanotube interconnects," *IEEE Electron Device Letters*, vol. 27, no. 5, pp. 338-340, 2006.

[113] A. Naeemi and J. D. Meindl, "Physical modeling of temperature coefficient of resistance for single-and multi-wall carbon nanotube interconnects," *IEEE Electron Device Letters*, vol. 28, no. 2, pp.135-138, 2007.

[114] H. Li, W. Y. Yin, K. Banerjee and J. F. Mao, "Circuit modeling and performance analysis of multi-walled carbon nanotube interconnects," *IEEE Transactions on electron devices*, vol. 55, no.6, pp. 1328-1337, 2008.

[115] A. Naeemi and J. D. Meindl, "Performance modeling for single-and multiwall carbon nanotubes as signal and power interconnects in gigascale systems," *IEEE Transactions on Electron Devices*, vol. 55, no. 10, pp. 2574-2582, 2008.

[116] M. K. Majumder, N. D. Pandya, B. K. Kaushik, and S. K. Manhas, "Analysis of MWCNT and bundled SWCNT interconnects: Impact on crosstalk and area," *IEEE Electron Device Letters*, vol. 33, no. 8, pp. 1180-1182, 2012.

[117] D. Rossi, J. M. Cazeaux, C. Metra, and F. Lombardi, "Modeling crosstalk effects in CNT bus architectures," *IEEE Transactions on Nanotechnology*, vol. 6, no. 2, pp. 133-145, 2007.

[118] Intl. Tech. Roadmap for Semiconductors (ITRS), 2013. [Online]. Available: http://public.itrs.net.

[119] J. Shioya, H. Matsubara, and S. Murakami, "Properties of AsF5-intercalated vapor-grown graphite," *Synthetic Metals*, vol. 14, no. (1-2), pp. 113-123, 1986.

[120] L. R. Hanlon, E. R. Falardeau and J. E. Fischer, "Metallic reflectance of AsF5-graphite intercalation compounds," *Solid State Communications*, vol. 24, no. 5, pp. 377-381, 1977.

[121] X. Chen, K. J. Lee, D. Akinwande, G. F. Close, S. Yasuda, B. Paul, ... and H. S. P. Wong, "High-speed graphene interconnects monolithically integrated with CMOS ring oscillators operating at 1.3 GHz," *in IEEE International Electron Devices Meeting (IEDM),* 2009*,* pp. 1-4.

[122] M. Katagiri, H. Miyazaki, Y. Yamazaki, L. Zhang, T. Matsumoto, M. Wada, ... and T. Sakai, "Electrical properties of multilayer graphene interconnects prepared by chemical vapor deposition," *in* IEEE *International Interconnect Technology Conference (IITC)*, 2013, pp. 1-3.

[123] F. Liang, H. Lin, and G. Wang, "Prediction of Crosstalk Effects in Future Multiwall Carbon Nanotube (MWCNT) Interconnects," *IEEE conference*, 2010, pp. 1031-1034.

[124] N. Srivastava and K. Banerjee, "Performance analysis of carbon nanotube interconnects for VLSI applications," *in Proceedings of the 2005 IEEE/ACM International conference on Computer-aided design IEEE Computer Society*, May 2005, pp. 383-390.

[125] P. Sharma, I. Kaur, S. Gupta and S. Singh, "Effect of temperature on the conductance of GNRFET," *in AIP Conference Proceedings*. *AIP Publishing LLC*, vol. 1724, no. 1, pp. 020075, 2016.

[126] W. S. Hwang, P. Zhao, K. Tahy, L. O. Nyakiti, V. D. Wheeler, R. L. Myers-Ward, ... and H. Xing, "Graphene nanoribbon field-effect transistors on wafer-scale epitaxial graphene on SiC substrates" *APL materials*, vol. 3, no. 1, pp. 011101, 2015.

[127] Y. Y. Chen, A. Rogachev, A. Sangai, G. Iannaccone, G. Fiori and D. Chen, "A SPICE-compatible model of graphene nano-ribbon field-effect transistors enabling circuit-level delay and power analysis under process variation," *in Proceedings of the Conference on Design, Automation and Test,* Europe, EDA Consortium, Mar 2013, pp. 1789-1794.

[128] E. R. Falardeau, G. M. Foley, C. Zeller, and F. L. Vogel, "Very high electrical conductivity in AsF_5–graphite intercalation compounds," *Journal of the Chemical Society,* vol. 11, pp. 389-390, 1977.

[129] F. L. Vogel, "The electrical conductivity of graphite intercalated with superacid fluorides: experiments with antimony pentafluoride," *Journal of Material Sci*ence, vol. 2, no. 5, pp. 982-986 1977.

[130] G. T. Foley, C. Zeller, E. R. Falardeau, and F.L. Vogel, “Room temperature electrical conductivity of a highly two dimensional synthetic metal: AsF_5-graphite,” *Solid State Communication,* vol. 24, no. 5, pp. 371-375, 1977.

[131] A. Naeemi and J. D. Meindl, “Conductance modeling for graphene nanoribbon (GNR) interconnects,” *IEEE Electron Device Lett*er, vol. 28, no. 5, pp. 428-431, 2007.

[132] M. Politou, X. Wu, I. Asselberghs, A. Contino, B. Soree, I. Radu, C. Huyghebaert, Z. D. Tokei, S. Gendt, and M. Heyns, “Evaluation of multilayer graphene for advanced interconnects,” *Microelectron. Engineering*. vol. 167, pp. 1-5, Jan 2017.

[133] J. Jiang, J. Kang, and K. Banerjee, “Characterization of self-heating and current-carrying capacity of intercalation doped graphene-nanoribbon interconnects,” *IEEE International Reliability Physics Symposium (IRPS),* 2017, pp. 6B-1.

[134] M. K. Majumder, P.K. Das, and B.K. Kaushik, “Delay and crosstalk reliability issues in mixed MWCNT bundle interconnects,” *Microelectrons Reliability*, vol. 54, no. 11, pp. 2570-2577, 2014.

[135] Predictive Technology Model (PTM). [Online]. Available: http://www.eas.asu.edu/~ptm/

[136] D. Das and H. Rahaman, “Analysis of Crosstalk in Single- and Multiwall Carbon Nanotube Interconnects and Its Impact on Gate Oxide Reliability,” *IEEE Transactions on Nanotechnology*, vol. 10, no. 6, pp. 1362-1370, Nov 2011.

[137] J. Cui, W. Zhao, W. Yin and J. Hu, “Signal Transmission Analysis of Multilayer Graphene Nano-Ribbon (MLGNR) Interconnects,” *IEEE Transactions on Electromagnetic Compatibility*, vol. 54, no. 1, pp. 126-132, Feb 2012.

[138] E. Pop, D.A. Mann, K.E. Goodson and H. Dai, “Electrical and thermal transport in metallic single-wall carbon nanotubes on insulating substrates,” *Applied Physics*, vol. 101, pp. 093710, 2007.

[139] P. K. Das, M. K. Majumder and B. K. Kaushik, “Dynamic crosstalk analysis of mixed multi-walled carbon nanotube bundle interconnects,” *The Journal of Engineering,* vol. 2014, no. 5, pp. 227-233, 2014.

[140] B. K. Kaushik and S. Sarkar, “Crosstalk analysis for a CMOS gate driven inductively and capacitively coupled interconnects,” *Microelectronics Journal,* vol. 39, no. 12, pp. 1834-1842, 2008.

[141] B. K. Kaushik, S. Sarkar and R.P. Agarwal, “Waveform analysis and delay prediction for a CMOS gate driving RLC interconnect load,” *Integration the VLSI Journal,* vol. 40, no. 4, pp. 394-405, 2007.

[142] B. K. Kaushik, S. Sarkar, R.P. Agarwal and R.C. Joshi, “Crosstalk analysis and repeater insertion in crosstalk aware coupled VLSI interconnects,” *Microelectronics International,* vol. 23, no. 55, 2006.

[143] V. R. Kumar, B. K. Kaushik, and A. Patnaik, "An accurate model for dynamic crosstalk analysis of CMOS gate driven on-chip interconnects using FDTD method," *Microelectronics Journal,* vol. 45, no. 441, 2014.

[144] D. Fathi, B. Forouzandeh, S. Mohajerzadeh and R. Sarvari, "Accurate analysis of carbon nanotube interconnects using transmission line model," *Micro Nano Letter,* vol. 4, no. 2, pp. 116–121, Jun 2009.

[145] V. R. Kumar, M. K. Majumder, A. Alam, N. R. Kukkam, and B. K. Kaushik, „Stability and delay analysis of multi-layered GNR and multi-walled CNT interconnects," *Journal of Computational Electronics,* vol. *14*, no. 2, pp. 611-618, 2015.

[146] L. Yin and L. He, "An efficient analytical model of coupled on-chip RLC interconnects," *in Proc. IEEE Design Automation Conf. Asian South Pacific*, Jan 2001, pp. 385–390.

[147] G. Chen and E. G. Friedman, "An RLC Interconnect Model Based on Fourier Analysis," *IEEE Transactions On Computer-Aided Design of Integrated Circuits and Systems*, vol. 24, no. 2, Feb. 2005.

[148] P. Heydari, S. Abbaspour, and M. Pedram, "Interconnect Energy Dissipation in High-Speed ULSI Circuits," *IEEE Transactions on Circuits and Systems,* vol. 51, no. 8, Aug 2004.

[149] S.-M. Kang and Y. Leblebici, *CMOS Digital Integrated Circuits Analysis and Design*. New York: McGraw-Hill, 1999.

LIST OF PUBLICATIONS

Published

[1] **Tajinder Kaur**, Mayank Kumar Rai, Rajesh Khanna, Effect of temperature on the performance analysis of MLGNR interconnects. *Journal of Computational Electronics*, vol. 18, no. 2, pp 722-736 (2019). **DOI**: 10.1007_s10825-018-01297-w **(SCI indexed, Impact factor: 1.5)**

[2] **Tajinder Kaur**, Mayank Kumar Rai, Rajesh Khanna, Analysis of Temperature-Dependent Functional and Dynamic Crosstalk Noise in Adjacent Interconnects of Doped Multilayer Graphene Nanoribbon with Armchair and Zigzag Edges, *Physica status solidi (a),* vol. 216, no. 22, pp-1900591-1-1900591-8, Oct 2019. **DOI**: 10.1002pssa.201900591 **(SCI indexed, Impact factor: 1.759)**

[3] **Tajinder Kaur**, Mayank Kumar Rai, Rajesh Khanna, "Temperature-Dependent Circuit Modeling and Performance Evaluation due to Crosstalk in Capacitively Coupled Interconnects of Intercalation Doped Multilayer Graphene Nanoribbon", *Arabian Journal for Science and Engineering*, published online, Sep 2020. **DOI**: 10.1007/s13369-020-04892-x **(SCI indexed, Impact factor: 1.711)**

[4] **Tajinder Kaur,** Mayank Kumar Rai, Rajesh Khanna, " Analytical Frequency-Domain Model for Coupled Interconnects of Doped Multilayer GNRs and Mixed CNT bundles", *Physica status solidi (a),* published online, Dec 2020. **DOI:** 10.1002/pssa.202000588 **(SCI indexed, Impact factor: 1.759)**

Conferences

[1] **Tajinder Kaur**, Mayank Kumar Rai, Rajesh Khanna, Influence of Temperature Variation on Frequency Spectrum Analysis of Intercalation Doped MLGNR Interconnects, in TENCON 2019 IEEE Region 10 Conference (TENCON), pp. 2533-2537, Oct 2019.